Implantable Self-resonant Tag for Passive Sensing

Baraa F. Al-Azzawi

Department of Electronic and Electrical Engineering

University of Sheffield

A Thesis submitted to the University of Sheffield for the degree of

Doctor of philosophy

September 2019

To my family

Abstract

Implantable medical devices have become an integral part of modern day's healthcare system. They can be used for telemetry and monitoring of different biological activities inside the body. They can also be employed to help the body regain certain functions such as restoring hearing sense and regulating heartbeats for arrhythmia patients. This research project suggests the use of self-resonant tag for passive sensing inside the body. The concept of passive sensing eliminates the need for any electronic components on the implant. A self-resonant tag manufactured from biodegradable material can be used to passively sense chemical changes inside the body and communicate this information with an off-body receiver by means of backscattering communications. It is proposed that a biodegradable self-resonant tag can be employed to monitor the healing process of soft tissue trauma. The tag would be implanted near a wound site in the final stages of surgery, and the status of healing tissues can be monitored through the resonance position of the tag.

Biodegradable materials have a certain degradation rate inside the body, when an infection occurs, a change in the degradation rate takes place due to the local increase in temperature and acidity. Thus, a biodegradable self-resonant tag with controlled and predetermined degradation pattern can reflect the state of the soft tissues through the rate of change of its resonance position. This project considers the electromagnetic challenges associated with the design of implantable self-resonant tag. The human body is a highly lossy environment; it causes high attenuation to communication signals. Hence, operation of physically and electrically small self-resonant tag inside human body represents a challenge.

Self-resonant tag was designed and tested experimentally at multiple resonant states (representing the degradation stages). Novel and systematic equivalent transmission line model for self-resonant tag within lossless multi-layer dielectric media has been derived. The equivalent model has been utilised to understand the impact of degradation on the electrical properties of the tag. Moreover, the impact of angle of incidence and surrounding media's thickness and permittivity has been analysed using the equivalent model parameters. The results of equivalent model have been compared to full-wave simulation and experimental measurements with excellent agreement. After that, the derived equivalent model has been extended to account for lossy dielectric media representing the human body environment. A step by step analysis of tag's response within bio tissues has been provided, and the impact of dielectric attenuation on the tag's response has been studied. To verify the equivalent model results, a dielectric phantom has been manufactured and tag's response has been tested with the phantom in a waveguide. Equivalent model and experimental results have shown good agreement. Moreover, an assessment of the electromagnetic exposure and SAR value for a self-resonant tag within multi-layer human body model has been carried out. SAR value at each bio tissue has been identified, and the maximum allowed transmitted power at different frequencies has been defined.

Due to the high dielectric attenuation imposed by the human body on the self-resonant tag, techniques to improve the resonance characteristics of the implantable tag has been investigated. FSS theory has been utilised to improve the response by using multiple elements arranged in an array form. Basic mathematical analysis of the difference between single-element, finite array, and infinite array surfaces has been provided, and experimental measurements comparing single-element tag to array tag has been conducted. Since size of the implant is a critical factor in deciding its suitability for operation inside the body, tag's miniaturisation techniques using capacitive loading has been investigated. Results have shown that it is possible to miniaturise the tag by 2.5 times without affecting its resonance position. Finally, *in-vitro* performance evaluation of miniaturised flexible tag with size of 36x36 mm^2 has been conducted.

Acknowledgments

I would like to express my deepest gratitude and appreciation to my supervisors Dr Jonathan Rigelsford and Prof Richard Langley for their support and guidance during the entire period of my study. It has been a great pleasure to work with them since I was a master's student. My time here at the University of Sheffield has made me a better researcher, engineer, and most importantly, a better person. This would not have been possible without them giving me the opportunity and helping me throughout this period to reach my targets.

Special thanks to Dr Lee Ford for his help and guidance to complete the experimental part of this work.

I would like to thank my family for their love, kindness, and unending support. Their encouragements have lifted me up during the difficult moments of my time as a PhD student.

Additional thanks go to my colleagues in the communication group. The time we have spent together and the memories we have created will be fondly remembered.

Moreover, I would like to thank my close friends for their continuous encouragement and support.

Lastly, I would like to express my gratitude to all the staff at the Electronic and Electrical Engineering department.

Publications

Journal papers

Published:

1- B. F. Al-Azzawi, J. M. Rigelsford, and R. J. Langley, "A Systematic Transmission Line Model for the Analysis of Self-Resonant Structures Within Multi-Layer Dielectric Media," *IEEE Transactions on Microwave Theory and Techniques,* pp. 1-12, 2019, doi: 10.1109/TMTT.2019.2930194. (Section 3.3)

2- B. F. Al-Azzawi, J. M. Rigelsford, and R. J. Langley, "Investigations into improving the detectability of self-resonant RFID tags," *IET Microwaves, Antennas & Propagation,* pp. 1-7, 2018. (Chapter five)

3- J. M. Rigelsford, B. F. Al-Azzawi, C. J. Davenport, and P. Novodvorsky, "A Passive Biodegradable Implant for Subcutaneous Soft-Tissue Trauma Monitoring," *IEEE Journal of Biomedical and Health Informatics,* vol. 19, no. 3, pp. 901-909, 2015, doi: 10.1109/JBHI.2015.2417754. (Some parts of chapter one)

To be submitted:

4- B. F. Al-Azzawi, J. M. Rigelsford, and R. J. Langley, "Analysis of Implantable Self-resonant Tag by an Equivalent Transmission Line Model," *IEEE Transactions on Biomedical Engineering.* (Chapter four)

5- B. F. Al-Azzawi, J. M. Rigelsford, and R. J. Langley, "Miniaturisation of Implantable Self-resonant Tag using Capacitive Loading," *IET Microwaves, Antennas & Propagation.* (Chapter six)

Conference papers

Conference Proceedings:

1- B. F. Al-Azzawi, J. M. Rigelsford, and R. J. Langley, "Equivalent circuit model analysis of reconfigurable self-resonant structures," in *2017 Int. Workshop Electromagn.: App. Student Innov. Compet.*, May 30 2017-June 1 2017, pp. 128-130, doi: 10.1109/iWEM.2017.7968804.

2- B. F. Al-Azzawi and J. M. Rigelsford, "Experimental investigation into improving the detectability of passive RFID tags," in *2016 Loughborough Antennas & Propagation Conference (LAPC)*, 14-15 Nov. 2016, pp. 1-4, doi: 10.1109/LAPC.2016.7807602.

Posters and Presentations:

3- B. F. Al-Azzawi, R. J. Langley, and J. M. Rigelsford, "Evaluating the benefits and limitations of miniaturisation using capacitive loading of implantable self-resonant RFID tags," in *2018 Loughborough Antennas & Propagation Conference (LAPC)*, 12-13 Nov.

4- B. F. Al-Azzawi, J. M. Rigelsford, and R. J. Langley, "Equivalent cituit model analysis of loop frequency selective surfaces," in *2017 Progress in Electromagnetic Research Symposium (PIERS)*, 19-22 Nov 2017.

5- B. F. Al-Azzawi, R. J. Langley, and J. M. Rigelsford, "Equivalent cituit model for active or degradable frequency selective surfaces," in *2017 Progress in Electromagnetic Research Symposium (PIERS)*, 19-22 Nov 2017.

6- B. F. Al-Azzawi and J. M. Rigelsford, "Analysis of M-ary PSK bio-degradable tag," in *2016 Progress in Electromagnetic Research Symposium (PIERS)*, 8-11 Aug. 2016, pp. 5026-5026, doi: 10.1109/PIERS.2016.7735823.

Table of content

LIST OF FIGURES

List of Tables

ABBREVIATIONS

AMR	Antimicrobial resistance
ANSI	American national standards institute
EC	Equivalent circuit
ECM	Equivalent circuit model
FDTD	Finite difference time domain
FIT	Finite integration technique
FSS	Frequency selective surface
FWS	Full wave simulation
HIS	High impedance surface
HOM	Higher order mode
HP	Homogenous phantom
IDC	Interdigital capacitor
IMD	Implantable medical device
MAE	Mean absolute error
MoM	Method of moments
MRI	Magnetic resonance imaging
PCB	Printed circuit board
PCL	Polycaprolactone
PGA	Polyglycolic acid
PLA	Polylactic acid
PP	Parallel plates
RF	Radio frequency
RFID	Radio frequency identification
SAR	Specific absorption rate
Si NM	Silicon Nanomembrane
SP	Solid phantom
SRS	Self-resonant structure

SSI Surgical site infection

TE Transverse electric

TEM Transverse electromagnetic

TLM Transmission line model

TM Transverse magnetic

VNA Vector network analyser

WG Waveguide

SYMBOLS

σ	Electrical conductivity
ρ	Tissue density
α	Attenuation constant
β	Phase constant
Γ	Reflection coefficient
ω	Angular frequency
μ_0	Free space permeability
μ_r	Relative permeability
ε_r	Relative permittivity
ε_{eff}	Effective permittivity
ε_0	Free space permittivity
ε_{r_c}	Complex relative permittivity
$\varepsilon_r{}'$	Real part of complex permittivity
$\varepsilon_r{}''$	Imaginary part of complex permittivity
ℓ	Wire length
k_0	Free space wavenumber
$k_{x/y,m}$	Modal transverse wavenumber
k_c	Complex wavenumber
Z_0	Free space intrinsic impedance
E	Electric field
L	Inductance
C	Capacitance
R	Resistance
G	Conductance
c	free space speed of light
f_g	Grating lobes frequency
$D_{x/y}$	Array inter-element spacing

θ	Incidence angle
$A_h^{TM \because TE}$	Excitation level of higher order modes
$N_{TE/TM}$	Number of higher order modes considered
n, m	Index for higher order mode number
$Z_{TM \because TE,mn}^{(\varepsilon_r)}$	Modal characteristic impedance
Z_d	Transmission line characteristic impedance
$Z_{C/L}$	Frequency dependent impedance of higher order mode
X_L	Inductor impedance
X_C	Capacitor impedance
γ_{mn}	Complex modal wavenumber
β_n	Phase constant of a dielectric layer
d_n	Thickness of a dielectric layer
d_c	Distance between parallel plates of a capacitance
A	surface area of a capacitor plate
φ	Phase response of SRS equivalent circuit
Z_{wg}	Transverse wave impedance of waveguide
λ_0	Free space wavelength
λ_{oc}	Cut-off wavelength of the waveguide
$tan\delta$	Loss tangent
Δx	Minimum Distance between cascaded blocks
w_i	Incident power density
w_t	Transmitted Power density
w_d	Power density at certain distance inside a dielectric medium
A_y	Magnetic poynting vector
J_y	Induced surface current density
U	Dyadic green's function in free space
r	An integer
N	number of fingers in an interdigital capacitor
D	Length of interdigital capacitor

W	Width of a finger in an interdigital capacitor
G	Spacing between adjacent fingers in an interdigital capacitor
f_0	Resonance frequency
$f_{c,mn}^{\varepsilon r}$	Modal cut-off frequency in dielectric medium

1. CHAPTER ONE

Background and Motivation

This chapter covers the background and motivation of this research project. The first part presents a general introduction and explains the main research question, the objectives, the areas of novelty and originality, and the structure of the thesis. On the other hand, the second part introduces the main hypothesis of this project along with the supporting evidence.

1.1 Introduction

To achieve high-quality standards within the healthcare sector, improved and robust health monitoring systems have become a necessity. Such systems can help to reduce the number of specialist medical consultations and hospital admissions. Additionally, they can make the process of establishing medical diagnoses less error prone [1, 2]. Implantable medical devices are being used frequently in diagnosis and treatment of a variety of medical conditions [3]. They can also be used to monitor physiological parameters, such as heart rate, blood pressure and body temperature [2], or glucose levels in blood [4]. Communication often occurs between the implantable device and the external reader via a wireless link.

Colorectal (bowel) cancer is the most commonly diagnosed cancer and the second most common cause of cancer deaths in Europe [5]. In 2008, there were 450 000 new cases of colorectal cancer, and 232 000 deaths caused by this condition within the World Health Organization European Region [6]. Due to location and nature of surgery required to remove this type of cancer, the risk of infection and complications to the wound site, deep within the lower abdomen, can be problematic to the patient. Additionally, shrapnel wounds caused by military combat operations or terrorist attacks are another (and unfortunately far too common) cause of soft-tissue trauma. In the first Gulf War (1990–1991) 80% of penetrating wounds on British personnel were caused by fragments from explosive munitions, such as shells, grenades, and improvised explosive devices, rather than bullets. Beyond the damage caused by shrapnel to tissue and organs within the body, infection will result in further progressive tissue damage and represents a key risk factor for the patient's recovery. Tissue healing may also be delayed by metal poisoning from the shrapnel itself [7]. Data obtained from the wound Data and Munitions Effectiveness Team database [7] show that although there is a 47% chance of the soft tissue being the primary injury site, less than 1% of these result in death. Conversely, injuries to the abdomen (8%) and chest (4%) account for 9% and 24% of fatal injuries, respectively, [8]. Despite the high survival rate from the initial soft-tissue trauma, there is significant potential for long-term complications for a patient who is likely to survive.

Complications and postoperative infections of soft-tissue traumas deep within the body can be difficult to monitor using conventional techniques, such as X-rays or CT/MRI scanners, although the wound site can be marked using medical staples. As the range of currently available effective antibiotics diminishes, treatment via prolonged or extensive doses of antibiotics becomes less feasible. Frequently, complications are only detected when the infection has spread and patient becomes acutely unwell.

This research project presents an investigation into the design of a biodegradable self-resonant tag which can be used to monitor the healing process within the patients who have sustained soft-tissue trauma. The proposed implant eliminates the need for implanting electronic components. It is envisaged that this passive device would be subcutaneously implanted near the wound site during the final stages of surgery. As the soft tissue around the wound site repairs itself, the implanted device will biodegrade and be safely absorbed into the body. This degradation of the device will result in a change to its radio frequency (RF) signature, which can be monitored from outside the patient. Suitable designs will result in a methodology, whereby the rate of tissue repair can be remotely assessed. Currently, complications caused by infection are only detected when the patient becomes acutely unwell, with localized swelling and redness, or with fever. Severe infections may lead to the wound weeping pus. Assessment of the patient using the proposed self-resonant tag can lead to early diagnosis of infection, hence, reducing the over reliance on excessive prescription of antibiotics, and help mitigating unnecessary additional surgery (which in itself can lead to further risk of infection and complications). The implanted self-resonant tag can be monitored from outside the patient using a measurement device similar to the hand held “wand” metal detectors used by airport security. Alternatively, the implant can be continuously monitored using a compact body worn antenna system.

1.1.1 Problem definition

It is well known that the response of a self-resonant tag is affected by the existence of dielectric media in the vicinity of the resonating element. Highly lossy dielectric media such as the human body causes frequency shift and power loss in the response of implantable self-resonant tag. On the other hand, size is a critical factor for any implantable device, as implants need to be as small as possible in order not to intervene with normal biological activities of the human body nor cause discomfort to the patient. Hence, the main research objective of this project is to study the impact of bio tissues on the response of a self-resonant tag. Moreover, investigating the possibility of designing a reasonably small self-resonant tag with electromagnetic response that can be tracked in the lossy media of the human body throughout degradation, to reflect the status of healing tissues.

The concept of passive sensing of the chemical changes inside the body using a biodegradable self-resonant tag raises many research questions in material and medical sciences as well as electromagnetics. In relation to material science, the selection of the biodegradable metal and polymer, their electrical properties and degradation rate inside the body, are all points that need to be addressed. On the other hand, the proposed biodegradable tag imposes some medical challenges. For example, absorbing tag’s remnants can be toxic to the hosting tissues if it exceeds a certain threshold. Hence, the removal rate of tag’s debris through the natural mechanism of human body needs to be precisely calculated based on the implants material, size of the implant, and position of implant inside the body [9, 10].

Although the material and medical challenges will be discussed in the theory and literature review, the technical part of this project will mainly focus on the electromagnetic challenges associated with the design of an implantable self-resonant tag. The objectives of this research project can be summarised in the following points:

- Self-resonant tag design and degradation pattern modelling.
- Investigating the impact of degradation on electrical properties of the tag.
- Examining the impact of dielectric properties of surrounding media on implantable tag response.
- Studying tag response at different angles of incidence.
- Building an equivalent model to help explaining the underlying physics of the structure.
- Investigating techniques to improve tag response to combat dielectric attenuation.
- Exploring miniaturisation techniques for self-resonant tag.
- Conducting SAR calculation and evaluating the level of electromagnetic exposure.

1.1.2 Areas of novelty and originality

A- Primary technical contribution

1- A new systematic procedure for deriving impedance expressions of self-resonant structures (SRS) within lossless multi-layer dielectric media. Novel sets of expressions derived to calculate SRS impedance for normal incidence on dielectric materials (3.27), and within dielectric layers (3.30). Equations (3.31) and (3.32) describe SRS impedance within dielectric materials for TE and TM at oblique angles of incidence, respectively.

2- A new simplified expression for calculating the forward transmission response of an SRS within multi-layer dielectric media has been presented in (3.40) and (3.41), this expression offers fundamental insights into the factors contributing to the S_{21} value.

3- A novel method for extracting the resistance value of the equivalent circuit for an SRS within lossy dielectric media. (Section 4.3.1)

4- A new method for extracting the equivalent circuit parameters of trapped modes for an SRS within lossy media. (Section 4.3.1.2)

5- A novel SAR analysis for far-field electromagnetic exposure by utilising the derived equivalent transmission line model. The impact of frequency of incident signal and tissue conductivity have been evaluated. (Section 4.4)

B- Secondary technical contribution

1- Derived impedance expressions have been utilised to extract equivalent circuit parameters of an SRS within dielectric media. Equivalent circuit values have been exploited to study tag degradation, impact of dielectric media thickness and permittivity, and angle of incidence on tag response and equivalent model accuracy.

2- A step-by-step analysis of the impact of human body on the response of self-resonant tag. The number of modelled bio-tissues and the associated dielectric attenuation of each tissue has been examined using the equivalent circuit values.

3- Conducting waveguide measurements of SRS on lossless and lossy dielectric media, and results have been compared to equivalent model.

4- Basic theoretical analysis for the differences between single-element SRS, finite array SRS, and infinite array SRS has been provided. A comparison between the response of single-element SRS and finite array SRS using experimental measurements has been presented.

5- Miniaturisation of self-resonant tag by 2.5 times using interdigital capacitor to make the tag more suited for implantation inside the body.

6- *In-vitro* performance evaluation of miniaturised flexible self-resonant tag.

1.1.3 Thesis outline

This thesis is comprised of seven chapters. Following the first chapter which covers the introduction and background of the project, the content of remaining chapters can be summarized as follows:

Chapter 2: Covers the theory and literature review of this work. It contains two parts; the first one reviews implantable medical devices, and the second part discusses self-resonant structures.

Chapter 3: Discusses self-resonant tag design, and analyses its response within lossless multi-layer dielectric media by resorting to an equivalent transmission line model representation.

Chapter 4: Studies the impact of lossy dielectric media characterised by a multi-layer human body model on self-resonant tag response using an equivalent transmission line model.

Chapter 5: Presents practical considerations on tag design and geometry. A theoretical analysis of the difference between single-element SRS and array SRS is provided along with experimental validation.

Chapter 6: Considers self-resonant tag miniaturisation techniques using capacitive loading. The response of miniaturised flexible tag is measured *in-vitro*.

Chapter 7: Summarises the main findings of the project and discusses future work.

1.2 Research hypothesis

If self-resonant tag is manufactured from biodegradable materials, it can be used to monitor the healing process of soft tissue trauma from outside the body. The passive tag would be subcutaneously implanted near the wound site during the final stages of surgery. As the soft tissue around the wound site repairs itself, the implanted device will biodegrade and be safely absorbed into the body. This degradation of the device will result in a change to its RF signature, which can be monitored from outside the patient. If the tag is designed to degrade in a predetermined and controlled manner, the rate of change of the resonance frequency can be indicative of the status of the healing soft tissues. When an infection occurs in the wound site during the healing process, the inflammatory response of the human body would cause an increase in temperature and acidity in the infected tissues, which in turn would accelerate the degradation process of the biodegradable material. Hence, a faster rate of change in the resonance frequency of the tag would indicate an infection. If the infection is discovered at an early stage, a small dosage of antibiotic can be used to treat the infection avoiding extra heath complications or prolonged antibiotic course. Next sections will elaborate on the research hypothesis and provide more details and references.

1.2.1 Inflammation mechanism

Inflammation can be defined as a nonspecific biological response of the human body to harmful stimuli, such as infection, radiation, and tissue damage [11]. It represents a nonspecific body defense mechanism in which a number of substances are released from damaged tissues. These further trigger various inflammatory cascades, leading to substantial changes in the surrounding area. Regardless of the cause, inflammatory response shares some common characteristics. It can be characterized by five key signs: heat, pain, redness, swelling and loss of function [12, 13]. It has been shown that injured tissues experience local acidosis - an increase in acidity level (defined by lower pH). This is explained mainly by the increase of lactic acid production as a result of anaerobic metabolism of infiltrated white cells (neutrophils), but also by production of fatty acid by-products of bacterial metabolism [14, 15]. Additionally, the intracellular pH of an activated neutrophil is very low, and this highly acidotic content gets released to the surrounding environment when neutrophils die [16].

1.2.2 Surgical site infections

Surgical site infection (SSI) is a generic term which refers to any postoperative infections developed at the site of surgery [17]. Statistics have shown that about 4–5% of all surgical patients will suffer from the postoperative infection [17, 18]. They are one of the significant causes of morbidity for patients who have undergone a surgery [18], and it has been suggested that SSIs are responsible for about one third of the postsurgical mortality [17]. It has been reported that SSIs can occur at any point up to 30 days after surgery [19]. Apart from the negative impact on the patient health, SSIs impose economic burdens on health services, with patients who suffer from SSIs requiring on average an additional 6.5 days in hospital.

Generally, SSIs are treated with antibiotics [19], although excessive prescription of antibiotics has led to an increase in antibiotic resistant bacterial strains [17].

1.2.3 Antimicrobial resistance

Antimicrobial resistance (AMR) can be defined as the resistance shown by a micro-organism to an antimicrobial medicine which was normally active against the infections caused by it. Pathogens including bacteria, parasites, fungi, and viruses naturally have the ability to adapt and develop a resistance against the drugs that has been effective to fight them [20]. Statistics have shown that between the year of 2000 and 2010 the consumption of antibiotics worldwide has increased by 40%. This enormous rise in antibiotic use, in addition to some improper practices of antibiotic consumption, have led to the rise of some drug-resistant bacterial strains. At the same time, discovering new antibiotics to combat these resistant strains of bacteria has become more difficult than it once was [20].

Nowadays resistant infections cause 700,000 people to die every year, while estimations show that this number would rise up to 10 million by 2050 if AMR issue were left without a solution. This would make AMR the major cause of death exceeding cancer, diabetes and road traffic accidents [20, 21]. Fig. 1.1 below shows the distribution of AMR-caused deaths per continent by 2050. By taking into account the negative impact AMR would have on the labour force, it is expected that AMR would cause a global Gross Domestic Product (GDP) loss of about $100.2 trillion by 2050. Moreover, without effective anti-biotic drugs, conducting normal surgery or applying cancer treatment procedure (i.e. chemotherapy) would become far more dangerous than it used to be [20, 21].

After explaining the effects antimicrobial resistance would have on the world in the future, it is important to discuss the solutions suggested in the literature to tackle this issue. Jim O'Neill

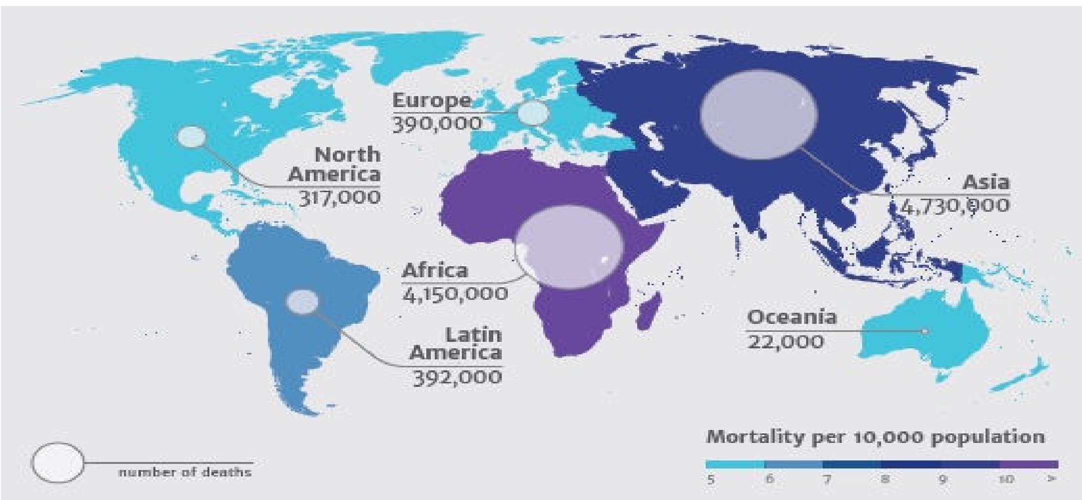

Fig. 1.1 Distribution of AMR-caused deaths per year by 2050 [20].

in his review on antimicrobial resistance in [22] proposed ten fronts to combat AMR, one of these points has suggested promoting a rapid diagnostic tool to limit antibiotic misuse. A reliable and rapid diagnostic tool would help doctors to make the right decision about type and amount of antibiotic needed at the right time and avoid unnecessary prescription. Clearly, reducing antibiotic consumption would help to slow down the emergence of bacterial resistant strains and would lower the urgent needs to discover new antibiotics [22].

The high cost associated with developing a new rapid diagnostic tool has been seen as a limiting factor [22]. Therefore, any attempt to develop a new diagnostic tool should consider this factor. This research project claims that self-resonant tag could offer an inexpensive and rapid diagnostic tool for surgical site infections. Table 1.1 below explains the stages of wounds infection. It can be seen that this process consists of six phases. Without any diagnostic tool, it is not possible to identify the infection until it reaches the last two phases. In other words, infection cannot be identified until the patient becomes acutely unwell with high-grade fever, swelling, and sometimes with more complications such as organs failure and lymph nodes inflammation. The suggested passive tag can identify infection while it is in third or fourth stage. Hence, it can give doctors the chance to treat the infection with low dose of antibiotics, and that would offer a partial solution to the AMR problem.

Table 1.1 Wounds infection stages (modified from [23]).

Infection level		Status of bacterial action	Bacterial effect on wound healing and clinical signs
1	Wound contamination	Availability of bacteria on wound surface but without proliferation	No clinical signs
2	Bacterial colonisation	Bacterial proliferation	No clinical signs
3	Wound surface infection	Biofilm formation (i.e. bacterial products)	Healing process is impaired with subtle clinical signs characterized by more excudate
4	Localized infection	Bacterial invasion to local tissues	More obvious clinical signs across the wound with more exudate, wound size increase, and wound temperature rise
5	Regional infection	Bacterial invasion has spread into neighbouring tissues	Patient may feel slightly unwell with low-grade fever
6	Systematic infection	Bacterial invasion has spread into distant organs through bloodstream	High-grade fever, lymph nodes inflammation, organs failure, etc.

1.2.4 Biodegradable materials for medical implants

Materials used for medical implants should be biocompatible, so they can be safe for the biological body and do not cause the immune system to react against them [24]. The operational time of implants vary according to their applications. For instance, implants used to restore a certain biological function, such as cardiac pacemakers and cochlear implants, are needed for prolonged period of time. Hence, the manufacturing materials should have certain properties to ensure steady performance over a long period of time. On the other hand, some implantable devices are only needed for short period of time, such as electronic pills for targeted drug delivery. Thus, biodegradable materials have been proposed for such implants in order to avoid the need for additional surgery to extract them. Biodegradation refers to the chemical process which converts implanted materials into simpler compositions, and finally into basic chemical elements [25]. With biodegradable materials, there is no need for human intervention to remove the implants after their lifetime has finished, as they will eventually be absorbed by the body. Biodegradable materials have four main types as follows:

1- Polymers

Two types of biodegradable polymers have been widely used in implantable devices; natural polymers such as silk protein, and artificial polymers such as polylactic acid (PLA) and polycaprolactone (PCL) [26]. Silk protein was used as a substrate material in a number of biodegradable implantable devices [27, 28], due to its distinct properties. Its degradation rate can be tailored to be as short as few hours or as long as few years. Moreover, the degradation products are amino acids that can be safely absorbed by the human body [29].On the other hand, PLA has gained special interest due to its ease of fabrication. It has been used in implants for growing cells [30].

2- Conductive polymers

Conductive polymers are organic polymers with high electric conductivity. They have been used in many biomedical applications including tissue engineering and biodegradable electronic devices due to their unique properties. Their electrical conductivity is approaching that of metals, while they maintain the biodegradability and biocompatibility properties of polymers. The conductivity of such polymers is controlled by a doping process in which dopants molecules are added to increase or decrease the number of electrons in the backbone of the polymer [31]. It has been reported that conductive polymers have been employed to manufacture biodegradable lumped components to form an implantable RLC resonant circuit [32]. Despite their high conductivity and quality factor compared to typical polymers, they are still inferior to conductors in this regard.

3- Semiconductors

Silicon (Si) has been indispensable in semiconductor industry in the manufacturing of diodes and transistors. Its unique characteristics has allowed the control of its conductivity by the means of doping using elements such as phosphorous (P) or boron (B) to increase the number of free electrons or holes. Si is normally a non-degradable element. However, it has been found that silicon in Nano-scale dimensions can become dissolvable. Thus, Silicon nanomembrane (Si NM) has been proposed as a potential building block for the new generation of implantable biodegradable semiconductors. Although it has been shown that Si NM is biocompatible even with the availability of some dopants, long-term effects of Si NM dissolution's bi-products on body still needs to be investigated [26, 30].

4- Metals

For several years, studies focused on developing an anti-corrosion versions of implantable metals [10]. Just recently, increasing demands for temporary metallic implants have reversed the paradigm, and made the idea of having corrodible metals a favourable option. Biodegradable metals can be defined as a gradually corroding metals inside the biological environment. They dissolve totally with no adverse effects caused by corrosion debris [9, 10]. Corrosion occurs, with the presence of electrolyte, as a result of an electrochemical reaction. The products of this reaction may include hydrogen gas, oxides, carbonates, and hydroxides (In addition to metal cations) [10]. Degradation should happen at a specific rate which assures that there is no over accumulation of bi-products near the implant site which might cause a bad consequences for the host tissues [9]. Therefore, the concentration of chemical elements in metallic implant along with degradation rate should be carefully studied. Taking into consideration that there is a tolerable limit for the concentration of any chemical element in one area within the body, if this condition is violated it could cause toxicity for the whole body.

Several elements have been used as biodegradable metals including magnesium (Mg), iron (Fe), zinc (Zn), and calcium (Ca). The choice among them depends on the dissolution rate of the implant, the implant potential lifetime, and the location inside the body (which decides the concentration threshold discussed earlier). However, sometimes implants composed of single elements break down quickly and degrade in a non-uniform way inside the body. Hence, some biodegradable metals have been developed as alloys [26]. Several alloys have been reported in the literature but the two most discussed types are Mg-based alloys and Fe-based alloys. Magnesium alloys have been used in aircrafts & automotive industry for a long time. Recently, some magnesium alloys were developed to be biocompatible and biodegradable such as Mg-Al, Mg-Zn, and Mg-Ca [10, 33]. Nowadays, Mg-based alloys are being used in different medical applications such as in orthopaedic implants as pins and screws, and as coronary stents [9]. Mg-based alloys have shown good biocompatibility properties with no adverse effect on the hosting tissues. On the other hand, Iron alloys were used as biodegradable implants due to their excellent mechanical Properties. Iron based alloys are being used in orthopaedic applications to support the healing process of defected bones [10, 34]. A comparison has been made in [32] between the performance of Mg, Fe, Mg-alloys, Fe-alloys, and a number of conductive polymers, as the manufacturing material for RLC resonance circuit. It has been found that Mg and Mg-alloys have shown the highest quality factors among others. Fe-alloys have shown better performance than Fe alone, whilst conductive polymers have shown the lowest quality factor alongside Fe.

From the discussion above, it can be inferred that alloys are preferred over pure elements in the fabrication of biodegradable implants, as they offer a degree of freedom for the designer to tailor their properties such as conductivity, concentration of elements, mechanical strength, and degradation time, to fulfil the intended task.

1.2.4.1 Degradation mechanism

Factors causing polymers to degrade in any medium can be classified as biotic and abiotic elements. The former refers to changes that occur by the help of biological environment, such as microorganisms or enzymes. On the other hand, abiotic agents are mainly environmental factors, such as mechanical forces, light, heat, and chemicals [35]. Degradation time of plastic polyesters in the human body depends on many factors ranging from the surface area and total size of the material, to the material composition itself and the acidity surrounding the implanted material. Research into this area is well documented [36-39]. In this project, we focus on PLA and PGA as a potential biodegradable material for the self-resonant tag's substrate. The difference in degradation between PLA-PCL and PGA-PCL composite fibres in both water and phosphate buffered saline are presented in [40]. This study shows that PGA composite degrades much quicker than the PLA, and copolymerization of the two can be used to control the speed of degradation finely. Furthermore, the effect of acidity on the degradation of PLA brushes over the course of a few weeks has been investigated [41], where results show that the neutral or slightly alkaline solutions result in the fastest breakup of PLA, whereas slightly acidic solutions severely reduce the rate of degradation.

The degradation of polymers and the factors affecting it is well studied, as it has been a research topic for around thirty years. On the other hand, research on biodegradable metals and semiconductors is fairly recent. It has been reported in [42] that the degradation rate of silicon nanomembrane (Si NM) semiconductor is accelerated with the increase of temperature and acidity of the surrounding environment. Similar findings have been reported in [43] for Mg-Al alloys.

1.3 Summary

This chapter has covered the background and motivation of this research project. The first part has discussed the research objectives and highlighted the structure of the thesis, while second part have presented the research hypothesis. This project focuses on the electromagnetic aspects that must be taken into consideration when designing a biodegradable self-resonant tag for subcutaneous soft-tissue trauma monitoring. Having examined how the two key signs associated with infection of soft tissues, namely increase in temperature and acidity can influence degradation behaviour of biodegradable materials, we intend to exploit this in our design of a self-resonant tag in order to detect postoperative infection at early stage, offering a partial solution to the rising problem of antimicrobial resistance.

Although the main objective of this project is to design a self-resonant tag to tackle the problem of surgical site infections, the concept of passive monitoring can be used for sensing different chemical changes in the biological environment from outside the body. The concept of passive sensing using biodegradable materials is described in Fig. 1.2.

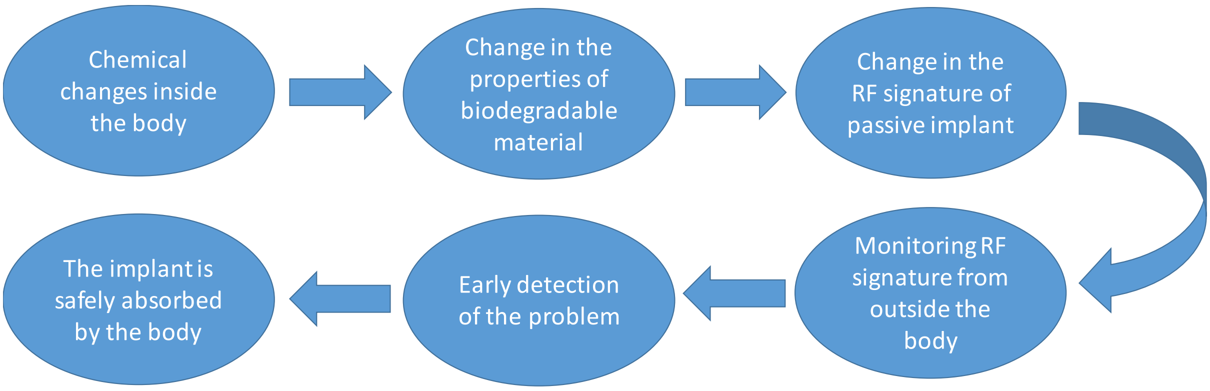

Fig. 1.2 The concept of passive sensing inside the body using biodegradable RF implant.

2. CHAPTER TWO

Theory and Literature Review

This chapter covers the theory and literature review of this research project. The first part discusses the categories and applications of implantable medical devices, followed by a discussion about the modelling of human body and specific absorption rate. The second part covers electromagnetic self-resonant structures. Finally, the concept of equivalent models is explained.

2.1 Implantable medical devices

Implantable medical devices (IMDs) are electronic based implants that perform a certain task inside the human body. They are usually implanted in the body after surgery for sensing and monitoring purposes, and they communicate with an off-body receiver to keep the doctors and nursing staff informed about the status of the patient underlying condition. Hence, IMDs improve patients healthcare and reduce the costs of health services as they help in avoiding extra health complications that may lead to unnecessary operations and prescriptions, or prolong patients stay in the hospital [44, 45].

Many challenges are associated with IMDs design. Firstly, any implantable device needs to be made of biocompatible material to ensure that they do not cause any negative reaction by the immune system. Secondly, they need to be as small as possible so they do not interfere with normal biological activities of the human body or cause a discomfort to the patient. Thirdly, the lossy nature of hosting biological tissues affect the performance of electronic components and impact the communication with the external receiver. In fact, lossy dielectric media can cause signal power dissipation, frequency shift, and antenna’s radiation pattern distortion. Fourthly, the power source of the implantable device is a major challenge due to size requirements and limitation of available energy in the surroundings of the implantable device [46]. IMDs can be categorised in terms of powering mechanism as follows:

1- Active devices

Active implantable devices have on-board battery as a power source for the on-board electronic circuitry. The main example of active IMDs is pacemaker. The latter is a small device implanted in the chest area of the patient and used for generating electrical pulses which help regulating heartbeats for patients suffering from arrhythmia [47]. The average lifetime of pacemaker battery is 10-15 years, and replacement surgery is needed to change the battery after its lifetime has finished. Some attempts have been made recently to investigate the possibility of using wireless power transfer instead of on-board battery for leadless pacemakers [48]. The second example of active IMDs is cochlear implant, which is basically used to restore hearing function in patients suffering from sensorineural hearing loss. Cochlear implant consists of two parts; an external part responsible for converting sounds into electrical signals, and an internal part implanted inside the head which receives the electrical signals via wireless link and use them to stimulate the auditory nerve. Although cochlear implants can be classified as active devices, they, unlike pacemakers, have the battery in the external unit [49].

Even though active devices can perform sophisticated functions inside the body due to the availability of on-board power source, the existence of batteries increase the size of the implant. Moreover, the limited lifetime of the on-board battery necessitates another surgery to replace them.

2- Passive devices

The term 'Passive' is used for any implantable device that do not have an on-board power source and relying on either an external or environmental power source, or operating in a completely passive mode. They can be categorised into three groups as follows:

a- Wireless power transfer

Electrical power can be transferred to the implant via wireless link. Four main types of wireless power transfer has been reported in the literature as follows:

- Inductive coupling
  Energy can be transferred into the in-body implant by alternating magnetic field, where energy is transferred from an off-body coil to a secondary coil implanted inside the body. The power received by the secondary coil can then be used as a power source for the electronic circuitry of the implant. It has been suggested in [50] that inductive coupling mechanism can be utilized to apply localized thermal therapy for targeted tissues. The power received by the in-body coil is used to drive electric current in an implantable resistor. The heat generated by power dissipation in the resistor would inhibit the bacterial growth in the wound site, and consequently preventing any possible infection. Although inductive coupling can be an efficient power transfer technique with low absorption loss, it only has high efficiency when there is perfect alignment between the two coils. Moreover, Inductive coupling is a near field phenomenon. Thus, transmitting and receiving coils have to be in the same proximity as magnetic field decays very fast with distance from the coil [46, 51].

- Capacitive coupling
  Few attempts have been made recently to use near-field capacitive coupling instead of inductive coupling for powering implants [52, 53]. It has been reported in [52] that by using two metal parallel plates across the skin, it is possible to transfer energy into the body. The off-body plate is connected to an AC source while the in-body plate is connected to the implant's circuitry. The bio-tissues between the two plates act as the capacitor's dielectric medium, and energy is transferred using generated displacement current. It has been shown that by using parallel patches with size of

20x20 mm^2 it is possible to transfer power up to 140 mW across the skin at frequency of 130 MHz. Although capacitive coupling is less sensitive to misalignment between sending and receiving plates than inductive coupling, it can cause temperature rise in the bio tissues between the parallel plates, raising some safety concerns. Moreover, similar to inductive coupling, distance between transmitting and receiving objects has to be short.

- Ultrasonic transmission
  By definition, ultrasonic waves has a frequency of more than 20 KHz. However, in biomedical applications ultrasonic waves usually have a frequency between 1-20 MHz. The mechanism of wireless power transfer using ultrasonic waves involves an off-body piezoelectric transducer which converts electrical waves into ultrasonic waves. The latter carries the energy through the bio tissues into an implanted transducer which in turn converts the ultrasonic wave back into electrical signal. The converted electrical power then rectified, filtered, and delivered to the electronic circuitry. The advantage of using ultrasonic waves is that they do not cause electromagnetic interference as they are basically mechanical waves. Moreover, with ultrasonic waves, energy can travel for longer distances than inductive and capacitive coupling. However, the energy transfer efficiency is usually low [46, 54]. It has been reported in [55] that an output power of 1 W was transmitted through water using ultrasonic waves for a distance of 40 mm with an efficiency of 27% at 673 KHz.

- Far field electromagnetic wave
  In order to avoid the drawbacks associated with near-field power transfer, namely the short propagating distance and the sensitivity to misalignment, it is possible to power the in-body implant using far field electromagnetic waves. Energy can be transmitted from an off-body antenna and received by an implantable antenna. Received power would then be rectified to convert the RF signal into a DC signal and delivered to the implant's circuitry. It has been suggested in [56] that the implantable antenna and the rectifier can be integrated together as a rectenna. A horn antenna with gain of 7.6 dBi was used as the off-body antenna, while the implanted antenna was attached to a piece of pork meat at a distance of 300 mm from the horn antenna. At -20 dBm input power, a DC voltage of 89 mV was obtained at the output of the in-body rectenna at 2.5 GHz.

b- Energy harvesting

A lot of research have been done over the years to investigate the possibility of harvesting energy from the body environment to generate electrical power for implantable medical devices. The two main types that has been reported in the literature are thermal energy and kinetic energy [54]. Thermoelectric generators is used inside the body to convert thermal energy into electrical energy by utilising the differences in temperature within the body. However, harvested power using this method is very low and usually in the range of micro watts only [57]. On the other hand, energy can be harvested from walking and normal body parts movement. It has been shown that it is possible to convert mechanical energy into electrical energy by utilizing piezoelectric effect (i.e., some materials can undergo electrical polarisation when suffering a mechanical strain). It has been possible to design an energy harvesting device which uses human walking to generate an electrical power of 8.3 mW [54, 58].

c- Backscattering communication

As discussed earlier, the existence of an on-board battery increases the size of the implant and limits its potential lifetime. Hence, some research papers have presented the concept of fully passive implants, in a similar way to passive chipless RFID systems [59]. An off-body reader interrogates the passive implant with a carrier signal (f_c), the passive implant modulates the carrier signal with the measured or recorder signal (f_n) and backscattered the modulated signal ($f_c + f_n$) back to the off-body receiver, which in turn demodulates the received signal to obtain the measured signal. A proposed method for recording brain neurpotentials using a multi-channel backscattering implant has been presented in [60]. The implant is interrogated by an RF carrier from external reader, a Schottky diode is used to record the neuropotential signal of certain brain neurons by the diode's nonlinear mixing technique. The mixing process generates the modulated signal which is then backscattered to the external reader by an on-chip antenna. The implant has a multi-channel design to help recording spatially separated neuropotential signals. All channels work in the same principle explained earlier, the selection between the channels is achieved by interrogating the implant with a light of a certain wavelength, the corresponding implanted photodiode would respond to activate the sensing and mixing operations in the intended channel.

On the other hand, some attempts have been made to use a self-resonant surface as a passive implant, where the changes inside the body is measured by the alterations in the resonance behaviour of the electromagnetic surface. A self-resonant surface comprised of an array of micro-sized split ring resonators has been proposed as a passive implant. The latter has a resonance frequency at terahertz range. The surface response was experimentally measured when implanted inside a rat. It has been suggested that the aforementioned surface can be integrated with other implantable devices for sensing and monitoring purposes inside the body [27].

2.1.1 Applications of implantable medical devices

Implantable medical devices have been utilised in different ways within the healthcare sector. The main application areas of IMDs can be summarised in the following points:

1- **Diagnosis:** implantable devices can be used for medical diagnosis. The prime example of diagnostic IMDs is the imaging capsule. The latter is a pill-sized electronic capsule equipped with imaging technique. The pill is swallowed by the patient to inspect the gastrointestinal tract as a potential replacement of the traditional wired endoscopy. The capsule sends images/videos via wireless link to an external receiver for additional post processing [61].

2- **Telemetry and monitoring:** several examples have been reported in the literature for implantable devices employed for monitoring purposes inside the body. Wireless implantable devices for glucose and blood pressure continuous monitoring have been proposed in [62] and [63], respectively.

3- **Therapy:** H. Tao et. al have proposed a wireless implantable device which delivers thermal therapy to tissues at wound site to prevent infections. The implant is powered via an inductive coupling link, and power dissipation in an implantable Mg-based resistor provides the required temperature rise [50].

4- **Drug delivery:** An electronic pill can be used to deliver drugs to a targeted location within the digestive system [64]. The capsule is activated by magnetic switch to release the drug once the targeted position is reached.

5- **Restoring a lost biological function:** In some cases, implantable devices can be used to help the body regain a certain function. Examples of such application have been discussed earlier such as cardiac pacemakers and cochlear implants.

2.1.2 Biodegradable implantable medical devices

Normally, a second surgery is needed to extract the implantable medical device after its lifetime has finished. This additional surgery can lead to a further risk of infection or cause extra health complications. Moreover, they increase the cost associated with healthcare and cause patients inconvenience. Recently, some attempts have been made to make partially or fully biodegradable medical implants using biocompatible and bioresorbable materials. Such implants do not need extraction surgeries as they can be dissolved and safely absorbed by the human body. A biodegradable implant for intracranial pressure measurement has been proposed in [65]. Monitoring of pressure inside the skull is important in treatment of patients with brain injuries. The device is comprised of a temperature sensor and piezoresistive sensor made of silicon nanomembrane responsible for measuring pressure, which in turn changes the resistivity of the material. The implant is connected to degradable wires, which takes the signal through the skull to a non-degradable wireless transmitter resides outside the body. Similarly, a biodegradable pressure sensor based on passive resonance concept has been suggested in [66]. A sensing cavity made of biodegradable PLLA polymer was used. Applied pressure changes the value of a variable capacitor connected to a coil to form a resonant circuit. The applied pressure value is measured by the amount of change in the resonance frequency of the LC circuit, the internal inductor is coupled with an off-body coil. The conducting parts of this device was made of a corrodible Zn-Fe bilayer metal (A little amount of iron was added to zinc to accelerate and control its degradation rate). The same idea of passive resonance sensing was reported in [67]. A stimulus causes a change in the resonance frequency of implanted RLC circuit which is detected by an external coil via inductive coupling.

However, in this work the lumped components were fabricated from biodegradable conductive polymers instead of conventional conductors. Two composites of conductive polymers were studied; PLLA-PPY and PCL-PPY. The DC conductivity and RF conductivity (@1.76 GHz) was measured for both composites. It has been found that PCL-PPY composite have higher value of conductivity (RF conductivity of 1500 S/m at 1.76 GHz has been obtained). Finally, H. Tao et al. have designed a biodegradable implantable device which applies thermal therapy to inhibit bacterial growth in infected tissues. An off-body coil coupled with an implanted Mg-based coil to derive electric current in an Mg-based resistor. The dissipated power in the resistor increases the local temperature around the implant. A fully degradable silk protein substrate was used to support the implanted inductor and resistor.

2.1.3 Human body modelling

Human models or phantoms are a representation of the human body using the electrical properties of its tissues. From the electromagnetic point of view, human body are an irregular stratified dielectric medium. Hence, any biological tissue can be adequately described by its permittivity and electrical conductivity values. Phantoms are used for many different reasons; they can be utilised to study the performance of implantable medical devices. Moreover, they are used to evaluate the level of electromagnetic exposure on the human body. Phantoms have been adopted to assess radiation dosimetry of ionising high frequency radiation, or to measure the specific absorption rate (SAR) of non-ionising low frequency electromagnetic fields. They can also be used to study the effect of human body on the wave propagation of mobile phones [68, 69].

Fig. 2.1 Physical phantom with a mobile phone in talking position [69].

The advances in medical imaging has allowed the precise measurements of the electrical properties of biological tissues. Hence, some numerical phantoms have been developed based on the 3-D measurement of permittivity and conductivity. These phantoms can have different resolutions based on the number and size of the smallest measurement unit which is known as a voxel. The description of these phantoms in terms of voxels has allowed the mapping of these points onto the meshing domain of some numerical techniques such as finite difference time domain (FDTD) and finite integration technique (FIT), which are the basis of electromagnetic simulation software [69, 70]. On the other hand, some physical phantoms have been developed for practical measurements of electromagnetic response of implantable and wearable devices. Phantoms representing full body or specific parts (such as head or torso) have been proposed using human dummies as shown in Fig. 2.1. Such phantoms are usually used to study mobile communication devices performance near the human body. In most cases, phantoms are just needed to reflect the electrical properties of human body tissues irrespective of the physical shape. Hence, some attempts have been made to create mediums with electrical properties resembling those of biological tissues from basic ingredients. The simplest form of phantoms are made from distilled water as the solvent with additives to change the dielectric properties. Sodium chloride is usually used to regulate the conductivity, while one of sugar, glycerol, and polyethylene is used to control the permittivity [71-73]. A liquid phantom with different concentrations of water, salt, and sugar has been used in [72] to test the performance of implantable antenna. The phantom has the permittivity and conductivity of skin at 403 MHz. Although liquid phantoms are inexpensive and easy to prepare, they have some drawbacks. Firstly, it is difficult to handle a liquid in some experimental procedures such as inside waveguides. Secondly, the containers that hold them may intervene with the electromagnetic measurements. Thirdly, it is difficult to produce the required permittivity and conductivity for wide frequency window.

To avoid some of the drawbacks of liquid phantoms, a gelling agent such as gelatine or agar can be added to the liquid to form a semi-solid medium. This would allow the phantom to hold itself without the need of a container. A semi solid phantom using agarose has been manufactured in [74] to mimic the properties of skin. Two recipes have been created to obtain the dielectric properties of skin at two different frequencies; 403 MHz and 2.4 GHz. The disadvantage of gel phantoms is that its properties changes over time because of water evaporation. Additionally, they tend to grow fungi. Some attempts have been made to prolong the lifetime of a gel phantom by adding preservatives. A gel phantom for magnetic resonance imaging (MRI) testing in the frequency range of 0.15-4.5 GHz has been manufactured in [75] from distilled water, sugar, salt, and agar, while benzoic acid was added as a food-quality preservative. Similarly, K. Ito has used sodium azide as preservative to his gel phantom [73]. Nevertheless, few attempts have been made to make a solid phantom which can last for a long time. In [76], a solid phantom made from carbon powder and rubber has been created. The achieved results have shown better matching to biological tissues properties than liquid or gel phantom for a wide frequency range (1-10 GHz). However, the preparation method is rather complex and needs special equipment.

2.1.4 Specific absorption rate

Specific absorption rate (SAR) is a measure of the power absorbed by the biological tissue per unit mass, hence, it has a unit of W/Kg. In the RF range of the electromagnetic spectrum (i.e., 3 KHz to 300 GHz), the radio frequency signal has a non-ionising effect on the bio tissues characterised by an increase in the local temperature. A persistent rise in temperature can have a negative effect on the heath and could lead to a range of symptoms such as high blood pressure, nausea, and dizziness [77]. SAR is directly related to the electric field value and can be calculated using [78]:

$$SAR = \frac{\sigma\,|E|^2}{\rho} \tag{3.1}$$

where σ is the electrical conductivity in (S/m), ρ is tissue density in (kg/m^3), and $|E|$ is the magnitude of the complex electric field value in (V/m). It is usually difficult to measure the value of SAR in practice, thus, it is normally calculated through some numerical and theoretical methods. An upper SAR limit of 1.6 (W/kg) for 1 g of tissue or 2 (W/kg) averaged over 10 g of tissue has been adopted globally [79].

2.2 Self-resonant structures

In present-day communication systems, the reliance on self-resonant structures (SRS) has increased remarkably. In their periodic form, SRS are known as frequency selective surfaces (FSS) and have found numerous applications in different parts of modern wireless systems. They can be implemented in wireless friendly building applications to enhance the isolation between different types of communication signals or to customize the propagation through walls [80, 81]. They are also employed in high impedance surfaces, absorbers, waveguide filters and many more microwave device [82-85]. Thus, FSS have been fundamentally important in the techniques used for improving different antenna parameters including directivity, operational bandwidths, and beam-switching [86-88], and in the design of dichroic sub-reflectors for space applications [89]. On the other hand, finite self-resonant structures are employed in RFID technology to offer low-cost identification tags having a long operational lifetime. Passive chipless RFID tags can embed information in the frequency response of the scattered signal in terms of the presence or absence of resonance peaks within a specified frequency window. These types of tags are mainly used as a replacement for traditional barcodes, offering non-line of sight object identification [90, 91].

Although the proposed self-resonant tag is not a conventional RFID tag, the system structure and the operating principle are similar. On the other hand, FSS theory have been utilised in the development of tag design. Hence, both RFID system and FSS theory are covered in the following sections.

2.2.1 Radio frequency identification

Radio-frequency identification (RFID) technology has become increasingly important in recent years, as it has found applications in various sectors ranging from manufacturing and automotive industry to health care and military applications. The basic components of any RFID system are tag, reader and the space between them which is known as the interrogation zone. Communication occurs between the reader and the tag through a wireless link; reader interrogates the tag asking for certain information or commanding the tag to do a certain task, the tag receives the request and act accordingly [92, 93].

The early use of communications for identifying objects can be traced back to the forties of the last century, as the British used it to identify their airplanes and distinguish them from the opponent's planes during World War II. After that, an important milestone towards current day's RFID technology was achieved when Harry Stockman wrote his paper about communications through reflected power in 1948. After that, research continued in the following years in various laboratories until the seventies which witnessed another RFID milestone, as the first commercial use of RFID to trace animals in the United States happened in 1979. However, mass production of RFID started in the nineties as it found numerous applications in different sections of business and technology as a result of the major development in fabrication material and the emergence of the internet. Since then RFID have been fundamental in manufacturing industry and other sectors to track and identify items and in quality assurance [92, 94]. In healthcare sector, RFID applications is no longer restricted to tracking and positioning of patients but it has been used as a monitoring device for different processes inside the human body [95]. RFID tags can be embedded in other implantable devices or prostheses to collect data or track chemical or physical changes in the surrounding environment [96, 97]. RFID systems can be classified into two main categories based on the powering mechanism as follows [92, 93]:

1- Active tags

The main components of active tags are integrated circuits, power source, and antenna to communicate back and forth with the reader. The availability of an on-board battery allows active tags to perform sophisticated functions in terms of sensing and processing and storing of information. Additionally, they can communicate with the reader at any time. The disadvantages of active tags is that their operational time are limited by the lifetime of the battery. Moreover, existence of battery, antenna and electronic components all together increase tag size and cost.

3- Passive tags

Passive tags do not have on-board power source and they rely on the power being transferred from the reader and stored in a charge pool and used on-demand to power the electronic components of the tag. They communicate with the reader through backscattering communication. Hence, they normally have a very short read range. Additionally, the lack of power source limits the operations the tag can perform. The advantages of these type of tags are low cost, long lifetime, lightweight, and small size.

When passive tags do not have on-board electronics they are called passive chipless RFID tags [94]. This type stores the information in the electromagnetic response of its passive resonator [98]. Recently, published work has discussed different aspects of passive chipless tags including improving the capacity and/or the spectral efficiency of the tags to embed more information into a narrower frequency spectrum. Costa et al. [90] discussed a multi-bit chipless RFID using a truncated high-impedance surface (HIS), the limited ground plane on the tag enhances its functionality when mounted on metallic objects and surfaces with high scattering properties. Jang et al. [99] presented a wireless sensor for crack monitoring. When a structural change in the surface where the tag is mounted occurs, the RF signature of the tag would change to indicate a structural fracture. Bhuiyan and Karmakar [98, 100] presented a multi-bit polarisation-dependent tag, where a micro change in the structure of the passive resonator would alter the radar cross section signature of the tag.

2.2.2 Frequency selective surfaces

Frequency selective surfaces (FSS) are a two dimensional array of similar elements extending to infinity in both planes. They act as spacial filters to electromagnetic waves. They allow transmission at certain frequencies and block the rest. Similar to lumped component filters, FSS can be a low/high pass filter or a bandstop/bandpass filter depending on the design [101]. The operating principle can be explained by taking a basic example of an incident wave striking a generic frequency selective surface as shown in Fig. 2.2. For the sake of brevity, the discussion will assume a metallic element with one electron and will consider the two extreme cases of total transmission and total reflection. When a plane wave impinge upon the FSS surface, total reflection will occur if the electric field vector is parallel to the oscillation plane of the electron of the metallic element. On the other hand, total transmission will occur when the electric field vector is perpendicular to the oscillation plane of the electron. In the first case (which is illustrated in Fig. 2.2a), the electron absorbs the electromagnetic energy and starts to oscillate. In this state, the electron acts like a dipole and radiates energy to the left and right of the FSS. If the radiated energy of the electron to the left is equal to the incident electric field, a total cancellation will occur and no transmission takes place through the FSS. In the second case (which is depicted in Fig. 2.2b), because of the orientation of electric field in relation to the oscillation plane of the electron, the latter will be ineffective to the incident field. Hence, a total transmission through the FSS will occur [102].

FSS can be categorised into passive and active arrays. The former means the FSS elements are excited externally by an incident plane wave, similar to the example shown in Fig. 2.2. On the other hand, active FSS have a voltage source connected to each element in the array. The voltage amplitude in every element should be equal, but with a progressive phase shift [101]. The focus in this section is on passive FSS as it is more relevant in the context of the project. According to Ben Munk [101], FSS elements can be categorised into three basic types; centre-connected element, loop type, and patch type. Nonetheless, a realistic FSS can have a combination of more than one of type. The type of FSS element can help the designer to predict the resonance frequency. For instance, loop type elements (which is the selected type

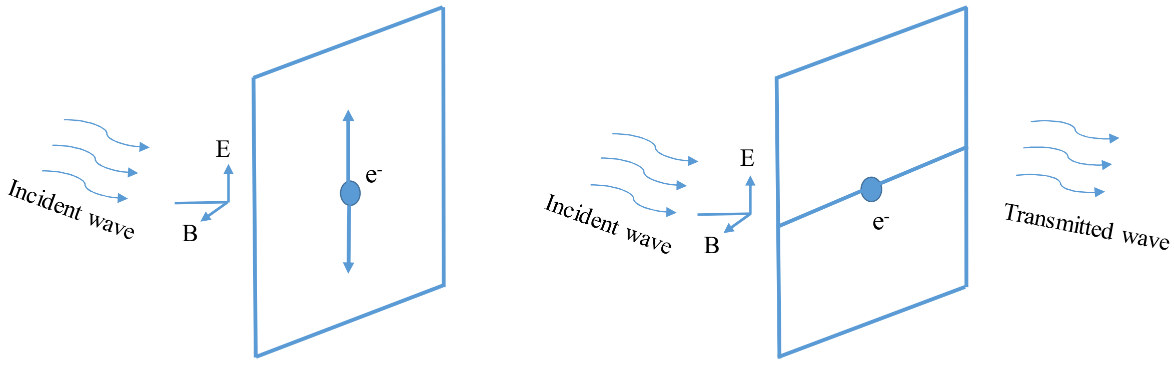

(a) (b)

Fig. 2.2 Plane wave incidence of FSS (a) the case of a total reflection (b) the case of a total transmission [102].

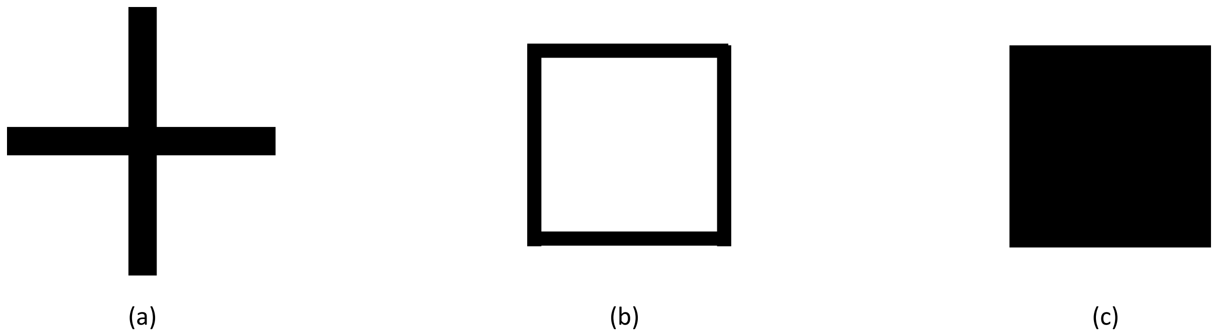

Fig. 2.3 Three main types of FSS elements (a) centre-connected FSS element (b) loop type FSS element (c) patch type FSS element.

for the tag's resonator in this project) resonate when the wavelength of incident wave is equal to their circumference. While for a dipole or a crossed dipole element (such as the one depicted in Fig. 2.3a), they resonate when the wavelength of incident wave is double the length of their big dimension.

When dielectric layer exists near the FSS resonator, it causes a significant down shift in the resonance frequency. If the thickness of dielectric media on both sides of the FSS is infinite, it causes the resonance frequency to drop by a factor of $1/\sqrt{\varepsilon_r}$. On the other hand, when the dielectric layer is on one side only of FSS, the change in the resonance frequency will be $1/\sqrt{(\varepsilon_r + 1)/2}$ (which is basically the average of the relative permittivity of the dielectric layer and the relative permittivity of free space). When the dielectric layer has a finite thickness, and because of the interaction between the electromagnetic field near the FSS and the surface of dielectric layer, trapped modes can form. The latter are modes which are originally evanescent in free space but propagative inside the dielectric media [101, 103].

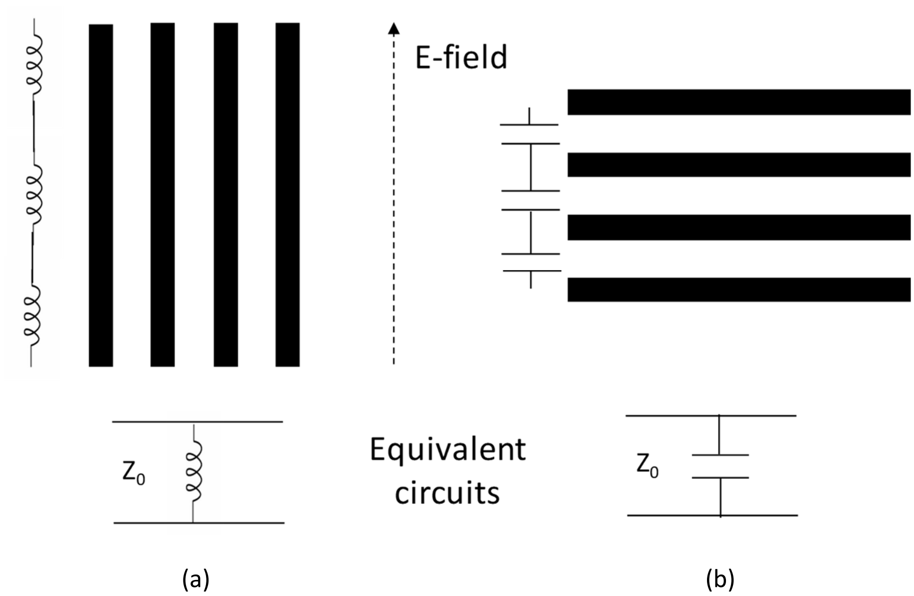

Fig. 2.4 Concept of equivalent circuit in FSS (a) inductive parallel strips (b) capacitive parallel strips.

Several methods have been used for FSS analysis and design, one of the methods that is widely adopted in the literature is the equivalent circuit method. The latter is based on an analogy between field theory and circuit theory. The advantage of using this method is it simplifies the electromagnetic problem through building a network-based equivalence, which can give some insights into the underlying physics of the structure. Moreover, it reduces the computational time remarkably. Fig. 2.4 explains the basic concept of FSS equivalent circuit, when incident electric field is parallel to conducting strips, they act as an inductor, and when the electric field is perpendicular to the conducting strips, they act as a capacitor. Hence, they have the circuit representation shown in the graph [101, 104, 105].

2.3 The concept of modelling

Equivalent models have been used over the years in many different fields to describe a certain physical phenomena in another domain. Building an equivalent model helps in simplifying a complex problem, as equivalent models would redefine the original problem by building an equivalent one with limited contributing factors, which makes the original problem easier to analyse and understand. Additionally, modelling gives the designer the freedom to choose the parameters that need to be taken into account from the original problem, and discard the parameters that are irrelevant in the phenomenon under study. Hence, equivalent models give the opportunity to understand the impact of each parameter alone on the response of the system.

In some cases, it is possible to benefit from the established techniques and tools in the equivalent domain to facilitate certain calculations that are difficult to conduct in the original domain. Irrespective of the field of application, modelling process have the following four stages [106, 107]:

- The first step is known as 'conceptualization' and focuses on choosing the domain of science that is applicable to the intended problem.
- The second stage deals with generating the appropriate mathematical formulations to describe the concept in the new domain, this stage is usually known by 'formulation'.
- The third stage considers the implementation of the mathematical formulas and computing the results.
- The last stage validates the achieved results both numerically and physically. It is very important to check the physical meaning of results in comparison to theory or another solution method.

If results show low accuracy or they are not physically reasonable, then some modifications are needed in the first three stages of the process. Finally, there are certain principles that should be maintained when building an equivalent model, they can be summarized in the following three points:

1. Equivalent models need to be as simple as possible, they just need to be good enough to describe the phenomena under study. Perfect models are usually over complicated in a way that leads to losing the insights.
2. All models have limitations and no model is valid under all circumstances. A good model show high accuracy under certain conditions only.
3. Equivalent models should be easier to understand than the original problem.

2.4 Summary

This chapter has covered the theory and literature review of this research project. The first part has provided an in-depth review of implantable medical devices. After defining the term, the challenges associated with designing an IMD have been explained. The restrictions in size, limited power, and manufacturing material have been discussed. Moreover, the impact of the biological environment on the performance of communication devices have been highlighted. Then, IMDs have been categorized according to their operating mechanism into active tags and passive tags. The former have on-board battery and can perform sophisticated tasks but have limited lifetime and relatively large size. Passive IMDs on the other hand can be classified into three types: IMDs that use backscattering communication, energy harvesting IMDs, and IMDs that rely on wireless power transfer from outside the body. It has been shown that four methods have been used in the literature for wireless energy transfer to implants including inductive coupling, capacitive coupling, ultrasonic transmission, and far field power transfer. The four types have been evaluated in terms of power generation, and the advantages and disadvantages of each type have been stated.

The areas of biodegradable medical devices have been reviewed. Few attempts have been made in the literature to design fully degradable implantable devices for a variety of applications. After that, the subject of human body modelling have been explained; phantoms can be categorised into two types: numerical and physical phantoms. The former is used for theoretical calculations (or in simulations) and the latter is adopted in experimental measurements. Three main types of physical phantoms have been used in the literature including liquid, semi-solid, and solid phantoms. The advantages and disadvantages of each type have been discussed. Lastly, the specific absorption rate has been defined and the recommended limit for safe exposure have been stated.

The second part of this chapter has discussed self-resonant structures. The system structure and operating principles of RFID have been explained, and recent publications in the area of passive chipless RFID have been reviewed. On the other hand, a brief explanation of the main concepts in FSS theory have been given. Lastly, the notion of equivalent models and the steps of every modelling process have been discussed.

3. CHAPTER THREE

Design and analysis of self-resonant tag inside multi-layer dielectric media

This chapter introduces the fundamental tag design concept and the modelling of tag's degradation process. The impact of surrounding media and angle of incidence are analysed by resorting to an equivalent transmission line model.

3.1 Fundamental tag design concept

In order to monitor the state of healing soft tissues, the implanted tag must have a response that can be tracked from outside the body. From basic FSS principles, the frequency response of a resonating element can be changed by altering its dimensions [101]. In this study, a uniform cross design has been adopted as the resonating element as shown in Fig. 3.1a. The chosen cross shape, besides its good resonance characteristic, allows the modelling of tag's degradation in a predefined manner. The interconnecting strips within each arm (numbered 1-3) can be designed to degrade in a predetermined sequence. These arms would degrade in turn changing the path length of the resonance loop, thereby, changing the resonance frequency over time. Realistically, degradation can be controlled by changing width and thickness of these metallic tracks. Small breaking points characterized by thinner track width can be set at both ends of each of those strips. Hence, these break points would degrade faster than the rest of the structure. An illustration of these break points is shown in Fig. 3.1b.

In this work, only discrete resonant states of the uniform cross tag is considered as the use of actual degradable materials is out of the scope of the project. The self-resonant tag in this

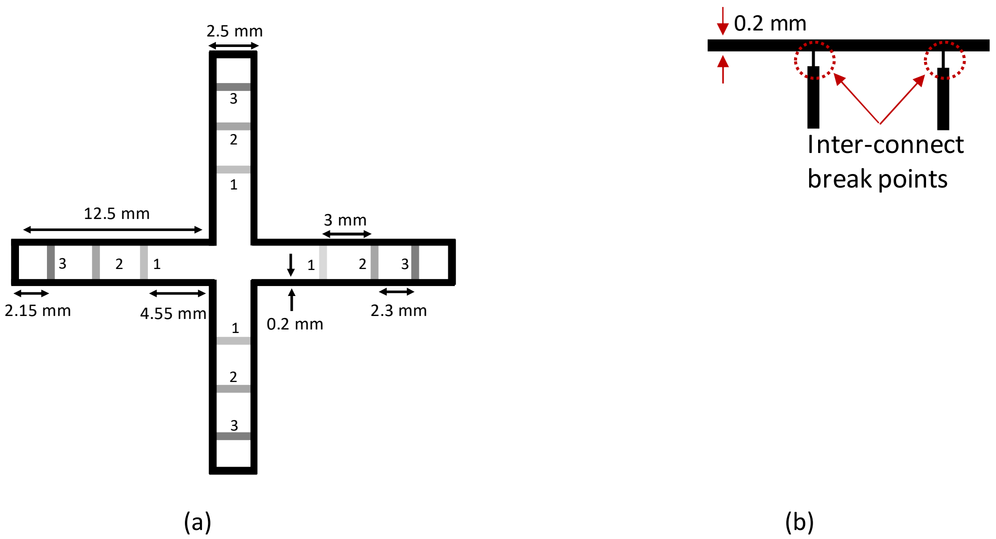

Fig. 3.1 (a) Proposed uniform cross tag structure with dimensions. (b) an illustration of break points to ensure sequential degradation.

project has four discrete resonant states as the four strips with the same number shown in Fig. 3.1a would be disconnected simultaneously at each stage.

3.1.1 Uniform cross tag response

The self-resonant uniform cross tag has been designed and simulated using CST MWS for a frequency range of 1-7 GHz using the frequency domain solver with automatic frequency point selection. 1001 data samples were set for the S-parameter calculation. Tetrahedral meshing with adaptive mesh refinement has been implemented. The simulated volume was 50x50x120 mm^3 with electrical and magnetic boundaries, while two waveguide ports were used as excitation sources. Fig. 3.2 illustrates the simulation setup. The forward transmission response of the tag at different degradation stages is shown in Fig. 3.3. Implanted tag has a certain degradation rate in healthy tissues, if an infection occurred and the immune system reacted through the inflammatory response discussed in chapter one, tag degradation rate will be accelerated and the tag resonant state will change accordingly. This change in the time needed to transition from one resonant state to the other is indicative of infection and can be monitored from outside the body.

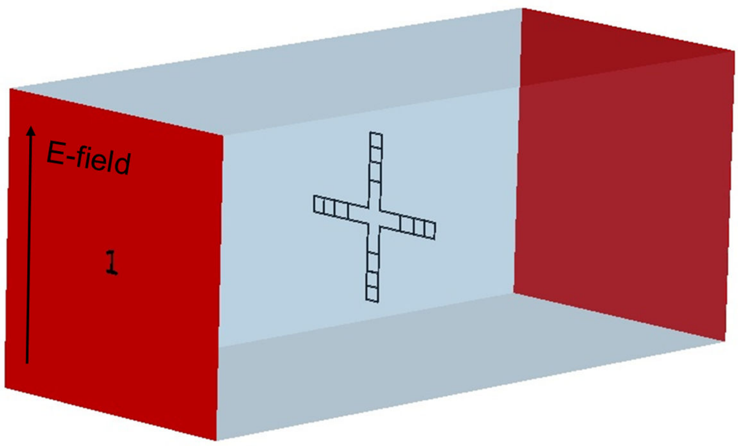

Fig. 3.2 Uniform cross tag simulation setup using CST MWS.

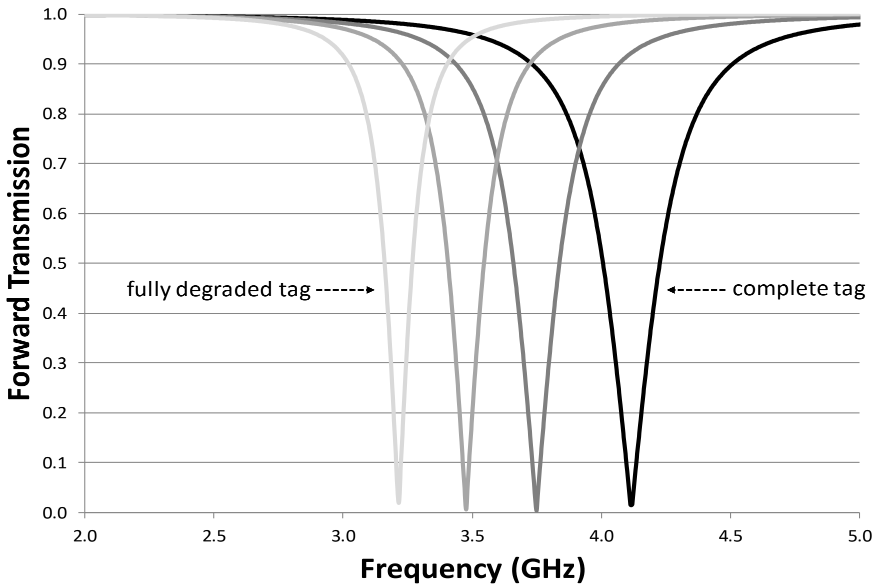

Fig. 3.3 Forward transmission of free-standing uniform cross tag at four different degradation stages [complete tag shown in black and lighter colour for each subsequent degradation stage].

3.1.2 Experimental validation of uniform cross tag response

The uniform cross tag has been manufactured using single sided copper clad FR4 substrate with thickness of 0.8 mm. Four discrete states of the tag have been fabricated each with a board dimension of 50x50 mm^2 as shown in Fig. 3.4 below. The forward transmission of the four states has been measured with a rectangular S-band waveguide (WG10) connected to a two-port Agilent 8720D vector network analyser (VNA). A three-step TRL calibration has been applied to remove unwanted reflections, and an operational bandwidth of 2.6-3.95 GHz with 201 frequency points has been set. The measurement setup is shown in Fig. 3.5. The measured S_{21} results are depicted in Fig. 3.6. It can be noticed that measured results have lower resonance frequency than simulated results because of the impact of the substrate. It can also be observed that the response of the last degradation stage of the tag occurs below the cut-off frequency of the waveguide.

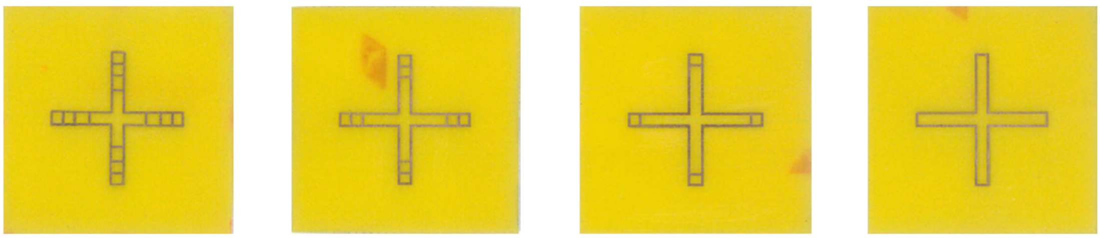

Fig. 3.4 Prototypes of uniform cross tag at four different degradation stages all on 50x50x0.8 mm^3 FR4 substrate.

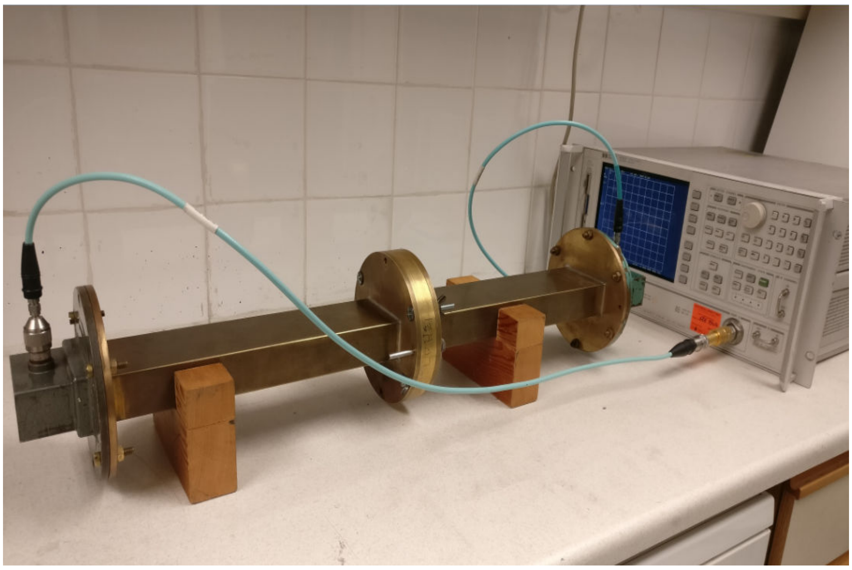

Fig. 3.5 Measurement setup: S-band waveguide and a two port vector network analyser.

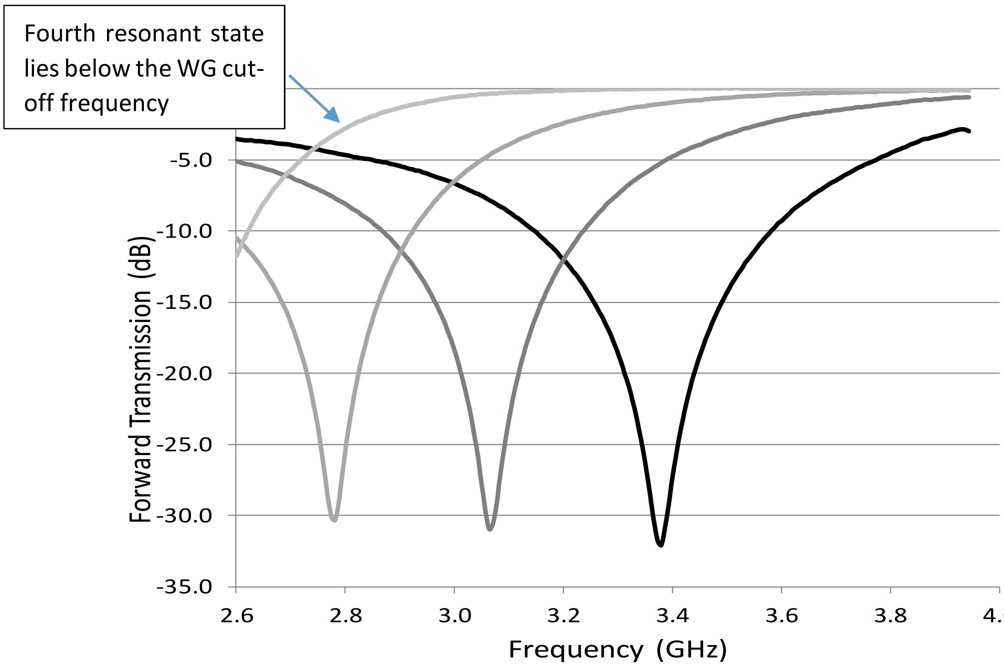

Fig. 3.6 Forward transmission of uniform cross tag on 0.8 mm FR4 at four different degradation stages measured inside a waveguide [complete tag shown in black and lighter colour for each subsequent degradation stage].

3.2 Transmission line model representation of self-resonant tag inside human body

Understanding the behaviour of electromagnetic structures is rather difficult and generally cannot be easily interpreted using simple expressions. Numerical full-wave simulation software is usually employed to obtain the response of electromagnetic surfaces. Although these types of simulation software offer an easy way for designing and testing of different types of surfaces, they are time consuming and normally requires high computing power.

Additionally, they do not help in providing insights about the physical principles on which these designs are based. Alternatively, equivalent circuit models have been widely used to offer a faster design and optimization approach as they principally provide some insights into the fundamental physics of the structure.

In this project, a transmission line model analysis for implantable self-resonant tag is proposed. There are key advantages to using an equivalent model representation for implantable tags. They can be summarised as follows:

- Understanding how degradation process alters the electrical properties of the tag.
- Studying the impact of surrounding tissues on the resonance characteristics of the tag.
- Identifying the losses imposed by the implantation medium.
- Compliments full-wave simulation results by offering more insights into the underlying physics.

Fig. 3.7a shows a tag implanted inside a multi-layer human body model, its equivalent transmission line model representation is shown in Fig. 3.7b. The equivalent model comprises a multi-segment transmission line, each section has different length and characteristic impedance, representing the corresponding human body layer. The tag is represented by an RLC network shunted across the transmission line.

3.2.1 Equivalent circuit model

The first step towards implementing a transmission line model representation is to find the configuration and parameters of the RLC network across the transmission line model (i.e., the equivalent circuit representation of the self-resonant tag). One of the early attempts to use equivalent circuits to model self-resonant structures was when Marcuitz proposed lumped component representations of an infinite parallel conducting strips [108]. Later, an important milestone in the evolution of equivalent circuit models for FSS was when Langley et al. proposed for the first time efficient empirical equations to model some of the widely used

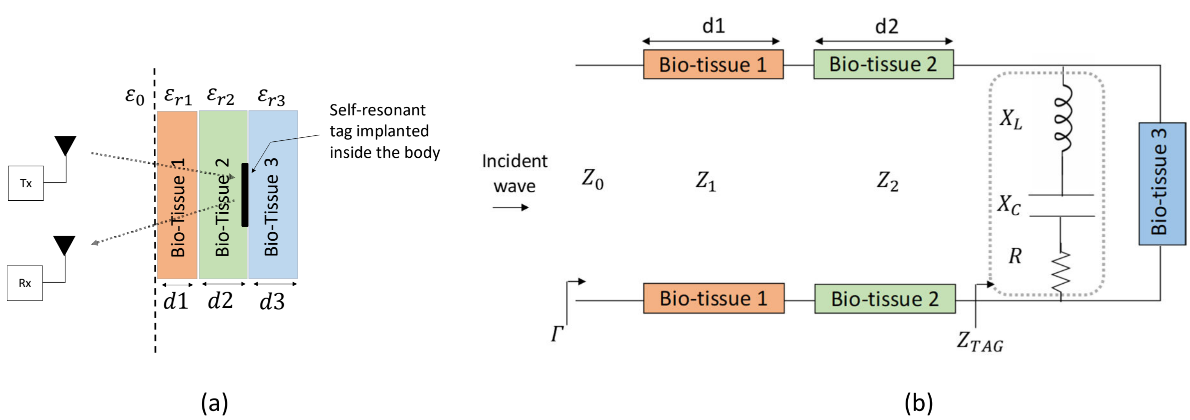

Fig. 3.7 (a) A self-resonant tag implanted inside a multi-layered human body model (b) A transmission line model representation of a tag implanted inside a multi-layered human body model.

FSS types including square loop, double square loop, and Jerusalem cross [109-111]. They also studied the effect of oblique incidence and the influence of supporting dielectric slabs on FSS response using circuit models [112, 113]. Despite the acceptable accuracy of these empirical equations, they are rather complex in a way that leads to losing the intuitive understanding of the working principle of these structures. In recent years and due to the remarkable development in computing technology, some techniques have been developed for determining equivalent circuit parameters using a priori knowledge or data from full-wave simulation software [104, 105, 114]. This approach has now become the new trend in finding the parameter values of these equivalent circuit models. The use of equivalent models has not been restricted to periodic structures, as Costa et al. have presented an analysis of the working principles of small chipless RFID tags constructed from a few number of high impedance surface (HIS) unit cells by resorting to their lumped components representation. [91].

3.2.1.1 Single-mode equivalent circuit model

It is known that SRS impedance has the same pole-zero properties as a passive RLC circuit [115]. Hence, the concept of equivalent circuit models has been widely adopted in the literature to study the response of such structures. The configuration of the circuit and the number of lumped elements follows the resonance behaviour of the SRS. The reactive part of the RLC circuit accounts for the resonance position and shape while the real component, besides affecting the bandwidth of the response, predominantly represents the losses in the circuit. For an SRS with dielectric loading, these losses can be either ohmic caused by electric current flowing in an imperfect conductor, or dielectric losses caused by the medium. At microwave frequencies, which is the frequency range of interest in this paper, ohmic losses are negligible [116]. On the other hand, dielectric losses depend on the material types in the vicinity of the electromagnetic scatterer. Generally, dielectric materials used in FSS and RFID such as FR4, glass, PTFE bases substrates etc., have loss tangents as low as 0.02 in the frequency range of interest therefore dielectric losses can be ignored at this stage of the project. The impact of lossy dielectric material on tag response will be discussed in the next chapter.

For the sake of brevity, the proposed model assumes a single resonant structure but it should be noted that this method works equally well for multi-resonant structures. The equivalent circuit of a single resonant SRS is represented by an LC circuit. The configuration of the circuit in series or parallel depends on whether it exhibits band-pass or band-stop properties. In this work the series configuration is considered. A free-standing SRS can be represented by a series LC circuit placed across a transmission line with a characteristic impedance Z_0 (i.e. free space intrinsic impedance), and this transmission line is terminated by its characteristic impedance as illustrated in Fig. 3.8 below.

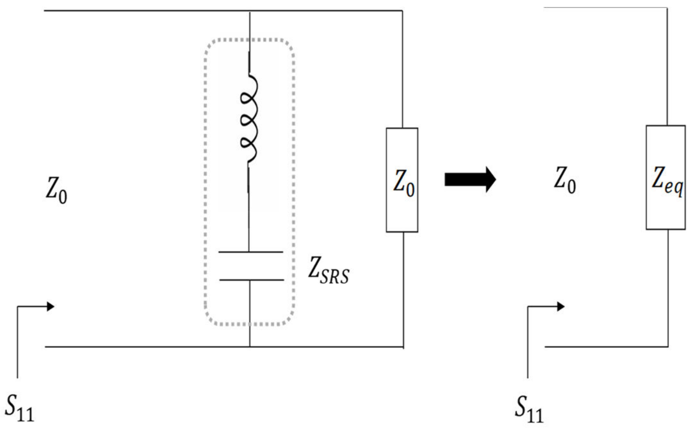

Fig. 3.8 Transmission line representation of a free-standing SRS.

Subsequently, the reflection coefficient can be calculated by:

$$\Gamma = \frac{Z_{eq} - Z_0}{Z_{eq} + Z_0} \tag{3.1}$$

where:

$$Z_{eq} = Z_0 \, /\!\!/ \, Z_{SRS} \tag{3.2}$$

Hence, the SRS's impedance can be given by:

$$Z_{SRS\_fs} = -\frac{Z_0(1+\Gamma)}{2\Gamma} \tag{3.3}$$

where Γ could be obtained from a full-wave simulation or experimental measurements.

The inductance and capacitance of the SRS can then be extracted based on error minimization criteria between SRS impedance in (3.3) and the impedance of a series LC circuit, which is given by:

$$Z\_sc = \frac{1 - \omega^2 LC}{j\omega C} \tag{3.4}$$

3.2.1.1.1 Analysis of uniform cross tag using single-mode equivalent circuit model

From basic FSS theory, it is known that when the E-field is perpendicular to a pair of conducting strips, they act as a capacitor. On the other hand, when the E-field is parallel to the conducting strip it acts as an inductor [101]. Therefore, under the hypothesis of negligible ohmic losses and based on the analogy between lumped network and electromagnetic resonators, the SRS response could be represented by a series LC resonance circuit. The distribution of the fictitious inductance and capacitance on the physical uniform cross resonator can be perceived as illustrated in Fig. 3.9.

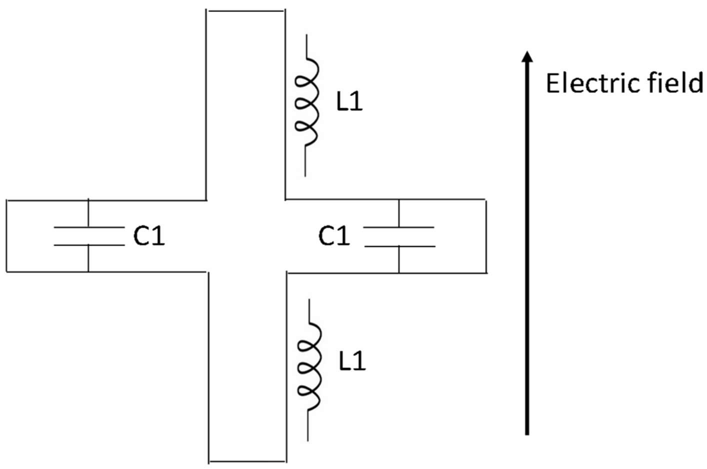

Fig. 3.9 Distribution of fictitious equivalent circuit components on the uniform cross SRS.

At this stage, the main objective is to study the impact of tag degradation on the equivalent circuit parameters. Later in this chapter, the impact of surrounding media and angle of incidence on the circuit parameters are analysed. The reconfigurable uniform cross array under study is shown in Fig. 3.10. A comparison between equivalent circuit model and full-wave responses is shown in Fig. 3.11 and Fig. 3.12 for the reflection coefficient (S_{11}) and forward transmission coefficient (S_{21}), respectively. Clearly, the equivalent circuit response shows an excellent agreement with the full wave response for the fundamental resonance zone.

Table 3.1 presents the values of the equivalent circuit at each resonance state; it can be seen that the inductance values increase significantly with each degradation stage. On the other hand, capacitance values show an insignificant change, with a maximum variation of only 2 fF.

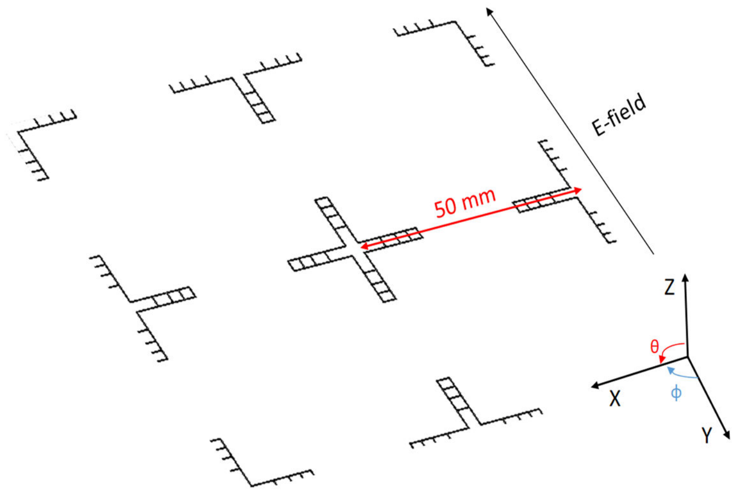

Fig. 3.10 Uniform cross array

Table 3.1 Equivalent circuit parameters of uniform cross SRS at different states

Resonance state	L (nH)	C (fF)
State 0	79.2	18.9
State 1	93.3	19.3
State 2	115.2	18.3
State 3	144.1	17.0

As explained earlier, one of the biggest advantages of equivalent circuit models is that they provide a greater understanding of the physical properties of the structure. In Table 3.1 it has been shown how inductance values increase with each state change, which is fundamentally characterized by a longer electrical length for the resonance loop. In order to understand the reason behind this behaviour, simple electrostatic principles can help to explain the relationship between the structure geometry and equivalent circuit values. The inductance of a single wire is given by [117]:

$$L = \frac{\mu_0 \, \ell}{8\pi} \tag{3.5}$$

Where ℓ is wire length and μ_0 is free space permeability. It is obvious from the equation that inductance is proportional to wire length, that means the same amount of electrical current would produce higher inductance if it flowed inside a longer wire. By looking at surface

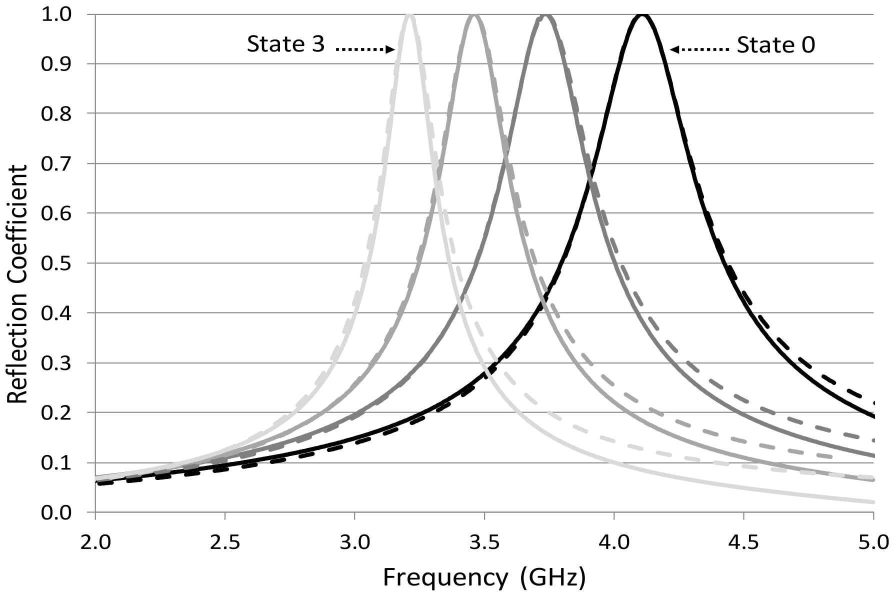

(a)

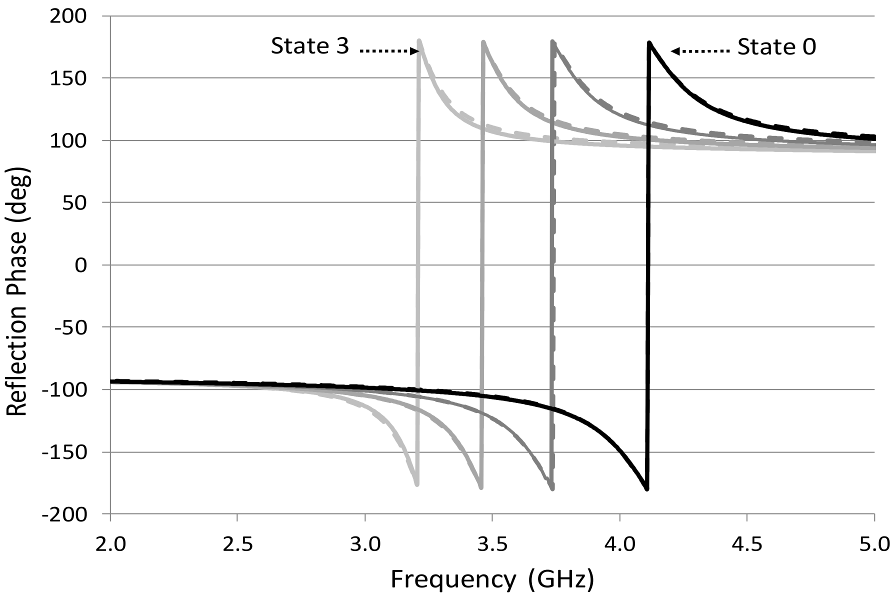

(b)

Fig. 3.11 A comparison between full-wave (solid) and equivalent circuit (dashed) response for (a) reflection coefficient (S_{11}) magnitude and (b) reflection phase [SRS states: first SRS state shown in black and lighter colour for each subsequent state].

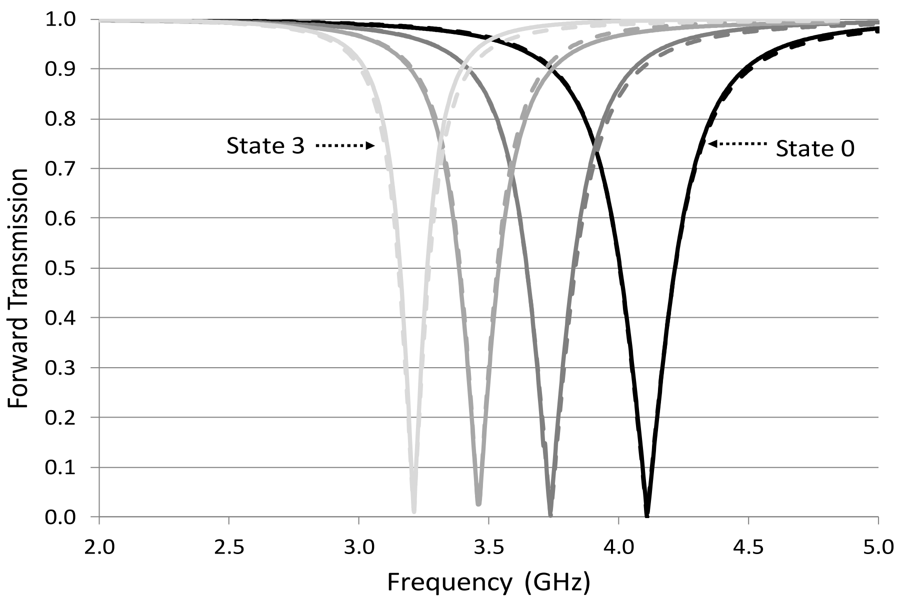

(a)

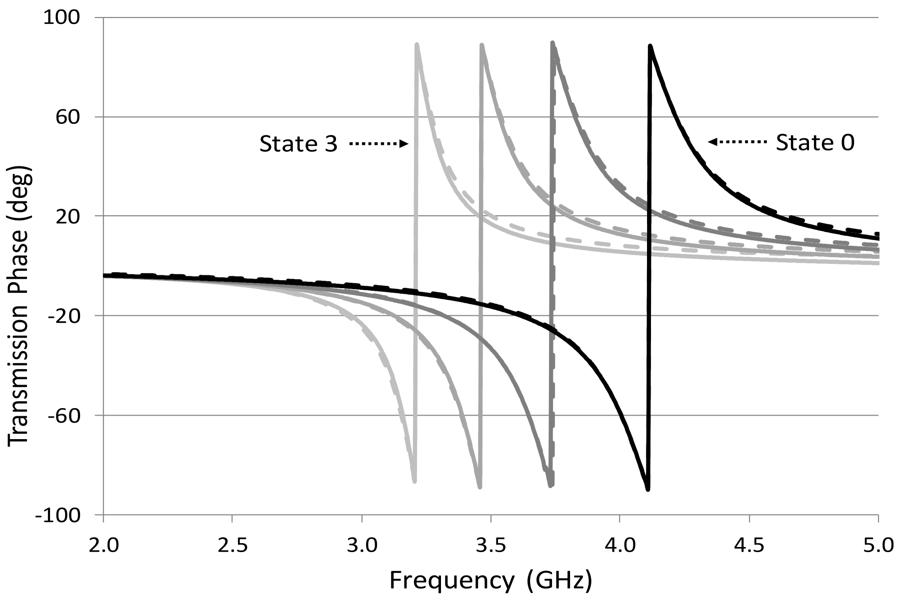

(b)

Fig. 3.12 A comparison between full-wave (solid) and equivalent circuit (dashed) response for (a) forward transmission coefficient (S_{21}) and (b) transmission phase [SRS states: first SRS state shown in black and lighter color for each subsequent state].

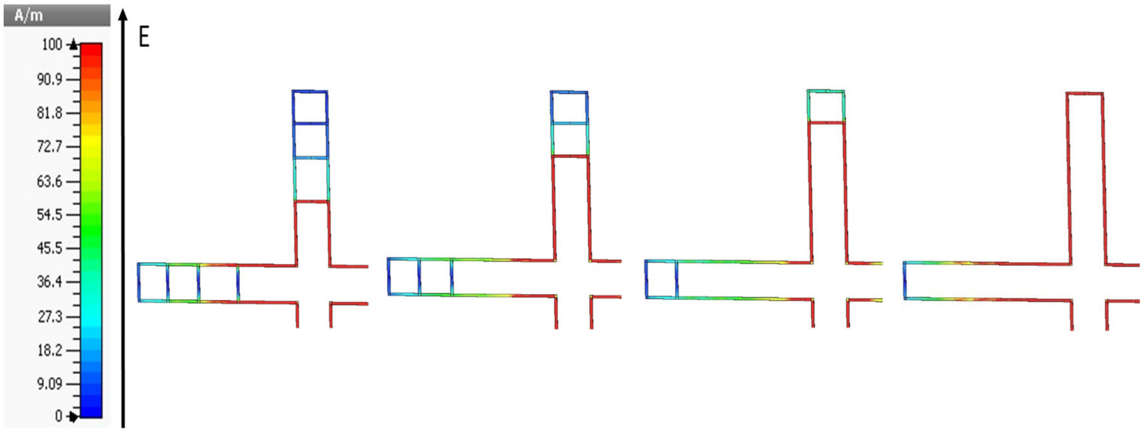

Fig. 3.13 Surface current distribution at different degradation stages of the SRS.

current distribution on the SRS's physical structure shown in Fig. 3.13, it can be seen that current distribution varies considerably at each stage. With each state change, the current is allowed to flow inside a longer strip parallel to the electric field vector and that would create more inductance as the equation suggests. This explanation justifies the trend of inductance values shown in Table 3.1.

3.2.1.2 Multi-mode equivalent circuit model

In order to extend the range of equivalent circuit response, higher order modes (HOM) need to be considered besides the main resonance mode. The approach for extracting the multi-mode equivalent circuit parameters has been introduced in [104], and in this section an explanation of the procedure is presented. Additionally, circuit parameters for the uniform cross tag are extracted and compared to the single-mode approach explained in the previous section.

After the onset of grating lobes, a number of higher order modes (also called space modes or floquet modes) are excited due to the periodicity of the structure [101]. In order to account for the effect of these floquet modes, two more impedances need to be added in series with the equivalent circuit of fundamental resonance mode [104, 118]. The multimode equivalent circuit model is shown in Fig. 3.14. Z_L & Z_C are higher order impedances which account for the excitation of TE & TM modes respectively.

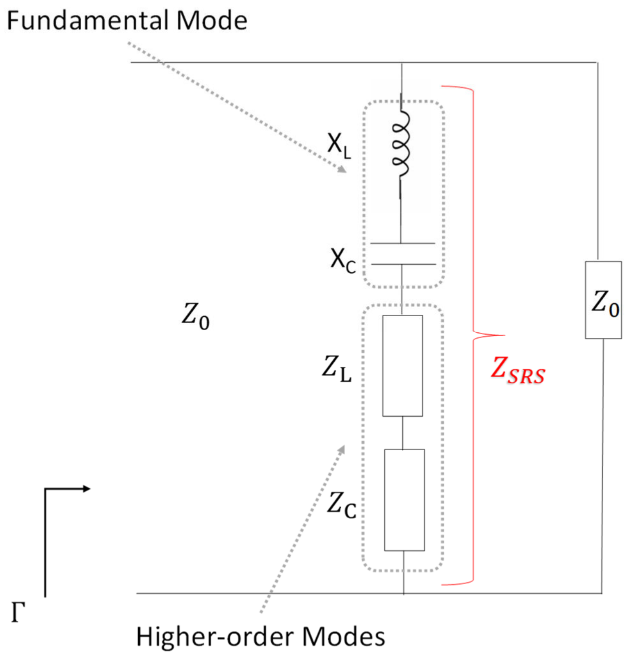

Fig. 3.14 Multi-mode equivalent circuit model (modified from [118]).

Therefore, the impedance of tag can be given by:

$$Z_{TAG\_multi\_mode} = X_L + X_C + Z_L + Z_C \tag{3.6}$$

where X_L, X_C, Z_L, and Z_C are given using [104]:

$$X_L = j\omega L \tag{3.7}$$

$$X_C = \frac{1}{j\omega C} \tag{3.8}$$

$$Z_L(\omega) = \sum_{h=1}^{N_{TE}} A_h^{TE} Z_{TE,h}^{in}(\omega) \tag{3.9}$$

$$Z_C(\omega) = \sum_{h=1}^{N_{TM}} A_h^{TM} Z_{TM,h}^{in}(\omega) \tag{3.10}$$

where $A_h^{TM\therefore TE}$ represents the level of excitation of a certain higher order mode h. N_{TE} & N_{TM} are the number of considered TE & TM modes respectively. $Z_{TM\therefore TE,h}^{in}$ is the modal input impedance and can be given by [104]:

$$Z_{TM\therefore TE,h}^{in}(\omega) = Z_{TM\therefore TE,h}^{left}(\omega) \mathbin{/\!/} Z_{TM\therefore TE,h}^{right}(\omega) \tag{3.11}$$

$Z_{TM\therefore TE,h}^{right}$ and $Z_{TM\therefore TE,h}^{left}$ represent the modal impedances seen from the right and the left of the array tag and can be given by [104]:

$$Z_{TM\therefore TE,h}^{left} = Z_{TM\therefore TE,mn}^{(\varepsilon_{r1})} * \frac{Z_{TM\therefore TE,mn}^{(1)} + j\, Z_{TM\therefore TE,mn}^{(\varepsilon_{r1})} \tan(k_{z,mn}^{(\varepsilon_{r1})} d_1)}{Z_{TM\therefore TE,mn}^{(\varepsilon_{r1})} + j\, Z_{TM\therefore TE,mn}^{(1)} \tan(k_{z,mn}^{(\varepsilon_{r1})} d_1)} \tag{3.12}$$

$$Z_{TM\therefore TE,h}^{right} = Z_{TM\therefore TE,mn}^{(\varepsilon_{r1})} * \frac{Z_{TM\therefore TE,mn}^{(1)} + j\, Z_{TM\therefore TE,mn}^{(\varepsilon_{r2})} \tan(k_{z,mn}^{(\varepsilon_{r2})} d_2)}{Z_{TM\therefore TE,mn}^{(\varepsilon_{r1})} + j\, Z_{TM\therefore TE,mn}^{(1)} \tan(k_{z,mn}^{(\varepsilon_{r2})} d_2)} \tag{3.13}$$

Fig. 3.15 Clarifies equations (3.12) and (3.13).

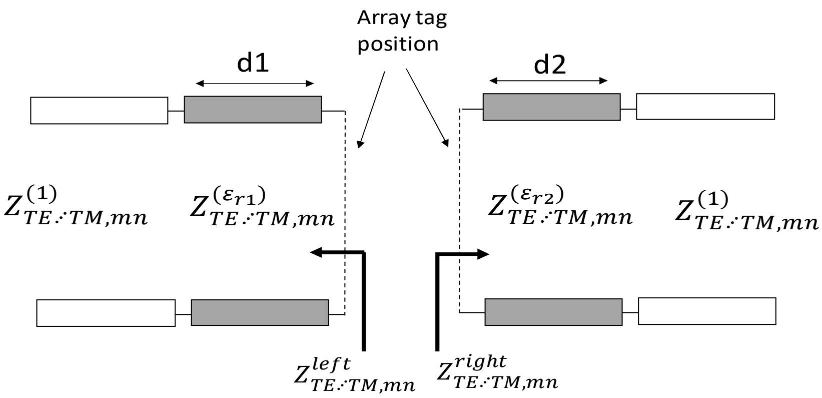

Fig. 3.15 Transmission line representation of modal input impedance (modified from [104]).

d1 and d2 represent the thickness of dielectric layer on both sides of the array tag. For a free-standing tag, d1 and d2 equal 0. Hence, equations (3.12) and (3.13) would become:

$$Z_{TM\therefore TE,h}^{left} = Z_{TM\therefore TE,h}^{right} = Z_{TM\therefore TE,mn}^{(1)} \tag{3.14}$$

Thus:

$$Z_{TM\therefore TE,h}^{in} = 0.5\, Z_{TM\therefore TE,mn}^{(1)} \tag{3.15}$$

$Z_{TM\therefore TE,mn}^{(1)}$ represents the modal characteristic impedance and can be calculated for each TE or TM mode using [104]:

$$Z_{TE,mn}^{(\varepsilon_r)}(\omega) = \frac{j\omega\mu_0}{\gamma_{mn}} \tag{3.16}$$

$$Z_{TM,mn}^{(\varepsilon_r)}(\omega) = -\frac{j\gamma_{mn}}{\omega\varepsilon_r\varepsilon_0} \tag{3.17}$$

where *mn* are unique integers used to define each TE or TM higher-order mode. μ_0 and ε_0 are the permeability and permittivity of free space, respectively. ε_r is the relative permittivity of the transmission medium. γ_{mn} is the complex wavenumber in the direction of incident wave (which is assumed to be along the z axis as shown in Fig. 3.10) and can be given by for any higher order mode using [104]:

$$\gamma_{mn} = \sqrt{k_{x,m}^2 + k_{y,n}^2 - k_0^2\varepsilon_r} \tag{3.18}$$

k_0 is the free space wavenumber, while $k_{x,m}$ and $k_{y,n}$ are the transverse components of the wavenumber. For a TE polarized wave, they can be given by [118]:

$$k_0 = \frac{\omega}{c} \tag{3.19}$$

$$k_{x,m} = k_0 \sin\theta + \frac{2m\pi}{D_x} \tag{3.20}$$

$$k_{y,n} = \frac{2n\pi}{D_y} \tag{3.21}$$

Where c is the speed of light in free space, D_x & D_y are the inter-element spacing in the x and y directions of the array, θ is the angle of incidence.

3.2.1.2.1 Calculation procedure of multimode equivalent circuit parameters

The steps for calculating the parameters of multi-mode equivalent circuit can be summerized as follows [104, 118]:

1- Determine the number of involved floquet modes (i.e. N_{TE} and N_{TM}) based on their cuttoff frequency which can be calculated using [104]:

$$f_{c,mn}^{\varepsilon_r} = \frac{1}{\varepsilon_r - \sin^2\theta} * \{\frac{mc}{D_x} \text{Sin}\,\theta + \sqrt{\varepsilon_r \left[\left(\frac{mc}{D_x}\right)^2 + \left(\frac{nc}{D_y}\right)^2\right] - \left(\frac{nc}{D_y}\sin\theta\right)^2}\} \tag{3.22}$$

2- Calculate the input impedance associated with each considered higher order mode using (3.11).

3- Calculate $Z_{TAG\_multi\_mode}$ using (3.3) and by obtaining the value of Γ at selected frequency points from a full-wave simulation. The number of points should be equal to the number of unknowns in (3.6).

4- L, C, and $A_h^{TM \therefore TE}$ (the degree of exitation of each mode) can be calculated by solving the resulting system of linear equations from (3.6) by using matrix inversion method or any alternative solver.

5- In order to get physically meaningful results, the frequency points needs to be chosen based on a specific criteria. It has been suggested in [104] that two frequency points should be selected as 0.01 and 0.03 times the frequency at which grating lobes occurs which can be calculated using [101]:

$$f_g = \frac{r * c}{D_x * (\sin\theta + 1)} \tag{3.23}$$

where *r* is an integer. The third and fourth frequency points should be chosen as 0.98 times the cutoff frequency of any considered higher order mode.

3.2.1.2.2 Analysis of uniform cross tag using multi-mode equivalent circuit model

The uniform cross array shown in Fig. 3.10 has been designed and simulated using ANSYS designer (ADS) full-wave simulator for a frequency range of 0-10 GHz. 2001 data samples were set for S-parameters calculation, and a fixed meshing was used with solution frequency of 30

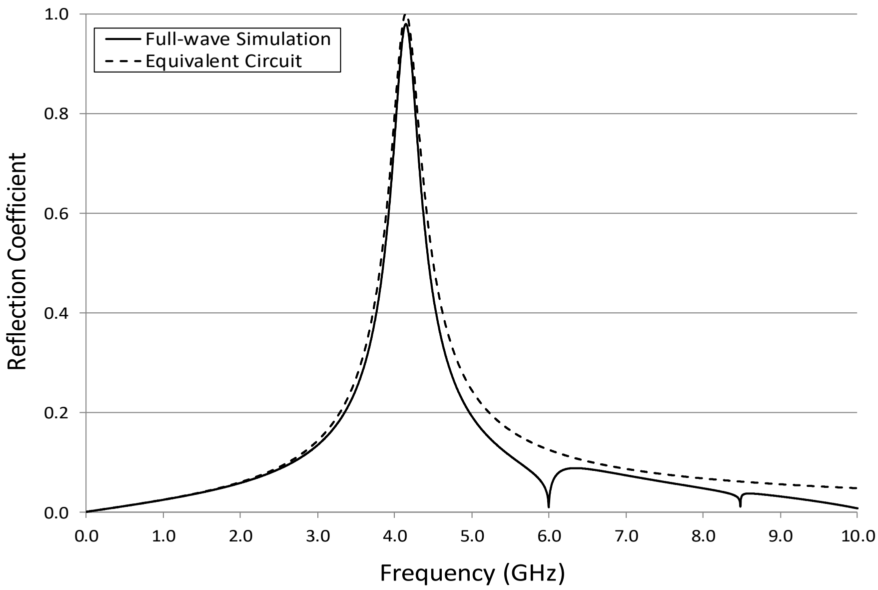

(a)

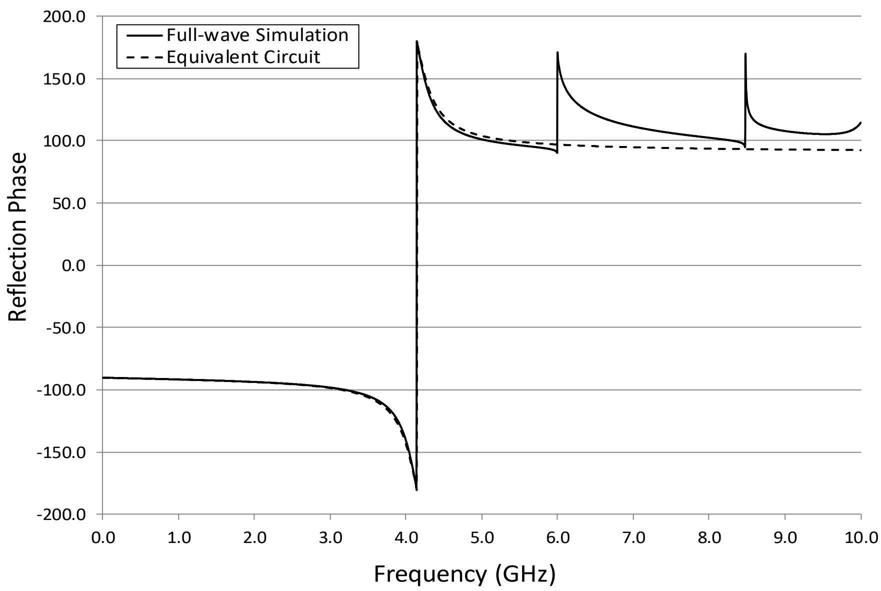

(b)

Fig. 3.16 A comparison between single-mode equivalent circuit and full-wave simulation for (a) reflection coefficient (b) reflection phase for uniform cross array.

GHz. The reason behind selecting ADS over CST in this section is because ADS (which employes method of moment (MoM) method to find the solution) gives more accurate results in the area beyond the onset of grating lobes. A comparison between the response of uniform cross array using MoM simulator and single-mode equivalent circuit model is shown in Fig 3.16 for reflection coefficient and reflection phase. Clearly, the response of the single-mode equivalent circuit model shows a very good agreement with full-wave simulation results for the fundamental resonance zone, but has a different behaviour after the onset of grating lobes. The equivalent circuit parameters are 76.31 nH and 19.32 fF. In order to increase the range of validity for the equivalent circuit response, the first higher order mode, TE10, was added to the circuit. The cut-off frequency of this mode calculated using (3.22) is 6 GHz. The equivalent circuit model including the impedance of the first HOM is shown in Fig. 3.17. It can be seen that the value of the inductance has dropped about 30 nH after the inclusion of the first higher order mode TE10. This significant decrease in inductance is because the impedance associated with TE modes is inductive. Hence, the inductance of the circuit is now shared between two components Z_L and X_L. It can also be noticed that the value of capacitance has remained unchanged.

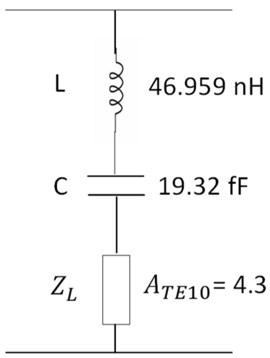

Fig. 3.17 Equivalent circuit model for the uniform cross array using the multi-mode approach with one higher order mode (TE10)

Fig. 3.18 shows a comparison between the response of multi-mode equivalent circuit (with TE10 mode) and full-wave simulation. It can be noticed that the inclusion of the first higher order mode has improved the matching of the fundamental mode and has correctly described the null at 6 GHz. The second higher order mode TE11 has been added to the circuit. The cut-off frequency of this mode is 8.485 GHz. The parameters of the equivalent circuit model including TE10 & TE11 modes are depicted in Fig. 3.19.

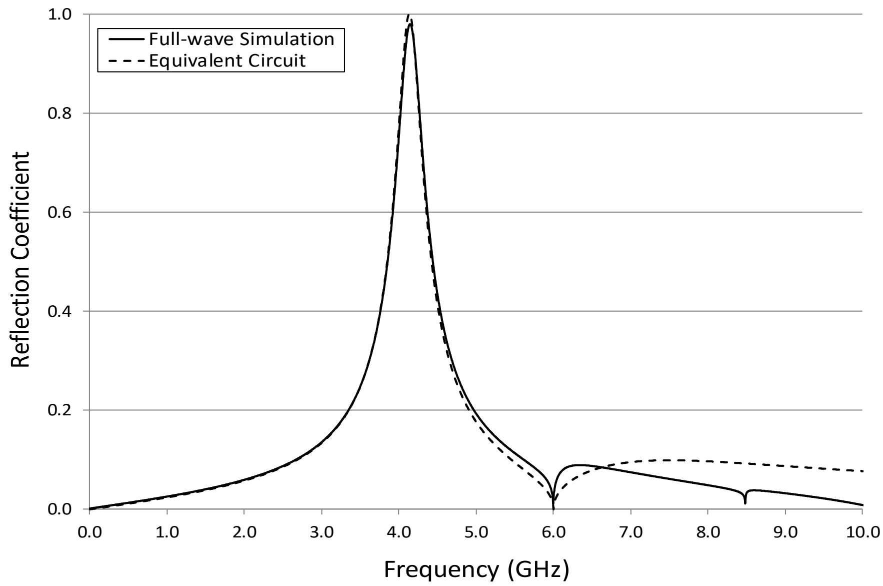

(a)

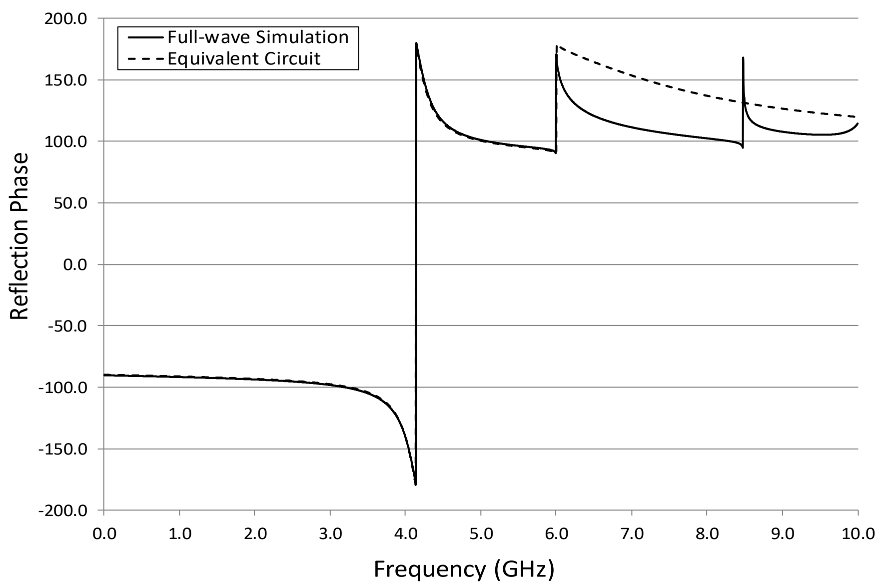

(b)

Fig. 3.18 A comparison between equivalent circuit model using multi-mode approach (with TE10 mode) and full-wave simulation of (a) reflection coefficient (b) reflection phase for uniform cross array.

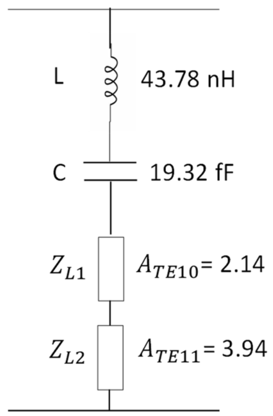

Fig. 3.19 Equivalent circuit model for the uniform cross array tag using the multimode approach with two higher order mode (TE10 & TE11).

After the inclusion of the second higher order mode (TE11), the inductance value has dropped again but this time by about 3 nH only. Additionally, the level of excitation of the first higher order mode A_{TE10} has dropped as well from 4.3 to 2.14. As explained before, that is caused by introducing another inductive impedance to the circuit, so the inductance of the circuit is now shared by three components X_L, Z_{L1}, and Z_{L2}. Fig. 3.20 shows a comparison between the response of multimode equivalent circuit (with TE10 & TE11 modes) and full-wave simulation.

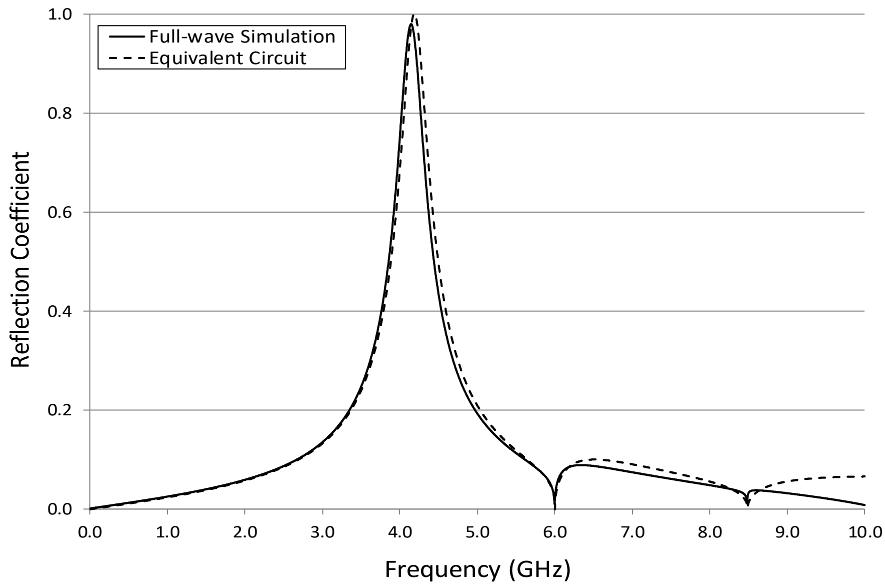

(a)

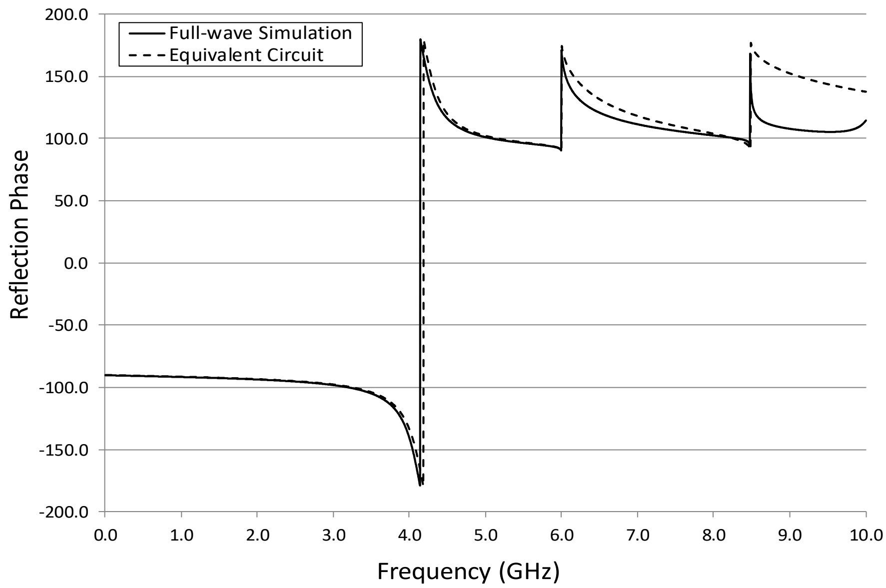

(b)

Fig. 3.20 A comparison between equivalent circuit model using multi-mode approach (with TE10 & TE11 modes) and full wave simulation of (a) reflection coefficient (b) reflection phase for uniform cross array.

It can be seen that the equivalent circuit shows a very good agreement with full-wave simulation until the onset of the second higher order mode TE11 at 8.485 GHz. More floquet modes can be considered to extend the validity range of equivalent circuit further. However, it has been noticed that as the number of higher order modes increases the circuit starts to lose the perfect matching in the fundamental resonance zone. As mentioned earlier, equivalent circuit model is not just a faster calculation method but it helps to explain the underlying physics of the structure as well. From Fig. 3.20, it can be inferred that the singularity points at 6 GHz and 8.485 GHz are caused by the onset of TE10 and TE11 modes respectively. The nulls at the onset of TE modes, also known as Wood's anomalies [104], occurs because the normal component of the wavenumber γ_{mn} becomes zero at these points (which is the cut-off frequency condition of floquet modes). Hence, the impedance of TE modes, Z_L, would diverge to infinity leading to an open circuit in the equivalent model, therefore, a total transmission occurs at these points.

To sum up, this section has introduced a multi-mode equivalent circuit model for a uniform cross array. The inclusion of higher order modes can result in more accurate equivalent circuit response and can give more insights about the underlying physics of the structure. Despite the added complexity, the multimode approach represents a good option for analysing free-standing structures. However, in order to study the impact of surrounding dielectric media on the self-resonant tag response, the single-mode approach is the better option. The impact of higher order modes diminishes as the thickness/permittivity of the surrounding dielectric media increases, as will be shown later in this chapter and in chapter four.

3.3 Impact of surrounding dielectric media on self-resonant tag response

So far in this chapter only free-standing self-resonant structures have been discussed. The presence of dielectric layers around the metallic resonator enforces certain changes to the frequency response of the SRS. They primarily cause a downward frequency shift in the resonance position, the amount of shift is proportional to the thickness and permittivity of the dielectric layer [101, 119]. They can also cause signal power loss depending on the attenuation constant of these layers. For material types that are used in FSS and RFID fabrication such as FR4, glass, and PTFE, the loss tangents are low in the frequency range of interest, hence, the dielectric losses can be ignored. On the other hand, in the case of implantable self-resonant tags, the dielectric losses imposed by the biological media are very high and affect the tag response remarkably. In the remainder of this chapter, the impact of lossless dielectric layers on the tag response will be studied using an equivalent transmission line model approach. The impact of lossy media will be investigated in the next chapter.

3.3.1 Derivation of impedance expressions

3.3.1.1 Normal incidence

As explained in 3.2.1.1, a free-standing SRS can be represented by a series LC circuit placed across a transmission line with a characteristic impedance Z_0, and this transmission line is terminated by its characteristic impedance. When a dielectric substrate is used to physically support the SRS or to shape its response, it can be added to the equivalent network as a distance, d_1, long transmission line section. The first step towards deriving the expression of SRS impedance on a dielectric layer is to find the impedance at the beginning of the transmission line section, namely Z_{Load1} as illustrated in Fig. 3.21, which can be calculated as follows:

$$Z_{Load1} = Z_{d1} * \frac{Z_0 + jZ_{d1}\tan(k_{z1}d_1)}{Z_{d1} + j\,Z_0\tan(\,k_{z1}d_1)} \tag{3.24}$$

After that, the equivalent impedance of Z_{Load1} and SRS impedance, Z_{SRS}, can be expressed as:

$$Z_{eq} = \frac{Z_{Load1} * Z_{SRS}}{Z_{Load1} + Z_{SRS}} \tag{3.25}$$

Thus, reflection coefficient can be calculated using:

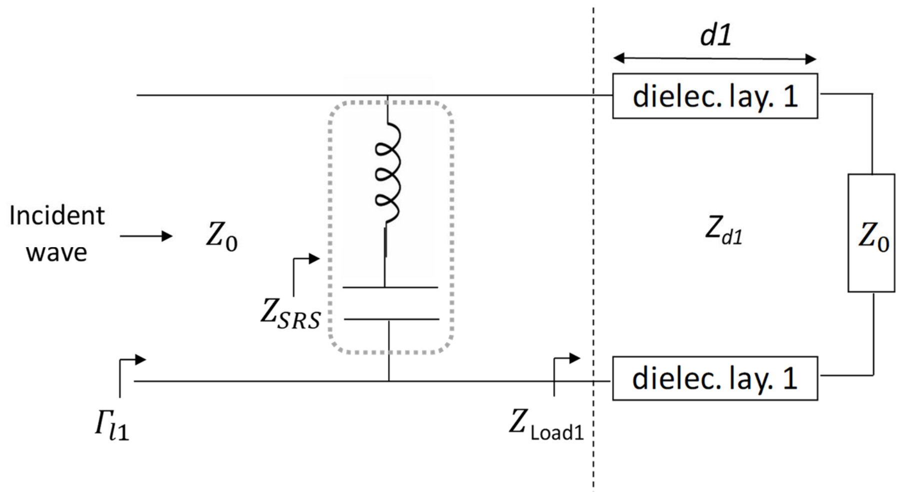

Fig. 3.21 Transmission line representation of an SRS on a dielectric layer. The dielectric media is represented by transmission line segment on the right of the SRS with length of d_1.

$$\Gamma_{l1} = \frac{Z_{eq} - Z_0}{Z_{eq} + Z_0} \tag{3.26}$$

By substituting (3.25) in (3.26), the SRS impedance on a dielectric layer can be expressed as:

$$Z_{SRS\_os} = -\frac{Z_{Load1}\, Z_0\, (\Gamma_{l1} + 1)}{Z_{Load1}\, (\Gamma_{l1} - 1) + Z_0\, (\Gamma_{l1} + 1)} \tag{3.27}$$

where Γ_{l1} is the reflection coefficient and could be obtained from a full-wave simulation or experimental measurements. Z_{d1} is the characteristic impedance of the dielectric layer and can be calculated using $Z_{d1} = \sqrt{\mu/\varepsilon}$, where μ *and* ε are the permeability and permittivity of the dielectric material. k_z is the normal component of the wavenumber (assuming the 2D metallic structure in the *xy* plane and the wave propagates in the *z* direction) and is given by $k_z = \sqrt{\varepsilon_r} * \omega/c$.

Similarly, when an SRS is embedded in a dielectric medium, a second transmission line segment are added to the left of the SRS impedance as illustrated in Fig. 3.22. Following the same procedure of deriving equation (3.27), the impedance of the whole structure seen from the source side, Z_{Load2}, can be calculated using:

$$Z_{Load2} = Z_{d2} * \frac{Z_{eq} + jZ_{d2}\tan(k_{z2}d_2)}{Z_{d2} + j\,Z_{eq}\tan(\,k_{z2}d_2)} \tag{3.28}$$

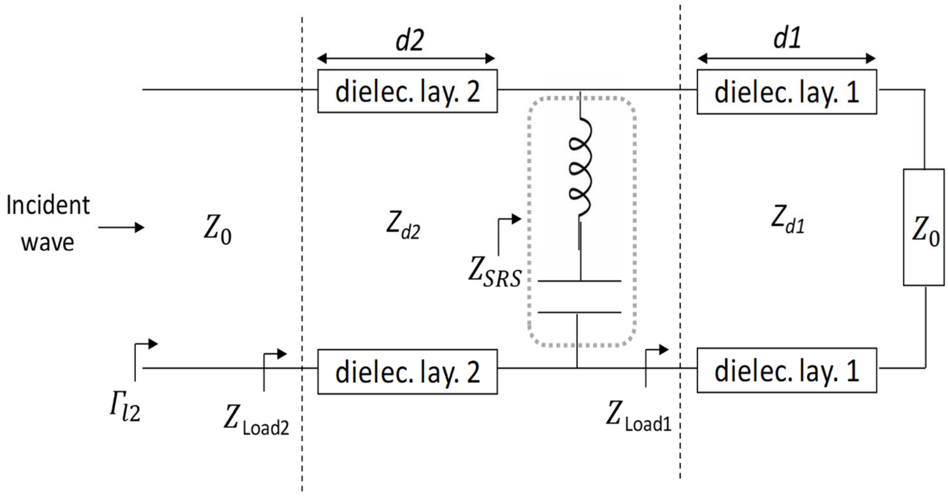

Fig. 3.22 Transmission line representation of an SRS inside a dielectric medium. The latter is represented by transmission line segments on the right and left of the SRS with length of *d*1 and *d*2, respectively.

Thus, reflection coefficient will be given using:

$$\Gamma_{l2} = \frac{Z_{load2} - Z_0}{Z_{load2} + Z_0} \tag{3.29}$$

By substituting (3.25) in (3.28), and (3.28) in (3.29), the SRS impedance inside a dielectric medium can be expressed as:

$$Z_{SRS\_id} = \frac{\begin{array}{c} j\, Z_{d2}^2 \tan(k_{z2} d_2)\, Z_{Load1}(\Gamma_{l2} - 1) + \\ Z_0 Z_{d2} Z_{Load1}(\Gamma_{l2} + 1) \end{array}}{\begin{array}{c} -Z_{d2} Z_{Load1}(\Gamma_{l2} - 1) - j\, Z_{d2}^2 \tan(k_{z2} d_2)(\Gamma_{l2} - 1) - \\ Z_0 Z_{d2}(\Gamma_{l2} + 1) - j \tan(k_{z2} d_2)\, Z_{Load1} Z_0 (\Gamma_{l2} + 1) \end{array}} \tag{3.30}$$

The inductance and capacitance of the SRS can be extracted based on error minimization criteria between SRS impedance and the impedance of a series LC circuit as explained in section 3.2.1.1.

3.3.1.2 Oblique incidence

The analysis presented in the previous section considers the case where the electromagnetic wave impinges upon the SRS at normal incidence angle. In order to account for incidence at any angle, some modifications need to be made in the wavenumber and characteristic impedance equations. The free space intrinsic impedance for a wave propagating at any angle of incidence for TE and TM incidences are $Z_{fs}^{TE} = Z_0/\cos\theta$ and $Z_{fs}^{TM} = Z_0 * \cos\theta$, respectively, where θ represents the angle of incidence. Similarly, the characteristic impedances of the dielectric slab when the wave impinges upon the SRS at oblique angles for TE and TM polarizations are $Z_d^{(TE)} = \omega\mu_0/k$ and $Z_d^{(TM)} = k/\omega\varepsilon_0\varepsilon_r$, respectively. k is the complex wavenumber with both normal and transverse components and can be calculated using $k = \frac{\omega}{c}\sqrt{\varepsilon_r - (\sin\theta)^2}$ [120]. Thus, the SRS impedance inside a dielectric medium at any angle of incidence can be calculated using the following equations for TE and TM incidences, respectively:

$$Z_{SRS\_is^{TE}} = \frac{j\,(\frac{\omega\mu_0}{k_2})^2 \tan(k_2 d_2)\, Z_{Load1}\,(\Gamma_{l2} - 1) + \frac{\omega\mu_0}{k_2}\; Z_0\, Z_{Load1}(\Gamma_{l2} + 1)}{-\frac{\omega\mu_0}{k_2}\, Z_{Load1}(\Gamma_{l2} - 1) - j\,(\frac{\omega\mu_0}{k_2})^2 \tan(k_2 d_2)(\Gamma_{l2} - 1) - \frac{\omega\mu_0}{k_2}\, Z_0\,(\Gamma_{l2} + 1) - j\tan(k_2 d_2)\, Z_{Load1} Z_0 (\Gamma_{l2} + 1)} \tag{3.31}$$

$$Z_{SRS\_is^{TM}} = \frac{j\,(\frac{k_2}{\omega\varepsilon_0\varepsilon_{r2}})^2 \tan(k_2 d_2)\, Z_{Load1}\,(\Gamma_{l2} - 1) + \frac{k_2}{\omega\varepsilon_0\varepsilon_{r2}}\, Z_0\, Z_{Load1}(\Gamma_{l2} + 1)}{-\frac{k_2}{\omega\varepsilon_0\varepsilon_{r2}}\, Z_{Load1}(\Gamma_{l2} - 1) - j(\frac{k_2}{\omega\varepsilon_0\varepsilon_{r2}})^2 \tan(k_2 d_2)(\Gamma_{l2} - 1) - \frac{k_2}{\omega\varepsilon_0\varepsilon_{r2}}\, Z_0(\Gamma_{l2} + 1) - j\tan(k_2 d_2)\, Z_{Load1} Z_0 (\Gamma_{l2} + 1)} \tag{3.32}$$

It is worth mentioning that the proposed model can predict the SRS's main resonance mode in addition to the frequency response of any involved dielectric layer.

3.3.2 Scattering parameters calculations of SRS inside multi-layer dielectric media

3.3.2.1 Scattering matrix

Once the L and C values have been calculated for the SRS on or inside a dielectric layer, the transmission matrix can be exploited to calculate the S-parameters. The ABCD parameters can be calculated for an SRS inside dielectric media using:

$$\begin{bmatrix} A & B \\ C & D \end{bmatrix} = [\text{dielectric layer\_1}] * [\text{SRS}] * [\text{dielectric layer\_2}] \tag{3.33}$$

where the transmission matrix of a dielectric layer is given by [121]:

$$[dielectric\ layer\_n] = \begin{bmatrix} \cos(\beta_n d_n) & \mathrm{j}\sin(\beta_n d_n) * Z_{d\_n} \\ \mathrm{j}\sin(\beta_n d_n) * 1/Z_{d\_n} & \cos(\beta_n d_n) \end{bmatrix} \tag{3.34}$$

while SRS transmission matrix can be found using [121]:

$$[\text{SRS}] = \begin{bmatrix} 1 & 0 \\ \dfrac{1}{Z_{SRS}} & 1 \end{bmatrix} \tag{3.35}$$

And the S-parameters of a 2-port system can be calculated using [121]:

$$S_{11} = \frac{A + \frac{B}{Z_0} - CZ_0 - D}{A + \frac{B}{Z_0} + CZ_0 + D} \tag{3.36}$$

$$S_{12} = \frac{2(AD - BC)}{A + \frac{B}{Z_0} + CZ_0 + D} \tag{3.37}$$

$$S_{21} = \frac{2}{A + \frac{B}{Z_0} + CZ_0 + D} \tag{3.38}$$

$$S_{22} = \frac{-A + \frac{B}{Z_0} - CZ_0 + D}{A + \frac{B}{Z_0} + CZ_0 + D} \tag{3.39}$$

3.3.2.2 Novel simplified formula

Although scattering matrix offers an easy and accurate way for calculating the scattering parameters, it does not provide insights into the parameters contributing into their values. Hence, in this section new simplified expression for calculating transmission coefficient is proposed. The calculation of the reflection coefficient can be achieved by following a backward recursion approach. Conversely, there is no direct relationship to calculate the forward transmission coefficient for such a model. Hence, the following principles have been considered when deriving the new simplified S_{21} expression:

- In the absence of losses, the summation of reflected and transmitted signals' power equals one, hence, knowing the reflection coefficient is enough to calculate the magnitude of the transmitted signal.
- The phase is a time delay, hence the signal at port 1 has an initial transmission phase of zero degree.
- The phase change of the transmitted signal through transmission line sections is governed by the phase constant of each dielectric layer and follows a complex exponential function.
- The effect of the SRS can be perceived as an LC filter shunted across a transmission line. Since no real part exists, it would only affect the phase response of the forward transmission coefficient.

Fig. 3.23 shows a schematic representation of incident signal traveling down an SRS shunted across a multi-segment transmission line. *R*1 and *R*2 represent the impedances of the input and output ports, and in this case they are both equal to Z_0. Thus, forward transmission coefficient can be expressed as:

$$S_{21} = \sqrt{1 - |S_{11}|^2}\, e^{-i(k_{z1}d_1 + k_{z2}d_{2+} \dots k_{zn}d_n)}\, e^{i\varphi} \qquad (3.40)$$

where φ represents the phase response of the SRS equivalent circuit and can be expressed as:

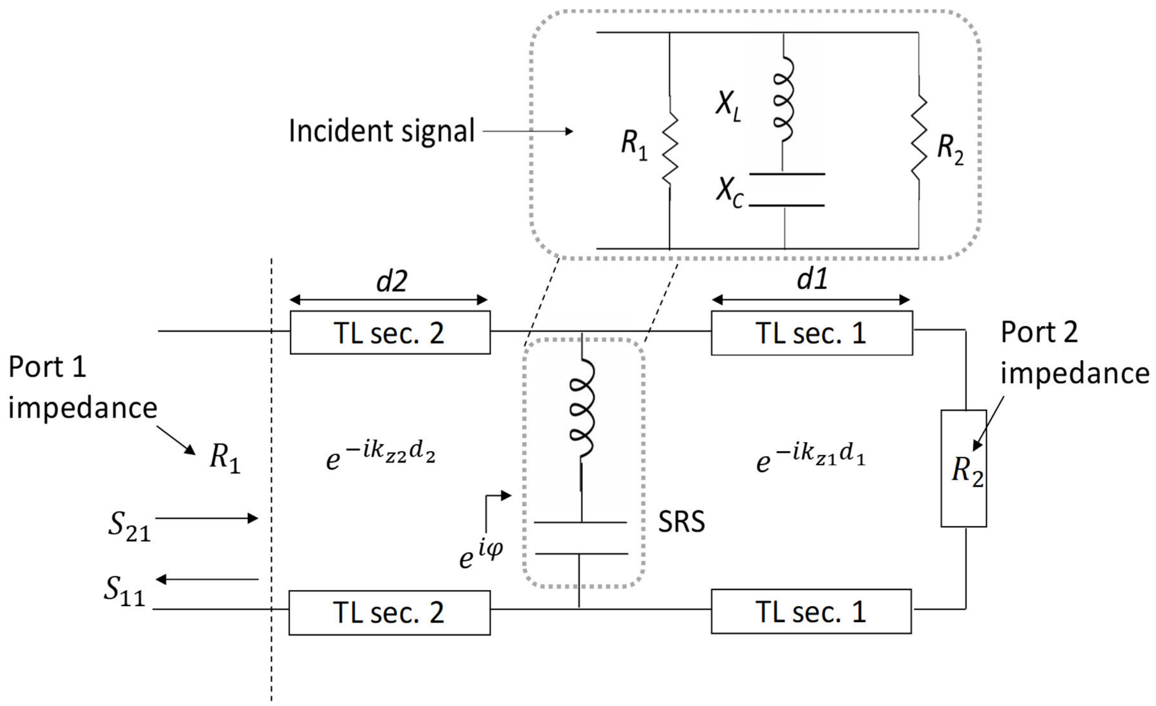

Fig. 3.23 SRS shunted across multi-segment transmission line representation.

$$\varphi = -\tan^{-1}\left(\frac{\omega C Z_0}{2(1-\omega^2 LC)}\right) \tag{3.41}$$

This section has presented a new and novel set of expressions derived to calculate SRS impedance for normal incidence on dielectric materials (3.27), and within dielectric layers (3.30). Equations (3.31) and (3.32) describe SRS impedance within dielectric materials for TE and TM at oblique angles of incidence. Subsequently, it becomes trivial to extend these for multi-layer applications. Additionally, a novel and simplified method for calculating the forward transmission coefficient of SRS inside multi-layered media has been derived, as presented in (3.40) and (3.41). The following section aims to validate these derivations and to assess their accuracy.

3.3.3 Analysis of dielectric loaded uniform cross tag

3.3.3.1 SRS on a dielectric substrate

The uniform cross SRS design shown earlier has been tested with three different substrate materials to investigate the effect of the material's dielectric constant on the equivalent circuit parameters. Dielectric substrates are mainly used to physically support the electromagnetic scatterer, but in some cases they are employed to shape the response or to stabilize the change in resonance frequency as angle of incidence is varied [101]. Fig. 3.24 shows capacitance values of the equivalent circuit with three different substrate materials and with different thicknesses. It can be seen that the capacitance increases with the thickness and permittivity of the substrate. These findings are in agreement with the static capacitance equation which can be given by [117]:

$$C = \varepsilon_r \varepsilon_0 \frac{A}{d_c} \tag{3.42}$$

where d_c is the distance between the parallel plates, A is the coupling area of the plate. It can be seen that the capacitance is directly proportional to the permittivity of the substrate. On the other hand, the relationship between the capacitance and dielectric slab thickness is not clear from this expression. However, an increase in slab thickness leads to higher effective permittivity which in turns increases the capacitance.

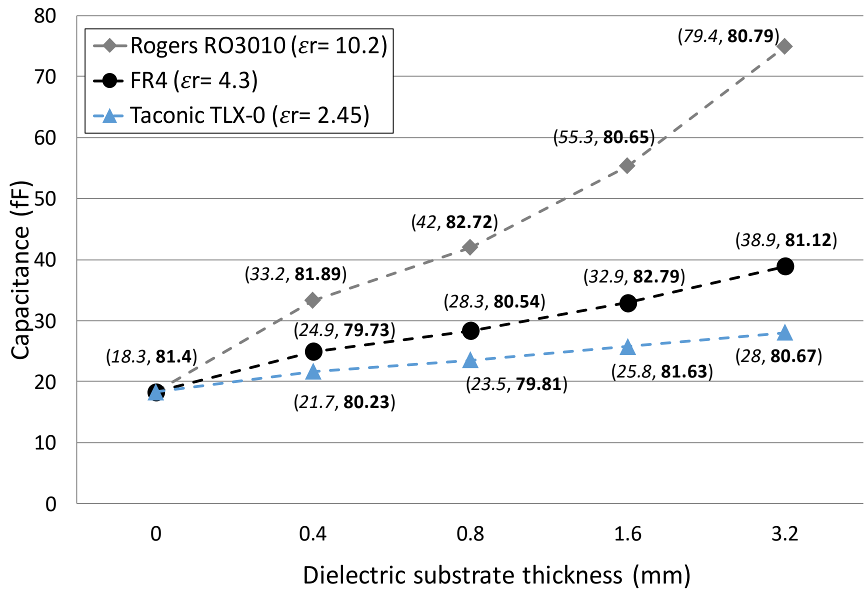

Fig. 3.24 Equivalent circuit capacitance of a uniform cross SRS on three different substrate materials at different thicknesses. Data labels are shown for L (nH) and C (fF) values, italic for capacitance values and bold for inductance.

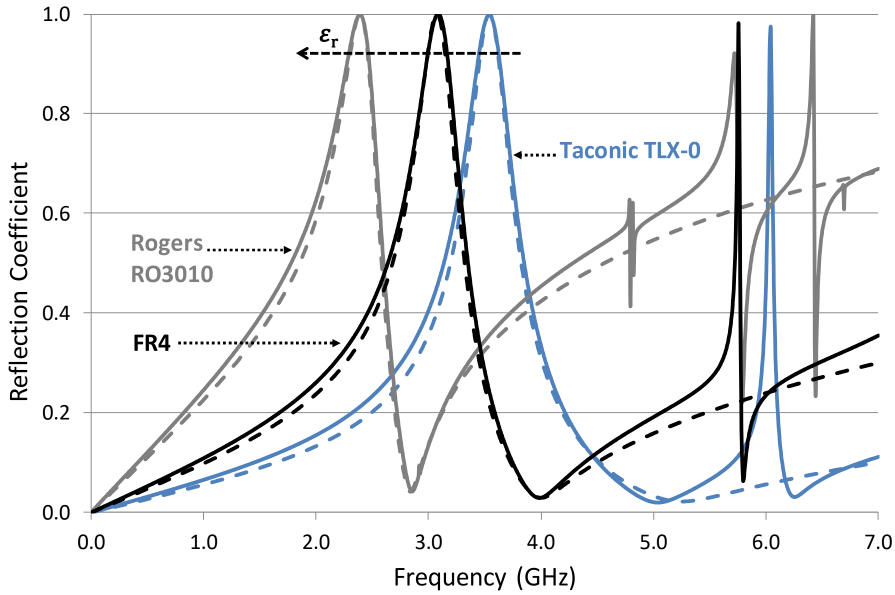

Fig. 3.25 A comparison between full-wave (solid) and equivalent circuit (dashed) response for reflection coefficient (S_{11}) for uniform cross resonator on three different substrate materials of 1.6 mm thickness.

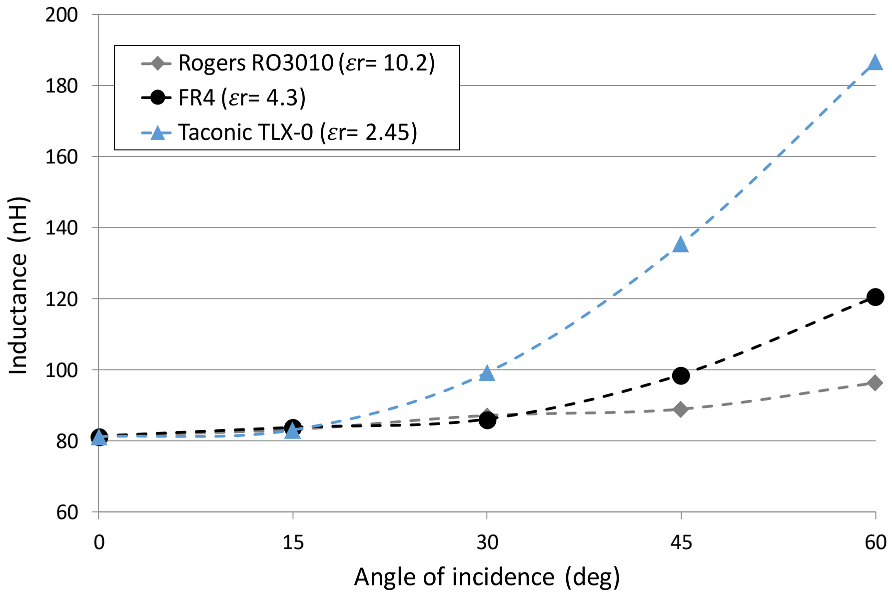

Fig. 3.26 Equivalent circuit inductance of a uniform cross SRS on three different substrate materials at different angles of incidence, TE polarization.

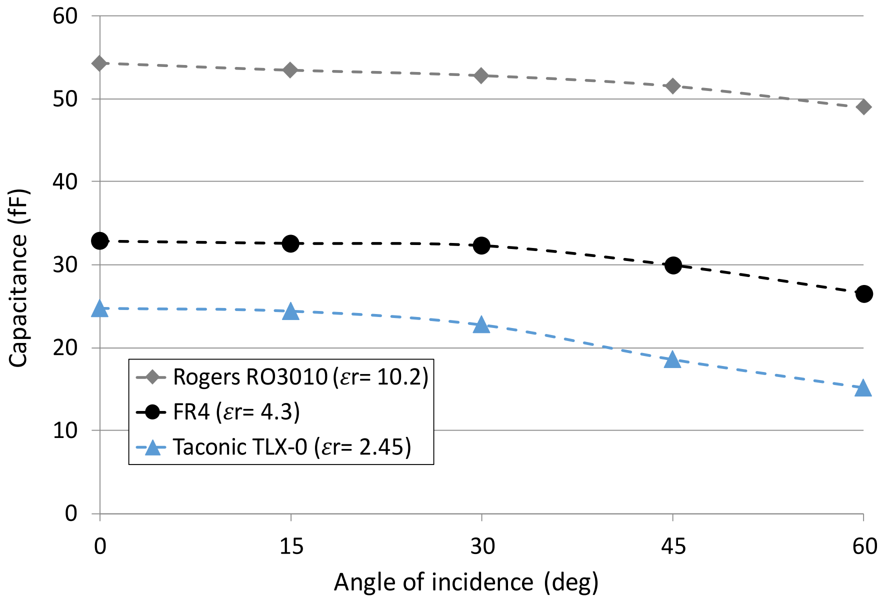

Fig. 3.27 Equivalent circuit capacitance of a uniform cross SRS on three different substrate materials at different angle of incidence, TE polarization.

Unlike capacitance, inductance values remain almost constant irrespective of the type or thickness of the dielectric layer as presented in the data labels of Fig. 3.24. It should be noted that the dielectric layer thicknesses are much less than half of the unit cell periodicity of the SRS which is the condition required to reach the limiting value of that material [105]. Fig. 3.25 shows a comparison between full wave simulation and equivalent circuit models for the reflection coefficient of a uniform cross resonator on these three substrate materials. It can

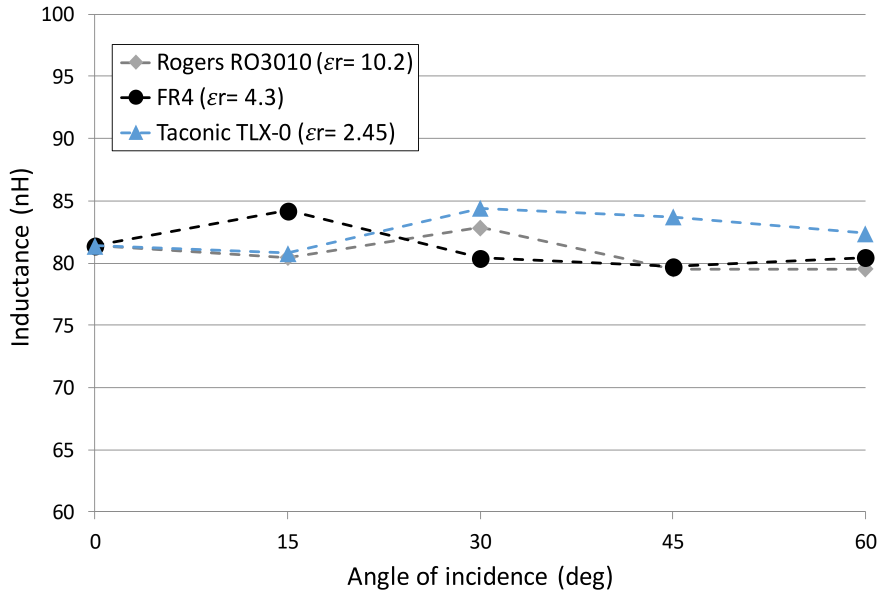

Fig. 3.28 Equivalent circuit inductance of a uniform cross SRS on three different substrate materials at different angle of incidence, TM polarization.

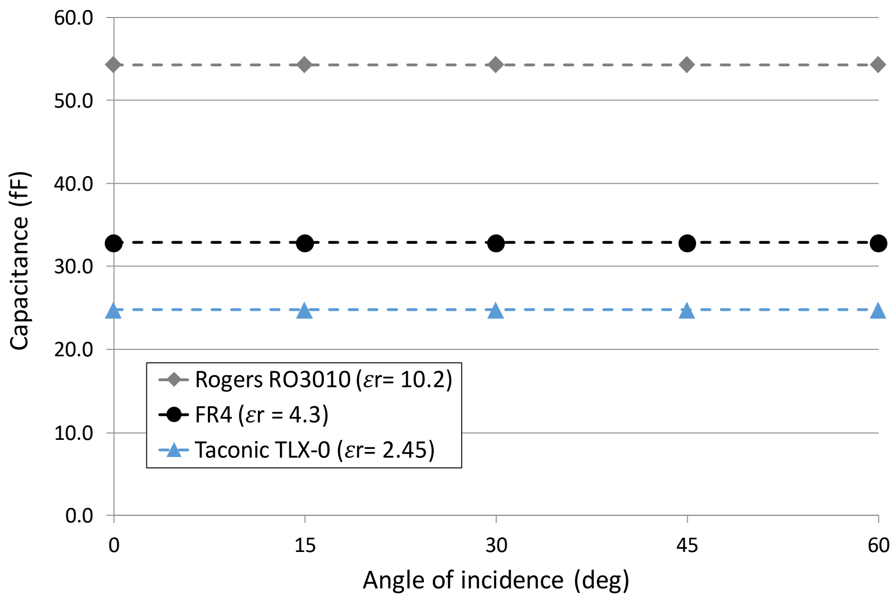

Fig. 3.29 Equivalent circuit capacitance of a uniform cross SRS on three different substrate materials at different angle of incidence, TM polarization.

be seen that our equivalent circuit model follows the full wave simulation curves very well for the main resonance mode.

The uniform cross resonator has been investigated on different substrate materials for different angles of oblique incidence and the equivalent circuit parameters have been extracted. For TE incidence, the SRS on the three substrate materials shows an increase in inductance with angle of incidence as depicted in Fig. 3.26. The reason behind this increase in inductance is due to the fact that uniform cross strips start to appear narrower as the angle of incidence increases. On the other hand, capacitance shows a slight decrease with progressive increase of incidence angle. This reduction in capacitance values is caused by the decrease in the coupling area between the parallel plates of the uniform cross arms (as illustrated in Fig. 3.9). The relation between coupling area and capacitance is evident in the static capacitance equation shown in (3.42). It is worth noting that the differences in capacitance values between the three substrate materials have been maintained as illustrated in Fig. 3.27. With TM incidence, the inductance values for the three substrate types do not show consistent trends and the values range between 80 and 85 (nH) for all cases. Similarly, capacitance values remained unchanged under different angles of incidence. The inductance and capacitance values for TM polarization with different angle of incidence are shown in Fig. 3.28 and Fig. 3.29, respectively.

One of the main benefits of the equivalent models is to simplify the design and optimization processes of electromagnetic structures by revealing some of the underlying physics. Fig. 3.30 shows a comparison between the response of uniform cross on 1.6 mm FR4 at normal incidence and at an angle of incidence of 60° under TM incidence. It can be seen that the two curves have the same resonance frequency, at the same time their equivalent circuits show the same values of inductance and capacitance at both incidence angles despite having a completely different angle response. In fact, this difference is merely attributed to the modelling of the dielectric substrate at oblique angles of incidence. The characteristic impedance of the dielectric substrate is dependent on the incidence angle as explained in 3.3.1.2. Thus, the characteristic impedance of any dielectric slab increases with angle of

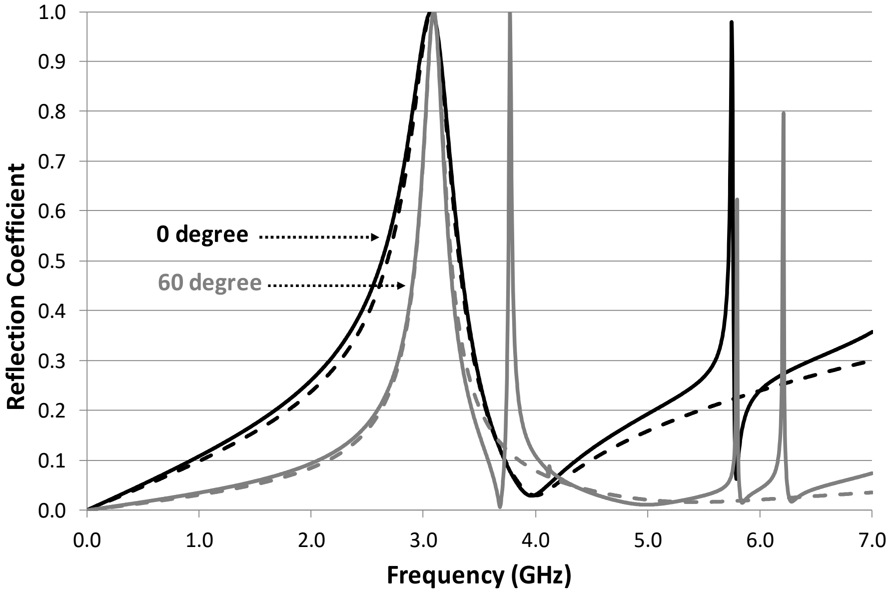

Fig. 3.30 A comparison between full-wave (solid) and equivalent circuit (dashed) response for uniform cross on 1.6 mm FR4 at normal incidence and at 60° TM incidence.

incidence with a TE polarized signal. Conversely, it decreases with TM polarization, the same applies for free-space intrinsic impedance. It is worth noting here that the two responses have different grating lobe onsets due to different angles of incidence.

It is known that all equivalent models have limitations and no single model is valid under all circumstances. Thus, in order to assess the accuracy of the proposed model, the response of the uniform cross SRS have been compared to the full-wave response using mean absolute error (MAE) criteria for the main resonance mode [122]. The evaluation has involved different angles of incidence, polarizations, substrate materials and thicknesses as shown in Table 3.2. From the results presented in the table, it can be seen that the model exhibits acceptable accuracy even for high incidence angles with a maximum error percentage of about 6.5%. For TE incidence, it can be noticed that accuracy is directly proportional to substrate thickness and inversely proportional to angle of incidence. Additionally, the equivalent circuit model shows higher accuracy with higher dielectric constant, Rogers RO3010 being the most accurate while Taconic TLX-0 is the least accurate. The inaccuracy with low permittivity substrates can be caused by the loading effect of some higher order evanescent modes. These modes have their highest amplitude at the air/dielectric interface and they decay exponentially with distance from the scatterer. By increasing the permittivity of the dielectric

Table 3.2 MAE of the equivalent model compared to full-wave results of uniform cross under different angles of incidence, polarizations, substrate materials and thicknesses [Key: *TACONIC TLX-0,* FR4, **ROGERS RO3010]**

Angle of Incidence	Thickness (mm)	Average MAE %					
		TE			TM		
0°	0.8	*1.58*	1.39	**1.37**	*1.58*	1.39	**1.37**
	1.6	*1.48*	1.47	**1.6**	*1.48*	1.47	**1.60**
	3.2	*1.18*	0.95	**1.02**	*1.18*	0.95	**1.02**
30°	0.8	*5.56*	4.51	**1.92**	*2.12*	1.86	**1.44**
	1.6	*5.15*	2.78	**1.67**	*1.73*	1.82	**1.99**
	3.2	*3.55*	1.67	**0.95**	*1.70*	1.23	**0.99**
45°	0.8	*5.69*	5.49	**4.84**	*2.79*	2.75	**1.82**
	1.6	*5.45*	5.16	**2.35**	*2.60*	2.31	**1.92**
	3.2	*5.05*	2.80	**1.02**	*2.67*	1.70	**1.02**
60°	0.8	*6.57*	6.51	**5.73**	*3.13*	2.83	**1.93**
	1.6	*6.25*	5.43	**3.73**	*2.98*	2.39	**1.81**
	3.2	*5.52*	4.87	**1.18**	*3.23*	2.10	**0.95**

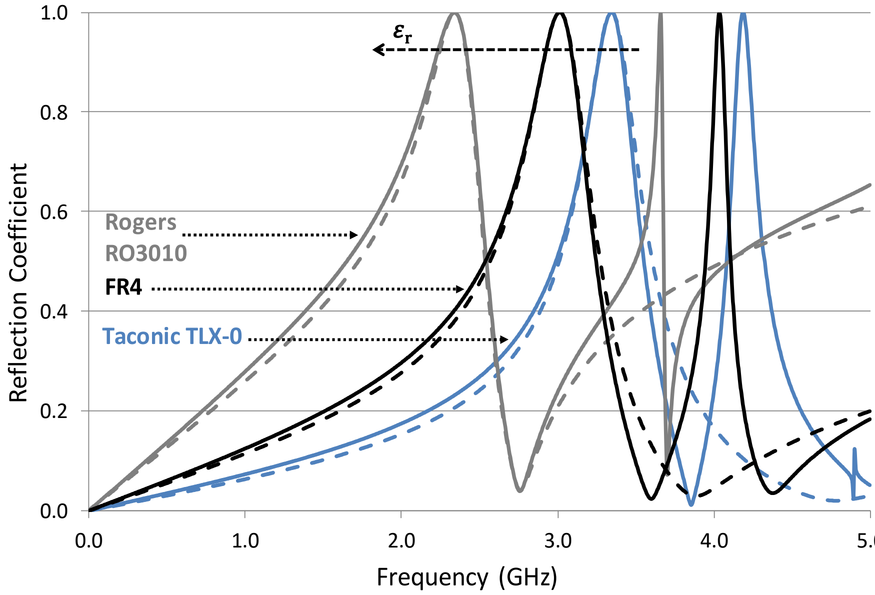

Fig. 3.31 A comparison between full-wave (solid) and equivalent circuit (dashed) response for reflection coefficient (S_{11}) for uniform cross resonator on three different substrate materials of 1.6 mm thickness at 30° TE incidence.

slab, their loading effect reduce thus the equivalent model response which only considers the main resonance mode resemble the full-wave response better, and same analysis applies for model accuracy and dielectric slab thickness. On the other hand, the progressive increase in the average MAE with the angle of incidence can be primarily caused by the grating lobes position of the SRS response. In addition to the impact on the equivalent lumped components values, it is known that as the angle of incidence increases, the onset of grating lobes is pushed down to a lower frequency [101]. In order to account for the grating lobes position in the equivalent model, at least one higher order mode needs to be considered besides the main propagating mode. These higher order modes (also known as Floquet modes as discussed in section 3.2.1.2) are evanescent before their cut-off frequency and propagative afterwards. The grating lobes position represent the cut-off frequency of the first higher order mode. The inclusion of the first TE mode in the equivalent model would force the S_{11} response of the uniform cross SRS to have a null at the onset of grating lobes, hence would result in better matching between full-wave simulation and equivalent model for the fundamental resonance zone. The singularity at the onset of TE modes happens because their associated impedance diverge to infinity at the mode's cut-off frequency leading to an open circuit in the equivalent model. Thus, the incident signal would bypass the SRS and only the frequency response of the dielectric medium can be seen in the overall response at the output port. This effect of higher order modes is more prominent with thin and low permittivity dielectric layers. As the dielectric layer thickness/permittivity increases the impact of higher order modes gradually diminishes. Generally, the number of included propagating modes in the equivalent model depends on the validity range needed for the intended application, as each extra mode adds additional complexity in the equivalent model generation. The proposed equivalent model in this section only considers the main propagating mode, which from the author's point of view is enough in most cases to avoid overcomplicating the model generation. The extraction of the higher order modes has been explained in section 3.2.1.2. Fig. 3.31 shows equivalent model response versus full wave simulation response for the three substrate types with a thickness of 1.6 mm at 30° TE polarized wave. It is clear that the equivalent model response is more accurate when the dielectric substrate has higher permittivity. For TM incidence, accuracy does not seem to follow any pattern. However, the model accuracy in general seems to be better.

3.3.3.1 SRS embedded inside a dielectric layer

The presented uniform cross SRS has been tested when embedded inside a 10 mm Pyrex glass layer (ε_r =4.82). The case of FSS inside glass is of practical importance. It has been reported in [123] and [124] that FSS layers can be used inside energy saving glasses and windows to improve electromagnetic signal transmission within a specific frequency band. Fig. 3.32 shows a comparison between the equivalent model and full-wave simulation. The transmission line model response combines the main resonance mode of the metallic resonator (in this case the uniform cross at state 0) in addition to the frequency response of two 5 mm layers of glass. Except for a higher order harmonic, the equivalent model matches the full-wave simulation better with thicker dielectric slabs, as previously explained in the last section.

The values of the equivalent circuits for the four states of the uniform cross in free-space versus the values inside a 10 mm glass layer are shown in Table 3.3. It can be seen that capacitance values have significantly increased while inductance values have maintained the same trend throughout the four resonant states of the uniform cross design.

A comparison between full-wave and equivalent model for the four resonant states of the uniform cross inside 10 mm glass layer is shown in Fig. 3.33 and Fig. 3.34 for forward transmission coefficient and transmission phase, respectively. The S_{21} expression introduced in (3.40) has been used to calculate the responses, it can be seen that a fairly accurate results have been obtained for both magnitude and phase for the main resonance mode. The accuracy between equivalent model and full wave responses have been assessed using the same MAE criteria for the four resonance states and under different incidence angles as presented in Table 3.4 It can be noticed that model accuracy has improved with thicker dielectric layer as the majority of MAE values fall below 1%.

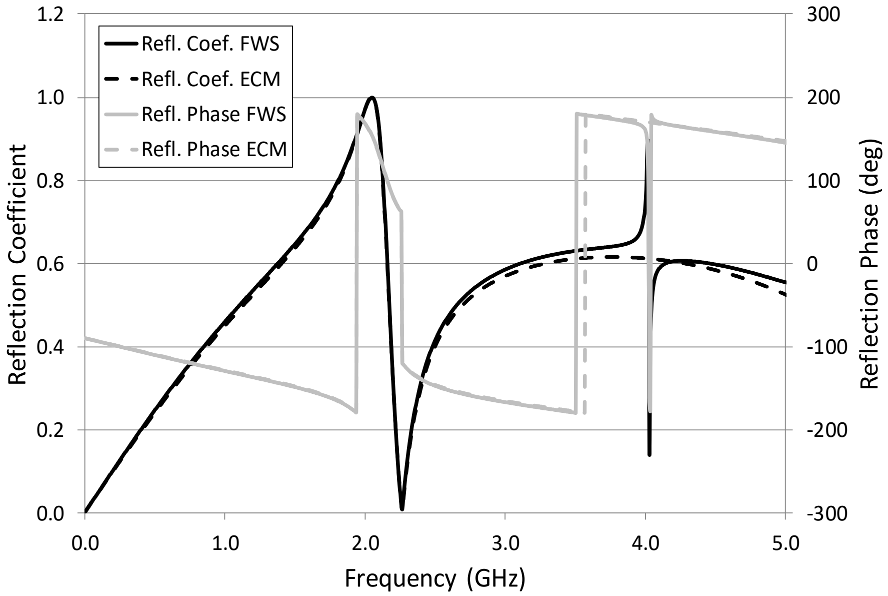

Fig. 3.32 A comparison between full-wave simulation (solid) and equivalent model (dashed) for reflection coefficient of uniform cross inside 10 mm layer of glass at normal incidence.

Table 3.3 Comparison between equivalent circuit parameters of uniform cross SRS at different resonant states inside 10 mm layer of Pyrex glass versus the free space values presented in Table 3.1

Resonance state	L (nH) free-st	L(nH) in glass	C (fF) free-st	C (fF) in glass
State 0	79.2	78.88	18.9	76.3
State 1	93.3	94.6	19.3	77.8
State 2	115.2	115.8	18.3	77.5
State 3	144.1	144.3	17.0	74.0

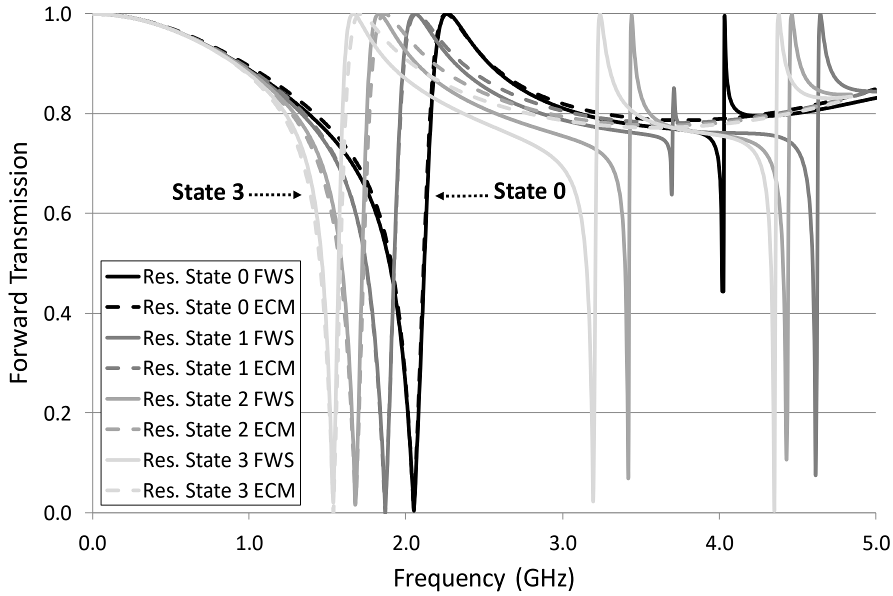

Fig. 3.33 A comparison between full-wave (solid) and equivalent circuit (dashed) response for forward transmission coefficient (S_{21}) magnitude [SRS states: complete SRS shown in black and lighter colour for each subsequent state].

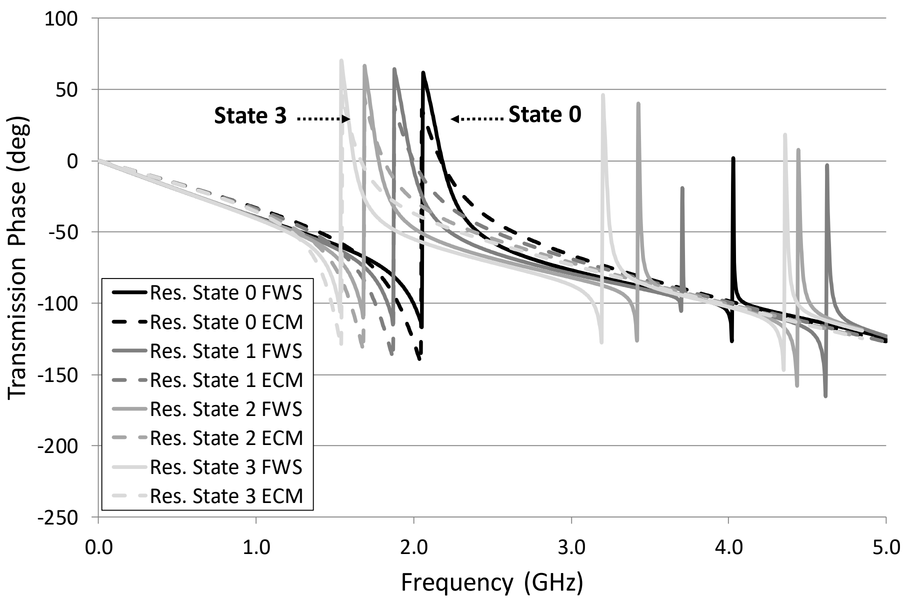

Fig. 3.34 A comparison between full-wave (solid) and equivalent circuit (dashed) response for transmission phase [SRS states: complete SRS shown in black and lighter colour for each subsequent state].

Table 3.4 MAE of the equivalent model compared to full-wave results for main resonance mode of uniform cross SRS inside 10 mm layer of glass at four resonance states and different incidence angles

Angle of incidence	Resonance state	Average MAE %	
		TE	TM
0°	State 0	0.79	0.79
	State 1	0.88	0.88
	State 2	1.57	1.57
	State 3	2.26	2.26
30°	State 0	0.63	0.60
	State 1	0.73	0.55
	State 2	0.92	0.65
	State 3	1.36	1.01
45°	State 0	0.35	0.75
	State 1	0.25	0.34
	State 2	0.18	0.37
	State 3	0.56	0.70
60°	State 0	0.63	0.85
	State 1	0.82	0.68
	State 2	0.62	0.67
	State 3	0.29	0.80

3.3.4 Experimental verification

To validate the accuracy of the presented transmission line model the response of the uniform cross SRS presented earlier has been measured inside a waveguide. A single element uniform cross SRS has been fabricated on 0.8 mm FR4 substrate. Additionally, two 3.6 mm thick PTFE slabs have been added representing the multi-layer dielectric media surrounding the SRS. The scattering parameters of an SRS inside a multi-layer dielectric media have been measured with a rectangular S-band waveguide (WG10) connected to a two port Agilent 8720D vector network analyser in a similar way to the measurement setup explained in section 3.1.2. The measurement setup is shown in Fig. 3.35a. The uniform cross unit cell presented in section 3.1.2 has dimensions of 50x50 mm^2. In order to replicate the response of a periodic structure inside a waveguide, the periodic structure must have a unit cell width equivalent to half the width of the waveguide broad dimension, ensuring that the required symmetry and boundary conditions are met. Therefore, the periodic structure should have a rectangular lattice with a broad dimension equal to 36.068 mm (which represents half the width of WG10) and a small dimension of 34.036 mm. This change in unit cell dimensions would alter the value of inductance and capacitance in the structure. Reducing inter-element spacing in the direction of electric field vector results in increased coupling between the elements and hence a higher capacitance value. It has also been noticed that this decrease in inter-element spacing leads to a reduction in the induced surface current and hence a decreased inductance value. The effect of periodicity change, and different dielectric slab loading, on uniform cross SRS are presented in Table 3.5.

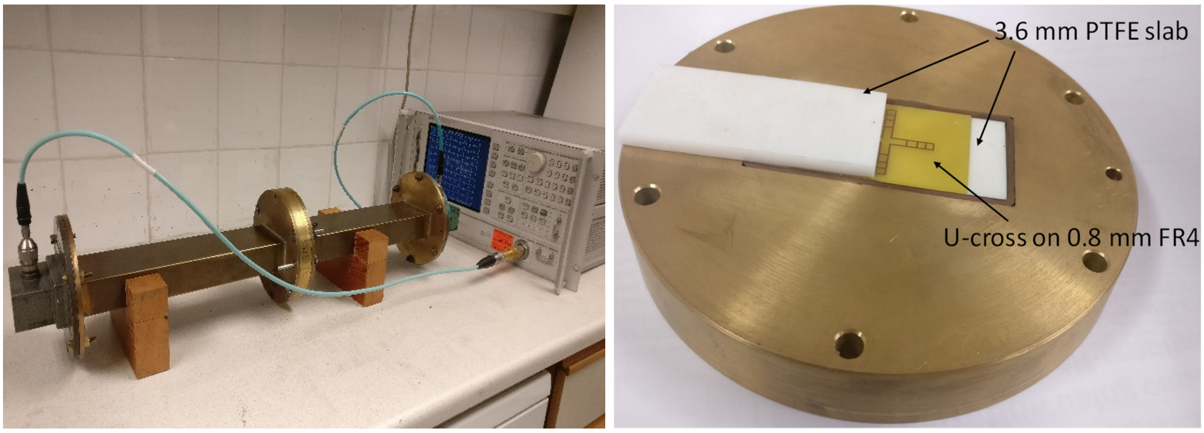

(a) (b)

Fig. 3.35 (a) Measurement setup: S-band waveguide and a two port vector network analyser (b) DUT: uniform cross SRS between two PTFE slabs inside a waveguide section.

Table 3.5 Equivalent circuit model values of uniform cross SRS with two different periodicities (P#1 is 50x50 mm^2 and P#2 is 36.068x34.036 mm^2) and with different dielectric slabs loading

U-cross array	L (nH)	C (fF)
Free standing P#1	79.2	18.1
Free standing P#2	32.2	44.8
P#2 on 0.8 FR4	32.2	68.7
+ 3.6 PTFE	32.2	84
+ 3.6 PTFE x2	32.2	96.3

It can be seen that changing the periodicity has led to higher capacitance value and decreased inductance. On the other hand, the effects of PTFE slabs on equivalent circuit values are demonstrated by higher capacitance values with no change in inductance.

The manufactured SRS response has been measured inside waveguide; without added slabs, with one 3.6 mm PTFE slab, and in between two 3.6 mm PTFE slabs. The samples under test are shown in Fig. 3.35b. The SRS impedance in each case has been calculated using the procedure explained in section 3.3.1. Subsequently, equivalent circuit values have been extracted. Once the equivalent circuit values have been calculated, the transmission matrix has been used to calculate the forward transmission magnitude and phase of uniform cross SRS inside PTFE slabs as follows:

$$\begin{bmatrix} A & B \\ C & D \end{bmatrix} = [WG] * [PTFE1] * [FR4] * [SRS] * [PTFE2] \tag{3.43}$$

where SRS transmission matrix can be represented using (3.35). On the other hand, propagation inside waveguide can be modelled using:

$$[\text{Waveguide}] = \begin{bmatrix} \cos(\beta_{wg} d_{wg}) & \text{j}\sin(\beta_{wg} d_{wg}) * Z_{wg} \\ \text{j}\sin(\beta_{wg} d_{wg}) * 1/Z_{wg} & \cos(\beta_{wg} d_{wg}) \end{bmatrix} \tag{3.44}$$

where Z_{wg} is the transverse wave impedance of waveguide and is given by [125]:

$$Z_{wg} = \frac{377}{\sqrt{1 - (\frac{\lambda_0}{\lambda_{oc}})^2}} \tag{3.45}$$

λ_0 is the wavelength in free space while λ_{oc} is the cutoff wavelength of the waveguide and can be calculated using [125]:

$$\lambda_{oc} = \frac{2}{\sqrt{(\frac{m}{a})^2 + (\frac{n}{b})^2}} \tag{3.46}$$

Where m and n represent the mode number, and for the rectangular waveguide in this experiment the dominant mode is TE_{10}, hence m = 1 and n = 0. While a and b are the broad and narrow dimensions of waveguide and in WG10 they are 72.136 mm and 34.036 mm, respectively. β_{wg} represents the phase constant of the waveguide and is given by [125]:

$$\beta_{wg} = \sqrt{\omega^2 \varepsilon_0 \mu_0 - \left(\frac{m\pi}{a}\right)^2 - \left(\frac{n\pi}{b}\right)^2} \quad (3.47)$$

d_{wg} is the distance the wave travels inside waveguide, and since it has been calibrated using TRL standard then d_{wg} represents the length of the waveguide section that holds the samples under test shown in Fig. 3.35b. In order to accurately model the transmission phase this length should be calculated based on the thickness of waveguide section (which is 20 mm in this case) minus the thickness of the samples inside.

PTFE and FR4 impedances matrices can be calculated in a similar way to the waveguide matrix presented but by calculating the characteristic impedances and propagation constant using TE incidence equations presented earlier. Therefore, complex forward transmission of an SRS embedded inside dielectric media inside a waveguide can be expressed as:

$$\mathrm{S21} = \frac{2Z_{wg}}{\left(A * Z_{wg}\right) + B + \left(C * Z_{wg}^2\right) + \left(D * Z_{wg}\right)} \quad (3.48)$$

Comparison between equivalent model and measured results for forward transmission is shown in Fig. 3.36. Clearly, very good agreement has been obtained, and mean absolute error values between have been 2%, 3%, and 6% for uniform cross on 0.8 mm FR4, with one PTFE slab, and between two PTFE slabs, respectively.

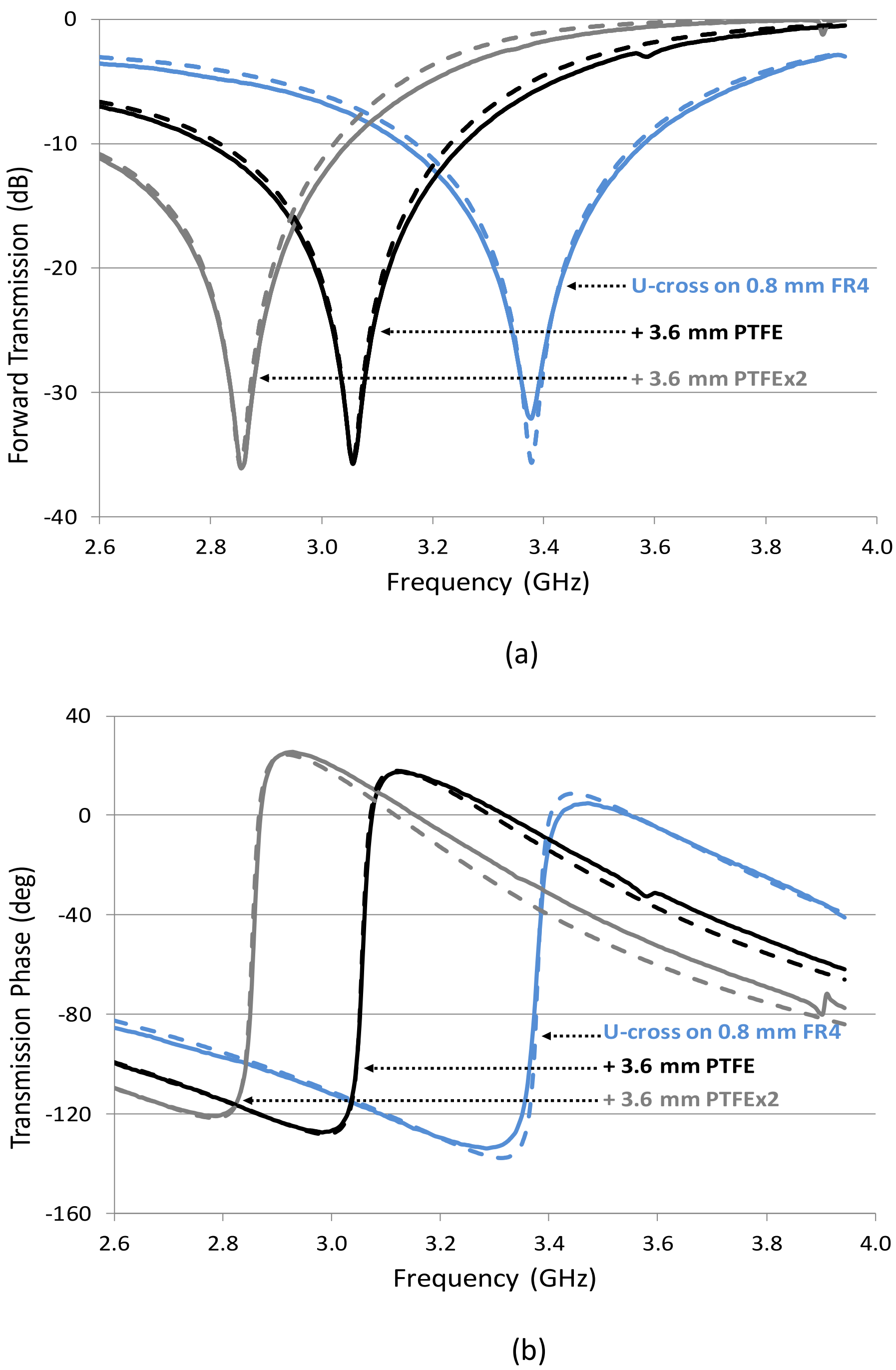

Fig. 3.36 A comparison between waveguide measured response (solid) and equivalent TLM (dashed) for forward transmission (a) magnitude in dB (b) phase, for uniform cross SRS on 0.8 FR4 substrate, with one 3.6 PTFE slab, and between two 3.6 PTFE slabs.

3.4 Summary

This chapter has presented the design of self-resonant tag and the modelling of its degradation pattern. The response of the manufactured tag at four different resonance states has been measured in a waveguide to prove the concept. In order to understand the impact of degradation on the electrical properties of the tag, an equivalent circuit model representation has been adopted. The uniform cross tag in free-standing situation has been used as a starting point in the equivalent circuit model analysis. Bothe single-mode EC and multi-mode EC models have been derived. The multi-mode approach have shown a better accuracy than single-mode approach but at the expense of higher complexity. Since the designed self-resonant tag is intended to operate inside a lossy media, the single-mode approach has been selected as higher order modes would subside because of the high level of dielectric attenuation. A transmission line model representation of a self-resonant structure with dielectric loading has been presented. Novel sets of expressions derived to calculate SRS impedance for normal incidence on dielectric materials (3.27), and within dielectric layers (3.30). Equations (3.31) and (3.32) describe SRS impedance within dielectric materials for TE and TM at oblique angles of incidence. Subsequently, it becomes trivial to extend these for any multi-layer applications. The model has been utilized to study the response of a uniform cross structure with multiple resonant states highlighting the effect of changing the physical and electrical dimensions on the equivalent circuit parameters. Hence, this analysis approach can be useful in analyzing active or degradable structures. The trends of equivalent circuit parameters when using dielectric layers with different properties and various thicknesses have been presented and analyzed. The effect of varying incidence angles and polarization has been discussed. Additionally, the accuracy of the model in comparison to full-wave simulation results have been assessed using mean absolute error criteria and it has been shown that model accuracy is proportional to both dielectric layer thickness and permittivity. Nevertheless, an average error of 2% has been obtained as illustrated in Tables 3.2 and 3.4. Experimental validation of model accuracy has been performed. A manufactured uniform cross SRS on thin FR4 substrate has been tested between two PTFE slabs with S-band waveguide and compared to equivalent model results with very good agreement.

A novel simplified expression for calculating the forward transmission coefficient has been presented in (3.40) and (3.41); this expression offers more insights into the factors contributing to the forward transmission response of an SRS on/in dielectric layers. Results calculated using this expression have been presented and good accuracy have been obtained. The proposed model can be extended to any single or multi-resonant structure and with any number of dielectric layers. Next chapter will consider SRS within highly lossy dielectric media representing the human body environment.

4. CHAPTER FOUR

Self-resonant tag inside human body model

In the last chapter, an equivalent transmission line model for self-resonant tag within lossless multi-layer dielectric media has been derived, the impact of dielectric constant, thickness, and angle of incidence on tag response and model accuracy have been investigated. In this chapter, tag response within lossy dielectric media representing human body model is studied using equivalent transmission line model.

4.1 Equivalent transmission line model for self-resonant tag within lossy dielectric media

4.1.1 Normal incidence

In the last chapter, the self-resonant tag in free-standing situation and within lossless dielectric media has been modelled as an LC resonance circuit. In the case where a self-resonant tag is placed on (or within) lossy dielectric media, a resistor needs to be added to the LC series circuit to account for the effect of lossy dielectric media in the vicinity of a metallic structure as has been suggested in [126]. Hence, derived self-resonant tag's impedance would have both real and imaginary parts. The former is responsible for the resistance value and the latter governs the reactance value in the circuit. The equivalent model of a self-resonant tag on lossy human body phantom is presented in Fig. 4.1. Similar to the procedure explained in the last chapter, the first step is to find the load impedance at the beginning of the transmission line segment which can be calculated as follows:

$$Z_{Load1\_l} = Z_{d1\_l} * \frac{Z_t + Z_{d1\_l}\tanh(\gamma_{d1}d_1)}{Z_{d1\_l} + Z_t\tanh(\gamma_{d1}d_1)} \tag{4.1}$$

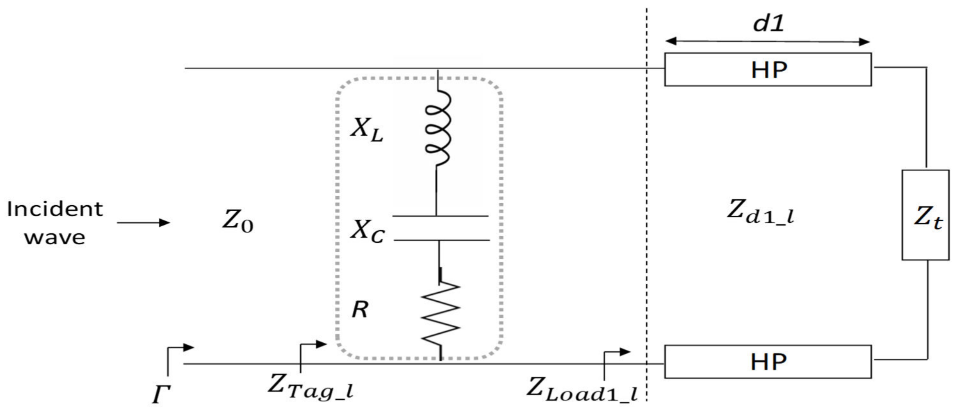

Fig. 4.1 Equivalent transmission line model of self-resonant tag on a single-layer (or homogeneous) human body phantom.

where Z_t is the load impedance at which the transmission line is terminated, in the case of a human body model, Z_t can be the characteristic impedance of a biological layer. However, because we are using full-wave simulation as the main benchmark for the equivalent model derivation and verification, the value of Z_t is considered as the value of the output port impedance and is equal to Z_0 (as we are only simulating discrete slabs of human body tissues and not a full human body phantom). The equivalent impedance between Z_{Load1_l} and the self-resonant tag impedance, Z_{Tag_l} will be given using:

$$Z_{eq1\_l} = \frac{Z_{Tag\_l} * Z_{Load1\_l}}{Z_{Tag\_l} + Z_{Load1\_l}} \tag{4.2}$$

Thus, reflection coefficient can be calculated using:

$$\Gamma = \frac{Z_{eq1\_l} - Z_0}{Z_{eq1\_l} + Z_0} \tag{4.3}$$

By substituting (4.2) in (4.3), the self-resonant tag impedance on a lossy homogeneous phantom can be expressed as:

$$Z_{Tag\_l\_op} = -\frac{Z_{Load1\_l}\, Z_0\, (\Gamma + 1)}{Z_{Load1\_l}\, (\Gamma - 1) + Z_0\, (\Gamma + 1)} \tag{4.4}$$

where Z_{d1_l} is the characteristic impedance of the homogeneous dielectric phantom and can be found using:

$$Z_{d1_l} = \sqrt{\frac{\mu}{\varepsilon}} * \frac{1}{\sqrt{1 - j(tan\delta)}} \tag{4.5}$$

$tan\delta$ is the loss tangent of the dielectric phantom over all frequency points. γ_{d1} is the propagation constant and can be given using $\gamma_{d1} = \alpha + j\beta$, where attenuation constant α in neper per meter can be calculated using:

$$\alpha^2 = \frac{\omega^2 * \mu * \varepsilon}{2} * (\sqrt{1 + (tan\delta)^2} - 1) \tag{4.6}$$

Or in db per meter using:

$$\alpha = 91.06 * \sqrt{\varepsilon_r} * F_{GHz} * tan\delta \tag{4.7}$$

This expression indicates clearly that dielectric constant, frequency, and loss tangent all directly proportional to the value of attenuation constant in lossy dielectric media.

Likewise, phase constant β in radian per meter is given by:

$$\beta^2 = \frac{\omega^2 * \mu * \varepsilon}{2} * (\sqrt{1 + (tan\delta)^2} + 1) \tag{4.8}$$

The inductance and capacitance of the tag can then be extracted based on error minimization criteria between the imaginary part of (4.4) and the impedance of series LC circuit in (3.4). On the other hand, the resistor of the self-resonant tag's equivalent circuit can be extracted from the real part of (4.4), it has been found that the value of the real part of (4.4) at resonance can be considered as the value of the frequency independent resistor of tag's equivalent circuit. It can be observed that hyperbolic functions are used instead of trigonometric functions to model lossy transmission line sections as propagation constant has both real and imaginary components in this case.

Similarly, when a self-resonant tag is embedded within a homogenous phantom, a second transmission line section is added on the left of the tag as illustrated in Fig. 4.2. In order to find the impedance expression for this case, load impedance at the beginning of the multi-segment transmission line structure, namely Z_{Load2_l}, can be calculated using:

$$Z_{Load2\_l} = Z_{d2\_l} * \frac{Z_{eq1\_l} + Z_{d2\_l}\tanh(\gamma_{d2}d_2)}{Z_{d2\_l} + Z_{eq1\_l}\tanh(\gamma_{d2}d_2)} \tag{4.9}$$

and reflection coefficient will be:

$$\Gamma = \frac{Z_{Load2\_l} - Z_0}{Z_{Load2\_l} + Z_0} \tag{4.10}$$

By substituting (4.2) in (4.9), and then (4.9) in (4.10), the tag's impedance expression within dielectric phantom can be derived as:

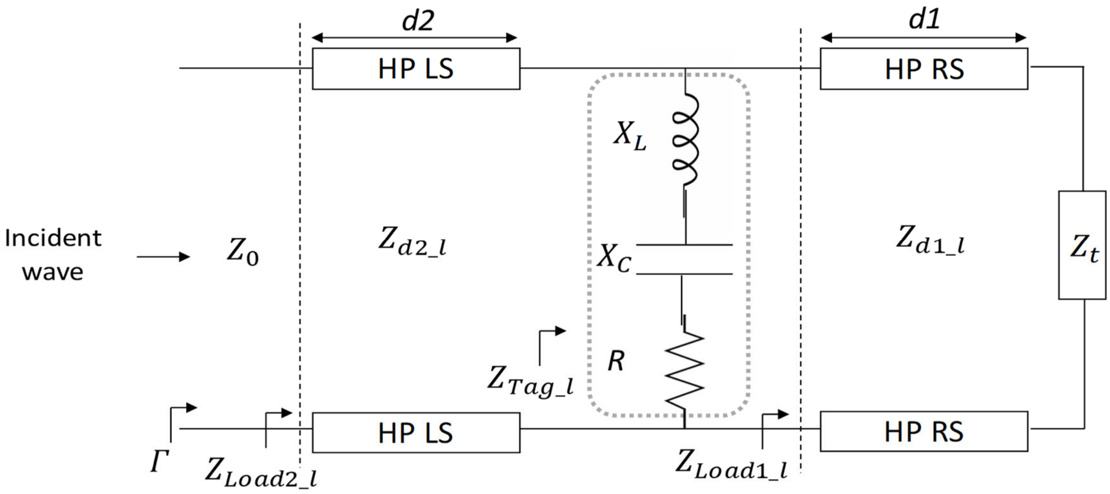

Fig. 4.2 Equivalent transmission line model of self-resonant tag within homogeneous human body phantom.

$$Z_{Tag\_l\_ip} = \frac{\begin{array}{c} Z_{d2\_l}^2 \tanh(\gamma_{d2} d_2)\, Z_{Load1\_l}\,(\Gamma - 1) \\ + Z_0 Z_{d2\_l}\, Z_{Load1\_l}(\Gamma + 1) \end{array}}{\begin{array}{c} -Z_{d2\_l}\, Z_{Load1\_l}(\Gamma - 1) - Z_{d2\_l}^2 \tanh(\gamma_{d2} d_2)(\Gamma - 1) \\ -Z_0 Z_{d2\_l}(\Gamma + 1) - \tanh(\gamma_{d2} d_2)\, Z_{Load1\_l}\, Z_0(\Gamma + 1) \end{array}} \tag{4.11}$$

In the same way, the suggested approach can be extended to model tag within multi-layer media, and theoretically it is possible to use this procedure for any number of layers. However, in practice, it becomes more difficult to find the impedance expression as the number of layers on the left of the tag (i.e., on the source side) increases, as the expression needs to have Z_{Tag} as a function of reflection coefficient Γ. On the other hand, the number of layers on the right of the tag (i.e., on the load side) does not impact the impedance expression, and it would only affect the calculation of load impedance. Derivation process and impedance expressions for two layers and three layers on each side of the tag are shown in appendix A.1.

4.1.2 Oblique incidence

The explanation presented in the last section has considered the normal incidence case. For implantable self-resonant tag, the incident signal of the external (off-body) reader may not impinge the tag at a normal angle. For the intended application of the tag explained in chapter one, the tag orientation may slightly change during wound suturing after the operation has finished. Therefore, it is important to study the response of the tag with oblique angles as well. Similar to the lossless case explained in chapter 3, oblique incidence mainly changes the characteristic impedance and the wavenumber calculation. The wavenumber of an obliquely propagating wave in a lossless dielectric media can be calculated using [105]:

$$k = \frac{\omega}{c}\sqrt{\varepsilon_r - (\sin\theta)^2} \tag{4.12}$$

where ε_r is the relative permittivity of the dielectric media and θ is the incidence angle. In lossy dielectric media, ε_r have both real and imaginary part, hence, it can be expressed as [117]:

$$\varepsilon_{r\_c} = \varepsilon_r{}' - j\varepsilon_r{}'' \tag{4.13}$$

Knowing that $tan\delta = \frac{\varepsilon_r{}''}{\varepsilon_r{}'}$, complex relative permittivity can be expressed as:

$$\varepsilon_{r\_c} = \varepsilon_r{}'(1 - jtan\delta) \tag{4.14}$$

Thus, complex wavenumber at any angle can be given using:

$$k_c = \frac{\omega}{c}\sqrt{\varepsilon_r{}'(1 - jtan\delta) - (\sin\theta)^2} \tag{4.15}$$

and propagation constant, γ_d, is related to the complex wavenumber through:

$$\gamma_d = jk_c = \alpha + j\beta \tag{4.15}$$

Consequently, characteristic impedance with TE and TM incidences can be calculated using (3.16) and (3.17), respectively but with complex relative permittivity. They can be rewritten as:

$$Z_{TE}^{(\varepsilon_r)}(\omega) = \frac{j\omega\mu_0}{\gamma_d} \tag{4.16}$$

$$Z_{TM}^{(\varepsilon_r)}(\omega) = -\frac{j\gamma_d}{\omega\varepsilon_0\varepsilon_{r\_c}} \tag{4.17}$$

4.2 Electrical representation of human body layers

In order to have a full electrical representation of human body model, a distributed lumped circuit model can be adopted, in a similar way to a transmission line. Wave propagation and electromagnetic fields within dielectric layers can be represented by a network-based model discretized in space instead of the continuous-in-space field theory. This spatial sampling allows the mapping of electromagnetic fields into cascaded sections of lumped components, as energy storage and dissipation in dielectric layers can be accounted for using parameters such as resistance, inductance, capacitance, and conductance. Fig. 4.3 shows a representation of multi-layer dielectric media using distributed lumped circuits. The distributed circuit parameters of a lossy transmission line can be calculated as follows [117]:

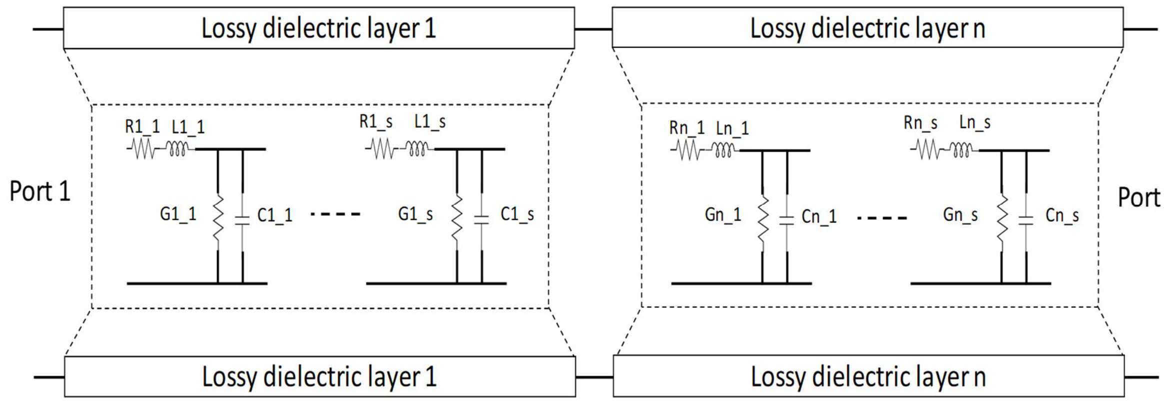

Fig. 4.3 Distributed circuit representation of lossy dielectric layers.

$$R_n = \alpha_n * Z_{dn} \quad (\Omega/\mathrm{m}) \tag{4.12}$$

$$L_n = \frac{Z_{dn} * \sqrt{\varepsilon_{rn}}}{c} \quad (\mathrm{H/m}) \tag{4.13}$$

$$C_n = \frac{\sqrt{\varepsilon_r}}{Z_{dn} * c} \quad (\mathrm{F/m}) \tag{4.14}$$

$$G_n = \frac{\alpha_n^2}{R_n} \quad (\mathrm{S/m}) \tag{4.15}$$

It can be noticed that the four distributed circuit parameters depend on the values of attenuation constant, characteristic impedance, and dielectric constant of the dielectric layer. Since all these parameters are frequency dependent for a human body layer, it is only possible to use a distributed circuit representation if just one frequency point is selected. Dielectric parameters for a fat layer at 3 GHz are as follows: $Z_d = 164.89\ \Omega$, $\alpha_d = 10.705\ np/m$, and $\varepsilon_r = 5.22$. And by using (4.12)-(4.15), the distributed circuit parameters for an 8 *mm* thick layer are presented as in Table 4.1. It can be seen that the value of each parameter is halved each time the number of blocks is doubled. The spatial sampling rate, or the number of cascaded blocks needed to accurately model a dielectric layer, depends on the length of the dielectric layer and the highest frequency of interest. A 'rule of thumb' has been suggested in [106] to determine the minimum distance required between cascaded blocks, it is given by in following equation:

$$\Delta x \leq \frac{\lambda}{10} \tag{4.16}$$

The equation suggests that the distance between cascaded blocks needs to be at least one tenth of the highest wavelength of interest. Comparisons between numerical full-wave simulation and distributed lumped components with different numbers of cascaded blocks of an 8 mm and 16 mm fat layer are shown in Fig. 4.4 and Fig. 4.5, respectively, for reflection coefficient. It can be noticed that the matching between full-wave simulation and distributed lumped circuit improves as the number of cascaded blocks increases. Theoretically, when the number of blocks approaches infinity, distributed circuit model will completely resemble the continuous-in-space electromagnetic field response for the chosen frequency point.

Table 4.1 Distributed circuit parameters of 8 mm fat layer

Parameters	per meter	per 8 mm 1 block	per 8 mm 2 blocks	per 8 mm 4 blocks	per 8 mm 8 blocks
R_n	1765 *ohm/m*	14.12 *ohm*	7.06 *ohm*	3.53 *ohm*	1.765 *ohm*
L_n	1256 *nH/m*	10.04 *nH*	5.02 *nH*	2.51 *nH*	1.255 *nH*
C_n	46.21 *pF/m*	0.369 *pF*	0.184 *pF*	0.092 *pF*	0.046 *pF*
G_n	0.0649 *S/m*	519.2 μS	259.6 μS	129.8 μS	64.9 μS

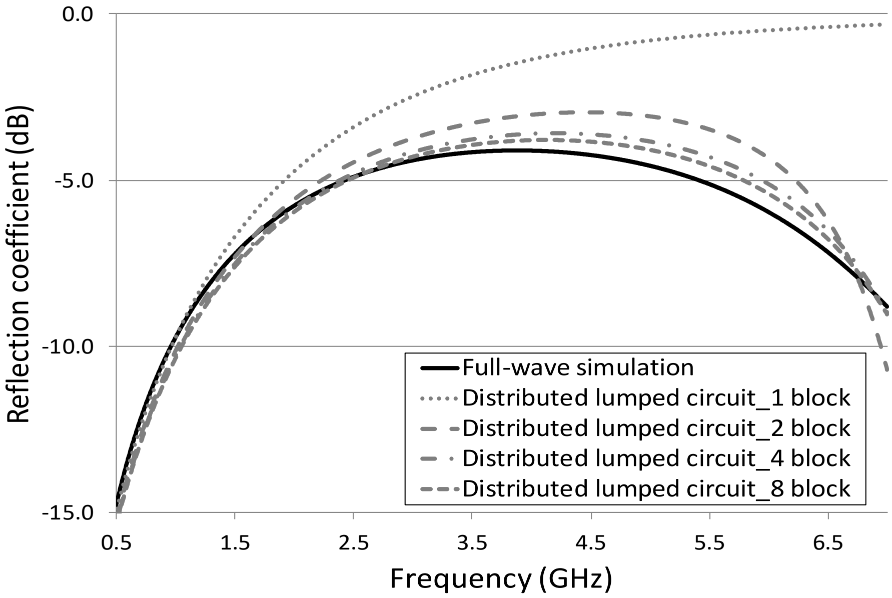

Fig. 4.4 Comparison between full-wave simulation and distributed lumped circuit of an 8 *mm* fat layer.

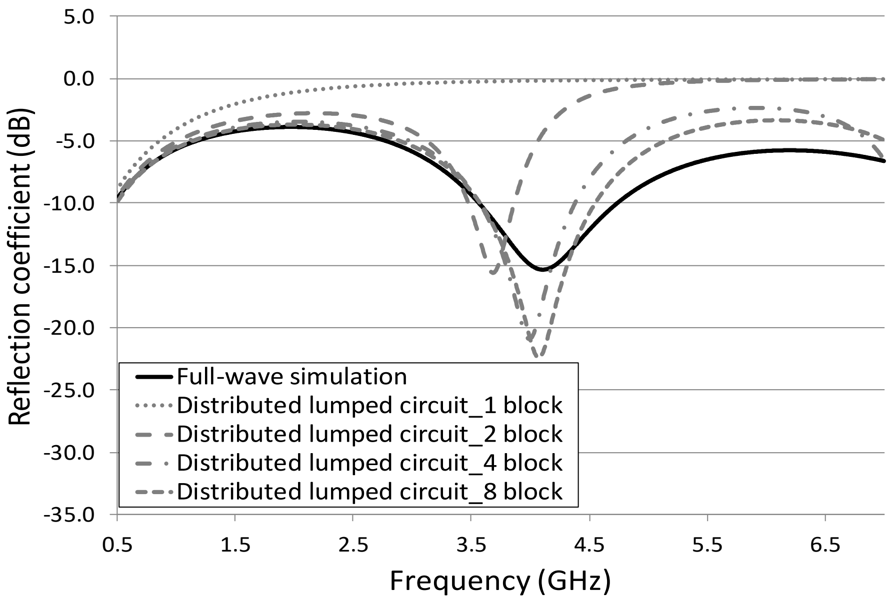

Fig. 4.5 Comparison between full-wave simulation and distributed lumped circuit of a 16 *mm* fat layer.

4.3 Analysis of implantable tag response using equivalent transmission line model

4.3.1 Tag implanted within two-layer human body model

We start the analysis of implantable tag response with an example of uniform cross tag embedded in the middle of an 8 mm fat layer. Although it may not be realistic to just consider a fat layer and ignore other layers such as skin and muscle, for analysis purposes it is important to understand the impact of dielectric attenuation of implantation medium on the self-resonant tag response. It is known that fat layer is a low loss layer due to its low water content. Besides that, fat layer has a relatively low dielectric constant, which means low dielectric attenuation as equation (4.7) suggests. Other biological layers with higher dielectric attenuation will be added to the model later on in the chapter as we progress in this analysis.

A schematic diagram of tag inside fat layer and its equivalent transmission line representation is illustrated in Fig. 4.6. The tag impedance has been calculated using the procedure explained earlier. The real and imaginary parts of the calculated Z_{Tag} is shown in Fig. 4.7. The value of the equivalent circuit resistor is the value of the real part of Z_{Tag} at resonance (which occurs at 2.11 GHz when the imaginary part of Z_{Tag} crosses the zero line as inductive and capacitive parts cancel each other), in this case the value of R is 96 Ω. On the other hand, L and *C* values are found using an error minimization technique between the encircled part of $Z_{Tag\_Imaginary}$ and the impedance of an LC series circuit in (3.4). It is worth mentioning that the extracted values of L and C using the aforementioned procedure should be checked for physical reasonableness rather than just considering the numerical matching. The extracted values of L and C are 75.6 nH and 75.25 fF, respectively. Comparisons between full-wave simulation and equivalent model responses calculated using the ABCD matrix method (explained in section 3.4.2) of uniform cross tag within a fat layer are shown in Fig. 4.8 and Fig. 4.9 for S_{11} and S_{21}, respectively. It can be seen that equivalent model results are in excellent agreement with full-wave simulation.

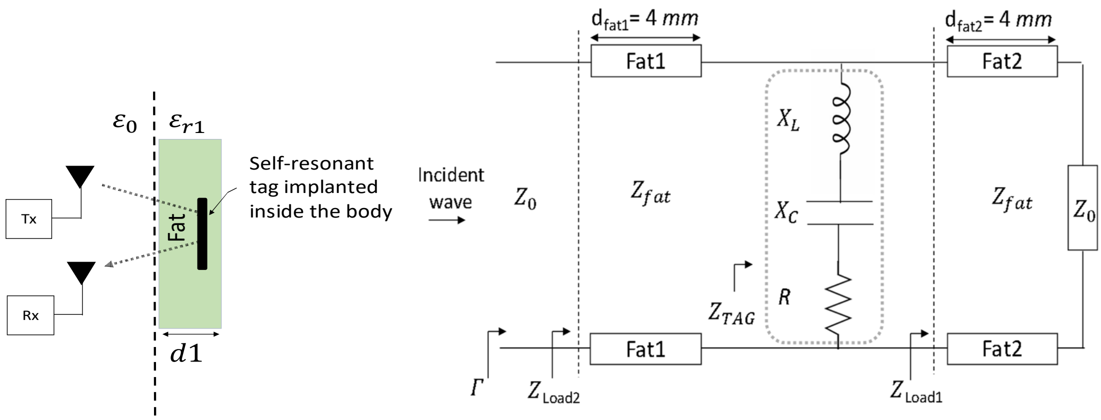

(a) (b)

Fig. 4.6 (a) A uniform cross tag inside 2-layer human body model (b) its equivalent transmission line model.

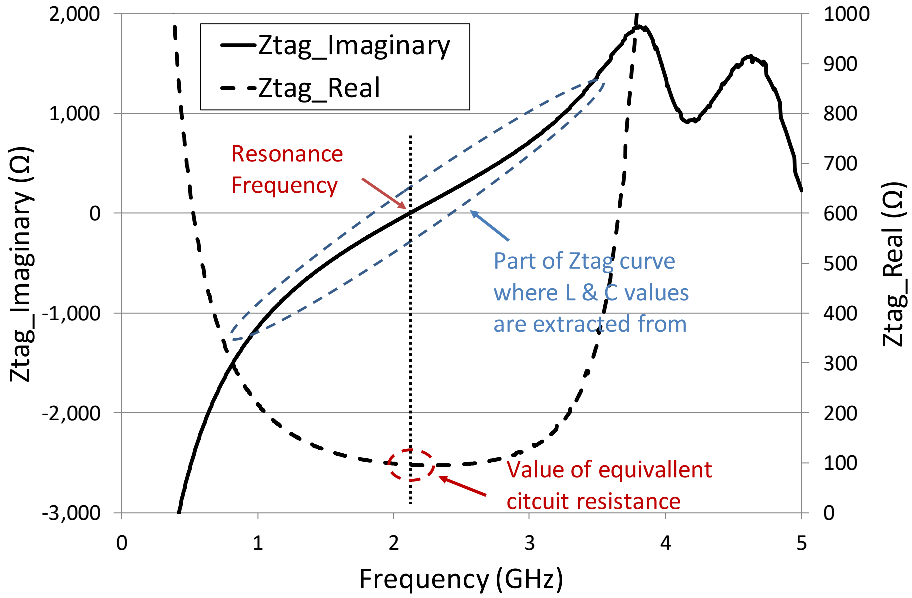

Fig. 4.7 Real and imaginary parts of calculated Z_{Tag} versus frequency for the tag within an 8 mm fat layer.

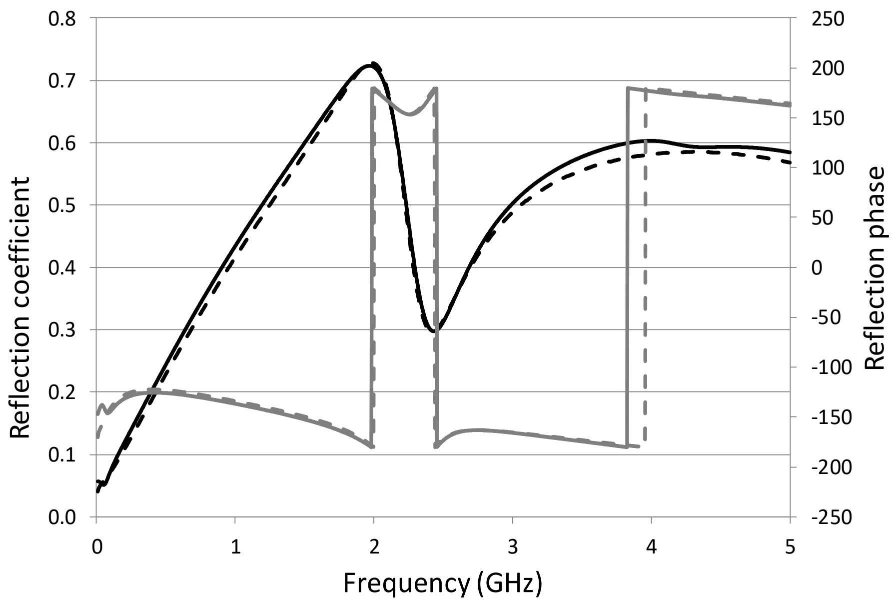

Fig. 4.8 Comparison between full-wave simulation (solid) and equivalent model response using ABCD matrix (dashed) of uniform cross tag within an 8 mm fat layer: black for S_{11} magnitude and grey for S_{11} phase.

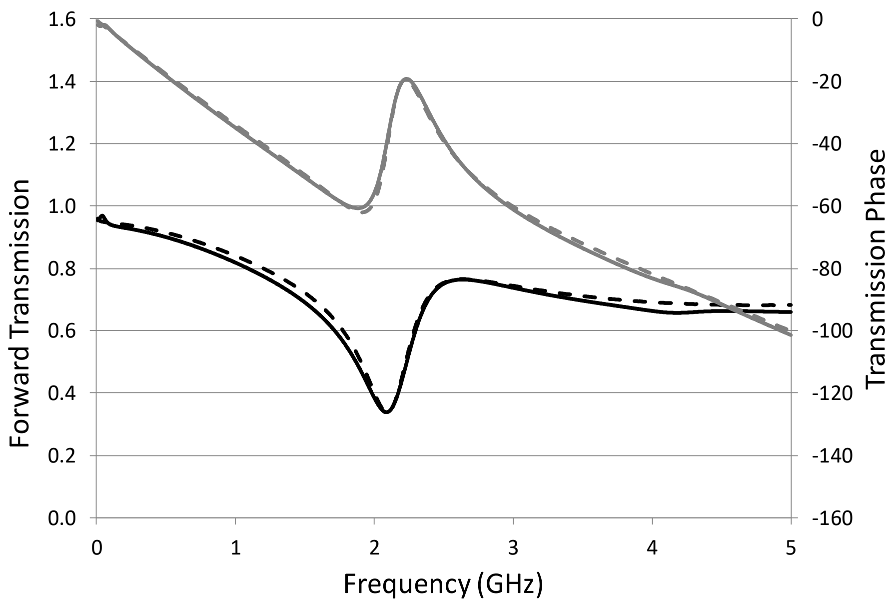

Fig. 4.9 Comparison between full-wave simulation (solid) and equivalent model response using ABCD matrix (dashed) of uniform cross tag within an 8 mm fat layer: black for S_{21} magnitude and grey for S_{21} phase.

As explained in section 4.2, it is possible to model human body layers by distributed lumped components. Fig. 4.10 shows a full electrical representation of equivalent model shown in Fig. 4.6b. Each of the two 4 mm fat layer is represented by 4 distributed components blocks, the distributed circuit parameters have been calculated at 3 GHz and their respective values are shown in the same figure. The S_{11} response of this equivalent model have been compared to full-wave simulation as depicted in Fig. 4.11. Although distributed lumped circuit parameters have been calculated at a single frequency point, it can be seen that this method has given good accuracy for both magnitude and phase. Nevertheless, if higher accuracy needed then ABCD matrix method needs to be adopted as has been demonstrated before in Fig. 4.8.

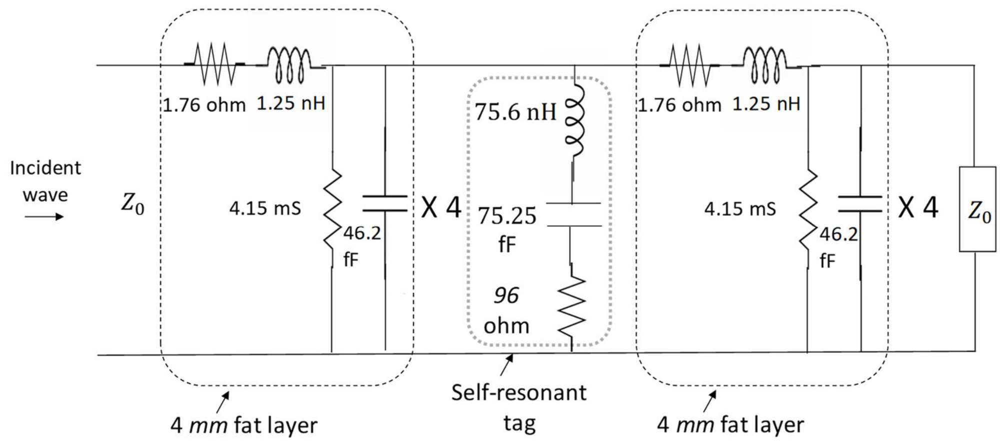

Fig. 4.10 Diagram of equivalent transmission line model of uniform cross tag in an 8 mm fat layer using distributed lumped circuits method.

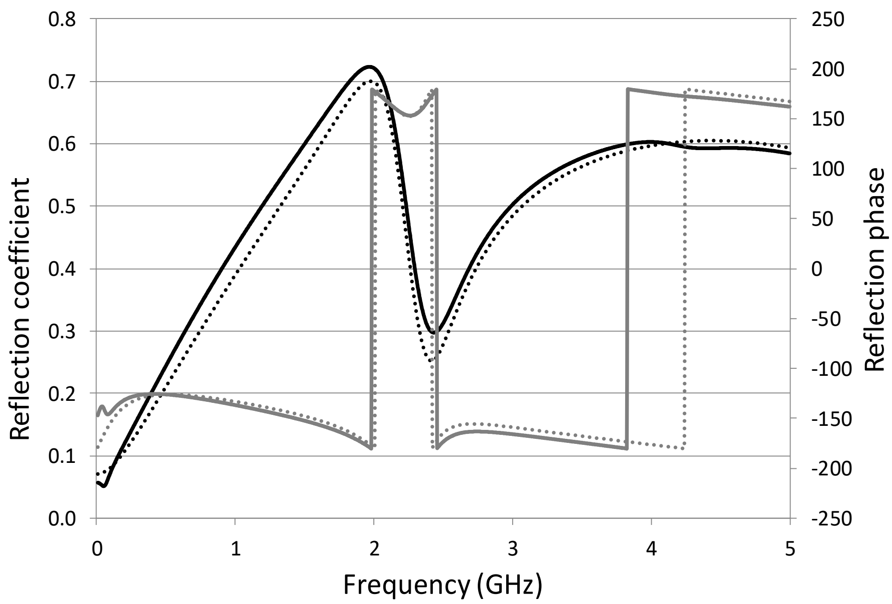

Fig. 4.11 Comparison between full-wave simulation (solid) and equivalent model response using distributed lumped components representation (dotted) for the reflection coefficient of uniform cross tag within a two-layer human body model: black for reflection coefficient and grey for reflection phase.

4.3.1.1 Degradation stages of tag within a fat layer

As mentioned before, the ultimate objective of this project is to develop a tag that degrades within the human body. Thus, it is important at this stage to study the response of the implantable tag at different degradation stages and examine the impact of implantation medium on the relationship between tag response at each stage. The forward transmission of the uniform cross tag inside an 8 mm fat layer at the four degradation stages is shown in Fig. 4.12. It can be noticed that the distance between the resonances at each stage have been shortened in comparison to the tag's degradation stages in free space as shown in Fig. 3.12. Moreover, the amplitude of the S_{21} response have reduced due to the dielectric attenuation imposed by the fat layer. The extracted equivalent circuit parameters for all degradation stages is presented in Table 4.2. It can be observed that inductance values have increased with the progress of degradation while capacitance values have only shown a slight variation. These findings are in agreement with the results presented in the last chapter for tag in free space and within lossless dielectric media. On the other hand, resistance values have progressively increased with degradation causing an amplitude reduction as can be seen in Fig. 4.12.

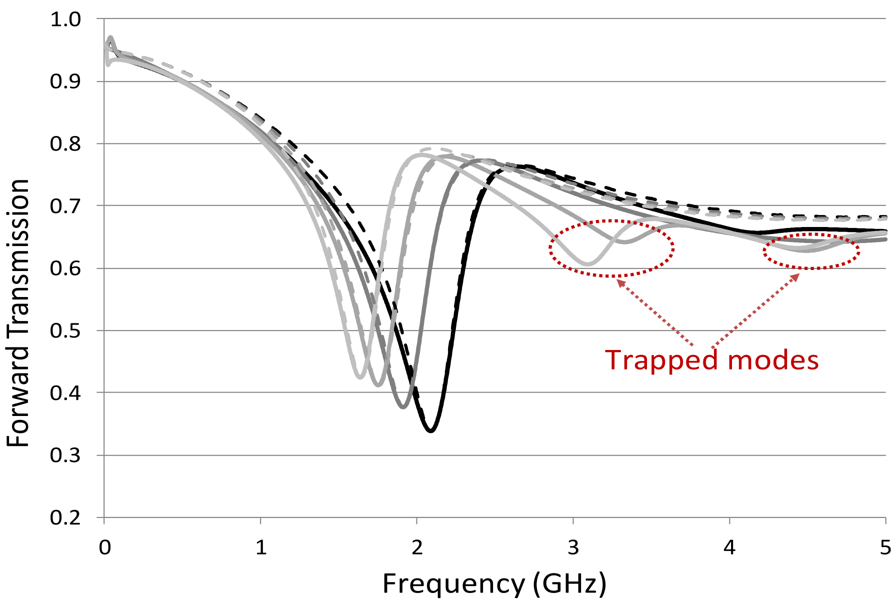

Fig. 4.12 Comparison between full-wave simulation (solid) and equivalent model response using ABCD matrix (dashed) of uniform cross tag within an 8 mm fat layer, intact tag is shown in black and lighter colour for each subsequent degradation stages.

Table 4.2 Comparison between equivalent circuit parameters of uniform cross SRS at different degradation stages inside 8 mm fat layer

Resonance state	L (nH)	C(fF)	R (Ω)
State 0	75.6	75.3	96
State 1	90.4	74.83	117
State 2	109.8	73.2	140
State 3	130.5	70.4	149.4

4.3.1.2 Emergence of trapped modes

It has been shown in the last chapter in section 3.3.2.2 that after the onset of grating lobes a number of higher order modes emerges in succession as the frequency increases. These modes are evanescent before their cut-off frequency and propagative afterwards, the onset of grating lobes represents the cut-off frequency of the first higher order mode. The cut-off frequency of these higher order modes is pushed down to a lower frequency when a dielectric layer exist in the vicinity of self-resonant tag. This phenomenon creates a frequency window for each mode, between free space cut-off frequency and dielectric cut-off frequency, in which the higher order mode will be propagative inside the dielectric media and evanescent in free space. Hence, the mode in this window is known to be 'trapped' and thus the name 'trapped modes'. From Fig. 4.12 it can be noticed that the S_{21} response of state 2 and 3 have small extra resonances after 3 GHz and 4 GHz (shown encircled by dotted red lines), these are examples of trapped modes.

In chapter three these modes have been modelled using frequency dependent impedances Z_L and Z_C for TE and TM modes, respectively. This method can still be used to model the higher order modes inside dielectric media. However, a simpler approach is to treat a dielectric-loaded SRS with trapped modes as a multi-resonant SRS. By looking at the impedance graph in Fig. 4.13 for a fully degraded tag, it can be seen that there are three resonances at 1.66 GHz, 3.11 GHz, and 4.41 GHz. Equivalent circuit parameters for trapped modes can be found in a similar way to the main resonance mode. Resistor value of each mode is the value of the real part of the derived impedance at the corresponding resonance frequency. On the other hand, inductance and capacitance values can be extracted from the impedance expression of a multi-resonant parallel LC circuit. Fig. 4.14 shows the equivalent circuit model of fully degraded uniform cross tag inside 8 mm fat layer with two trapped modes. Since the values of L_1 and C_1 are known, the values of L_2 and C_2 can be found from the impedance expression of a double resonance circuit as follows [105]:

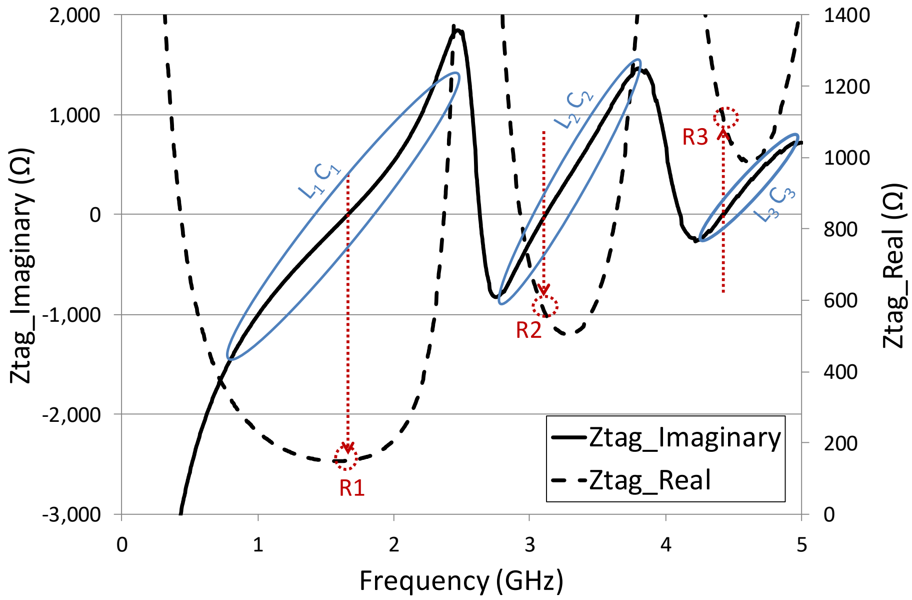

Fig. 4.13 Real and imaginary part of calculated Z_{Tag} versus frequency for fully degraded of tag within an 8 mm fat layer.

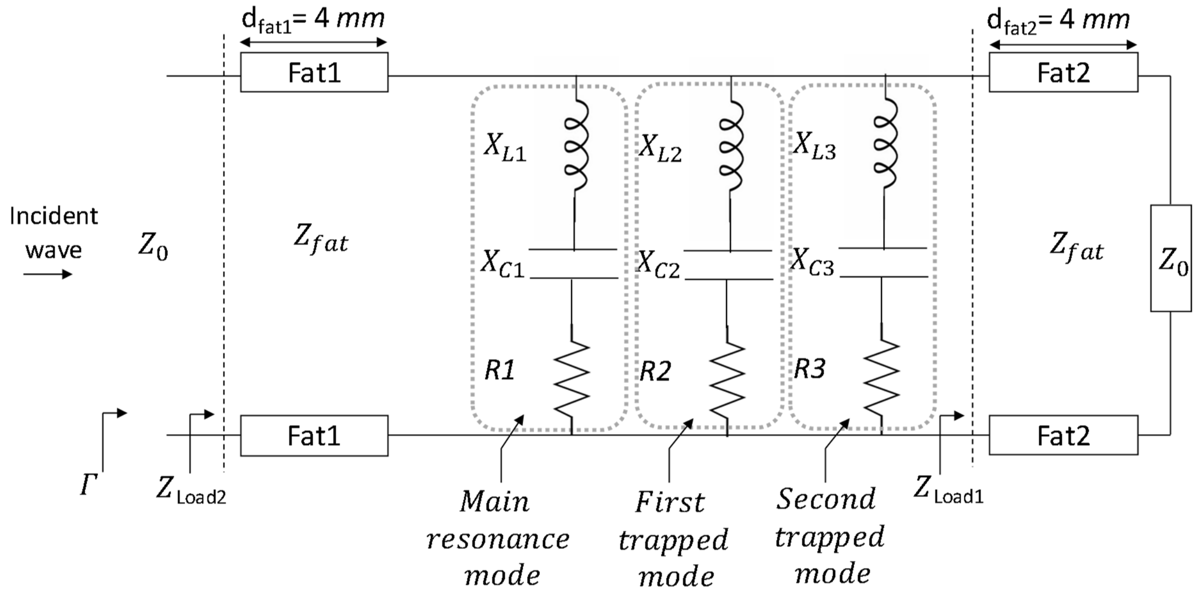

Fig. 4.14 Equivalent circuit model of self-resonant tag inside 8 mm fat layer with two trapped modes.

$$Z_{drs} = (X_{L1} + X_{C1}) \mathbin{/\!/} (X_{L2} + X_{C2}) \tag{4.17}$$

After simplification Z_{drs} will be:

$$Z_{drs} = \frac{(1-\omega^2 L_1 C_1)(1-\omega^2 L_2 C_2)}{j\omega\,[C_2 + C_1 - \omega^2 C_1 C_2 (L_1 + L_2)]} \tag{4.18}$$

The zeros can be found by equating the numerator to zero:

$$(1-\omega_{z1}{}^2 L_1 C_1)(1-\omega_{z2}{}^2 L_2 C_2) = 0 \tag{4.19}$$

Thus, inductance and capacitance of each resonance are related using:

$$C_1 = \frac{1}{\omega_{z1}{}^2 L_1} \; and \; C_2 = \frac{1}{\omega_{z2}{}^2 L_2} \tag{4.20}$$

On the other hand, the poles can be found by equating the denominator to zero as follows:

$$j\omega_{p1}\,[C_2 + C_1\; - \omega_{p2}{}^2 C_1 C_2 (L_1 + L_2)] = 0 \tag{4.21}$$

It is clear that the first pole occurs at 0 GHz and this is obvious in Fig. 4.13 as the imaginary part of the impedance diverges to a very low value at that frequency. The inductance expression of the first trapped mode L_2 can be found using:

$$[C_2 + C_1\; - \omega_{p2}{}^2 C_1 C_2 (L_1 + L_2)] = 0 \tag{4.22}$$

By substituting C_2 from (4.20) in (4.22) the equation will be:

$$[\frac{1}{\omega_{z2}{}^2 L_2} + C_1\; - \omega_{p2}{}^2 C_1 \frac{1}{\omega_{z2}{}^2 L_2}(L_1 + L_2)] = 0 \tag{4.23}$$

Hence, L_2 can be expressed as:

$$L_2 = \frac{\omega_{p2}{}^2 L_1 C_1 - 1}{C_1(\omega_{z2}{}^2 - \omega_{p2}{}^2)} \tag{4.24}$$

where L_1 and C_1 can be taken from Table 4.2, $f_{z2} =$ 3.11 GHz, and $f_{p2} =$ 2.47 GHz. Thus, $L_2 = 121.4\,nH$. C_2 can then be calculated from (4.20) and is equal to 21.5 fF and R_2 can be found from Fig. 4.14 and it is equal to 560 ohm. It is worth mentioning that the second and third poles in Fig. 4.13 do not cause the impedance to diverge to infinity (which is the mathematical definition of a pole or a singularity) because of the effect of dielectric media. Similarly, equivalent circuit parameters of second trapped mode can be found by solving a parallel circuit between first and second trapped modes and following the same procedure explained earlier. Hence, the second trapped mode's equivalent circuit parameters are: $L_3 = 133\,nH,\; C_3 = 9.7\,fF,\; R_3 = 1122\,ohm.$ Comparisons between the full-wave simulation, equivalent model with just the main mode, and equivalent model with two trapped modes for S_{11} and S_{21} are shown in Fig. 4.15 and Fig. 4.16, respectively. Clearly, the accuracy of the equivalent model in the frequency window after the main resonance zone has improved after including the two trapped modes.

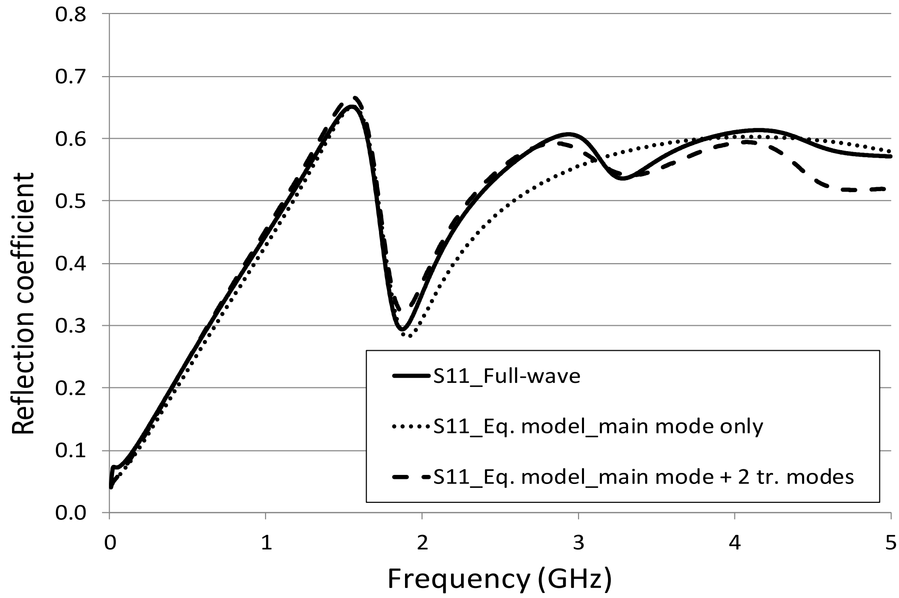

Fig. 4.15 Comparison between full-wave simulation and equivalent model with trapped modes for S_{11} of fully degraded of tag within an 8 mm fat layer.

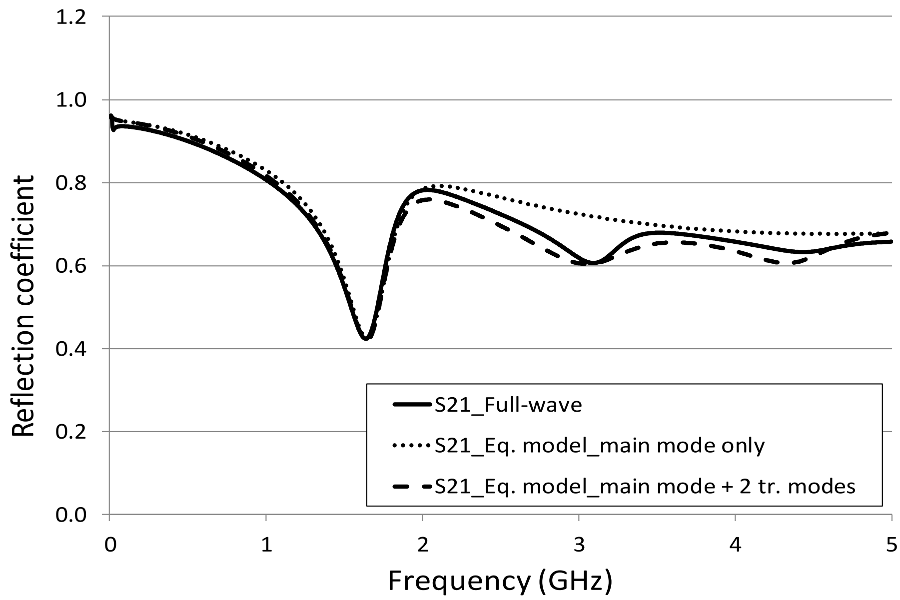

Fig. 4.16 Comparison between full-wave simulation and equivalent model with trapped modes for S_{21} of fully degraded of tag within an 8 mm fat layer.

4.3.1.3 Impact of incidence angle on response of tag within a fat layer

Once the tag is implanted inside the body there is no guarantee that it will maintain the same position inside the body because of the dynamic nature of living tissues. Hence, incident signal from the external reader may not strike the tag at a normal angle. Therefore, it is important to study the response of the tag with oblique incidence. For an implantable tag, it is unlikely to have an incidence angle wider than 45 degree when interrogating the tag from an off-body receiver. Fig. 4.17 and Fig. 4.18 show how the response of implantable tag changes with angle of incidence for TE and TM incidences, respectively. It can be noticed that with TE incidence, the progressive increase in angle has slightly pushed the response down in frequency (and led to the emergence of one trapped mode in the fully degraded tag state). On the other hand, the response has been pushed upward as angle of incidence increases with TM polarization. Table 4.2 presents the equivalent circuit parameters with different incidence angles. For TE incidence, inductance values have shown a small increase with incidence angle, while capacitance values have slightly decreased. These findings are in agreement with the results presented in the last chapter in Fig. 3.25 and Fig. 3.26 for tag on lossless dielectric layer. On the other hand, with TM incidence capacitance values have remained unchanged while inductance values have slightly changed but without a clear trend. It is worth noting that despite the change in the response with angle of incidence shown in Fig. 4.18, no significant change in the equivalent circuit values can be observed with TM incidence. These changes are primarily attributed to the change in the frequency response of fat layers with incidence angles rather than a change in the response of self-resonant tag. Conversely, resistance values have shown a similar trend for both TE and TM incidences with increasing values as angle of incidence increases. A comparison between full-wave simulation and equivalent circuit response for reflection coefficient at 45 degree is shown in Fig. 4.19. It can be noticed that the matching between both curves for the fundamental resonance mode is excellent for both TE and TM incidences.

Table 4.3 Comparison between equivalent circuit parameters of uniform cross SRS within 8 mm fat layer at various incidence angles for both TE and TM incidences

Angle	TE			TM		
	R	L	C	R	L	C
0	96	75.6	75.25	96	75.6	75.25
15	105.5	78.1	74.39	106.8	76.1	75.1
30	106.6	81.2	73.51	107.2	76.05	75.16
45	109	83.43	72.6	109	75.93	75.29

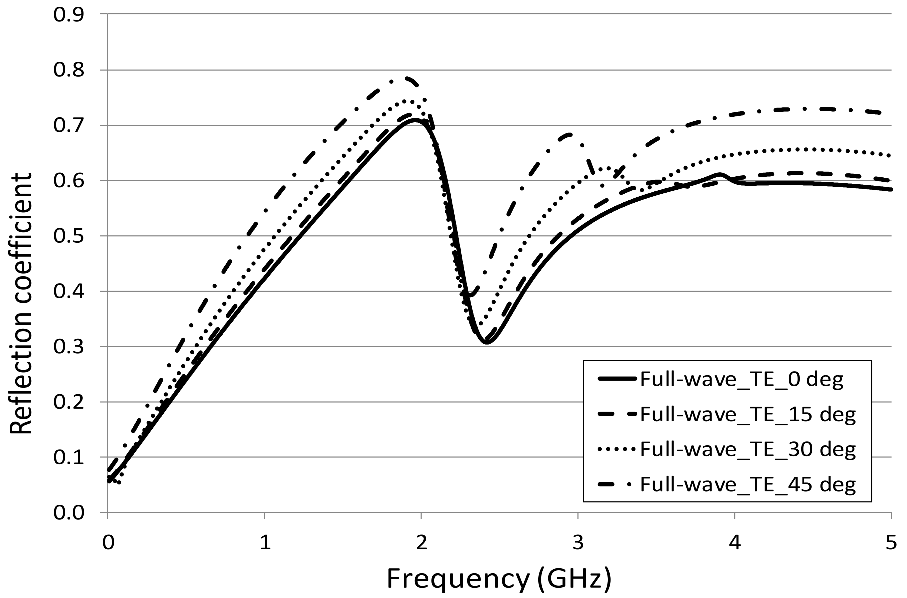

Fig. 4.17 S_{11} of implantable uniform cross tag within 8 mm fat at various angles of incidence TE incidence.

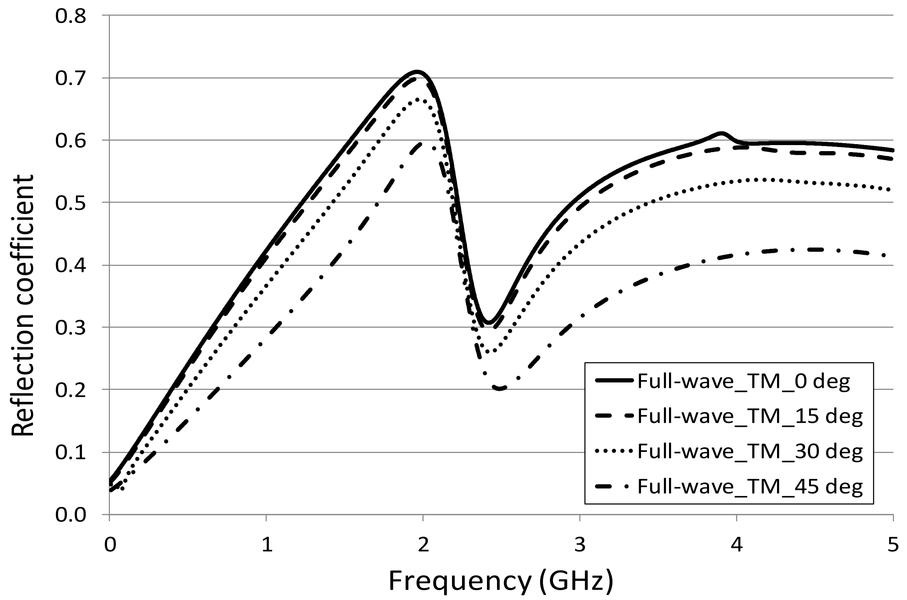

Fig. 4.18 S_{11} of implantable uniform cross tag within 8 mm fat at various angles of incidence TM incidence.

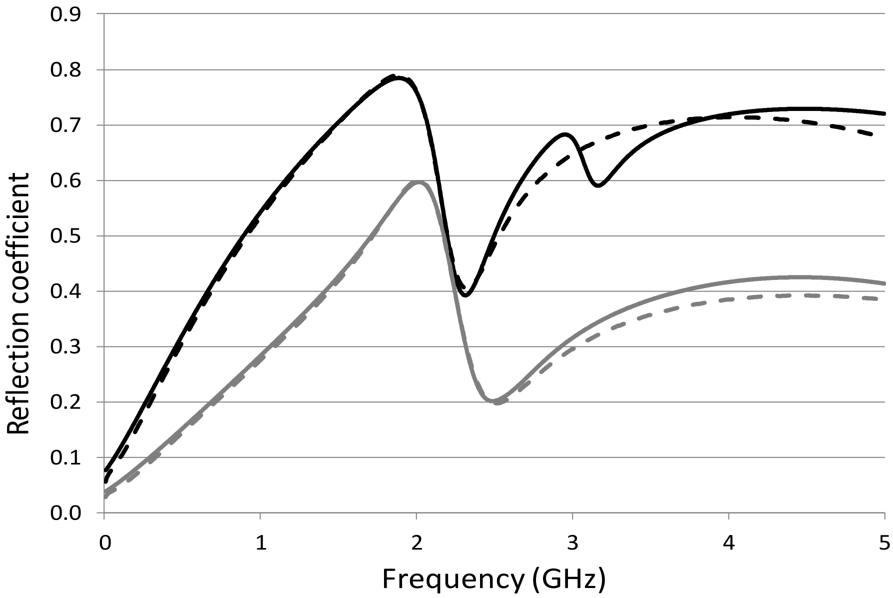

Fig. 4.19 Comparison between full-wave (solid) and equivalent circuit (dashed) response for reflection coefficient of implantable uniform cross tag within 8 mm fat at 45 degree of incidence, black represents TE Incidence and grey refers to TM incidence.

4.3.2 Tag implanted within three-layer human body model

In the last section, the uniform cross tag within a human body model comprised of an 8 *mm* fat layer has been studied. However, a more realistic human body model would involve more than just one biological layer. In this section, we will examine the impact of adding a skin layer to the human body model presented earlier. The equivalent transmission line model of a tag within a three-layer human body model is shown in Fig. 4.20 below. A 1 *mm* thick skin layer has been chosen while the tag is situated in the middle of an 8 *mm* thick fat layer. The tag impedance has been calculated using the procedure explained earlier. The real and imaginary parts of the calculated Z_{Tag} is shown in Fig. 4.21. From this graph, it can be seen that the resonance has been pushed down in frequency and the slope of the imaginary part has decreased in comparison to Fig. 4.7. In this case the resonance occurs at 1.98 GHz and the value of R is 135 Ω. Inductance and capacitance values have been extracted using the procedure explained in the last chapter and they are 79.2 nH and 86.48 fF, respectively. By comparing these values with the equivalent circuit parameters of the tag within fat layer only, it can be seen that inductance have a similar value while capacitance value have increased. This change in capacitance is caused by both the increase in thickness and permittivity of the implantation media as has been discussed in chapter three. On the other hand, resistor value have also increased due to the extra attenuation caused by the skin layer. The dielectric attenuation imposed by each biological layer can be calculated using (4.7). The attenuation constant of fat layer at 3 GHz is 92.9 dB/m, and for an 8 mm thick fat layer the attenuation is 0.74 dB. On the other hand, the attenuation constant of skin layer at 3 GHz is 466.73 dB/m, and for a 1 mm thick skin layer the attenuation is 0.46 dB. This shows how much attenuation skin adds despite its thinness.

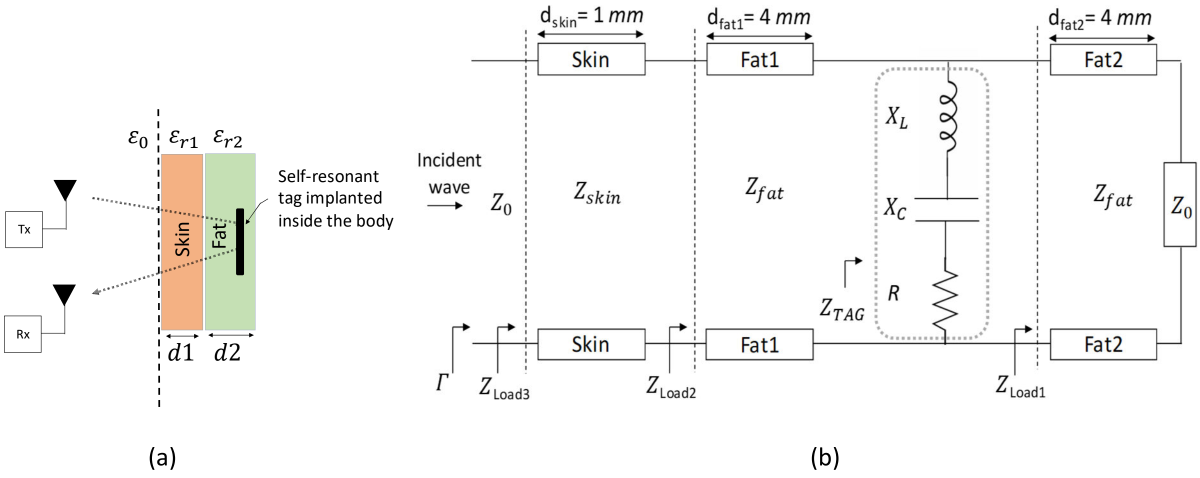

Fig. 4.20 A uniform cross tag inside three-layer human body model (b) Its equivalent transmission line model.

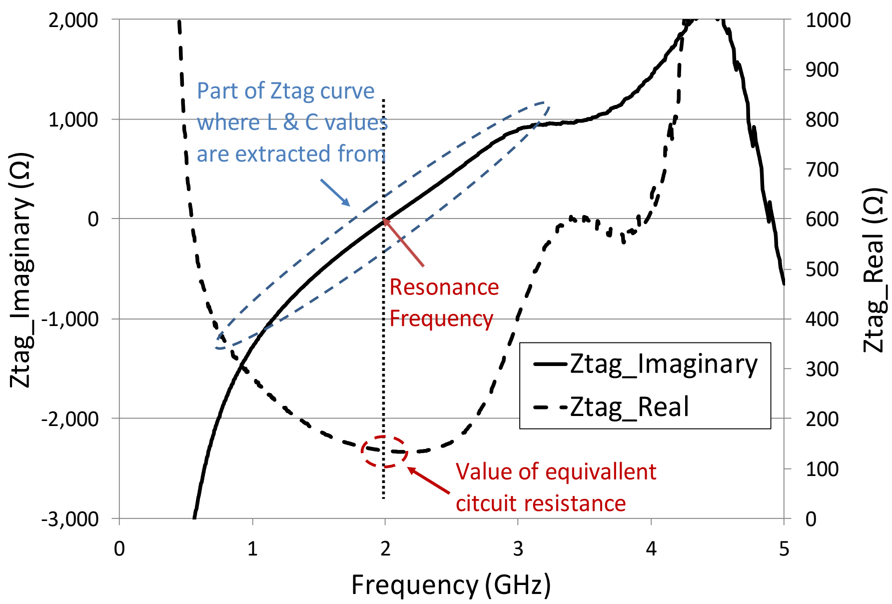

Fig. 4.21 Real and imaginary part of calculated Z_{Tag} versus frequency for a tag within three-layer human body model.

Comparisons between full-wave simulation and equivalent model responses, calculated using the ABCD matrix method, are shown in Fig. 4.22 and Fig. 4.23 for reflection coefficient and forward transmission coefficient, respectively. It can be seen that resonance amplitude has reduced in comparison to the example of a two-layer model presented earlier. This reduction is caused by the additional attenuation imposed by the skin layer and is demonstrated by a higher equivalent circuit resistance. Nonetheless, equivalent model and simulation results are in excellent agreement.

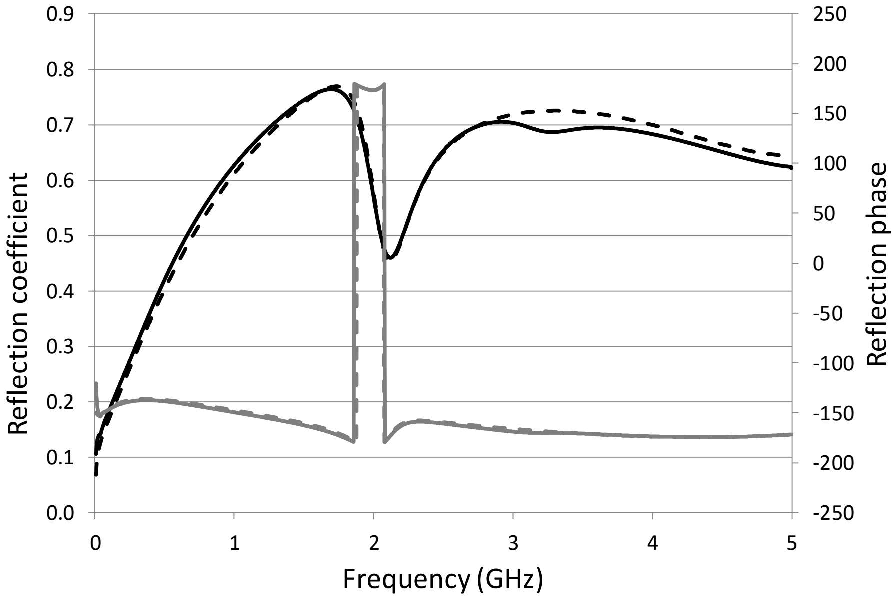

Fig. 4.22 Comparison between full-wave simulation (solid) and equivalent model response using ABCD matrix (dashed) for the reflection coefficient of uniform cross tag within a three-layer human body model, black represents magnitude and grey refers to phase.

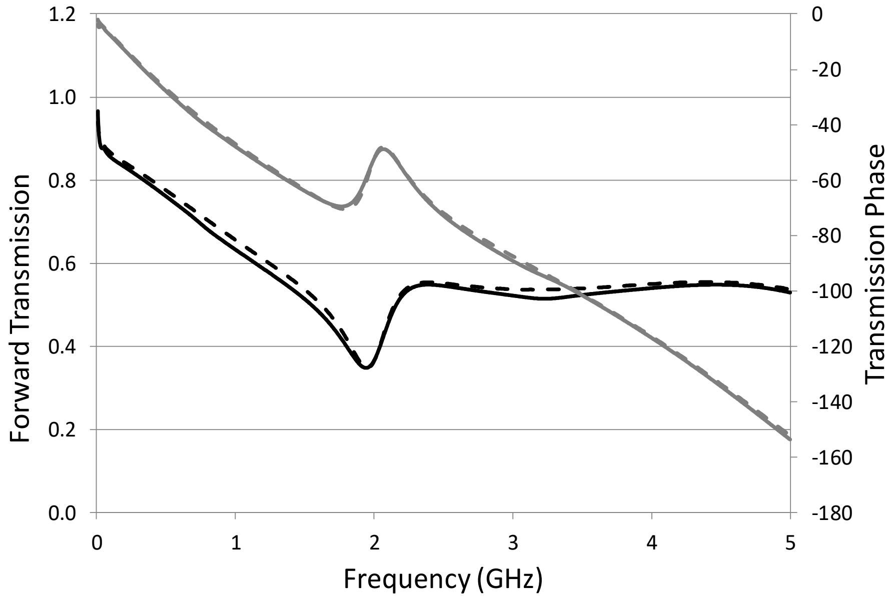

Fig. 4.23 Comparison between full-wave simulation (solid) and equivalent model response using ABCD matrix (dashed) for the forward transmission of uniform cross tag within a three-layer human body model, black represents magnitude and grey refers to phase.

Distributed lumped components representation of the tag in a three-layer model is depicted in Fig 4.24 below. The 1 mm skin layer is modelled by two distributed components blocks while the two 4 mm fat layer each represented by four blocks. The distributed circuit parameters have been calculated at 3 GHz. The reflection coefficient of the distributed lumped components have been compared to full-wave simulation as shown in Fig. 4.25. It is clear that this method has given good accuracy for both magnitude and phase.

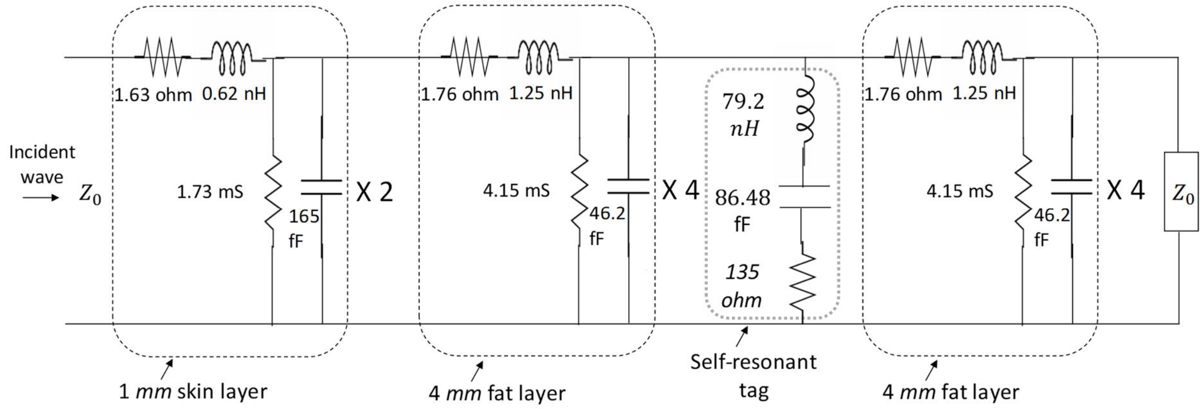

Fig. 4.24 Diagram of equivalent transmission line model of uniform cross tag in a three-layer human body model represented using distributed lumped circuits.

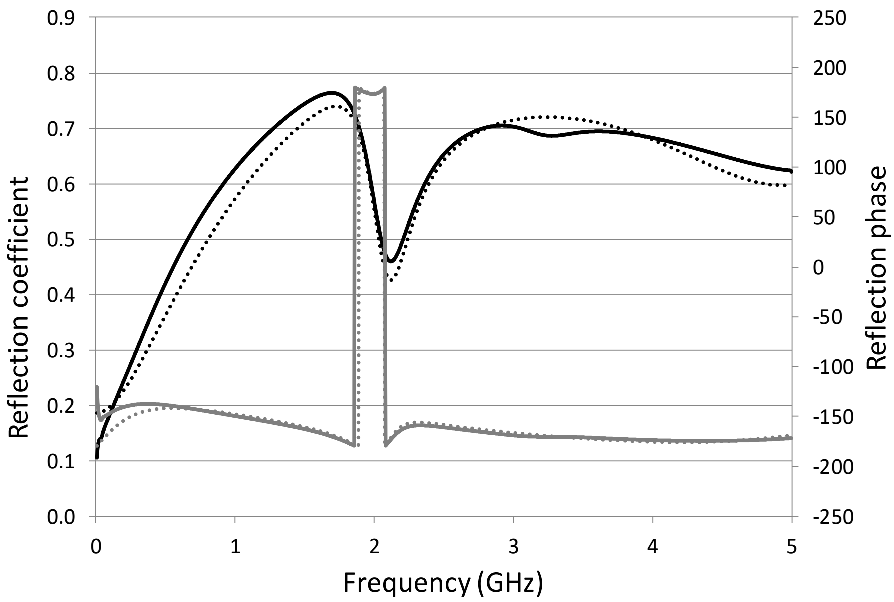

Fig. 4.25 Comparison between full-wave simulation (solid) and equivalent model response using distributed lumped components representation (dotted) for the reflection coefficient of uniform cross tag within a three-layer human body model, black represents magnitude and grey refers to phase.

Forward transmission response of degradation stages of the tag inside the three-layer model is depicted below in Fig. 4.26. It can be noticed that in addition to the reduction of the amplitude of the main resonance mode, the trapped modes seen in Fig 4.12 have disappeared (although they can still be seen in the impedance graph but with much lower value) because of the extra attenuation caused by the skin layer. The equivalent circuit responses match the full-wave results in an excellent way, equivalent circuit parameters are shown in Table 4.4. The trends are in agreement with what has been presented earlier in Table 4.2.

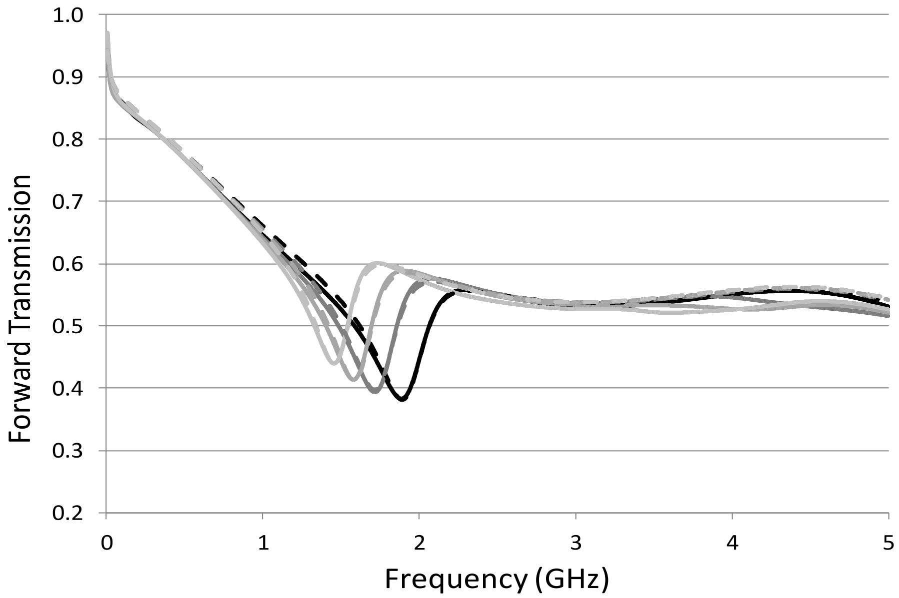

Fig. 4.26 Comparison between full-wave simulation (solid) and equivalent model response using ABCD matrix (dashed) of uniform cross tag within a human body model comprised of 1 mm skin and 8 mm fat, intact tag is shown in black and lighter colour for each subsequent degradation stages.

Table 4.4 Comparison between equivalent circuit parameters of uniform cross SRS at different degradations stages inside a human body model comprised of 1 mm of skin and 8 mm fat

Resonance state	L (nH)	C(fF)	R (Ω)
State 0	79.2	86.48	135
State 1	93.3	89.05	153
State 2	115.2	84.8	172
State 3	144.1	80.25	208

The uniform cross tag's response within the three-layer model has been studied at different angles of incidence with both TE and TM polarizations as depicted in Fig. 4.27 and Fig. 4.28, respectively. The impact of changing the angle of incidence on the response of the tag is similar to the example of tag within two-layer model discussed earlier. The values of equivalent circuit parameters at different angles of incidence are presented in Table 4.5.

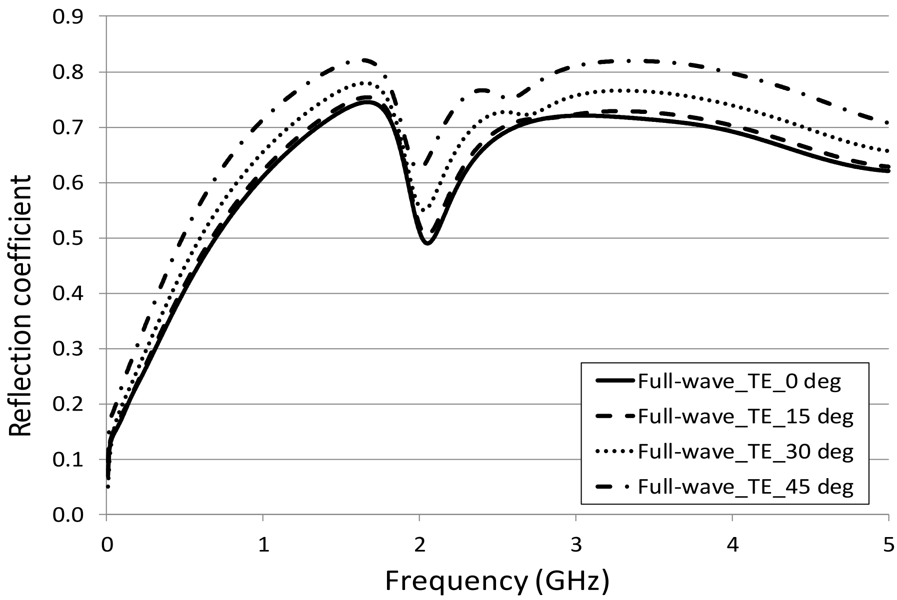

Fig. 4.27 Reflection coefficient of implantable uniform cross tag inside a three-layer human body model at various angles of TE incidence.

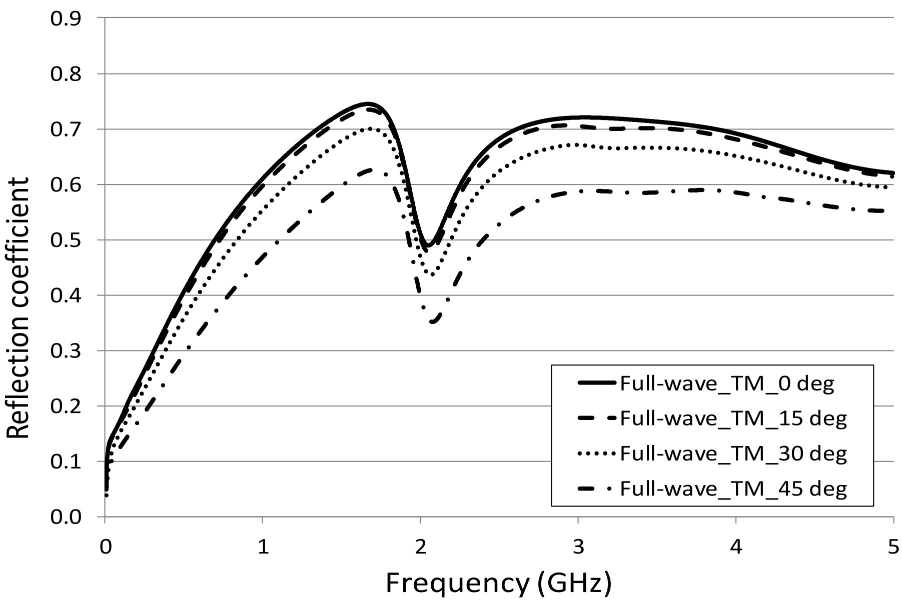

Fig. 4.28 Reflection coefficient of implantable uniform cross tag inside a three-layer human body model at various angles of TE incidence.

Table 4.5 Comparison between equivalent circuit parameters of uniform cross SRS within 8 mm fat layer at various incidence angles for both TE and TM incidences

Angle	TE			TM		
	R	L	C	R	L	C
0	135	79.2	86.48	135	78.79	86.48
15	136	79.2	86.48	134.8	78.47	86.48
30	141.8	82.6	84.06	135.2	78.22	86.48
45	150.5	85.3	83.13	136	78.22	86.48

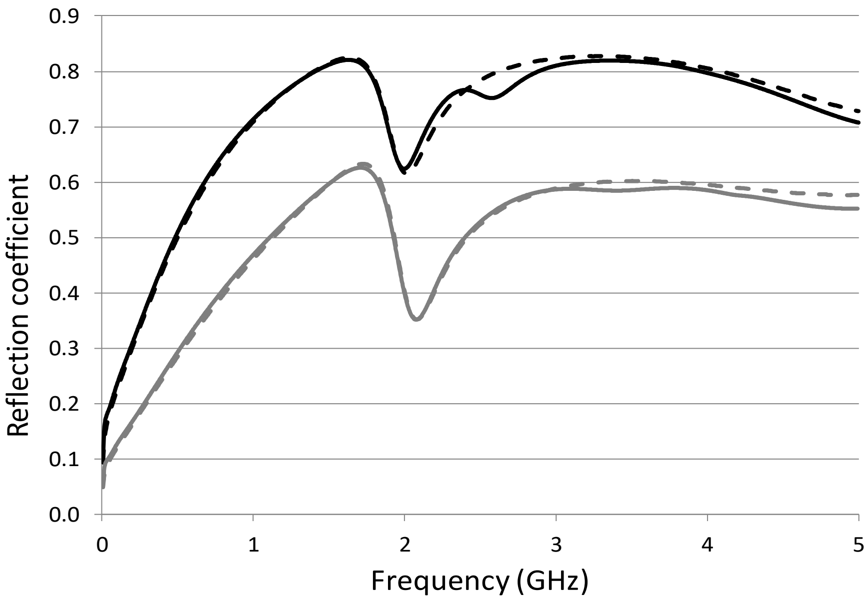

Fig. 4.29 Comparison between full-wave (solid) and equivalent circuit (dashed) response for S_{11} of implantable uniform cross tag inside a human body model comprised of 1 mm skin and 8 mm fat at 45 degree of incidence, black for TE Incidence and grey for TM incidence.

For TE incidence, both inductance and resistance have increased with the angle of incidence while capacitance have slightly decreased. On the other hand, inductance, capacitance, and resistance have almost maintained the same values with TM incidence and the changes in the response are merely caused by the changes in the frequency response of the human body layers with angle of incidence. A comparison between equivalent model and full-wave simulation is shown in Fig. 4.29. Clearly, the two curves show a very good agreement for both incidences.

4.3.3 Tag implanted within four-layer human body model

A 2 mm muscle layer has been added to the human body model presented in the previous section. The self-resonant tag within four-layer model is shown in Fig. 4.30. Generally, muscle layer are very lossy with high dielectric constant and high loss tangent, thickness of muscle layer vary considerably depending on the body part. In this example a 2 mm thick muscle layer is used. According to (4.7), attenuation of muscle tissue at 3 GHz is 487.04 db/m, and for a 2 mm layer the attenuation is 0.974 db. Reflection and forward transmission coefficients for self-resonant tag within four-layer human body model are shown in Fig. 4.31 and Fig. 4.32, respectively. It can be seen that equivalent model and full-wave simulation results are in

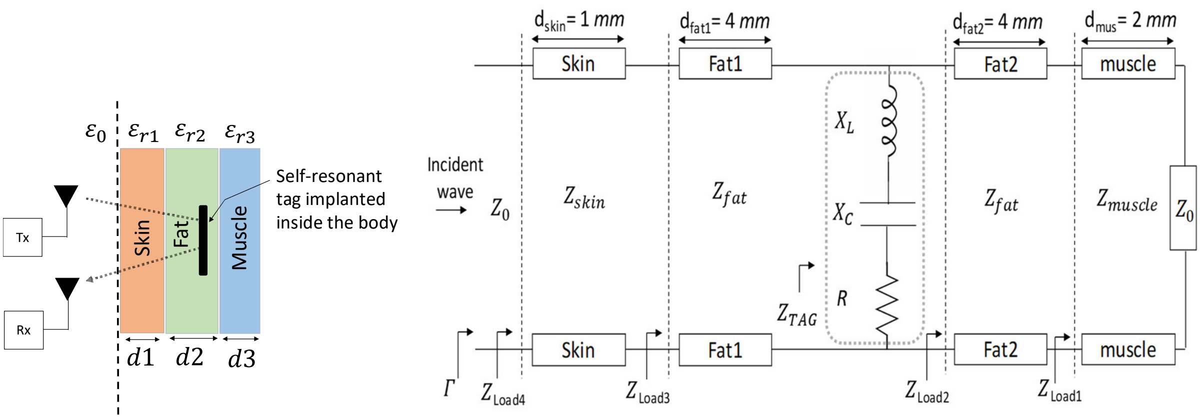

(a) (b)

Fig. 4.30 (a) A uniform cross tag inside four-layer human body model (b) Its equivalent transmission line model.

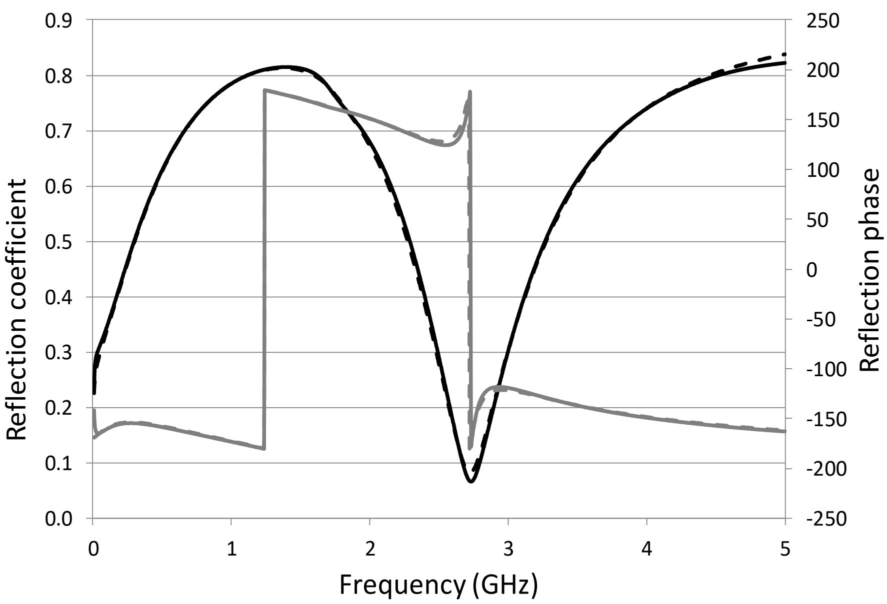

Fig. 4.31 Comparison between full-wave simulation (solid) and equivalent model response using ABCD matrix (dashed) for the reflection coefficient of uniform cross tag within a four-layer human body model, black represents magnitude and grey refers to phase.

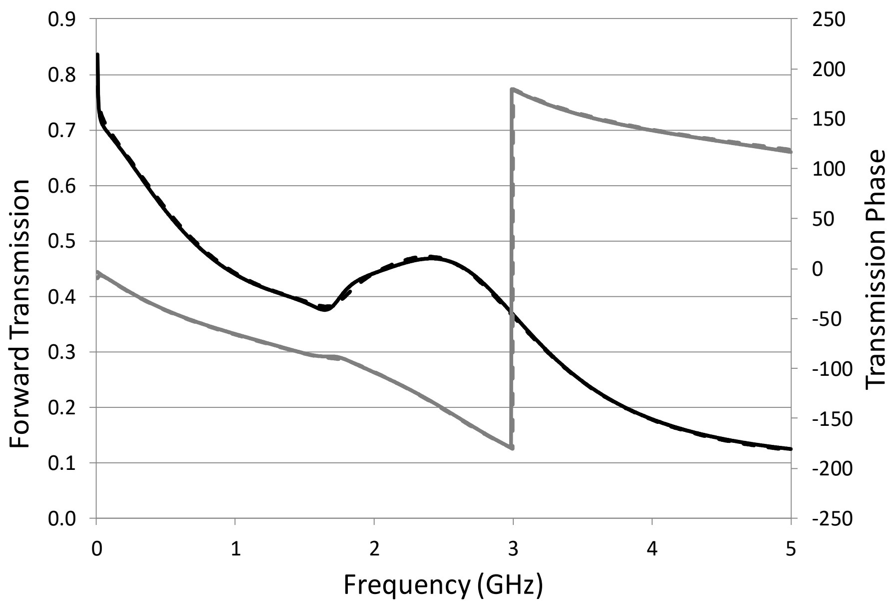

Fig. 4.32 Comparison between full-wave simulation (solid) and equivalent model response using ABCD matrix (dashed) for the forward transmission of uniform cross tag within a four-layer human body model, black represents magnitude and grey refers to phase.

excellent agreement for both magnitude and phase. The perfect matching of the two curves is attributed to the dielectric layers' frequency response being dominant over the tag's response. As explained in chapter three, the proposed equivalent transmission line model accounts for the main resonance mode of the SRS in addition to the dielectric material's response. As dielectric attenuation increases, the higher order modes of the SRS subsides, hence equivalent model results look closer to full-time simulation results.

Table 4.6 Comparison between equivalent circuit parameters of uniform cross SRS at different degradation stages inside a four-layer human body model

Resonance state	L (nH)	C(fF)	R (Ω)
State 0	79.2	106.61	190.2
State 1	93.3	113	186.7
State 2	115.2	103.1	193.2
State 3	144.1	95	227.48

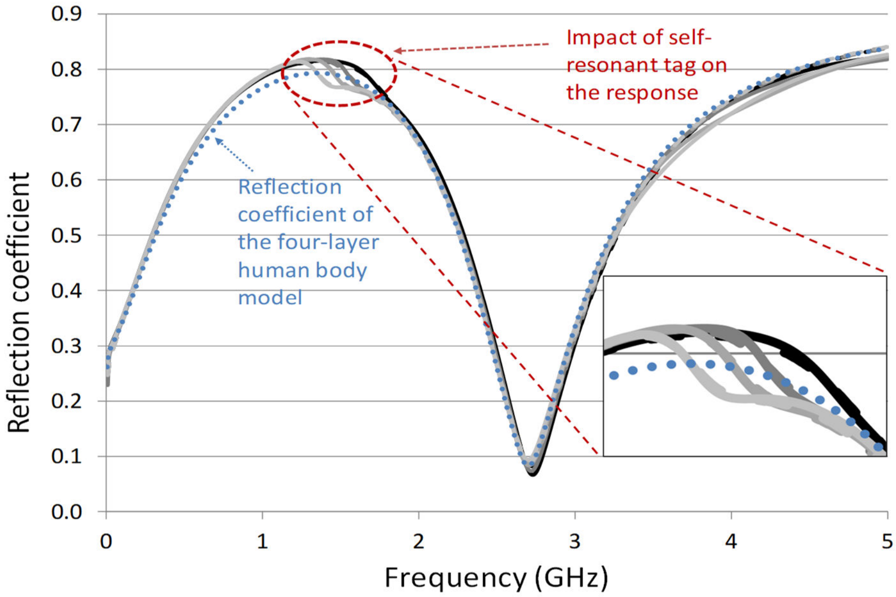

Fig. 4.33 Comparison between full-wave simulation (solid) and equivalent model response using ABCD matrix (dashed) of reflection coefficient of uniform cross tag within a four-layer human body model, intact tag is shown in black and lighter colour for each subsequent degradation stages.

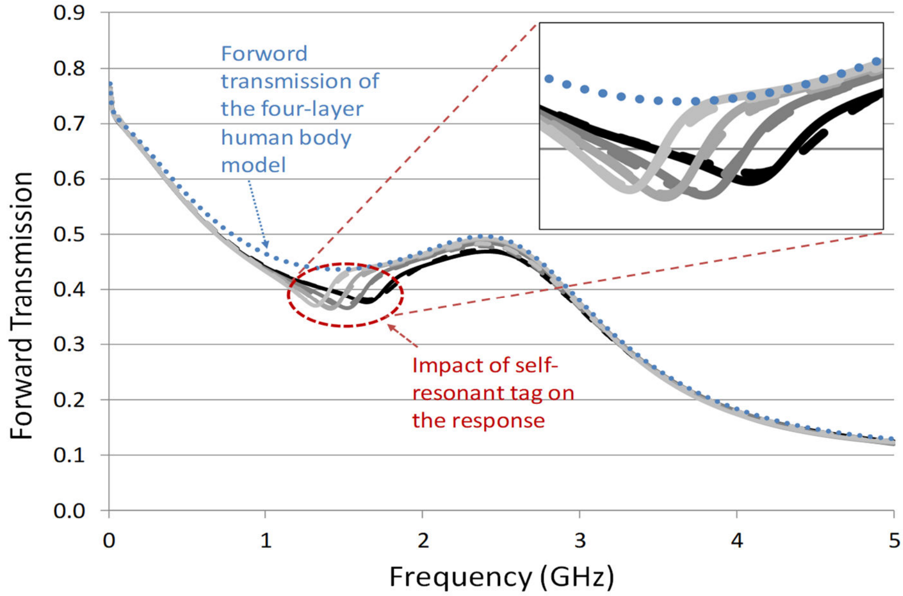

Fig. 4.34 Comparison between full-wave simulation (solid) and equivalent model response using ABCD matrix (dashed) of forward transmission of uniform cross tag within a four-layer human body model, complete tag is shown in black and lighter colour for each subsequent degradation stages.

Tag's response throughout degradation stages using full-wave simulation and equivalent model is shown in Fig. 4.33 and Fig. 34 for reflection coefficient and forwards transmission coefficients, respectively. The response of the human body model alone is shown in dotted blue line. It can be clearly seen how the overall response in shaped by the human body model response, while self-resonant tag's response has remarkably minimized. However, the changes in the response due to tag degradation are still noticeable. Equivalent circuit parameters for all degradation stages are presented in Table 4.6. The trends for inductance, capacitance, and resistance are in line with the values shown in both Table 4.2 and Table 4.4. Inductance in all three tables have shown similar values and it has been demonstrated that

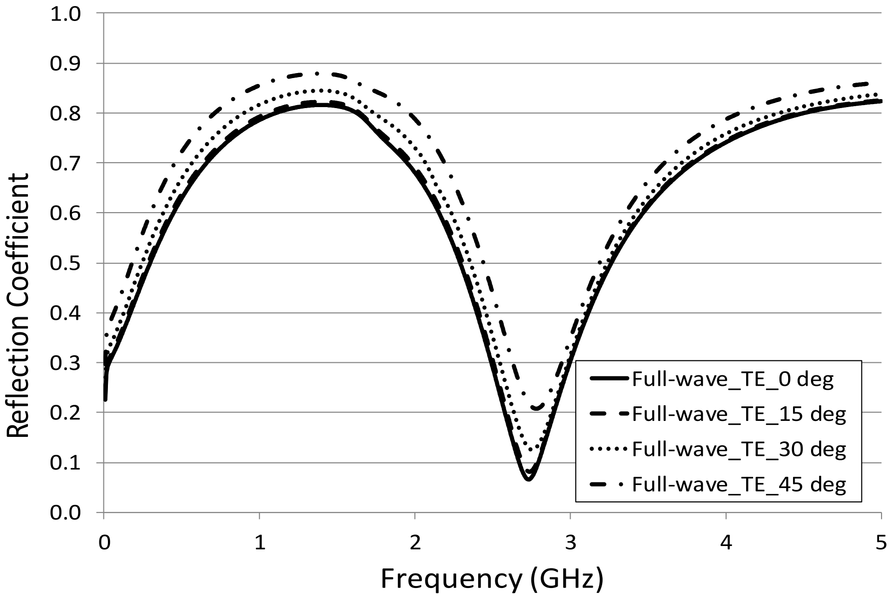

Fig. 4.35 Reflection coefficient of implantable uniform cross tag inside a four-layer human body model at various angles of TE incidence.

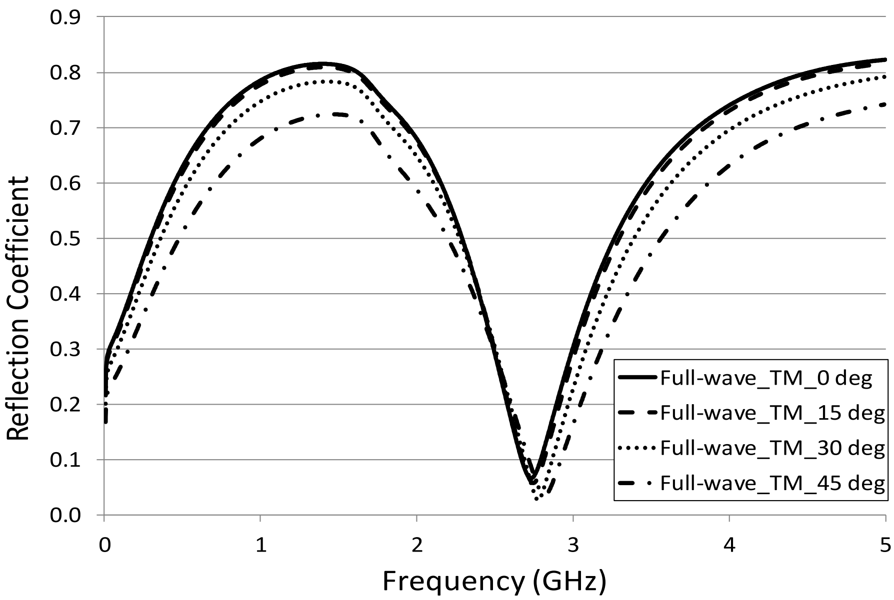

Fig. 4.36 Reflection coefficient of implantable uniform cross tag inside a four-layer human body model at various angles of TM incidence.

Table 4.7 Comparison between equivalent circuit parameters of uniform cross SRS inside a four-layer human body model at various incidence angles for both TE and TM incidences

Angle	TE			TM		
	R	L	C	R	L	C
0	190.2	79.2	106.61	190.2	79.2	106.6
15	202.5	80.3	106.61	187	80.1	106.5
30	254.8	81	103.3	186.7	79.4	106.5
45	208.7	82	97.4	180.2	78	106.6

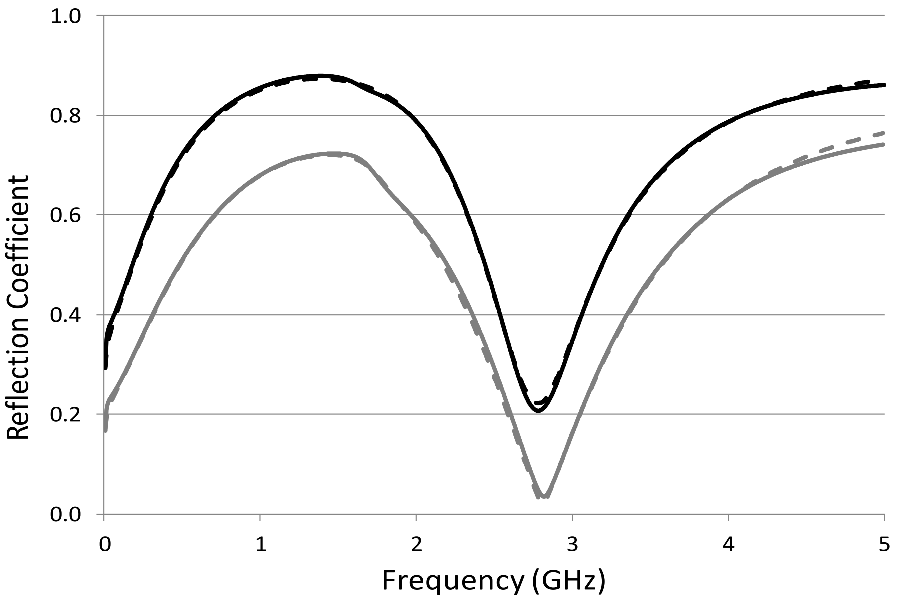

Fig. 4.37 Comparison between full-wave (solid) and equivalent circuit (dashed) response for REFLECTION coefficient of implantable uniform cross tag inside a four-layer human body model at 45 degree of incidence, black for TE Incidence and grey for TM incidence.

inductance value is govern by the state of the tag rather than the surrounding dielectric media. On the other hand, both capacitance and resistance have shown continuous rise as more biological layers included in the model. The increase in resistance is due to the higher attenuation levels of the extra layers while capacitance is proportional to both permittivity and thickness of the dielectric media as static capacitance equation suggests in (3.42). The changes in the response at different oblique incidence angles are shown in Fig. 4.35 and Fig. 4.36 for TE and TM incidence, respectively, while equivalent circuit parameters at different angles of incidence are shown in Table 4.7. It can be observed that the changes in inductance and capacitance values are minimal. This can clearly indicate that the changes that can be seen in the response in Fig. 4.35 and Fig. 4.36 are mainly caused by the frequency response of the human body model, and the impact of self-resonant tag has diminished. A comparison between equivalent model and full-wave simulation at 45 degree is shown in Fig. 4.37 for both TE and TM incidence, an excellent agreement can be clearly seen.

From the presented analysis in this section, it can be seen that as the thickness of the surrounding dielectric media increases, the self-resonant tag's response starts to subside and the frequency response of the dielectric media becomes more dominant, and at some point it will not be possible to track the changes in the response of the degrading tag. This problem will be addressed in chapter five and six. Some alterations to tag design will be discussed to make the tag response more resilient.

4.4 Specific absorption rate calculation using equivalent transmission line model

With any implantable medical device it is fundamentally important to assess the level of power absorbed by the human body to prevent any detrimental impact on the hosting biological tissues. Electromagnetic signals in the microwave frequency range have a non-ionising effect on the human body. As electromagnetic waves travel through the human body some of the power is absorbed by the biological tissues causing a localised increase in temperature, and a constant heat rise for certain duration of time can lead to a permanent tissue damage.

The safety of electromagnetic exposure is usually assessed using specific absorption rate (SAR) metric. SAR is a measure of power absorbed by the biological tissues per unit mass and has a unit of W/Kg. Different standardisation institutions have set various SAR limits for different applications. According to ANSI, the recommended SAR value for a partial body exposure is 1.6 W/kg per any 1 g of biological tissue [79]. In this section, the SAR value of self-resonant tag inside the human body is studied using the derived transmission line model. The analysis assumes an off-body receiver some distance from the body with plane wave incidence (i.e., SAR caused by the near field of Tx/Rx antenna is beyond the scope of this study). Although SAR value is primarily dependent on the power of transmitted signal rather than the passive self-resonant tag design, the aim of this study is to determine the threshold for maximum allowed power to be used when designing a self-resonant tag reader.

Fig. 4.38 shows an equivalent transmission line model of a self-resonant tag within a four-layer human body model. The parameters in this equivalent model are identical to the example presented in the last section. However, it can be noticed that in this case the transmission line is terminated by the characteristic impedance of bone layer instead of Z_0

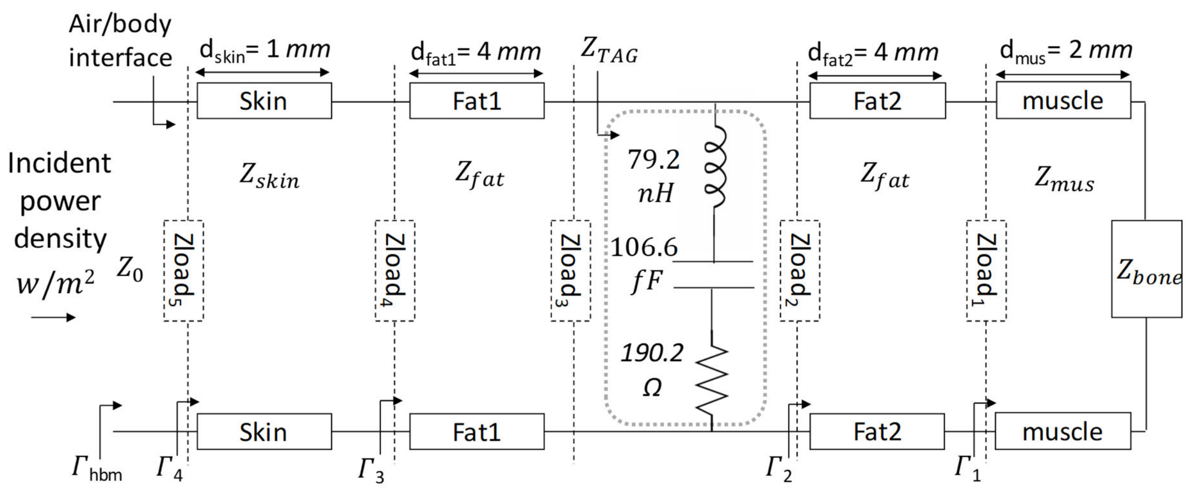

Fig. 4.38 SAR calculation of uniform cross tag inside four-layer human body model using equivalent transmission line model representation

(Although equivalent circuit parameters of the self-resonant tag may slightly change, terminating the transmission line model with Z_{bone} is a more realistic scenario). Since it is possible to calculate lost power and transmitted/reflected power at each intersection of the transmission line, it is possible to calculate SAR value at each layer of the human body model. It is worth noting here that this method can be generically used to calculate SAR level for any types of far field electromagnetic exposure including wireless power transfer for in-body implants or even impact of base station signals on human body.

The first step to calculate SAR value is to find the load impedance at each transmission line segment, starting from right side of the transmission line model (i.e., the far end from the source), $Zload_1$ can be calculated using (4.1). Subsequently, load impedance at each other segment can be calculated in the same way. One the other hand, reflection coefficient at each segment is calculated using:

$$\Gamma = \frac{load\ impedance - charcteristic\ impedance}{load\ impedance + charcteristic\ impedance} \tag{4.25}$$

Hence, at each intersection, part of the power is reflected and the other part is transmitted based on the impedance matching between the characteristic impedance and the corresponding load impedance. Transmitted power density can be calculated using [78]:

$$w_t = (1 - |\Gamma|^2) * w_i \tag{4.25}$$

where w_i is incident power density in (W/m^2).

Transmitted power dissipates exponentially as it passes through the lossy transmission line segment. Thus, power at a certain distance within the dielectric media can be given using [78]:

$$w_d = w_t * e^{-2\alpha d} \tag{4.26}$$

where α is the attenuation constant of the dielectric layer and can be calculated using (4.6), while d is the layer thickness.

SAR value of any biological tissue can be calculated using [127]:

$$SAR = \frac{2\sigma w_d}{\rho\ Re\left(\frac{1}{Z_d}\right)}\ (W/\ kg) \tag{4.27}$$

where σ is tissue conductivity in *(S/m)*, ρ is tissue density in *(kg/m^3), and* Z_d is the characteristic impedance of the biological layer and can be calculated using (4.5).

Parameters of the skin, fat, muscle, and bone layers have been calculated at 1 GHz as presented in Table 4.8. Firstly, an incident power density of 1 W/m^2 have been adopted, and assuming that the effective surface area of the incident wave on human body is 50x50 mm^2 (which is about 1.4 times bigger than the final tag design shown in chapter 6), the incident power would be 2.5 mW.

Calculated SAR values with incident power density of 1 W/m^2, 30 W/m^2, and 50 W/m^2 are shown in Table 4.9. It can be observed that with 1 W/m^2 and 30 W/m^2 all SAR values are below the recommended upper limit of 1.6 W/Kg. On the other hand, with 50 W/m^2 incident power density the SAR at skin layer has exceeded the recommended value, while SAR at muscle layer has significantly increased but still within the safety range.

Table 4.8 Human body model parameters at 1 GHz

Parameters	Skin	Fat	Muscle	Bone
ρ *(kg/m^3)*	1100	910	1041	1850
σ *(S/m)*	0.9	0.0535	0.978	0.156
ε_r	40.9	5.45	54.8	12.4
tanδ	0.395	0.177	0.321	0.226
α (neper/m)	25.98	4.31	24.59	8.28
β (radian/m)	136.53	49.11	157.08	74.26
Z_d (Ω)	55.8 + 10.62i	159.51 + 14i	49.06 + 7.68i	105+11.71i

Table 4.9 Incident power and specific absorption rate of bio-tissues at 1 GHz

Incident power density (W/m^2)	Power per 50x50 mm^2 (mW)	Power transferred into the body (W/m^2)	SAR in skin layer (W/kg)	SAR in fat1 layer (W/kg)	SAR in fat2 layer (W/kg)	SAR in muscle layer (W/kg)
1	2.5	0.56	50.25 *10^{-3}	9.47 *10^{-3}	8.17 *10^{-3}	33.11 *10^{-3}
30	75	16.8	1.5	284.1 *10^{-3}	236.9 *10^{-3}	920 *10^{-3}
50	125	28	2.51	473.8 *10^{-3}	395 *10^{-3}	1.53

Since bio tissues properties are frequency dependent, SAR value have been investigated at 5 GHz as well with the three values of incident power density. Calculated Parameters of the skin, fat, muscle, and bone layers are presented in Table 4.10. It can be observed that conductivity and attenuation levels for bio-tissues are higher at 5 GHz than at 1 GHz. SAR values have been calculated at this frequency as introduced in Table 4.11. It can be noticed that SAR values are generally higher than the corresponding values at 1 GHz. SAR values are above the recommended limit at skin for both 30 W/m^2 and 50 W/m^2 incident power density. However, it can be noticed that SAR at muscle is less at 5 GHz than the corresponding values at 1 GHz because of higher reflection coefficients and higher attenuation in the transmission line model (i.e., less power is delivered to muscle layer).

For a self-resonant tag, it is interesting to investigate SAR values at resonance, as maximum current flows through the series RLC circuit at that frequency. The resonance frequency of the equivalent transmission line model in Fig. 4.38 occurs at 1.73 GHz. Human body model parameters have been calculated at this frequency as presented in Table 4.12. SAR values at this frequency are shown in Table 4.13, and by looking at these values it can be concluded that SAR values at the resonance frequency shows similar trend to SAR values at 1 GHz but with slightly higher figures, which are solely the impact of a higher frequency.

Table 4.10 Human body model parameters at 5 GHz

Parameters	Skin	Fat	Muscle	Bone
ρ *(kg/m^3)*	1100	910	1041	1850
σ *(S/m)*	3.06	0.242	4.05	0.962
ε_r	35.8	5.03	49.5	10
tanδ	0.308	0.173	0.294	0.345
α (neper/m)	95.29	20.27	107.1	56.4
β (radian/m)	633.94	235.8	745.3	336.8
Z_d (Ω)	60.89 + 9.15i	166.14 + 14.28i	51.89 + 7.45i	114 + 19.09i

Table 4.11 Incident power and specific absorption rate of bio-tissues at 5 GHz

Incident power density (W/m^2)	Power per 50x50 mm^2 (mW)	Power transferred into the body (W/m^2)	SAR in skin layer (W/kg)	SAR in fat1 layer (W/kg)	SAR in fat2 layer (W/kg)	SAR in muscle layer (W/kg)
1	2.5	0.32	91.67 $*10^{-3}$	7.76 $*10^{-3}$	4.29 $*10^{-3}$	6.97 $*10^{-3}$
30	75	9.63	2.75	234.4 $*10^{-3}$	129.9 $*10^{-3}$	213.1 $*10^{-3}$
50	125	16.05	4.58	390.4 $*10^{-3}$	216.3 $*10^{-3}$	354.07 $*10^{-3}$

Table 4.12 Human body model parameters at resonance – 1.73 GHz

Parameters	Skin	Fat	Muscle	Bone
ρ *(kg/m^3)*	1100	910	1041	1850
σ *(S/m)*	1.16	0.08	1.3	0.26
ε_r	38.99	5.36	53.64	11.83
Tanδ	0.31	0.15	0.25	0.23
α (neper/m)	34.52	6.15	33.26	14.33
β (radian/m)	229	84.14	267.6	125.3
Z_d (Ω)	58.31 + 8.79i	161.46 + 11.81i	50.26 + 6.24i	107.4 + 12.26i

Table 4.13 Incident power and specific absorption rate of bio-tissues at resonance- 1.73 GHz

Incident power density (W/m^2)	Power per 50x50 mm^2 (mW)	Power transferred into the body (W/m^2)	SAR in skin layer (W/kg)	SAR in fat1 layer (W/kg)	SAR in fat2 layer (W/kg)	SAR in muscle layer (W/kg)
1	2.5	0.6	$70.3*10^{-3}$	$12.4*10^{-3}$	$8.01*10^{-3}$	$24.2*10^{-3}$
30	75	18	2.1	$376.3 *10^{-3}$	$247*10^{-3}$	$738.49*10^{-3}$
50	125	30	3.51	$626.3*10^{-3}$	$410.3*10^{-3}$	1.22

Although some SAR values in these tables are higher than the 1.6 W/Kg limit, it is unlikely to cause any harm to the hosting tissues, as the exposure time is very short in the intended application of this research project. The resonant state of the implanted self-resonant tag is measured at discrete intervals throughout the day using backscattering communications. Temperature rise in bio tissues due to electromagnetic exposure varies depending on many factors including blood flow and metabolic rate. Nevertheless, a simple way to calculate the temperature rise in any bio tissues approximately can be expressed as [128]:

$$\text{Temperature rise} = \frac{exposure\ time\ (s) * SAR}{tissue\ heat\ capacity} \tag{4.28}$$

where skin heat capacity is 3.5*10^3 J/(kg °C) and for a skin SAR value of 4.58 (highest calculated value) and exposure time of 30 seconds, the temperature rise in skin would be 0.039 °C only.

From the SAR analysis presented in this section, the following concluding remarks can be made in relation to SAR of a self-resonant tag inside the human body:

- Skin always have the highest SAR among other bio tissues because it receives most of the power. Deeper layers receives less of the incident power because of wave reflection and power loss in the more superficial layers.
- For the same incident power, skin and muscle have higher SAR values that fat and bone layers because the formers have higher conductivity.
- SAR is directly proportional to the frequency of incident signal.
- Even when SAR is higher than the recommended limit, there is no significant increase in the temperature because of the short exposure time.
- SAR at muscle layer at 5 GHz is less than the corresponding value at 1 GHz because power delivered to muscle is less because of higher dielectric attenuation and higher reflection coefficients as can be seen in Table 4.14 below.

Table 4.14 Reflection coefficients at different points of the human body model at different frequencies

Frequency (GHz)	Γ_{hbm}	Γ_4	Γ_3	Γ_2	Γ_1
1	0.66∠175.2	0.16∠16.6	0.37∠-171.5	0.37∠-153.8	0.36∠-3.05
Resonance-1.73	0.63∠159.48	0.41∠62.4	0.55∠173.7	0.49∠-154.2	0.36∠-0.69
5	0.82∠-162.5	0.78∠-10.8	0.59∠-78.7	0.68∠-179	0.38∠-1.5

4.5 Experimental validation of derived equivalent transmission line model

4.5.1 Dielectric phantom preparation

Different methods have been proposed in the literature to create dielectric mediums that mimic the electrical properties of certain biological tissues. One of the simplest methods for modelling human body tissues is by forming a homogeneous liquid phantom comprised of distilled water, sodium chloride, and sugar [72, 129]. Although with this method it may not be possible to match the properties of certain biological tissues over wide frequency band, it offers a quick and easy way for preparing lossy dielectric mediums with various properties. This method has been adopted in this project to create a dielectric phantom and to test the response of self-resonant tag on it.

First of all, the impact of varying the concentration of sodium chloride and sugar separately on the dielectric properties of distilled water have been studied. An Agilent 85070E dielectric probe kit connected to an E5071B network analyser have been used to measure the dielectric constant and loss tangent of the liquid phantom. The kit has been calibrated using three steps procedure starting with open circuit (air) followed by a short circuit using the specified shorting block and finally with distilled water. 1001 measurement point have been taken over 8 GHz bandwidth (from 0.5-8.5 GHz). The measurement setup is illustrated in Fig. 4.39 below. The properties of 50 ml distilled water sample have been measured using the performance probe. An amount of sodium chloride were added to the liquid at an increment of 5 g each time until 15 g. The properties of the solution were measured at each stage as shown in Fig. 4.40 and 4.41 for dielectric constant and loss tangent, respectively. It can be observed that sodium chloride lowers the dielectric constant remarkably, and at the same time leads to a big increase in the loss tangent, especially for frequencies below 3 GHz. On the other hand, sugar have also shown to lower the dielectric constant but to a much lesser extent than sodium chloride, while the impact on loss tangent is minimal as shown in Fig. 4.42 and 4.43, for dielectric constant and loss tangent respectively.

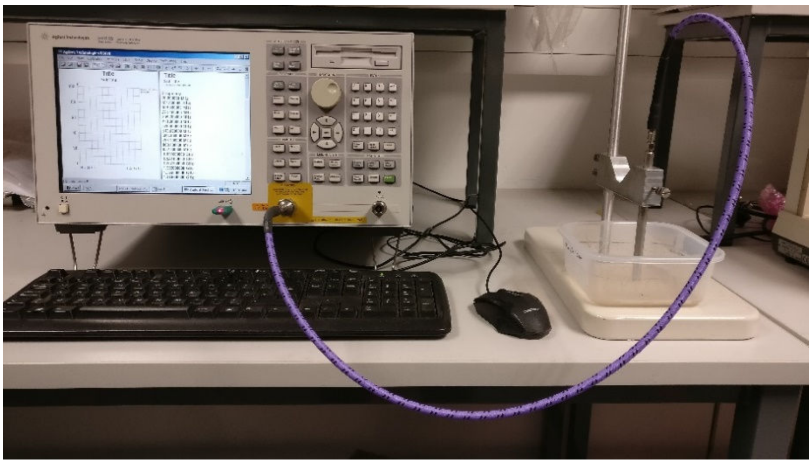

Fig. 4.39 Dielectric measurement probe connected to network analyser.

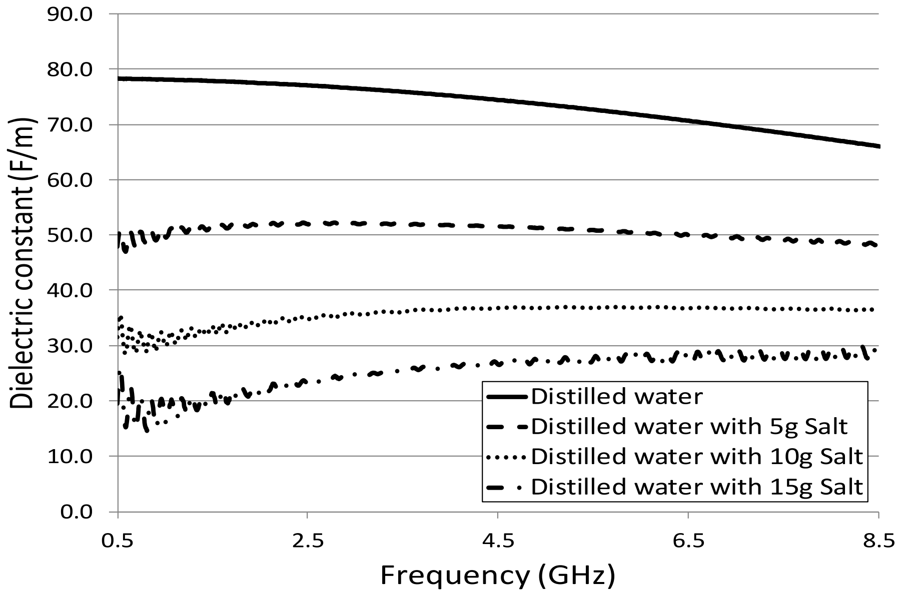

Fig. 4.40 Impact of sodium chloride concentration on dielectric constant of 50 ml distilled water.

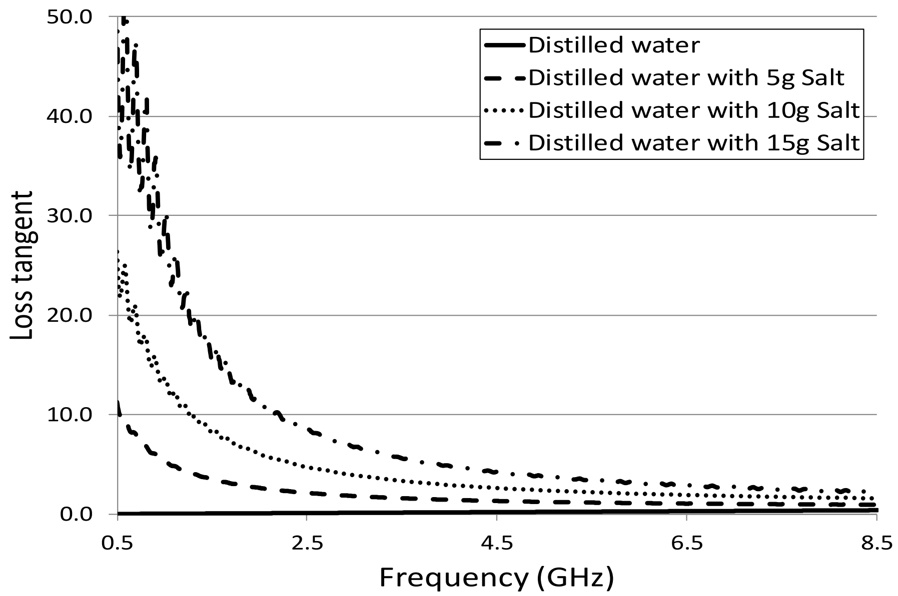

Fig. 4.41 Impact of sodium chloride concentration on loss tangent of 50 ml distilled water.

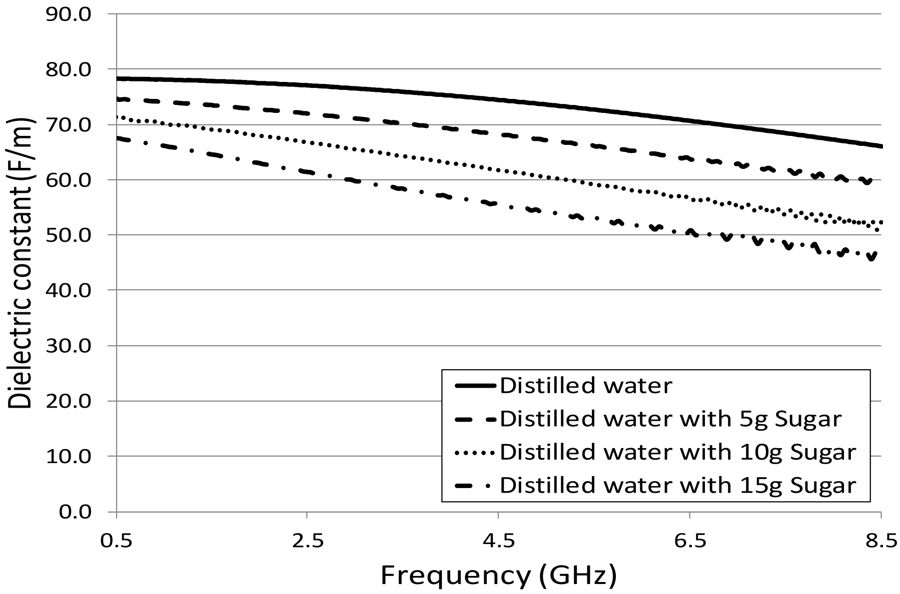

Fig. 4.42 Impact of sugar concentration on dielectric constant of 50 ml distilled water.

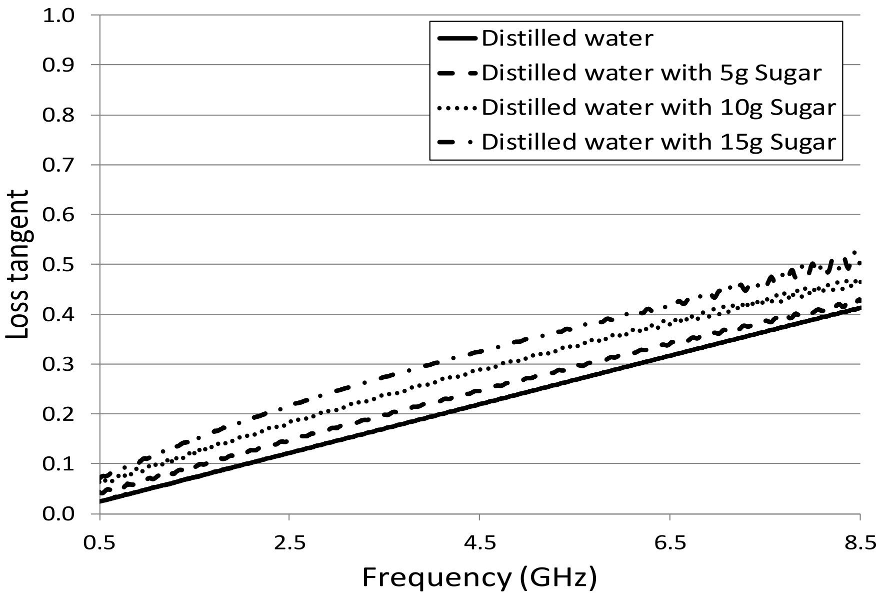

Fig. 4.43 Impact of sugar concentration on loss tangent of 50 ml distilled water.

Several mixtures have been tried in order to reach a solution with properties similar to a biological media. At this stage of the project, it is not necessary to test the tag response inside a specific biological tissue type. Therefore, a homogeneous phantom with dielectric properties similar to the average properties of skin-fat-muscle layers has been created. The ingredients of the phantom are presented in Table 4.15. Measured properties of dielectric phantom is illustrated Fig. 4.44.

Table 4.15 Ingredient of manufactured dielectric phantom

Ingredients	Dielectric phantom
Distilled water	34.5%
Sodium chloride	0.5%
Sugar	65%

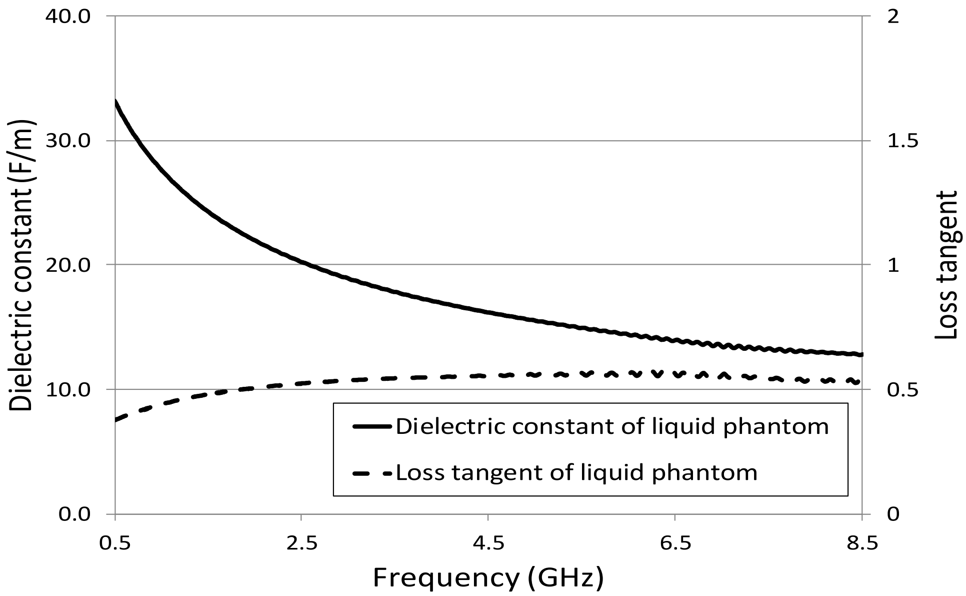

Fig. 4.44 Measured Dielectric properties of manufactured dielectric phantom.

4.5.1 Waveguide measurements

As part of the validation for the derived transmission line model, the self-resonant tag needs to be tested with the manufactured lossy dielectric phantom inside a waveguide, in a similar way to the experimental validation presented in chapter 3. However, handling a liquid in a waveguide imposes some technical challenges. Therefore, a small amount of a gelling substance called Agar were added to the solution to turn the liquid phantom into semi-solid state. 2 grams of Agar were added for each 50 ml of the liquid phantom to solidify the solution. The mixture were heated up in a microwave oven up to the boiling temperature to reach the gelling point and then was left to cool down in room temperature. The use of Agar for preparing solid phantoms have been proposed in the literature as in [74]. The properties of the solid phantom were re-measured to investigate the impact of Agar on the dielectric properties of the phantom. It has been found that dielectric constant has remarkably decreased without changing the shape of frequency response. On the other hand, loss tangent has slightly increased, especially above 2.5 GHz as shown in Fig. 4.45.

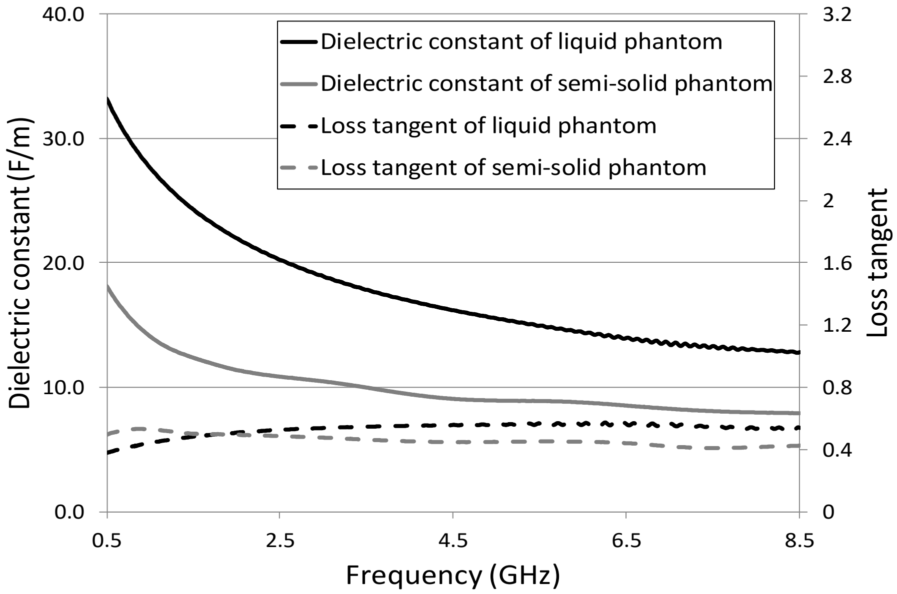

Fig. 4.45 Comparison between dielectric properties of liquid and semi-solid dielectric phantom.

The liquid solution with Agar was casted into the waveguide section shown in Fig. 4.46a. The estimated thickness of the solid phantom was about 5 mm. The response of the tag shown in Fig. 4.46b was tested on the solid phantom inside a Waveguide in a similar way to the experimental verification of chapter three. The full explanation of the experiment and tag design is discussed in chapter 6, but the main focus in this section is to compare the measured tag response to the equivalent model result. The ABCD matrix of this structure is given by:

$$\begin{bmatrix} A & B \\ C & D \end{bmatrix} = [\text{Waveguide}] * [\text{Semi} - \text{solid phantom}] * [\text{FR4}] * [\text{SRS}] \tag{4.29}$$

where waveguide transmission matrix can be calculated using (3.44). Semi-solid phantom and FR4 matrices are given by:

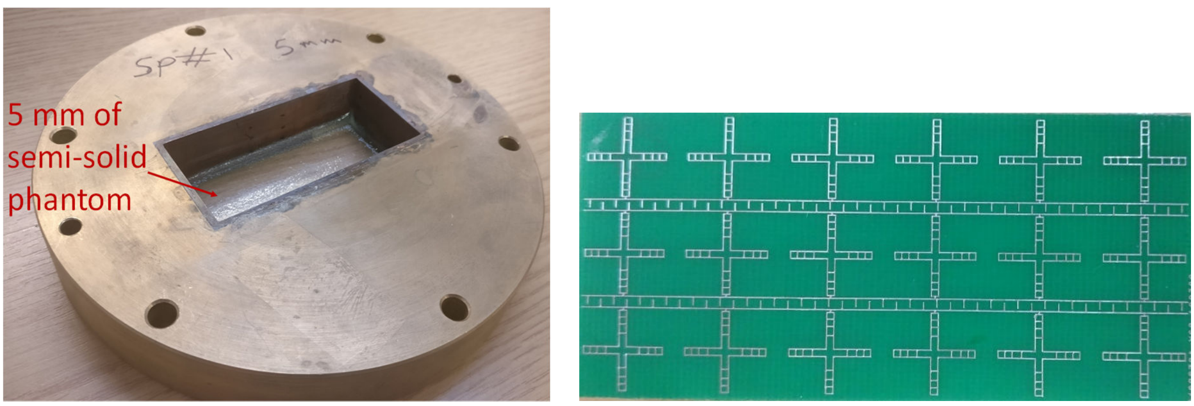

(a) (b)

Fig. 4.46 (a) semi-solid phantom in a waveguide section (b) uniform cross array tag.

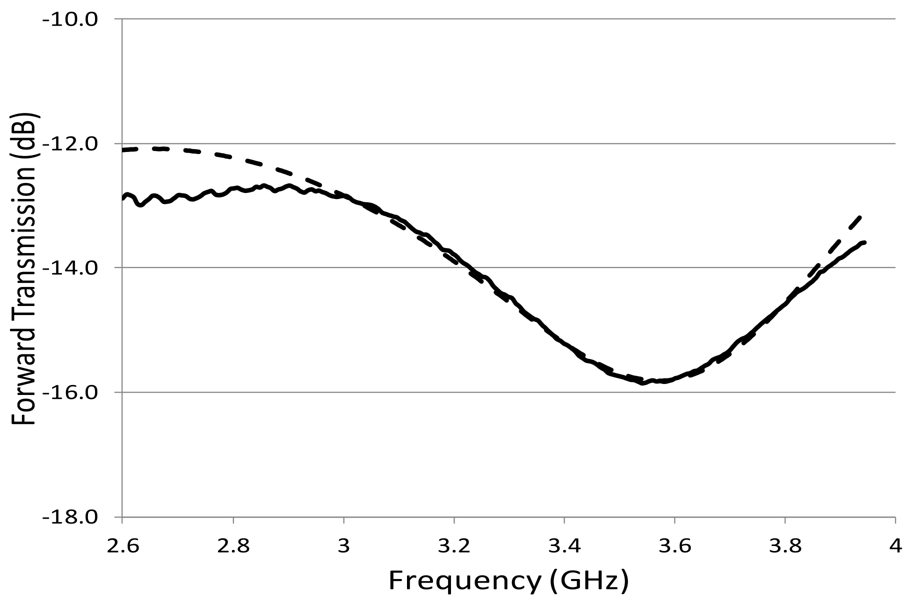

Fig. 4.47 A comparison between waveguide measured response (solid) and equivalent TLM (dashed) for forward transmission for uniform cross array tag on 0.6 FR4 substrate and 5 mm of dielectric phantom.

$$[\text{Semi} - \text{solid phantom}] = \begin{bmatrix} \cosh(\gamma_{SP} d_{SP}) & \sinh(\gamma_{SP} d_{SP}) * Z_{SP} \\ \sinh(\gamma_{SP} d_{SP}) * 1/Z_{SP} & \cosh(\gamma_{SP} d_{SP}) \end{bmatrix} \quad (4.30)$$

$$[\text{FR4}] = \begin{bmatrix} \cosh(\gamma_{FR4} d_{FR4}) & \sinh(\gamma_{FR4} d_{DR4}) * Z_{FR4} \\ \sinh(\gamma_{FR4} d_{FR4}) * 1/Z_{FR4} & \cosh(\gamma_{SP} d_{SP}) \end{bmatrix} \quad (4.31)$$

where d_{SP} is 5 mm and d_{FR4} is 0.6 mm. The Propagation constant and characteristic impedance of each of the layers can be calculated using (4.15) and (4.5), respectively. A comparison between measured result and equivalent transmission line model result is shown in Fig. 4.47. It can be seen that the two curves generally show a good agreement. However, at the beginning and at the end of the window there is slight discrepancy between the two curves and this is caused by a difference in the frequency response of the phantom. There is a margin of error in the measured dielectric properties of the phantom using the dielectric probe kit. Moreover, the accuracy of the phantom ingredients, preparation method, storage condition and duration are also factors that affect the properties of the phantom (in fact two different phantoms were used for dielectric properties and waveguide measurements). The calculated equivalent circuit parameters of the tag are: R = 37.2 Ω, L = 8.09 nH, and C= 237.6 fF. It can be noticed that the capacitance have remarkably increased compared to the measure results in chapter 3. The rise in the capacitance is caused by both the introduction of the additional interdigital capacitor (as discussed in chapter 6), and by the dielectric phantom layer as well. On the other hand, the decrease in the inductance is because the uniform cross strips parallel to the electric field is much shorter that the single-element tag used in the waveguide experiment in chapter three. Lastly, the resistance represent the losses imposed by the phantom on the circuit.

4.6 Summary

This chapter has presented analysis of self-resonant tag within multi-layer human body model. The derived impedance expressions introduced in chapter three has been extended to account for lossy dielectric layers. These impedance expressions have been utilised to extract the reactance and resistance of the equivalent circuit of the self-resonant tag inside multi-layer human body model. A step by step analysis for implanted self-resonant tag has been followed in order to identify the impact of bio tissues on the tag's response, and equivalent circuit values have been utilised to get more insights into the underlying physics of the model. A representation of human body layers by distributed lumped components has been discussed and the effect of increasing the number of blocks on the frequency response has been explained.

SAR and electromagnetic exposure have been analysed by utilising the equivalent transmission line model representation. SAR values with different incident power and at three different frequency points have been calculated. It has been shown that SAR value is proportional to tissue conductivity and frequency of incident signal. It has been demonstrated that even high SAR values do not cause an effective temperature rise due to short exposure time. For the maximum calculated SAR value (4.51 W/Kg), a temperature rise of only 0.039 °C have been obtained (assuming an exposure time of 30 seconds).

A homogeneous dielectric phantom has been manufactured, the impact of each of its ingredients on the dielectric properties of the phantom has been studied. A specialized dielectric probe kit has been used to measure the dielectric properties of the phantom. The response of the self-resonant tag on dielectric phantom have been measured inside a waveguide. The measured response has been compared to equivalent transmission line model response with good agreement. The next chapters will discuss practical aspects of self-resonant tag design and investigate techniques to improve tag's response to combat the attenuation of the implantation media.

5. CHAPTER FIVE

Practical considerations on tag design and geometry

This chapter discusses different practical aspects of self-resonant tags including the challenges associated with physically and electrically small tags, impact of surrounding media, and techniques to improve tag response.

5.1 Finite versus infinite self-resonant structure

Self-resonant structures with small physical and electrical sizes impose additional challenges compared with the corresponding structures with large apertures. Generally, the electromagnetic problem involving finite self-resonant structures is more challenging to solve than a periodic structure problem. With infinite periodic structures the boundary effects are not considered simply because by definition they extend to infinity; therefore, the problem can be reduced into a single unit cell problem with only one unknown which is the current density over that cell, while the current distribution on other cells in the structure is only different by a progressive phase shift. Therefore, computational burdens using numerical methods such as the method of moments (MoM) is manageable as the spectrum of the induced current is discreet. Conversely, for finite structures, current distribution on each individual cell in the array is different and is no longer solely related to the currents on other cells by only a phase shift. This makes the number of unknowns for an N×N array to be N^2 times the number of unknowns of a similar periodic problem in the MoM matrix. Moreover, the problem of calculating the current density on every element is more difficult as there is no general relationship between the current on a single cell and current on other cells in the array [130, 131]. Despite the difficulty of the problem and the high computational requirements, some attempts have been made to design a full-wave simulation software that can deal with finite self-resonant structures. It has been reported in [132] that a 3D full-wave simulator based on a special algorithm has been used to simulate a finite capacitive FSS. The simulated results of a 4 × 4 and 4 × 22 elements FSS have been compared with the measured results for the same FSS structures. In both cases, some discrepancies between simulated and measured results have been observed. Some of these discrepancies were caused by the approximations used in the modelling of the FSS array itself in the simulation, but the main source of error was caused by the size of illuminating beam, as for small-sized structures the relative size of antenna beam to the array size is of special importance because of boundary effects. With small structures, the edge effects need to be carefully accounted for as they contribute significantly to the scattering characteristics of the structure. Owing to this limitation in simulation software in dealing with finite self-resonant structures, the response of such kinds of structures can be more accurately analysed by practical measurements. The experimental setup, size of illuminating antenna beam and the effect of measurement environment, all significantly contribute to the observed resonance characteristics of the self-resonant structure under test.

5.2 Single resonating element versus array

From array theory, it is known that the gain of a single element can be improved by using multiple elements arranged in a uniform way − the more elements used the higher gain achieved [133]. Once the number of elements increases and the aperture of the array becomes multiple wavelengths long, then these structures can be considered as an FSS [101]. This assumption can be easily verified by considering a simple two-dimensional (2D) passive dipole array as shown in Fig. 5.1. This array has y-directed conducting dipoles of infinitesimal width in the x-direction. Such an array represents the simplest case, where induced surface currents have one component only. Thus, the incident electric field on one dipole can be expressed as [134]:

$$E_y^{inc} = -\frac{1}{j\omega\varepsilon_0}\left(\frac{\partial^2}{\partial y^2} + k_0^2\right) \times A_y \tag{5.1}$$

Where A_y is the magnetic poynting vector and can be expressed by:

$$A_y = U * J_y \tag{5.2}$$

In this representation, U is the dyadic green's function in free space and J_y is the induced surface current density in a conducting dipole, while the asterisk sign ($*$) refers to the convolution process in the spatial domain.

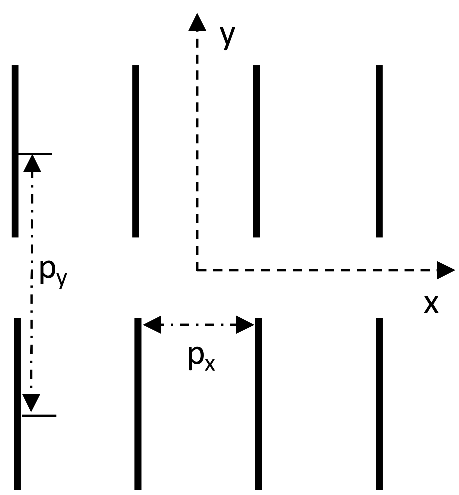

Fig. 5.1 A generic 2D dipole array with the major dimension along y axis.

For a perfectly conducting dipole the tangential electric field equals to zero, therefore the scattered and incident fields are related to each other by [134]:

$$E_{y\_tangential} = E_{y\_tangential}^{scat} + E_{y\_tangential}^{inc} = 0 \tag{5.3}$$

Thus, the scattered field from a single dipole element will be:

$$E_y^{scat} = \frac{1}{j\omega\varepsilon_0}\left(\frac{\partial^2}{\partial y^2} + k_0^2\right) \times A_y \tag{5.4}$$

For an array of elements, the induced surface currents in the conducting dipoles array increase due to two factors, firstly due to the direct illuminating incident plane wave and secondly due to the electric fields generated by the induced currents in other elements in the array (i.e. mutual coupling). The latter is less effective and can be neglected in most cases without affecting the response. Thus, the total scattered electric field from an *N*-element dipole array will therefore be [135]:

$$E_y^{scat} = \frac{1}{j\omega\varepsilon_0}\sum_{n=1}^{N}\left(\frac{\partial^2}{\partial y^2} + k_0^2\right) \times A_{y\_n} \tag{5.5}$$

Unsurprisingly, it can be seen that for the case where mutual coupling can be ignored, the resultant scattered field is N times larger than that of a single element. However, this can only be completely correct under the assumptions of no ohmic or dielectric losses and when similar current distribution over all elements occurs. Modification of the above equations can be used to express the total scattered field from more complex element geometries.

5.3 Free space measurements of self-resonant tag

5.3.1 Measurement setup

Manufactured self-resonant tags have been tested experimentally in free space by measuring their forward transmission coefficient (S_{21}) in a similar way as to that described in [98] and [136], using a measurement setup comprising of two Rohde & Schwarz HF906 double-ridged waveguide horn antennas and a two port Agilent 8720D vector network analyser. Fig. 5.2 illustrates the measurement setup. The two antennas are spaced 600 mm apart, and measurement samples are placed on a large polystyrene block (600 mm x 600 mm) which is 200 mm thick and has RF transmission properties close to air (i.e. $\varepsilon_r \approx 1.02$). A block of absorptive material was placed under the measurement table in order to avoid reflecting signals off the floor which might affect the result.

The measurements were carried out for a frequency range of 0.5 - 18 GHz with 1601 discrete sample points. (Δf=10.93 MHz). An intermediate frequency bandwidth of 1 kHz was used. Additionally, a time gate having a span of 1 ns was used to eliminate any multipath or scattered signals. For clarity, results are presented as the average of four frequency sweeps and a 0.5% smoothing factor has been applied.

In all cases, a response and isolation calibration was performed, with the isolation being measured using an aluminium sheet having the same dimensions as the testbed (600 mm x 600 mm). Two different techniques were evaluated to measure the efficiency of the response (thru) calibration. Initially, this was achieved using just the empty testbed, and then using a metal sheet with an aperture cut from its centre (as shown in Fig. 5.2). The aperture measured 240 mm x 240 mm and provides a restricted propagation path for the forward transmission. This technique is known to improve measurement sensitivity in certain circumstances when measuring electrically small objects.

5.3.2 Uniform cross

The measured forward transmission (S_{21}) responses for the single-element uniform cross tags shown in section 3.4 are presented in Fig. 5.3 It can be seen that the main resonance shifts down in frequency by 200 to 300 MHz with each degradation stage, which is basically characterized by a change in the electrical length of the resonator. However, the resonance amplitude is around 0.5 dB only, as expected considering the small aperture of the tag compared to the size of the waveguide horn antennas used in the measurements.

As explained in section 5.2, the resonance characteristics of the tag can be improved by using multiple elements arranged in an array form to make the aperture of the tag electrically larger

Fig. 5.2 Experimental forward transmission measurement system used for characterizing the self-resonant tags.

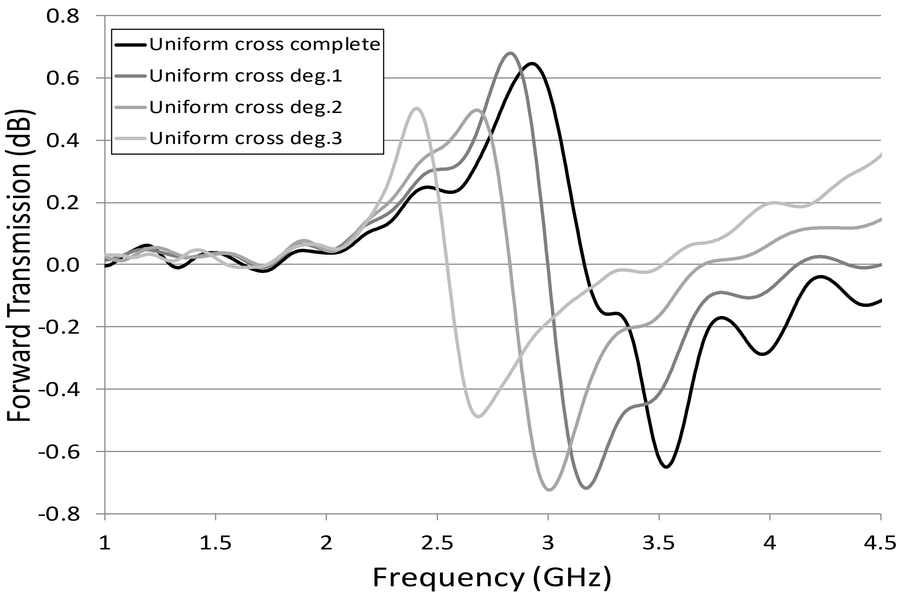

Fig. 5.3 Measured S_{21} results for the uniform cross tag at different degradation stages [substrate thickness is 0.8 mm FR4, restricted calibration has been used].

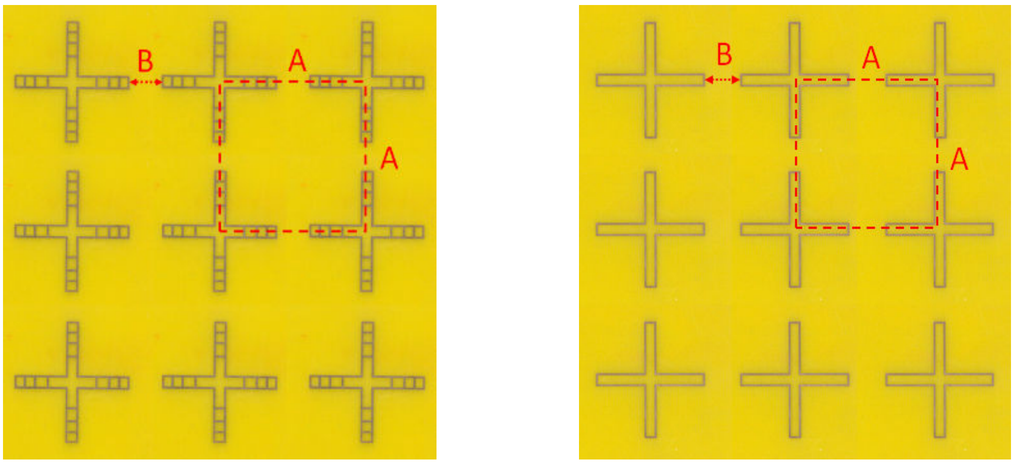

(a) (b)

Fig. 5.4 Prototypes of 3x3 uniform cross array on 104x104 mm^2 FR4 substrate for (a) complete array (b) fully degraded array, where A = 34 mm and B = 6.5 mm.

in terms of wavelengths. Nevertheless, this comes at the expense of increasing the physical size of the tag. Ultimately, the aim of this work is to improve the detectability of self-resonant tags through enhancing their resonance characteristics, hence allowing the tags to operate in mediums with higher levels of losses such as the human body.

In this work, a 3x3 array of the uniform cross resonator was designed in order to provide better resonance characteristics and hence improved detectability. Two arrays were manufactured, the first one represents the complete tag, the second one representing the fully degraded case, as shown in Fig. 5.4a. and Fig. 5.4b respectively.

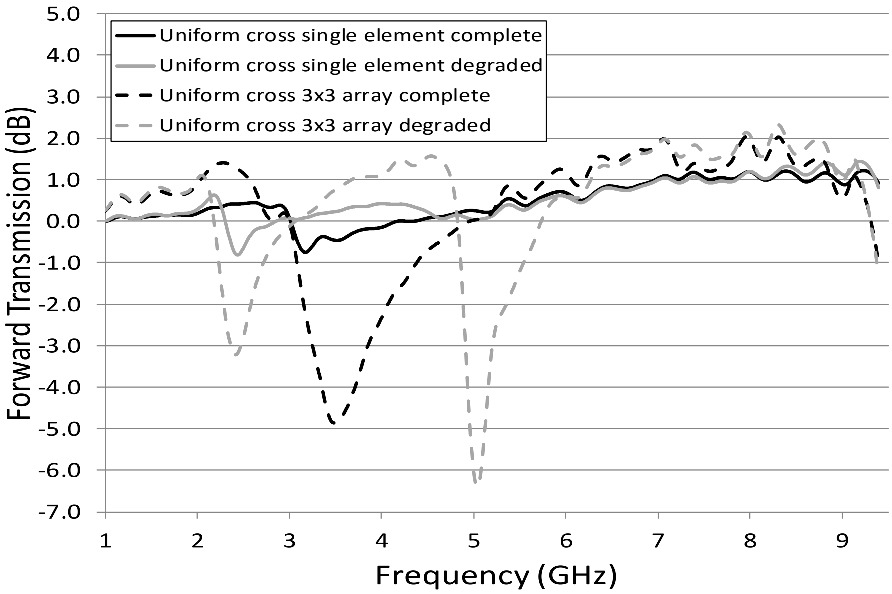

Fig. 5.5 A comparison between measured S_{21} results for the 3x3 uniform cross array tag versus single-element tag for both complete and fully degraded states [open calibration has been used].

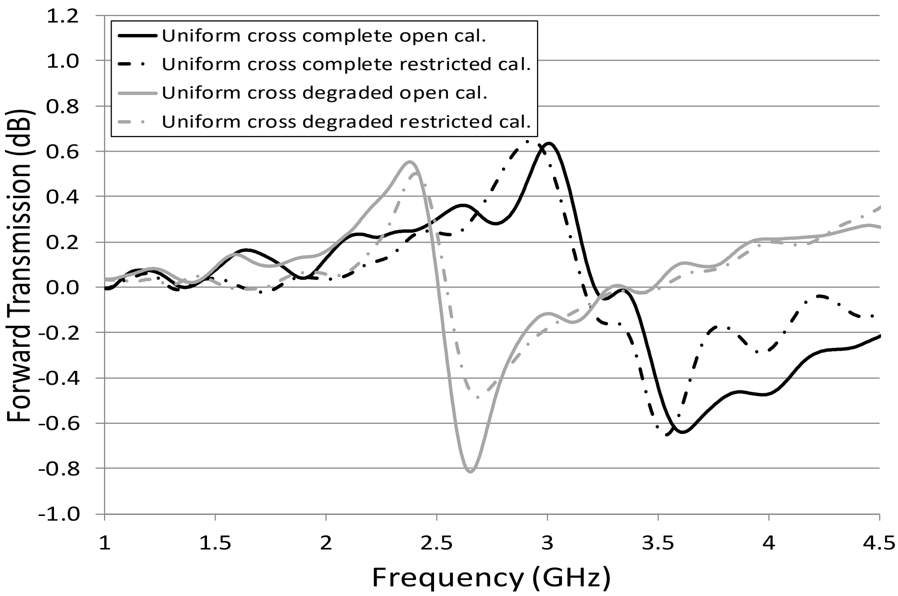

Fig. 5.6 Measured S_{21} results for the uniform cross tag both complete and fully degraded using two different calibration methods [substrate thickness is 0.8 mm FR4].

A 3x3 array of the uniform cross was tested and compared to a single element tag as illustrated in Fig. 5.5 Clearly, the amplitude of resonance has improved by using arrays of elements. Interestingly, the fully degraded array has shown a second resonance in the fundamental resonance zone, and this resembles the resonance behaviour of a periodic surface counterpart.

The S_{21} measurements for the single element tag and array tag were repeated but this time using the restricted calibration method explained earlier, with the aim of finding out the most

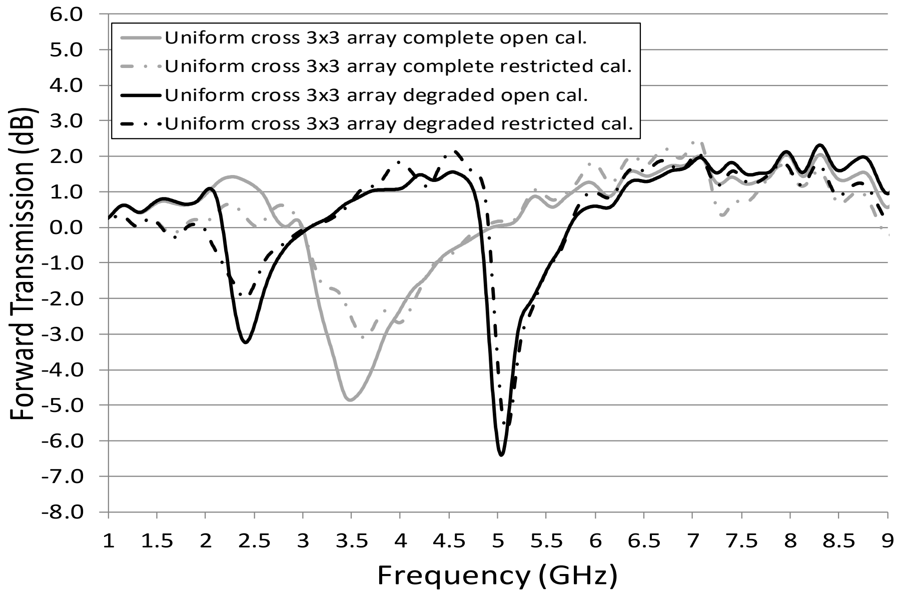

Fig. 5.7 Measured S_{21} results for the uniform cross 3x3 array for both complete and fully degraded tags using two different calibration methods [substrate thickness is 1.6 mm FR4].

suitable calibration settings required to obtain the optimum forward transmission response of small aperture tags. Fig. 5.6 illustrates the S_{21} response of a uniform cross single-element tag using open versus restricted calibration settings. Both settings have comparable values with a slightly better response with the open calibration. In the same way, the two calibration settings were used to test the response of uniform cross array tags and similar findings are seen in Fig. 5.7.

5.3.3 Gammadion cross

In the last section, the response of uniform cross tag has been discussed. It has been shown that by using array of elements the resonance characteristics can be improved. However, this improvements comes at the expense of increasing the tag's size. In this section, miniaturisation of tag's resonating element is investigated.

By folding the four arms of the uniform cross by 90° a significant size reduction in the tag's aperture is attained. Through simple maths it can be proven that the proposed Gammadion cross has a physical aperture 45% smaller than that of a uniform cross. The Gammadion cross has the same number of resonant states as those of the uniform cross. The Gammadion cross design and dimensions are shown in Fig. 5.8.

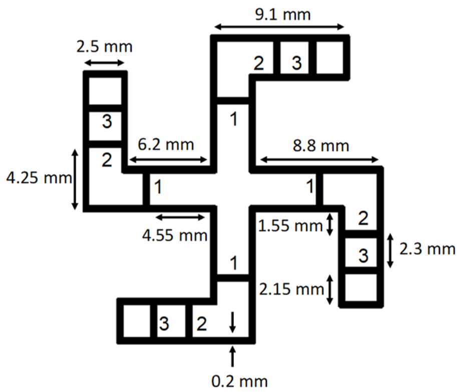

Fig. 5.8 Dimensions Gammadion cross resonator.

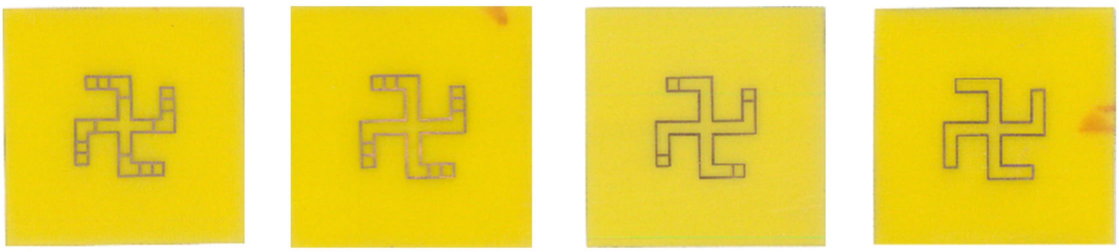

Fig. 5.9 Prototypes of Gammadion cross tag at four different degradation stages, all on 50x50 mm^2 FR4 substrate.

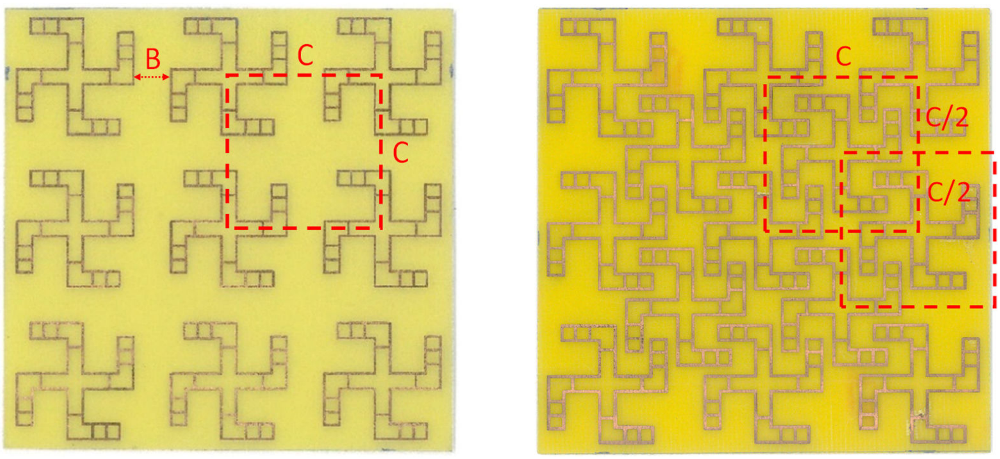

(*a*) (*b*)

Fig. 5.10 Prototypes of Gammadion cross arrays on 80x80 mm^2 FR4 substrate for (a) 3x3 Gammadion cross array (b) 13 elements (interlaced) Gammadion cross array, where C = 27.5 mm and B = 6.5 mm.

Four states of Gammadion cross tags were manufactured from the single sided copper clad flame retardant-4 (FR4) substrate as shown in Fig. 5.9. Additionally, a 3x3 array of Gammadion cross elements was designed. This array has 40% smaller physical aperture than the uniform cross array shown in Fig. 5.4, given that both arrays have the same spacing between the edges of their elements. Four extra elements were interlaced in the gaps of the 3x3 Gammadion cross array with the aim of providing a greater response without increasing the tag's physical

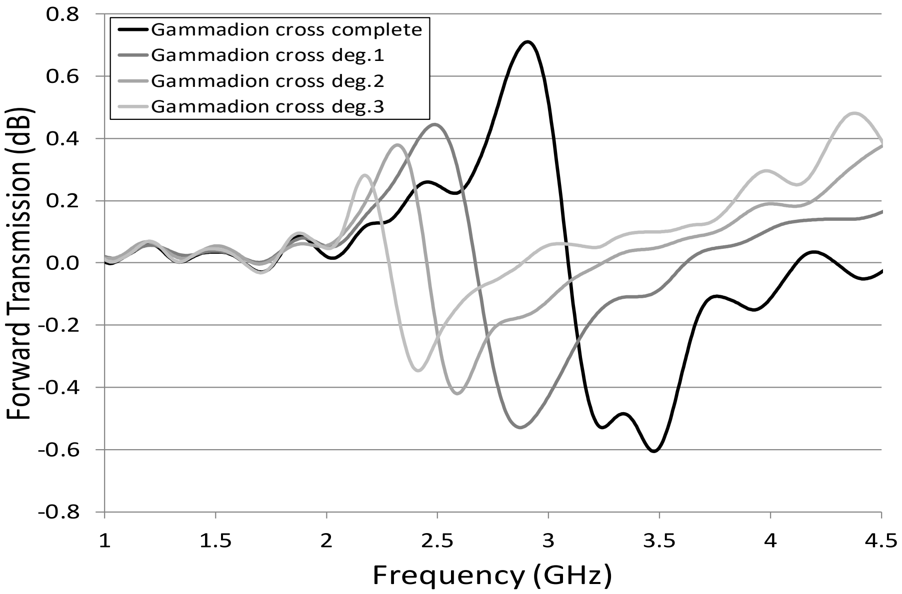

Fig. 5.11 Measured S_{21} results for the Gammadion cross tag at different degradation stages [substrate thickness is 0.8 mm FR4, restricted calibration has been used].

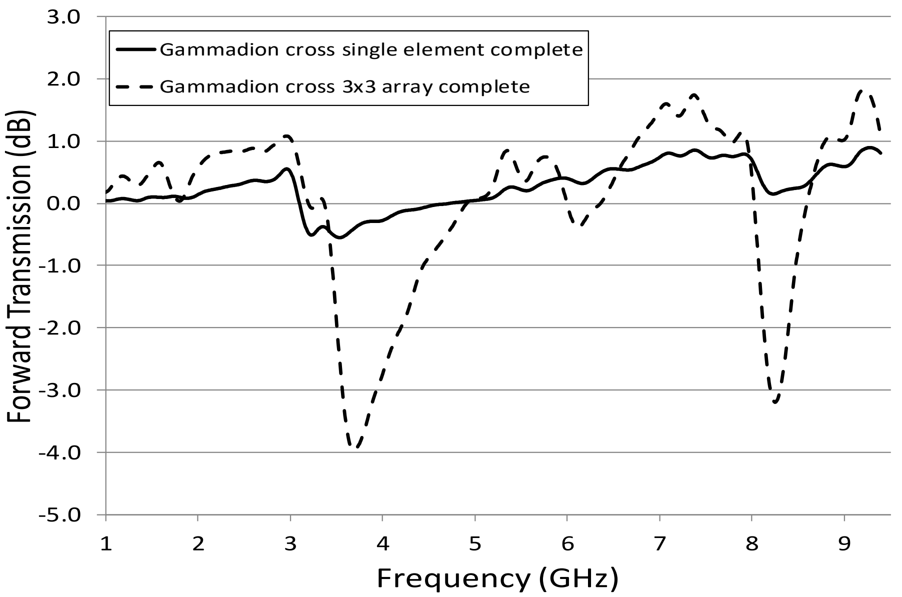

Fig. 5.12 A comparison between measured S_{21} results for the 3x3 Gammadion cross array tag versus single element tag [substrate thickness is 0.8 mm FR4, open calibration has been used].

aperture. Fig. 5.10a and Fig. 5.10b illustrate the fabricated 3x3 Gammadion cross array and the 13 elements interlaced array, respectively. The forward transmission (S_{21}) response of the single-element Gammadion cross tag at different degradation stages are depicted in Fig. 5.11. It can be noticed that the frequency shift between the complete tag and first degradation stage is bigger than the shift of the corresponding uniform cross states, and that is basically attributed to the longer electrical loop resulted from bending the arms by 90˚. Additionally, the resonance amplitude is smaller than that of the uniform cross presented in Fig. 5.3.

The results of the Gammadion cross tag with 3x3 elements shown in Fig. 5.10a were compared to single-element tag as presented in Fig. 5.12. The array tag exhibits a much stronger resonance than the single element tag with a slight increase in resonant frequency. Moreover, it shows a second resonance at 8 GHz. An advantage of the Gammadion cross over the uniform cross resonator is that, in addition to being physically smaller, more elements can be interlaced in the gaps of the 2-D array. These added elements aim to provide a stronger resonance without increasing the tag's physical aperture. Fig. 5.13 presents measured S_{21} responses for the Gammadion cross 3x3 array and the Gammadion cross interlaced array (see Fig. 5.10a and 5.10b). The advantage of the interlaced array over the 3x3 array is primarily demonstrated by a stronger higher order resonance at 14 GHz. The reason behind this strong higher order resonance in the interlaced array cannot be easily interpreted due to the complexity of the array geometries, however it can be attributed to the higher mutual coupling resulting from entwining array elements. Finally, restricted calibration settings for the VNA were used again to test the S_{21} response of Gammadion cross resonator. Fig. 5.14 and Fig. 5.15 present a comparison between open versus restricted calibration settings for Gammadion single-element tag and Gammadion 3x3 array tag, respectively. Again we can see similar figures for both calibration settings with a slight advantage with the open calibration.

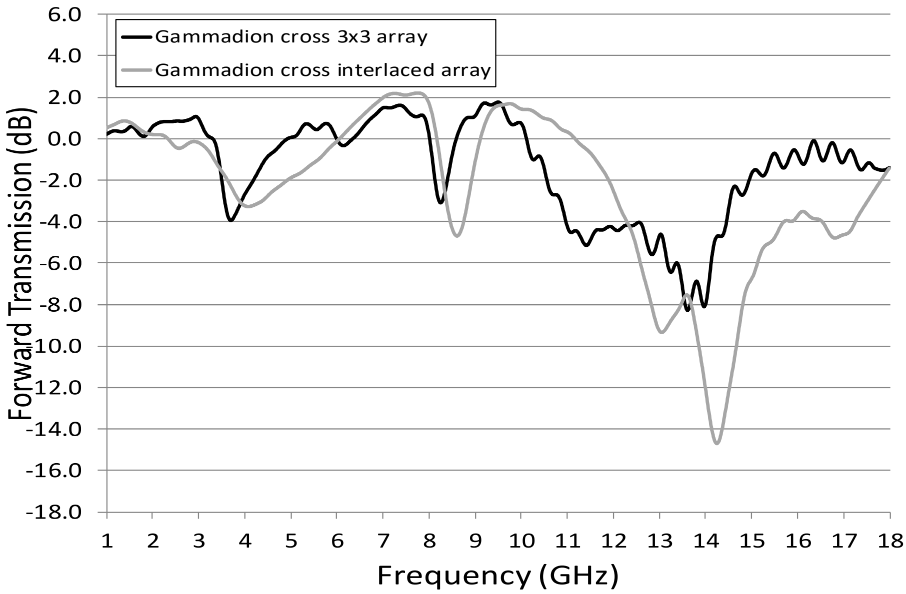

Fig. 5.13 A comparison between measured S_{21} results for the 3x3 Gammadion cross array versus Gammadion 13 elements interlaced array [substrate thickness is 0.8 mm FR4, open calibration has been used].

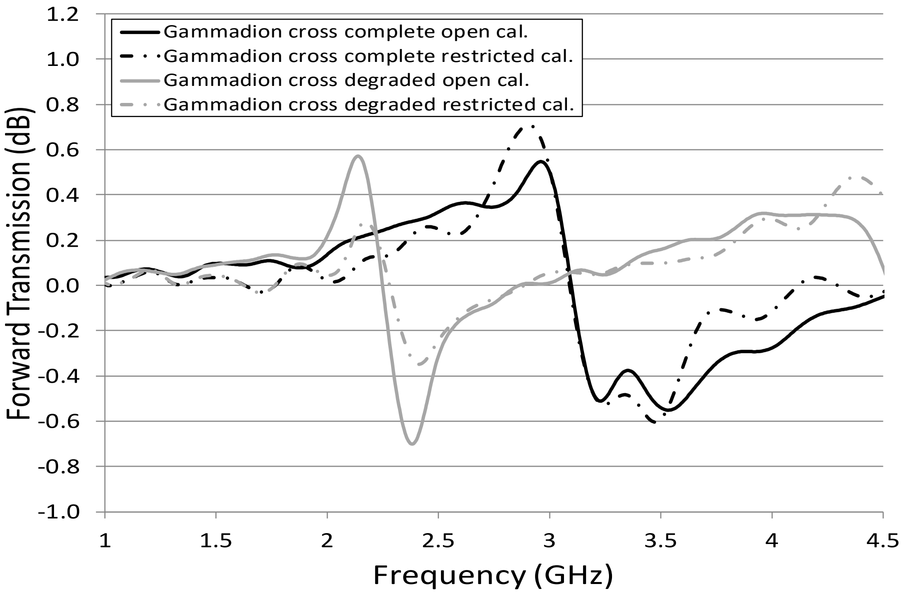

Fig. 5.14 Measured S_{21} results for the Gammadion cross single element tag both complete and fully degraded using two different VNA calibration methods [substrate thickness is 0.8 mm FR4].

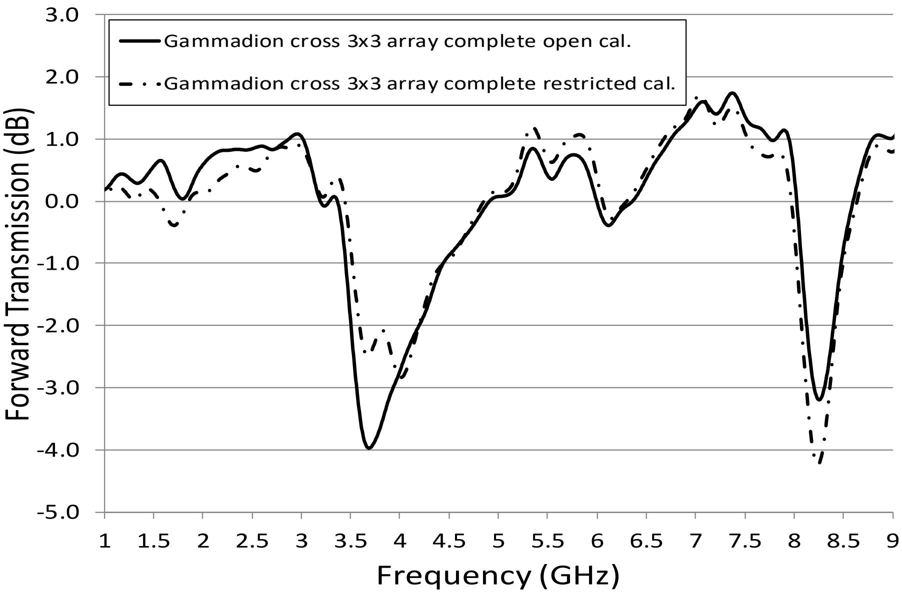

Fig. 5.15 Measured S_{21} results for the Gammadion cross 3x3 array for both complete and fully degraded tags using two different VNA calibration methods [substrate thickness is 0.8 mm FR4].

5.3.4 Impact of substrate thickness

The effects of varying the substrate thickness on the resonance characteristics of self-resonant tag have also been studied. Having a thicker substrate imposes more dielectric losses on the tag, and this can be analogous to the effect of operating the tag in mediums characterized by higher losses. Fig. 5.16 shows a comparison between the responses of uniform cross tag on 0.8 mm FR4 and 1.6 mm FR4 for both the complete cross and the fully degraded one. Unsurprisingly, the fundamental resonance shifts downward in frequency by about 0.5 GHz in both cases. Doubling the substrate thickness and the changes it causes to the measured S_{21} response of the Gammadion cross tag have also been examined. Fig. 5.17. presents a comparison between measured S_{21} results of complete and degraded Gammadion cross tags on a 0.8 mm substrate versus 1.6 mm substrate. The responses were shifted downward in frequency by about 250 MHz in both cases. The effect of increasing the substrate thickness on the interlaced Gammadion cross array is illustrated in Fig. 5.18. It can be observed that the 1.6 mm substrate has shifted all the resonances down in frequency. Moreover, a slight damping in the amplitude has been noticed.

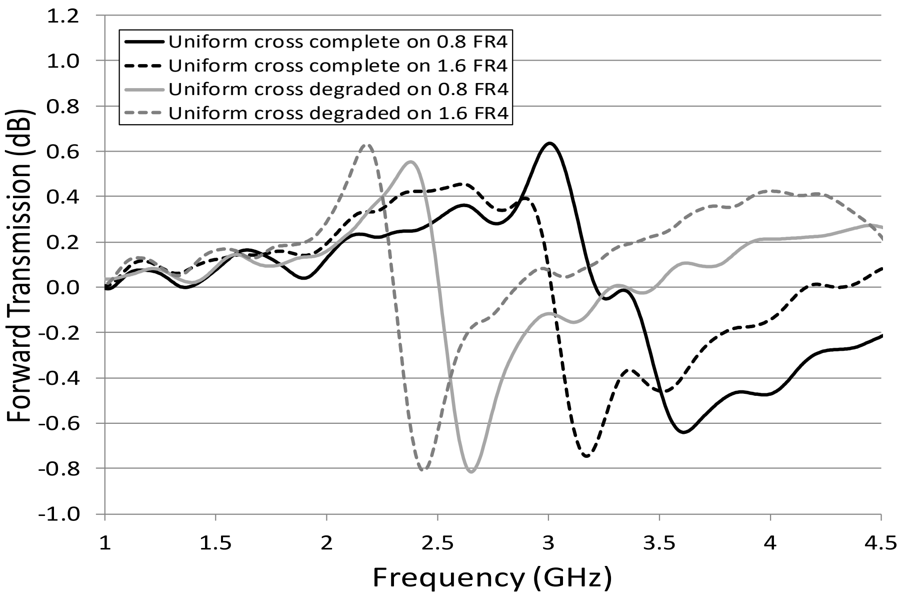

Fig. 5.16 A comparison between measured S_{21} results for the uniform cross tag on 0.8mm and 1.6mm thick FR4 substrate [open calibration has been used].

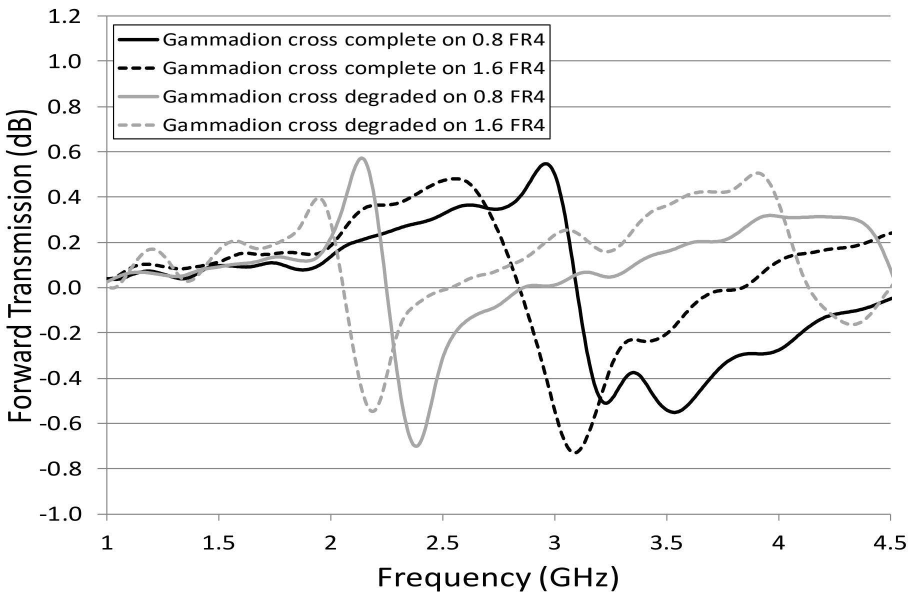

Fig. 5.17 A comparison between measured S_{21} results for the Gammadion cross tag on 0.8mm and 1.6mm thick FR4 substrate [open calibration has been used].

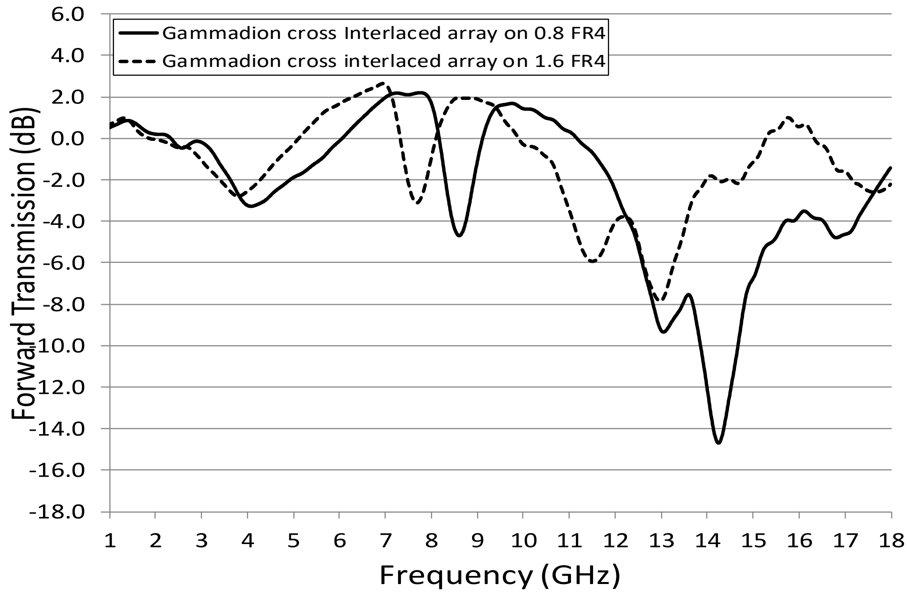

Fig. 5.18 comparison between measured S_{21} results for the Gammadion cross interlaced array on 0.8mm and 1.6mm thick FR4 substrate [open calibration has been used].

5.3.5 Comparison and evaluation

The results presented earlier have revealed quite similar responses for the uniform and Gammadion cross resonators. In applications where the size of the resonator is a critical factor, the Gammadion cross would be a favourable option. It is not only a smaller resonator but it can also accommodate more elements on the same sized platform through interlacing, as demonstrated in Fig. 5.13 where a stronger higher order resonance has been observed when 4 extra elements were added to the original 3x3 array. Fig. 5.19 shows a comparison for the response of the single element uniform cross versus Gammadion cross. Clearly, the Gammadion cross resonates at a slightly lower frequency, and this is resulting from the fact that the Gammadion cross has longer arm lengths. Fig. 5.20 compares the measured S_{21} response between uniform cross array and Gammadion cross array. It shows that uniform cross array has a larger amplitude at the main resonance by about 2 dB. However, the Gammadion cross array exhibits a second resonance at 7.5 GHz.

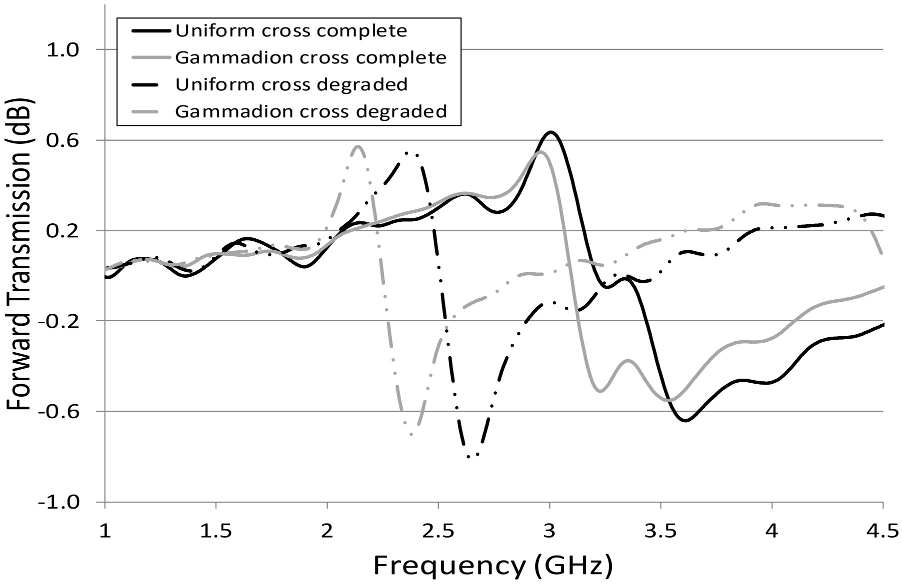

Fig. 5.19 Measured S_{21} results for single element uniform cross versus Gammadion cross [substrate thickness is 0.8 mm FR4, open calibration has been used].

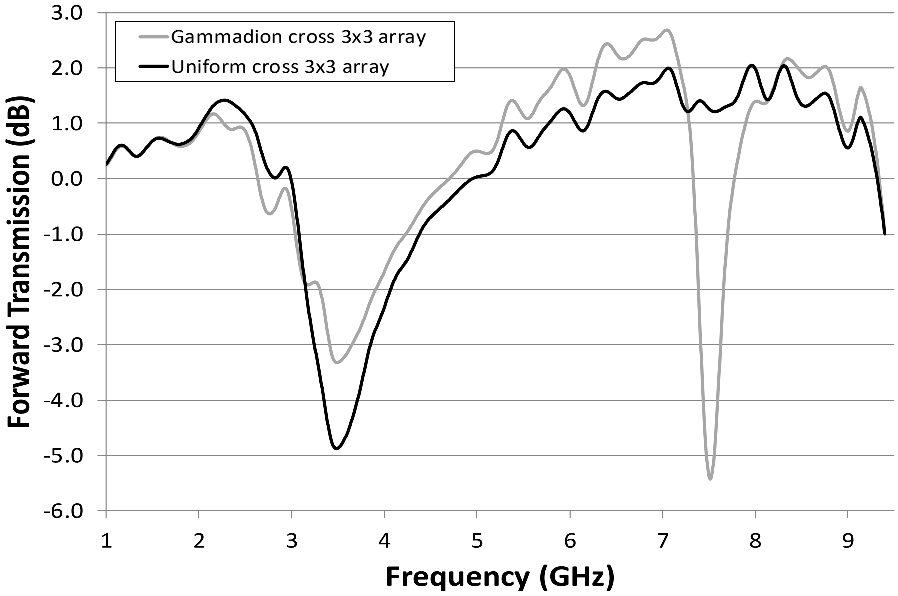

Fig. 5.20 Measured S_{21} results for 3x3 uniform cross array versus 3x3 Gammadion cross array [substrate thickness is 1.6 mm FR4, open calibration has been used].

5.4 Summary

This chapter has presented an investigation into improving the detectability of self-resonant tags. Firstly, basic theoretical analysis for the differences between single-element SRS, finite array SRS, and infinite array SRS has been provided. The forward transmission response of uniform and Gammadion cross resonators have been studied. Gammadion crosses have shown comparable responses to the uniform cross despite having a physical aperture 45% smaller. The detectability of the tags has significantly improved by using arrays of elements and by using the Gammadion cross it has been possible to accommodate more elements on the same sized platform through interlacing giving a better higher order resonance compared to the normal 3x3 array. The effect of doubling the tag's substrate thickness has shown to decrease the resonance frequency in both single element and array tag, also some amplitude damping has been observed with the array tag when using a 1.6 mm substrate, however this effect has not been clear in the single-element tag. Measurement settings and VNA calibration and their impact on the measured results have been studied. It has been shown that open calibration has given slightly better responses for both single element and array tags. It can be noticed that in all measured forward transmission coefficient (S_{21}) results shown in this chapter, some S_{21} values above zero dB have been observed and this behaviour is not expected in passive tags. These nonlinearities can be attributed to edge effects as all the tested samples have physical apertures smaller than the size of the waveguide horn antennas used in the experiment. In order to reduce this nonlinear behaviour, an illuminating antenna with a narrow or focused beam needs to be considered when designing an RFID receiver for these types of tags.

Although the concept of using array of elements have led to better resonance characteristics, it comes at the expense of increasing the physical size of the tag which is non desirable for an implantable medical device. Next chapter will discuss techniques for array miniaturisations and analyse their response on dielectric phantom.

6. CHAPTER SIX

Miniaturisation techniques: towards implantable self-resonant tag

This chapter investigates self-resonant tag miniaturization using capacitive loading. In the last chapter, it has been shown that by using multiple elements arranged in an array, it is possible to improve the response of the tag. However, this increases the size of the implantable tag. finite array miniaturization without affecting its resonance position is examined in this chapter using experimental measurements.

6.1 Self-resonant tag miniaturization

The size of implantable self-resonant tag is a critical factor in determining its suitability for implantation inside the human body. Self-resonant tags need to be as small as possible in order to prevent any additional disruption to normal biological activities. Moreover, from the patient's perspective, smaller tag is less likely to cause a discomfort than a bigger one. Hence, it is important to investigate the techniques that can be implemented to miniaturise self-resonant tags and to assess their suitability for in-body application and how they impact the response of the tag.

The size of a self-resonant tag is primarily governed by the size of the resonating element. Thus, tag miniaturization can be made by reducing the dimensions of the resonator. However, this change normally pushes the resonance position higher in frequency – potentially causing the tag to work outside the specified operational bandwidth of the reader. Another undesired effect of this phenomenon is that it leads to higher dielectric losses of substrates and surrounding medium in the case when the self-resonant tag is used as an implant. This is due to the material properties being frequency dependent, and for a given material thickness, the electrical length of the material increases as the wavelength decreases. The relationship between frequency and dielectric attenuation has been discussed in chapter four and they are related using (4.7). In this section, we discuss the techniques that can be implemented for tag miniaturization whilst maintaining the same resonance frequency.

6.1.1 Capacitive loading using lumped components

It has been shown in [137] that by using a lumped capacitor between adjacent elements of an AMC surface it is possible to push the resonance position down in frequency, and the shift in frequency is proportional to the value of the capacitor. Thus, it enables miniaturising the surface unit cell while maintaining the same resonance position. A 3x3 uniform cross array has been simulated with six lumped capacitors between array elements as shown in Fig. 6.1a, the lumped capacitors have been used to provide the additional capacitance required for the array to resonate at a lower frequency window. It has been shown that by increasing the value of the capacitor the resonance has gradually shifted down in frequency, as shown on the AMC

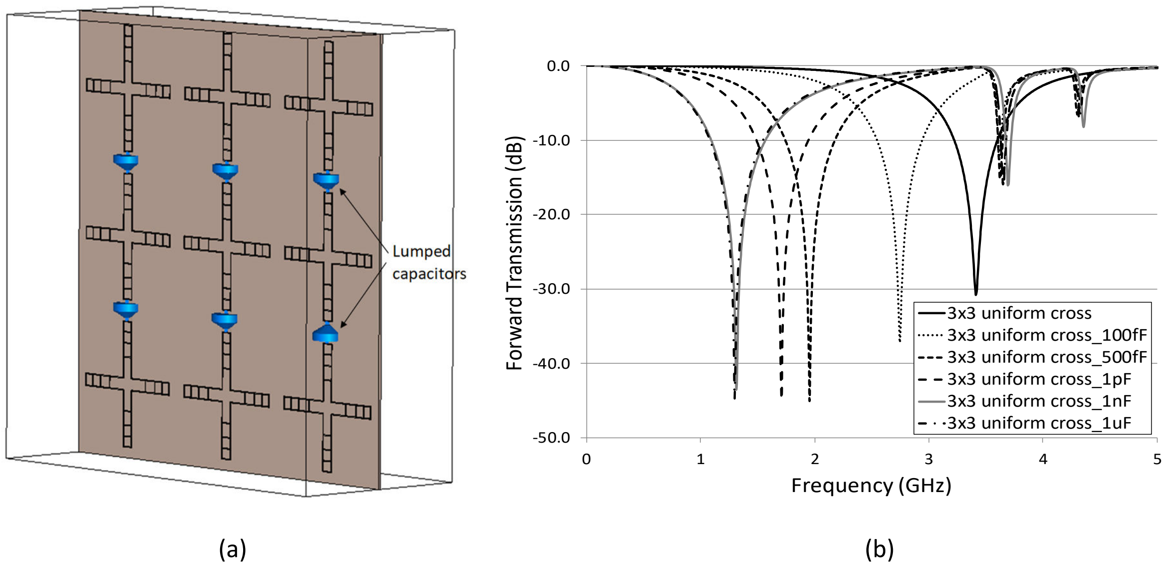

Fig. 6.1 (a) Simulated 3x3 uniform cross array with loaded lumped capacitors (b) Forward transmission coefficient of a simulated 3x3 uniform cross array loaded with lumped capacitors of different values.

surface in [137]. It has been found that the shift in resonance frequency reaches a limit, where increasing the capacitance beyond a certain value will lead to no further shift in the resonance frequency. In the case of the 3x3 uniform cross array, the resonance frequency is at 1.29 GHz when the lumped capacitance value is around 1 nF, increasing capacitance value has led to no change in the frequency response of the array as shown in Fig. 6.1b.

6.1.2 Capacitive loading using parallel plates

In the last section, it has been shown that lumped capacitors loading on self-resonant tag can can be used for tag miniaturisation. However, the use of lumped components in practice introduces some ohmic resistance. Moreover, lumped capacitors are not preferred in an implantable self-resonant tag as they raise concerns in relation to the biocompatibility properties of the implant. Thus, the six capacitors have been replaced with two long pairs of parallel plates between the elements as shown in Fig. 6.2a. The introduction of parallel plates to the uniform cross array have shown similar effect to the lumped capacitors, the capacitance of parallel plates follows the static capacitance equation presented in (3.42), and the shift in resonance frequency has been shown to be inversely proportional to the distance between the plates. Moreover, a substrate with higher dielectric constant can lead to higher capacitance and hence a bigger shift in the resonance frequency. The impact of these parallel plates on the array response is shown in Fig. 6.2b. A frequency shift of about 1.6 GHz in the main resonance can be observed, and by reducing the distance between the plates additional shift in resonance can be obtained.

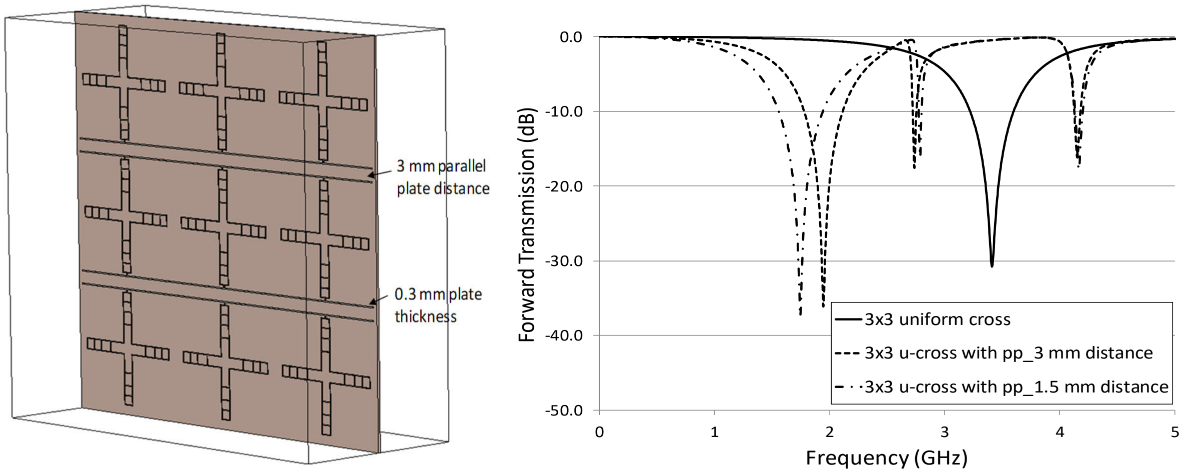

(a) (b)

Fig. 6.2 (a) Simulated 3x3 uniform cross array with parallel plates (b) Forward transmission coefficient of a simulated 3x3 uniform cross array loaded with parallel plates.

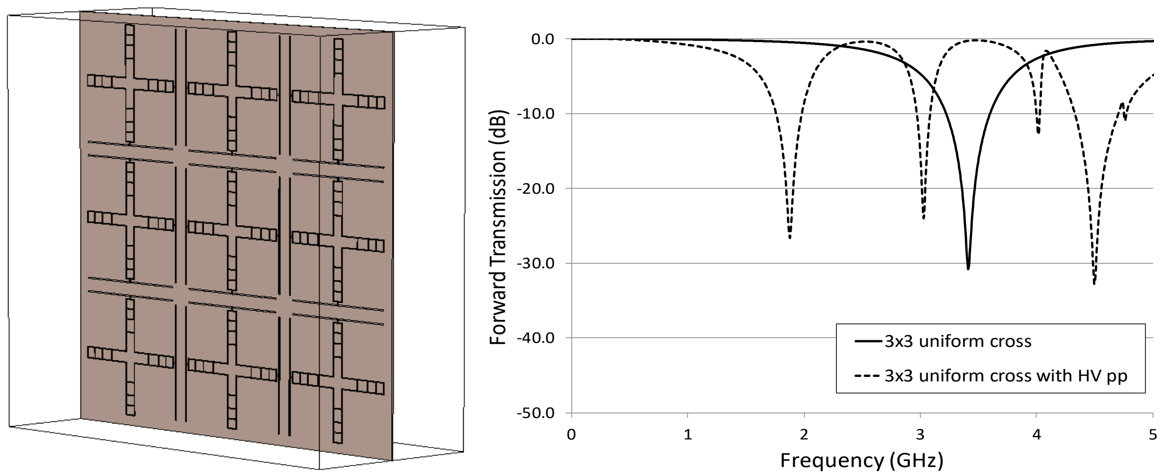

(a) (b)

Fig. 6.3 (a) Simulated 3x3 uniform cross array with horizontal and vertical parallel plates (b) Forward transmission coefficient of a simulated 3x3 uniform cross array loaded with horizontal and vertical parallel plates.

For the both lumped capacitive loading and parallel plate loading examples presented earlier, the electrical field vector of incident signal has to be perpendicular to the capacitor in order to cause a frequency shift. In order to account for both polarisation planes, horizontal and vertical parallel plates can be added between array elements as illustrated in Fig. 6.3a. A frequency shift of the main resonance mode can be observed alongside two strong harmonics as shown in Fig. 6.3b.

6.1.3 Capacitive loading using interdigital capacitor

It has been shown in the last section that at high microwave frequencies parallel conducting strips in between array elements can have a similar effect to lumped capacitors. One technique to increase the capacitance of parallel plates is add a number of intertwined conducing fingers on each side of the parallel plates. The additional capacitance is basically generated in the narrow gaps between the fingers. The value of produced capacitance depends mainly on the length of the meandered path that is created between the parallel plates. It is of essential importance to keep the size of the interdigital capacitor very small compared to the resonance wavelength of the original array in order to work as a capacitor. Moreover, the length of the fingers needs to be kept as short as possible to avoid creating undesired inductance. Fig. 6.4 below shows a 3x3 uniform cross array with horizontal parallel plates and interdigitated fingers.

An approximation equation for the value of capacitance generated from an interdigital capacitor (IDC) has been proposed in [138] as follows:

$$C_{IDC} = \frac{\varepsilon_{eff} * 10^{-3}(N-1)D}{18\pi} \frac{K(k)}{K`(k)} \quad (pF) \tag{6.1}$$

where ε_{eff} represents the effective permittivity of the substrate, N is the number of fingers, D is the finger length in microns, and *K(k)* is the elliptic integral of the first kind and its complement *K`(k)* and can be given using:

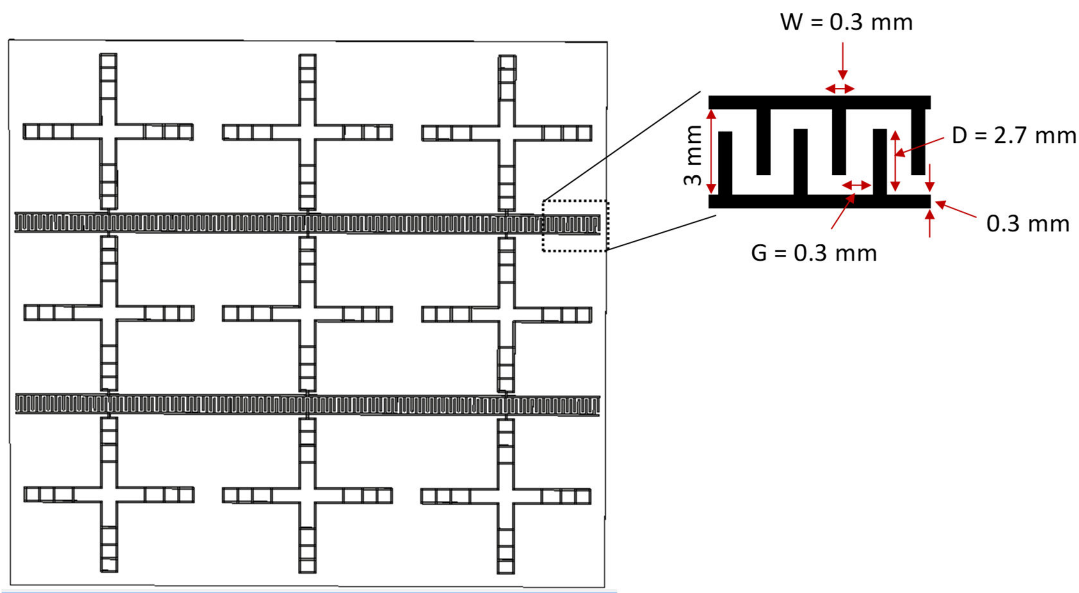

Fig. 6.4 3x3 uniform cross array with horizontal parallel plates and interdigitated fingers.

$$\frac{K(k)}{K`(k)} = \begin{cases} \frac{1}{\pi} \ln\left[2\frac{1+\sqrt{k}}{1-\sqrt{k}}\right] & 0.707 \leq k \leq 1 \\ \frac{\pi}{\ln\left[2\frac{1+\sqrt{k`}}{1-\sqrt{k`}}\right]} & 0 \leq k \leq 0.707 \end{cases} \tag{6.2}$$

And

$$k = tan^2\left(\frac{a\pi}{4b}\right), a = \frac{W}{2}, b = \frac{W+G}{2}, k` = \sqrt{1-k^2} \tag{6.3}$$

W and *G* are the width of the finger and the spacing between adjacent fingers, respectively. On the other hand, the effective permittivity is dependent on the substrate thickness with an upper limit approaching $\frac{\varepsilon_r+1}{2}$ as substrate thickness approaches infinity for SRS on a dielectric layer.

The uniform cross array with horizontal parallel plates and interdigitated fingers shown in Fig. 6.4 has 163 digits and printed on 0.6 mm FR4 substrate. Assuming the FR4 substrate has relative permittivity of 4.4 in the frequency range of interest, the upper limit of effective permittivity would be 2.7. Hence, using the IDC characterization expressions shown earlier the generated capacitance is 10.46 pF. A comparison between the results of horizontal IDC versus equivalent lumped capacitor calculated using (6.1) - (6.3) is shown in Fig. 6.5. The value of each of the six lumped capacitors is 3.48 pF. It can be seen from the graph that characterization of IDC using the aforementioned equations can give approximate values, a frequency shift of about 165 MHz between the two resonances can be noticed.

From (6.1) it has been shown that the produced capacitance of IDC is proportional to the number of digits. However, it has been found that, just as with lumped capacitors, the shift in frequency reaches a limit where increasing the number of digits lead to no further shift in the main resonance mode. Interestingly, the upper limit of the resonance frequency shift was at 1.29 GHz with 163 digits, increasing the number of digits to 198 has led to no change in the main resonance mode position, as has been the case with lumped capacitors.

.

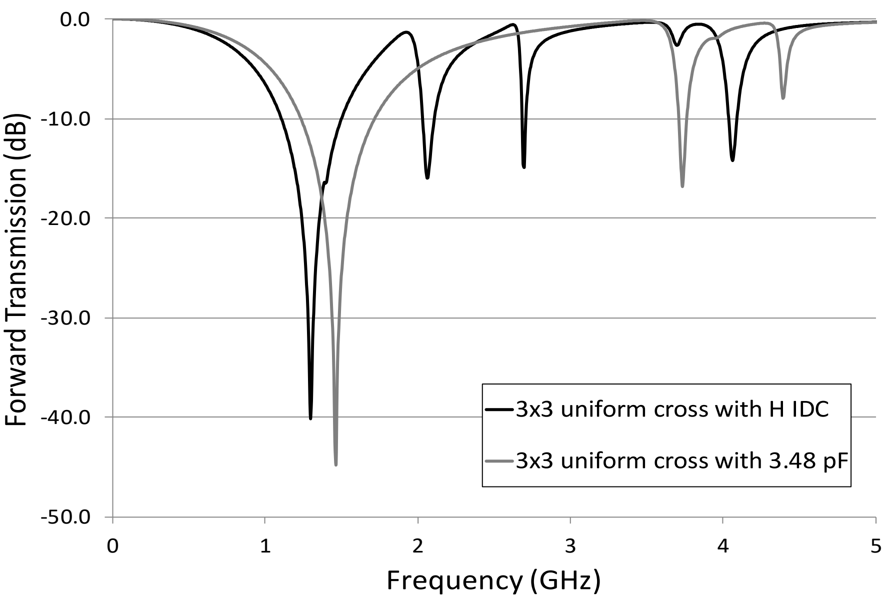

Fig. 6.5 Forward transmission coefficient of 3x3 uniform cross array with horizontal IDC versus equivalent lumped capacitor with six capacitors each with a value of 3.48 pF.

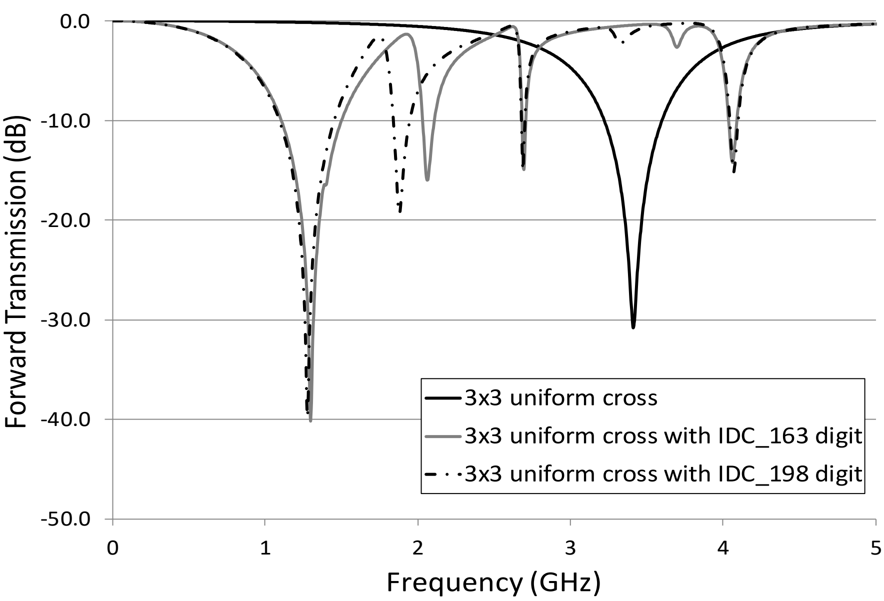

Fig. 6.6 Forward transmission coefficient of 3x3 uniform cross array with horizontal IDC.

We have seen with capacitive loading that the electrical size of the surface in relation to the resonance frequency has significantly decreased, as the electrical size of the unloaded surface is 1.18 λ while it is 0.64 λ and 0.43 λ for the surface loaded with horizontal parallel plates and interdigital capacitor, respectively.

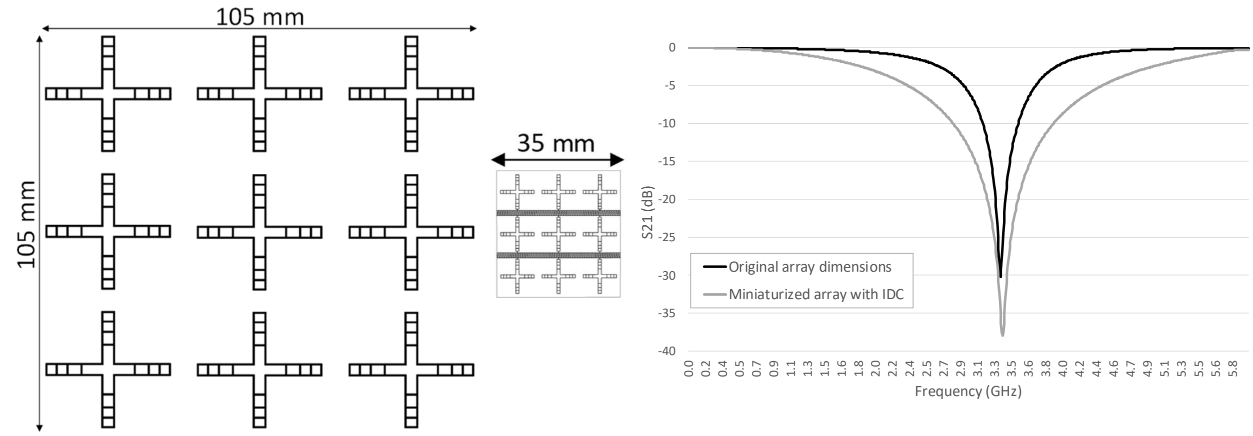

(a) (b) (c)

Fig. 6.7 (3) 3x3 uniform cross array with dimensions of 105x105 mm^2 (b) miniaturised 3x3 uniform cross array with dimensions of 35x35 mm^2 (c) response comparison of original array versus miniaturised array.

These results have demonstrated that with IDC it is possible to reduce the size of uniform cross resonator by 3-4 times whilst maintaining the same resonance behaviour. Fig. 6.7a and Fig. 6.7b show the original size of the uniform cross array versus a miniaturized array using interdigital capacitance loading. It has been possible to reduce the size of the tag by three times while maintaining the same resonance position. However, the miniaturized surface has shown a noticeably wider bandwidth as depicted in Fig. 6.7c.

6.1.4 Experimental verification of uniform cross tag with capacitive loading

The tag miniaturisation techniques presented earlier in this chapter has been validated experimentally using a similar procedure to that explained in chapter 5, except for the distance between the two horn antennas as they have been pushed closer to each other (170 mm apart) and the polystyrene block in the middle has been removed. It has been found that when the antennas are closer to each other, it would be easier to follow and understand the behaviour of the surfaces under test (noting that for the intended application of this project the response of the tags does not necessarily have to be measured in the far field region as with FSS surfaces as an example). All the tags tested in this section have been fabricated on 0.6 mm FR4 substrate.

Firstly, the response of unloaded 3x3 uniform cross array has been compared to loaded array with 1 nF lumped capacitors, the tested arrays are shown in Fig. 6.8. The introduction of the lumped capacitors has pushed the resonance frequency downward by 2.5 GHz. However, around 7 dB loss in amplitude can be observed as in Fig. 6.9. Similarly, a 3x3 uniform cross array with horizontal parallel plates has been tested, and a frequency shift of 1.69 GHz has been obtained in addition to a 7 dB reduction in amplitude. Additionally, the response of a uniform cross array with horizontal interdigital capacitor comprises of 163 digits has been measured. The introduction of interdigitated fingers have caused an extra shift in frequency.

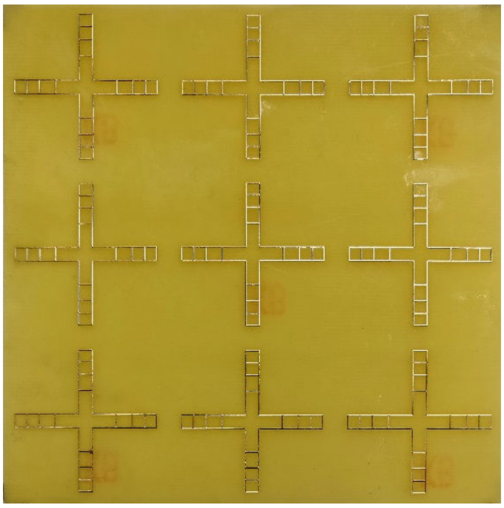

(a)

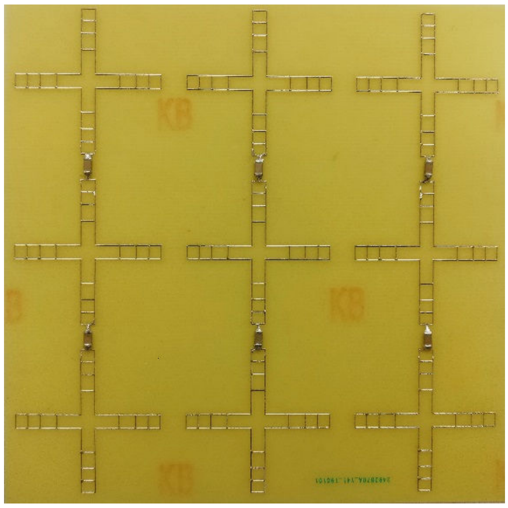

(b)

Fig. 6.8 (a) 3x3 uniform cross array with dimensions of 100x100 mm^2 (b) 3x3 uniform cross array loaded with six lumped capacitors each with value of 1 nF.

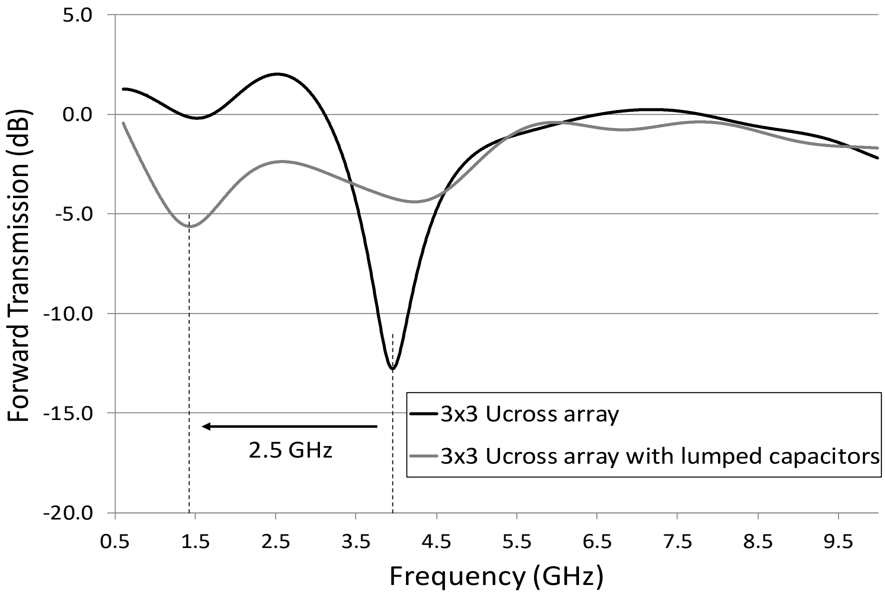

Fig. 6.9 A comparison between measured forward transmission coefficient of unloaded 3x3 uniform cross array versus loaded array with 1 nF lumped capacitor.

The arrays with horizontal parallel plates and horizontal IDC are depicted in Fig. 6.10a and 6.10b, respectively. While their measured response is shown in Fig. 6.11.

Although the presented arrays with loaded horizontal parallel plates and IDC have provided the required capacitance to push the resonance down in frequency (and thus the possibility of array miniaturization), they only work when the direction of electric field is perpendicular

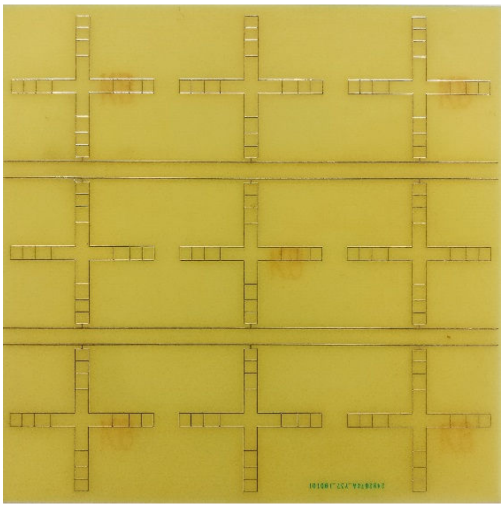

(a)

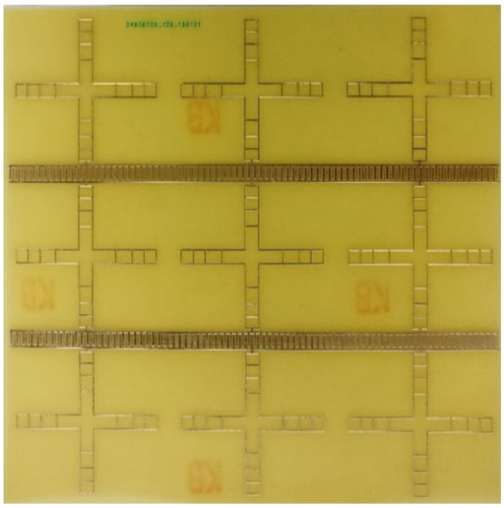

(b)

Fig. 6.10 (a) 3x3 uniform cross array with horizontal parallel plate (b) 3x3 uniform cross array loaded with horizontal interdigital capacitor.

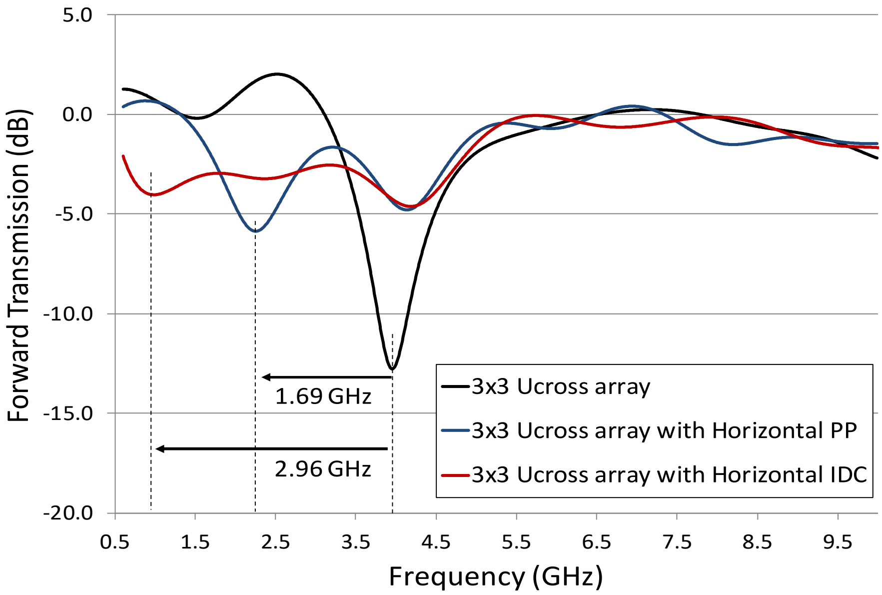

Fig. 6.11 A comparison between measured forward transmission coefficient of unloaded 3x3 uniform cross array versus loaded array with horizontal parallel plate and loaded array with horizontal interdigital capacitor.

to the capacitor. Hence, a uniform cross with loaded capacitance in both planes has been tested. The measured tags are shown in Fig. 6.12 and their forward transmission coefficient is illustrated in Fig. 6.13. It can be noticed that the main resonance has been shifted by 2.71 GHz. A strong higher order resonance can also be noticed around 5 GHz in both cases.

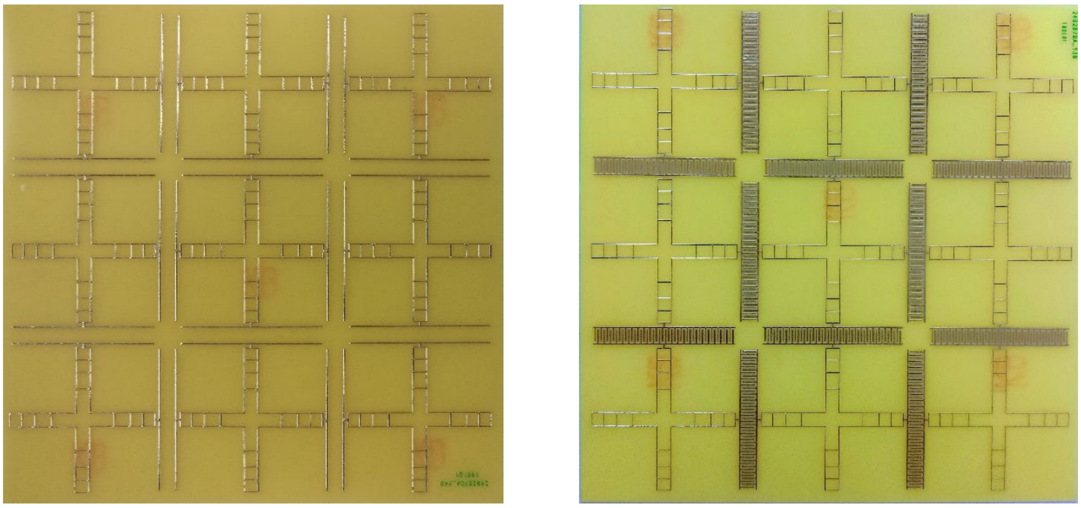

(a) (b)

Fig. 6.12 (a) 3x3 uniform cross array with horizontal and vertical parallel plate (b) 3x3 uniform cross array loaded with horizontal and vertical IDC.

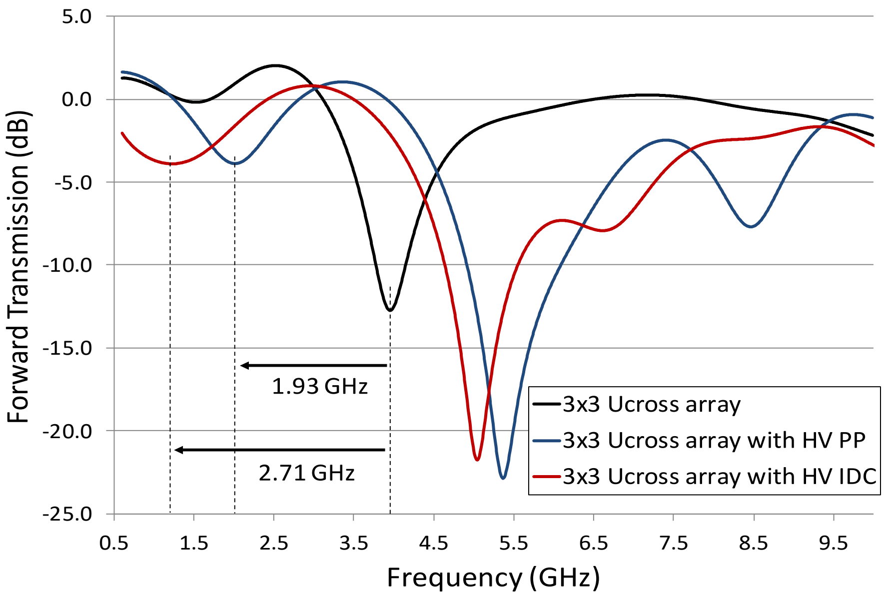

Fig. 6.13 A comparison between measured forward transmission coefficients of unloaded 3x3 uniform cross array versus array loaded with horizontal and vertical parallel plate, and another array loaded with horizontal and vertical IDC.

6.2 Maltese cross tag design

The capacitive loading of uniform cross array using parallel plates and interdigital capacitor has been proven to be a viable technique for array miniaturisation. Since the impact of capacitive coupling between adjacent elements is a key parameter in array miniaturisation, it would be advantageous to consider a unit cell with an inherently wider coupling area. Thus, a Maltese cross unit cell has been considered as depicted in Fig. 6.14. Maltese cross unit cell occupies less physical space than a uniform cross unit cell for the same resonance position. Moreover, degrading the Maltese cross by removing the inner interconnecting strips numbered 1-3 (in a similar way to the uniform cross degradation stages) would result in a more identifiable degradation stages as the difference between the length of resonance loops at each stage is bigger.

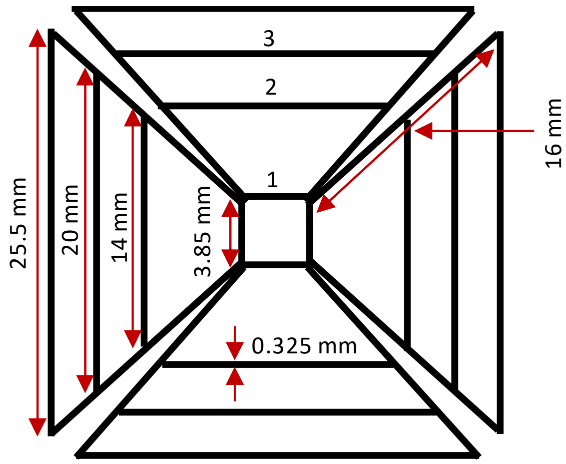

Fig. 6.14 Maltese cross dimensions.

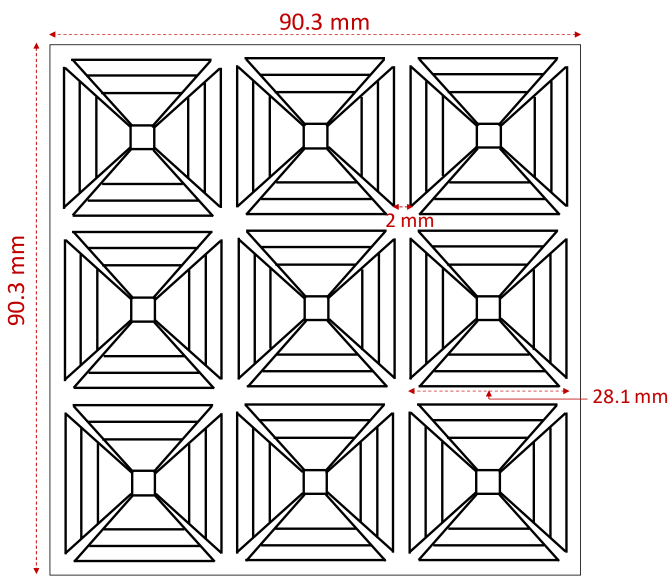

Fig. 6.15 3x3 Maltese cross array with dimensions of 90.5x90.5 mm^2.

Fig. 6.16 shows a comparison between uniform cross array and Maltese cross array. It can be seen that Maltese cross array have a lower resonance frequency than uniform cross despite being physically smaller. This can be attributed to the larger coupling area as explained earlier. A number of interdigitated fingers were added between the Maltese cross array elements to increase the capacitance further, Fig. 6.17 shows a comparison between the response of Maltese cross array with and without interdigitated fingers. Interestingly, the resonance frequency of Maltese cross with interdigitated fingers have reached the same limiting value as the uniform cross with IDC displayed in Fig. 6.6. Nevertheless, Maltese cross design is still superior as it has smaller physical size.

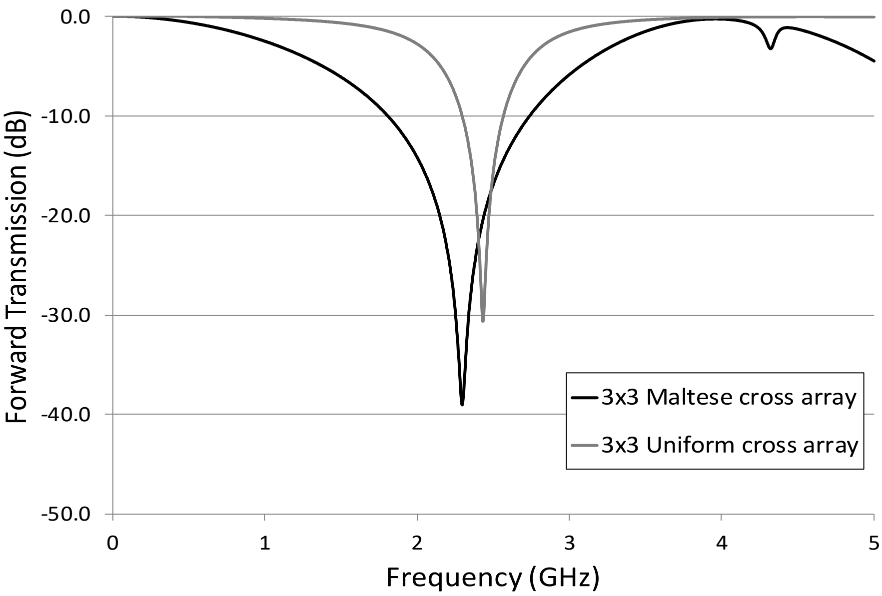

Fig. 6.16 Simulated response of Maltese cross array with and without interdigitated fingers.

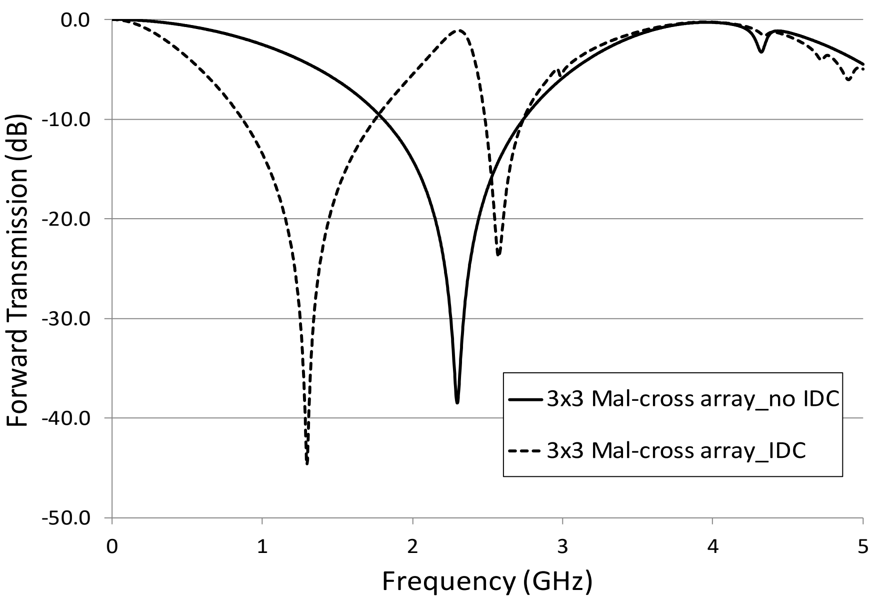

Fig. 6.17 Simulated response of Maltese cross array with and without interdigitated figures.

The response of manufactured Maltese cross array illustrated in Fig. 6.18 have been measured experimentally and compared to simulated results. It can be seen in Fig. 6.19 that measured response shows similarities to simulated result. However, measured response has a smaller amplitude while the two resonance nulls are slightly further apart in frequency. In comparison to Fig. 6.13, it can be seen that practically Maltese cross exhibits a stronger resonance than uniform cross array.

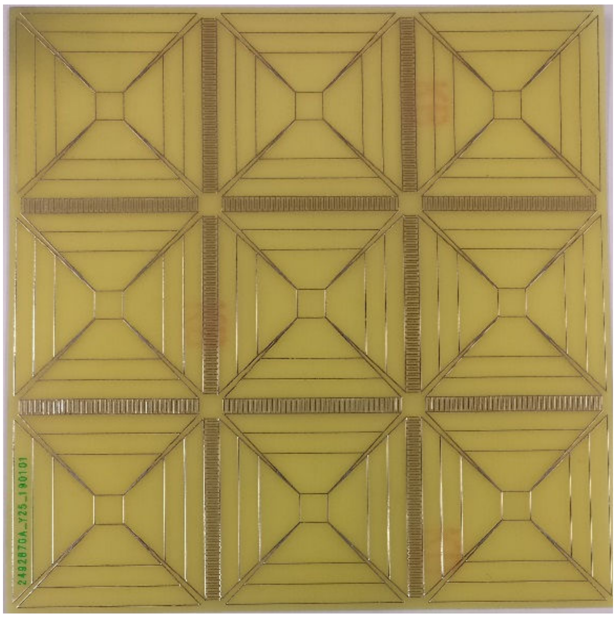

Fig. 6.18 Manufactured Maltese cross array with interdigitated fingers on 0.6 mm thick FR4 with dimensions of 90.3 x 90.3 mm^2.

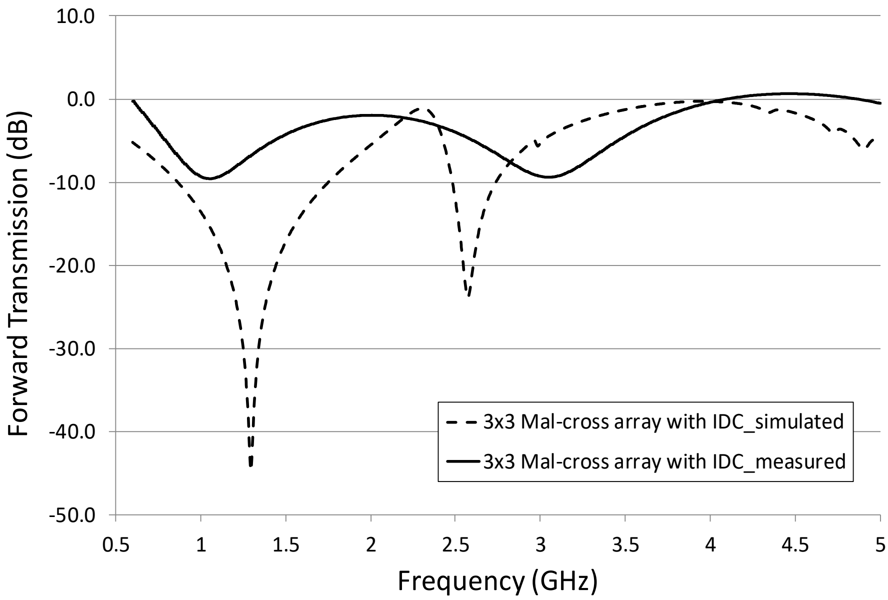

Fig. 6.19 Measured forward transmission coefficient of 3x3 Maltese cross array with IDC.

6.3 Miniaturised tags response

The main target of this research project is to design a self-resonant tag with small physical size suitable for implantation inside the human body. At the same time, maintaining a strong resonance characteristics and a response that can be tracked inside the lossy media throughout the degradation stages of the tag. Earlier in this chapter, it has been experimentally shown that it is possible to shift the resonance position down in frequency through capacitive loading of finite self-resonant arrays. In this section, the response of miniaturised uniform cross and Maltese cross arrays are tested and compared to the response of original size arrays.

A 3x3 uniform cross array with IDC with dimensions of 40x40 mm^2 has been manufactured for the four resonant stages of the tag as illustrated in Fig. 6.20. Measured forward transmission response is shown in Fig. 6.21. It can be seen that the miniaturised tag shows a strong resonance at around 3.3 GHz for the complete tag. The degradation stages of the tag shows a slight frequency shift, with stage 1 and 2 showing similar frequency response. The reason behind the small distances between degradation stages is because of the small difference in the electrical length of resonance loops created by isolating the interconnecting strips.

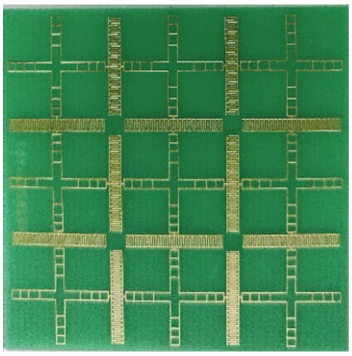

(a)

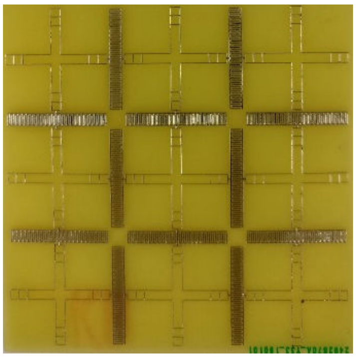

(b)

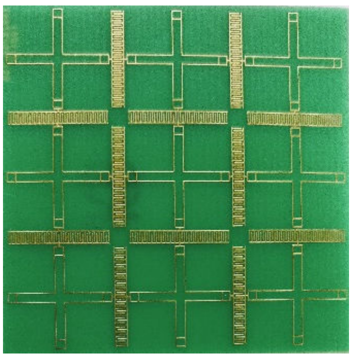

(c)

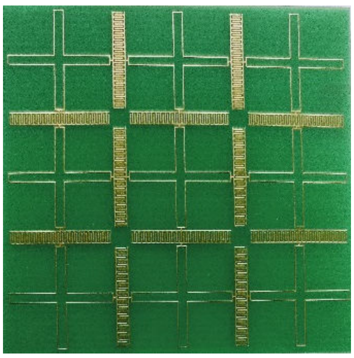

(d)

Fig. 6.20 Prototypes of miniaturised 3x3 uniform cross array at four different degradation stages all with size of 40x40 mm^2 on 0.6 mm thick FR4.

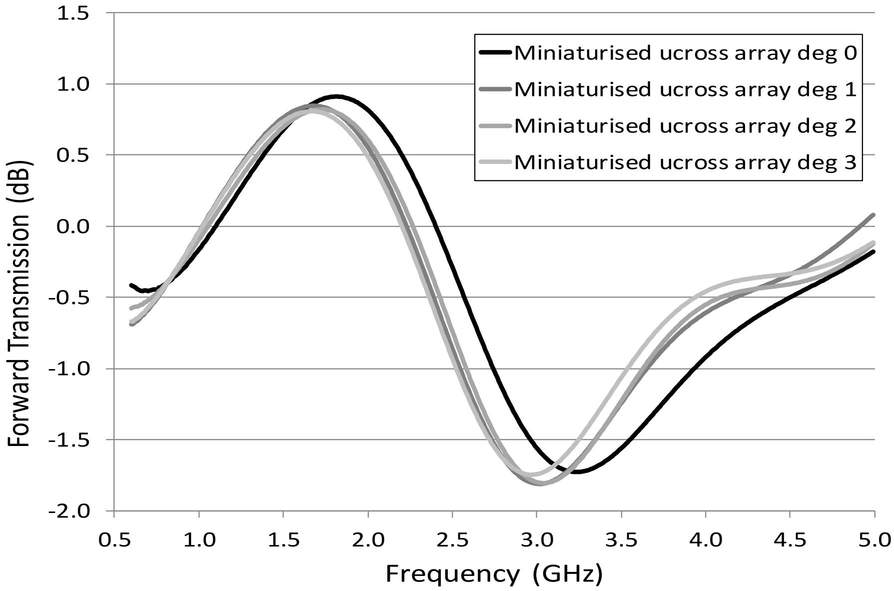

Fig. 6.21 Measured forward transmission coefficient of miniaturised 3x3 uniform cross tag throughout degradation stages.

Similarly, A 3x3 Maltese cross array with interdigitated fingers with dimensions of 36x36 mm^2 has been manufactured for the four resonant stages of the tag as illustrated in Fig. 6.22. The measured S_{21} response is shown in Fig. 6.23. It can be seen that the distance between the response of degradation stages are bigger than that of uniform cross tag.

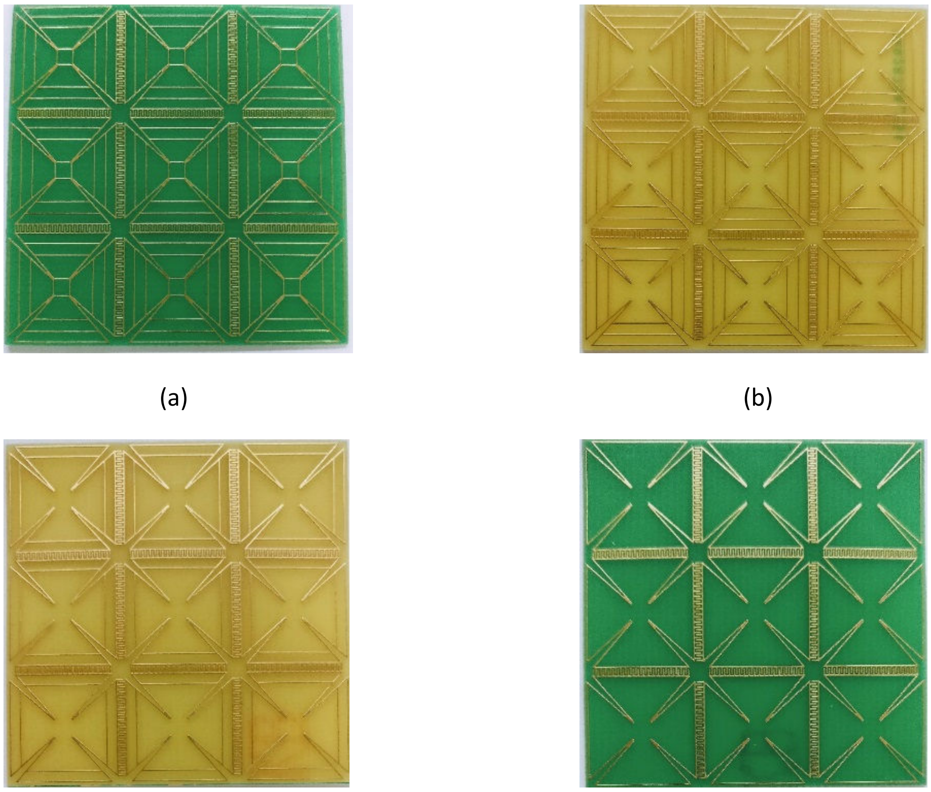

(a) (b)

(c) (d)

Fig. 6.22 Prototypes of miniaturised 3x3 Maltese cross array at four different degradation stages all with size of 36x36 mm^2 on 0.6 mm thick FR4.

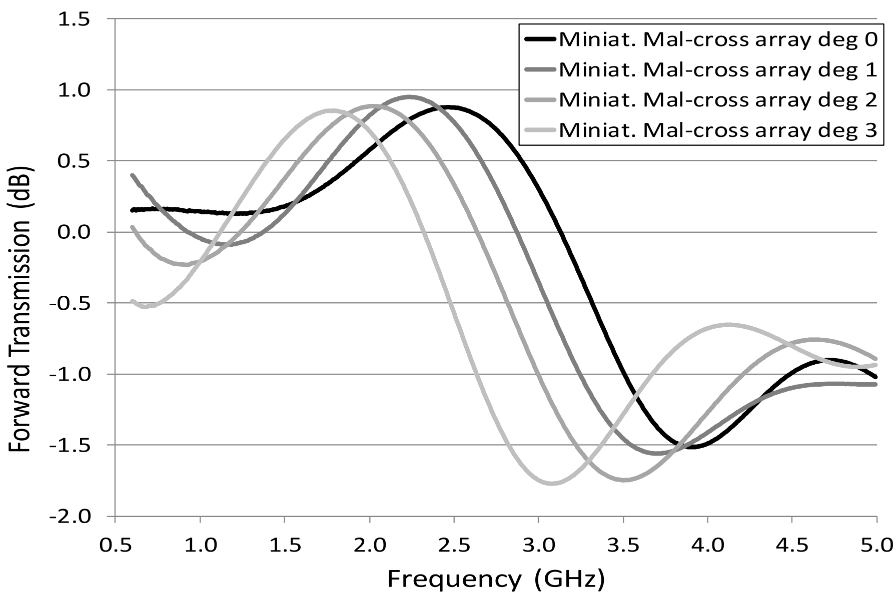

Fig. 6.23 Measured forward transmission coefficient of miniaturised 3x3 uniform cross tag throughout degradation stages.

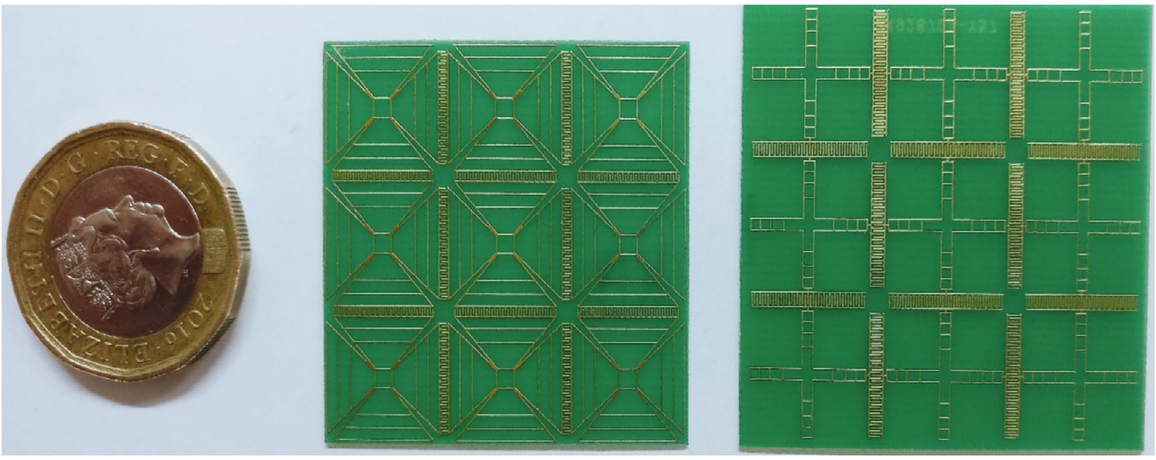

Fig. 6.24 Size of miniaturised uniform cross tag and miniaturised Maltese cross tag in relation to a coin.

Fig. 6.24 shows the size of manufactured uniform cross and Maltese cross tags in relation to a coin. Although the tag can be miniaturised further, the current size makes it a sensible option as an implantable medical device and at the same time allows the measurement of its response using the available measurement facilities (which are not particularly designed to measure the response of physically small surfaces). A comparison in the response of uniform cross and Maltese cross tags are shown in Fig. 6.25. It can be seen that Maltese cross tag has higher resonance than uniform cross tag.

In theory, the response of miniaturised uniform cross array can be identical to the response of original array except for a wider bandwidth as seen in simulation results in Fig. 6.7c. However, in practice the measured response of self-resonant arrays are affected by the physical size of the surface as the amount of reflected/transmitted electromagnetic field will be less for smaller arrays. Hence, miniaturised arrays are expected to have less amplitude than original size arrays. Fig. 6.26 shows a comparison between miniaturised uniform cross array shown in Fig. 6.20a and original size uniform cross array depicted in Fig. 6.8a. Despite that miniaturised array being 2.5 times smaller than original array, it has a lower resonance frequency. A big difference in the amplitude of both arrays can be clearly observed as well. Nevertheless, miniaturised array shows better resonance characteristics than original size single-element tag, which are comparable in size as shown in Fig. 6.27. The measured forward transmission of both tags are illustrated in Fig. 6.28. The latter has clearly demonstrated the key advantage of miniaturisation using interdigital capacitor.

So far in this chapter, the response of different tag designs have been studied in free space, and the benefit of tag miniaturisation using capacitive loading have been demonstrated. Next section will investigate tags response in a homogenous human body phantom.

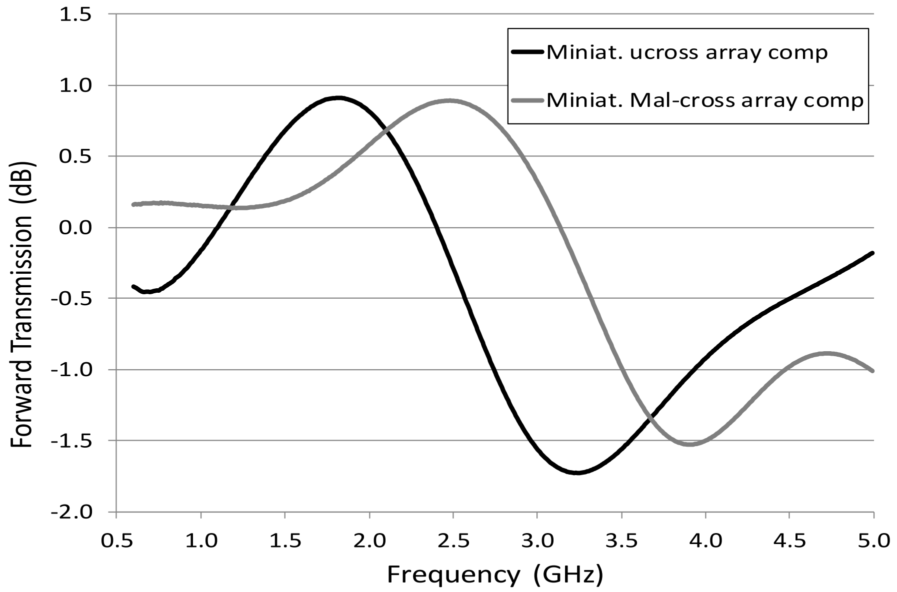

Fig. 6.25 Comparison between miniaturised uniform cross array and miniaturised Maltese cross array for forward transmission.

Fig. 6.26 Comparison between original size uniform cross array (100x100 mm^2) and miniaturised uniform cross array (40x40 mm^2).

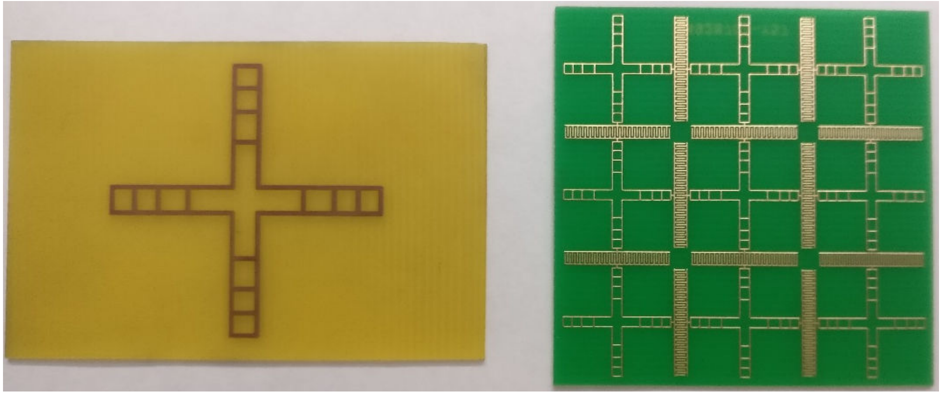

Fig. 6.27 Size of miniaturised uniform cross tag versus single-element original size ucross.

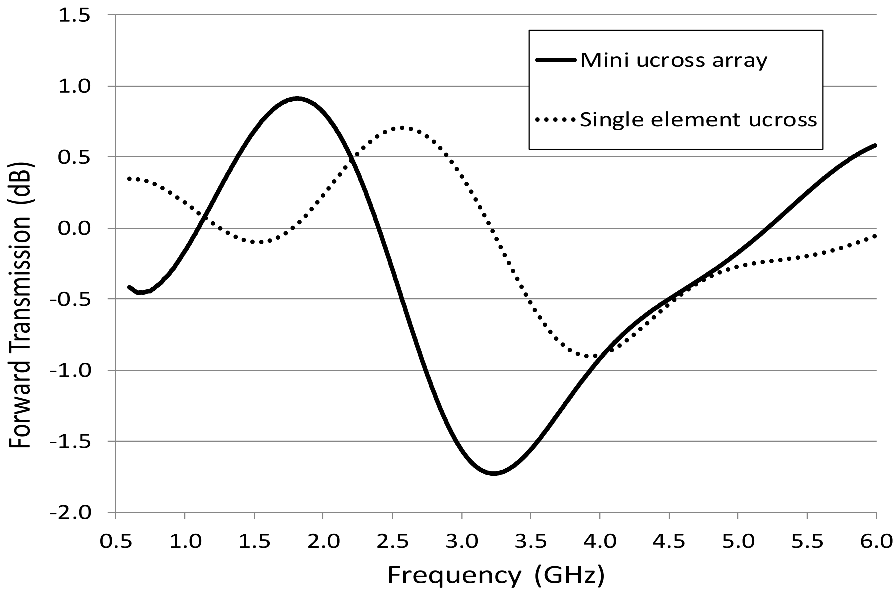

Fig. 6.28 Comparison between miniaturised uniform cross array and single-element original size uniform cross.

It has been shown in Fig. 6.21 that the distances between the resonance positions of degradation stages are small which makes it difficult to differentiate between the subsequent stages. One way to increase the distance between resonance positions is by gradually reducing the capacitance of the tag as it degrades. This can be achieved by introducing breaking points in the added parallel plates, while keeping the uniform cross intact. The new four degradation stages of the uniform cross tag are shown in Fig. 6.29. The measured responses of these four tags are illustrated in Fig. 6.30. It can be seen that the resonance frequency of the tag increases with degradation as opposed to the previous method. This key difference can be clearly explained using the resonance frequency expression of any RLC circuit which is given by:

$$f_0 = \frac{1}{2\pi\sqrt{LC}} \tag{6.4}$$

With the previous degradation method, it has been shown that inductance increases with tag's degradation as has been proven in Table 3.1 and Fig. 3.13. Hence, the response of the tag shifts towards lower frequencies as the tag's degrades. On the other hand, with the new degradation method the capacitance decreases with tag's degradation. Thus, the response of the tag shifts towards higher frequencies.

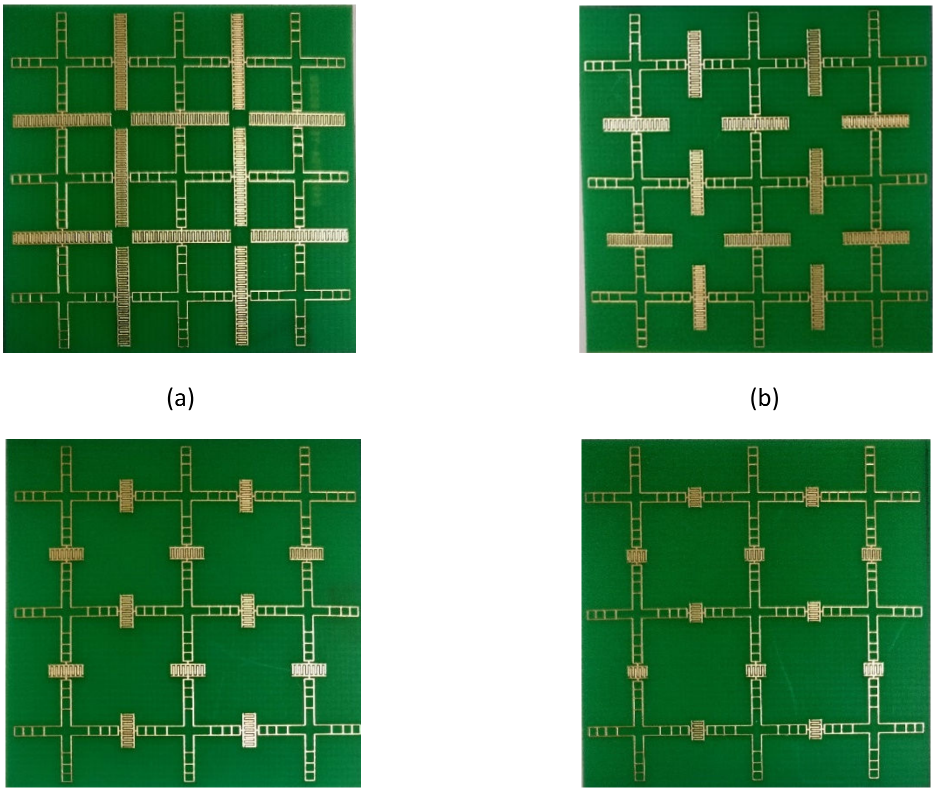

(a) (b) (c) (d)

Fig. 6.29 Prototypes of miniaturised 3x3 uniform cross array at four different states using IDC degradation method.

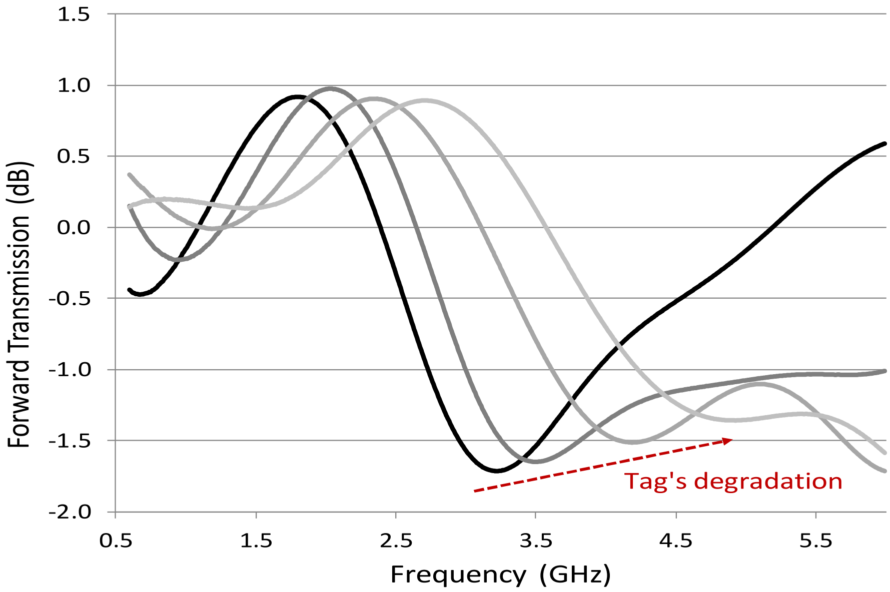

Fig. 6.30 Measured forward transmission coefficients of miniaturised 3x3 uniform cross tags using IDC degradation method.

6.4 Tag response on dielectric phantom

6.4.1 Free space measurements

In the last section, it has been shown that miniaturised uniform cross and Maltese cross tags have good resonance characteristics in free space. These miniaturised arrays have exhibited a stronger resonance than single-element original size tags. However, the objective is to operate them inside the human body. Hence, in this section the response of uniform cross and Maltese cross tags is investigated with dielectric phantom.

The created semi-solid dielectric phantom (which have been discussed in chapter four) have been casted in a 14x14 mm^2 low-loss plastic containers with a thickness of 5 mm and 10 mm, to study the impact of implantation depth on the response of the tag. The dielectric attenuation of the phantom at 3 GHz using (4.7) is 419.6 dB/m, and for 5 mm and 10 mm thick layers the attenuation is 2.09 db and 4.19 db, respectively. The dielectric phantom used in the experiment is shown in Fig. 6.31. The phantom were placed in the middle in between transmitting and receiving antennas and tags were placed on top of the phantom. The measurement setup is shown in Fig 6.32.

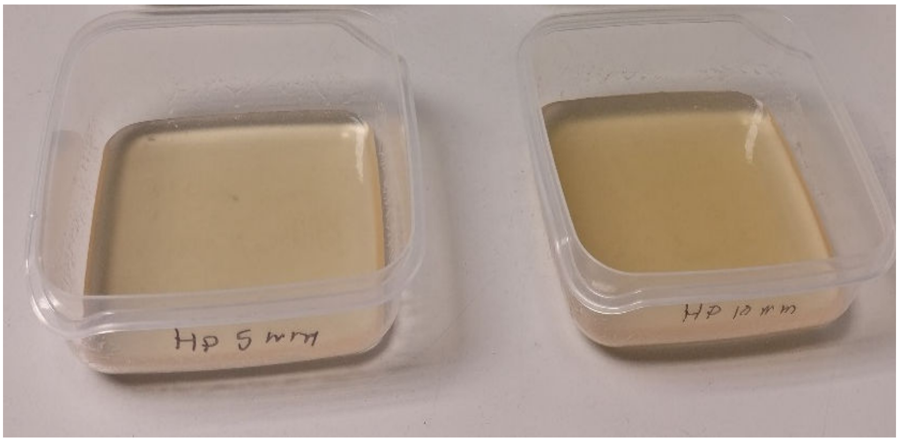

Fig. 6.31 Dielectric phantom in 14x14 m^2 plastic containers, a 5 mm and 10 mm thick layers.

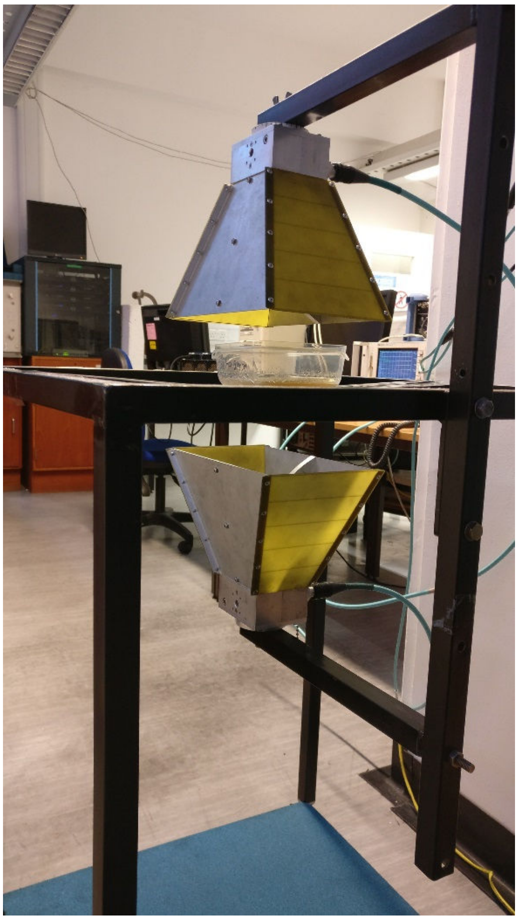

Fig. 6.32 Measurement setup of self-resonant tag response on semi-solid dielectric phantom.

Firstly, 3x3 uniform cross original size array has been tested on dielectric phantom with 5 mm and 10 mm thick layers, the forward transmission response is shown in Fig. 6.33. The array shows a typical FSS response with dielectric media which is characterised by frequency shift, decrease in amplitude, and a wider bandwidth. On the other hand, the response of miniaturised uniform cross array in free space and on dielectric phantom is shown in the Fig. 6.34. A clear frequency shift can be noticed while the amplitude has increased on the dielectric media compared to free space. The response of single-element uniform cross tag on dielectric media is shown in the Fig. 6.35. It can be observed that it has a similar behaviour to the miniaturised array. However, considering the frequency response of the phantom (shown in the black dotted line), it is clear that the miniaturised uniform cross array shows a superior performance to single-element tag both in free space and on dielectric media.

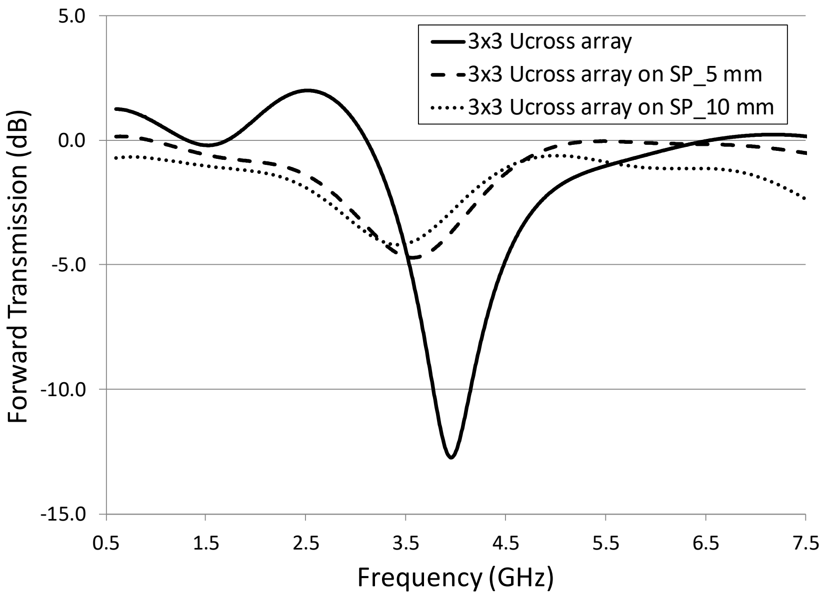

Fig. 6.33 Forward transmission of 3x3 uniform cross array on homogeneous dielectric phantom.

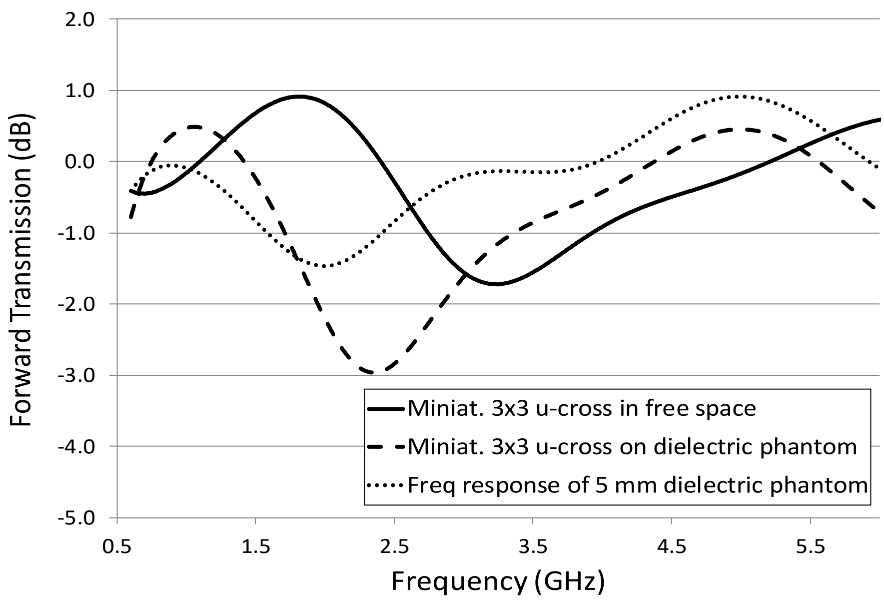

Fig. 6.34 Forward transmission of 3x3 miniaturised uniform cross array in free space and on dielectric phantom.

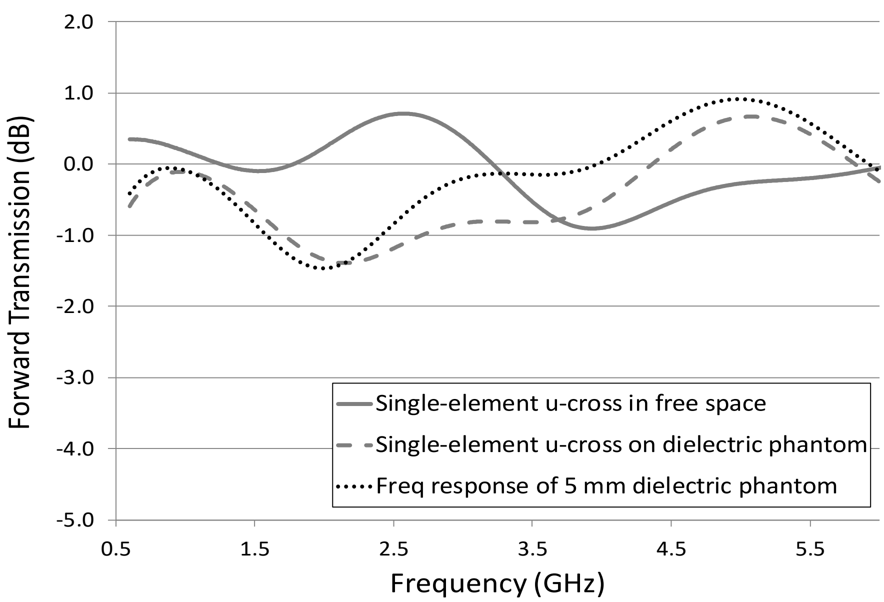

Fig. 6.35 Forward transmission of single-element uniform cross in free space and on dielectric phantom.

By having a look on the response of miniaturised array on dielectric media for a wider frequency range, as in Fig. 6.36, it can be inferred that the response is dictated by both the frequency response of the tag in free space and the frequency response of the dielectric media as has been discussed in chapter four.

The response of the miniaturised uniform cross and Maltese cross tags on dielectric phantom throughout degradation stages are shown in Fig 6.37 and Fig. 6.38, respectively. It is clear that the dielectric media has minimised the distance between degradation stages. However, miniaturised Maltese cross shows a better performance than uniform cross as the distance between degradation stages are more visible. On the other hand, doubling the thickness of phantom has led to an extra frequency shift in the response of miniaturised uniform cross arrays as shown in Fig. 6.39.

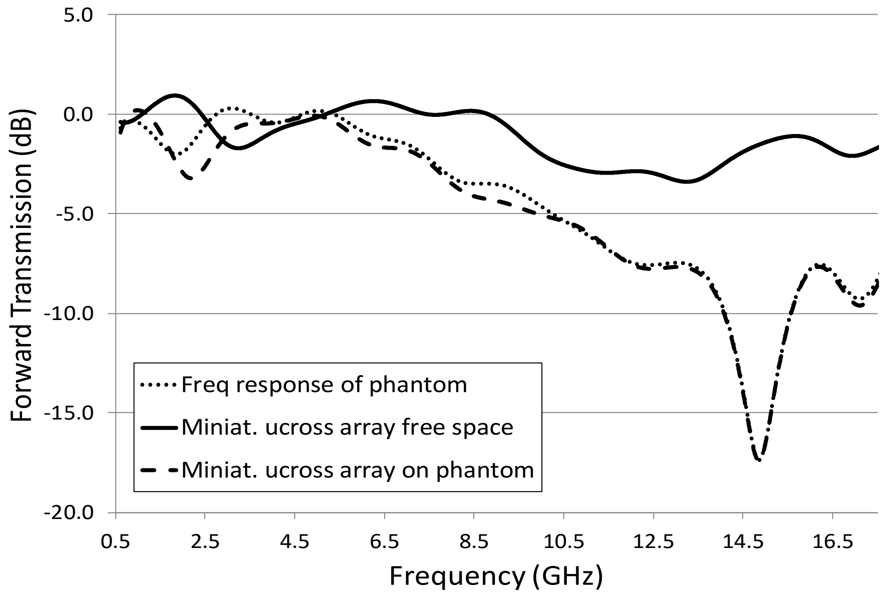

Fig. 6.36 Forward transmission of 3x3 miniaturised uniform cross array in free space and on dielectric phantom for the whole frequency range.

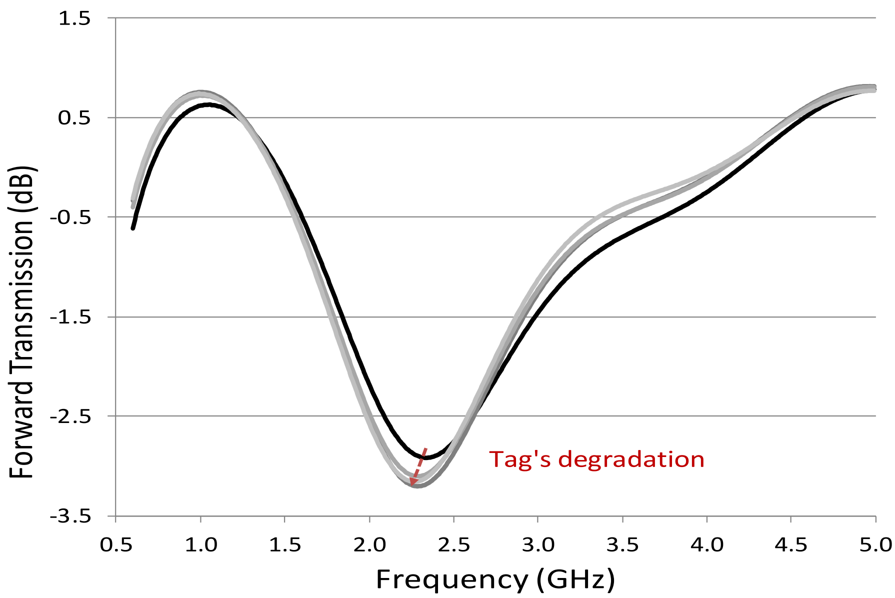

Fig. 6.37 Forward transmission of 3x3 miniaturised uniform cross array at four degradation stages on dielectric phantom.

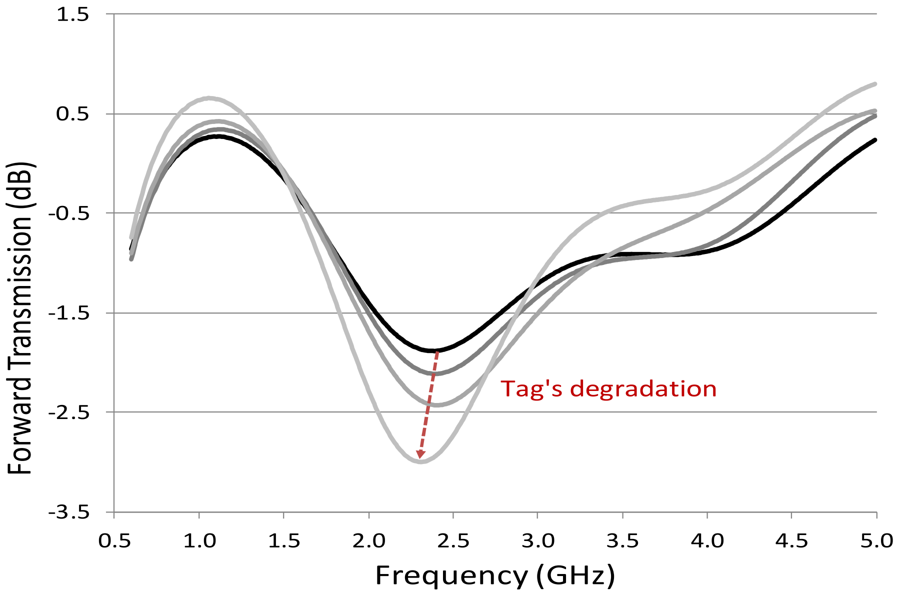

Fig. 6.38 Forward transmission of 3x3 miniaturised Maltese cross array at four degradation stages on dielectric phantom.

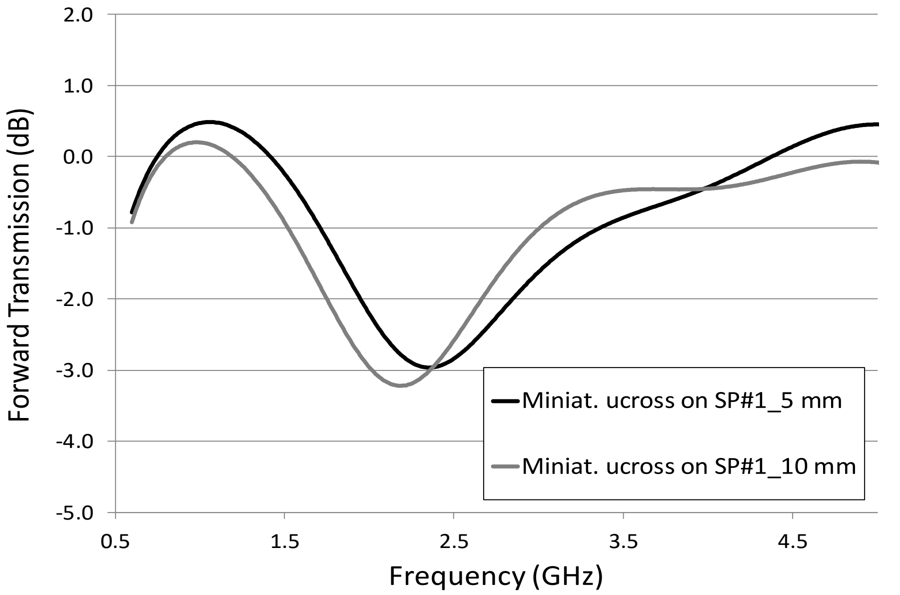

Fig. 6.39 Impact of doubling the surrounding dielectric media thickness on miniaturised uniform cross array response.

Finally, the response of uniform cross tag when degrading the IDC (as shown in Fig. 6.29) is depicted in Fig. 6.40. Interestingly, the tag's response in this method shows opposite behaviour to the Maltese cross tag during degradation as the amplitude increased with degradation.

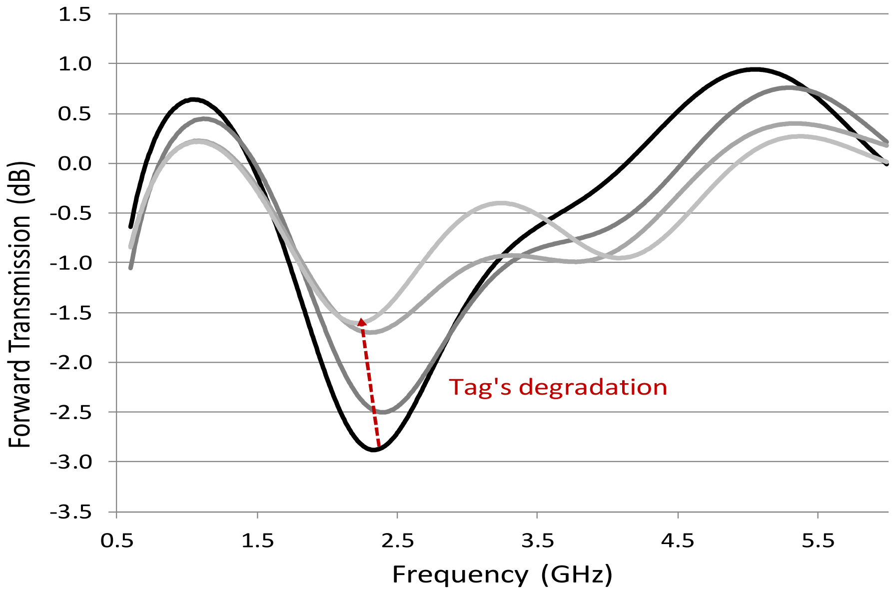

Fig. 6.40 Forward transmission of 3x3 miniaturised uniform cross using IDC degradation method on dielectric phantom.

6.4.2 Waveguide measurements

In the last section, the impact of dielectric phantom on the response of self-resonant tag in free space have been discussed. It this section the relationship between the number of resonating elements in a tag and the impact of dielectric phantom is analysed using a waveguide. The dielectric phantom was casted in the waveguide sections shown in Fig. 6.41 below with 5 mm and 10 mm thick layers. Despite the accuracy of waveguide results, the narrow operational window represents a limiting factor. For the waveguide used in this experiment (WG10), the window is between 2.6 and 3.95 GHz. It has been shown before in

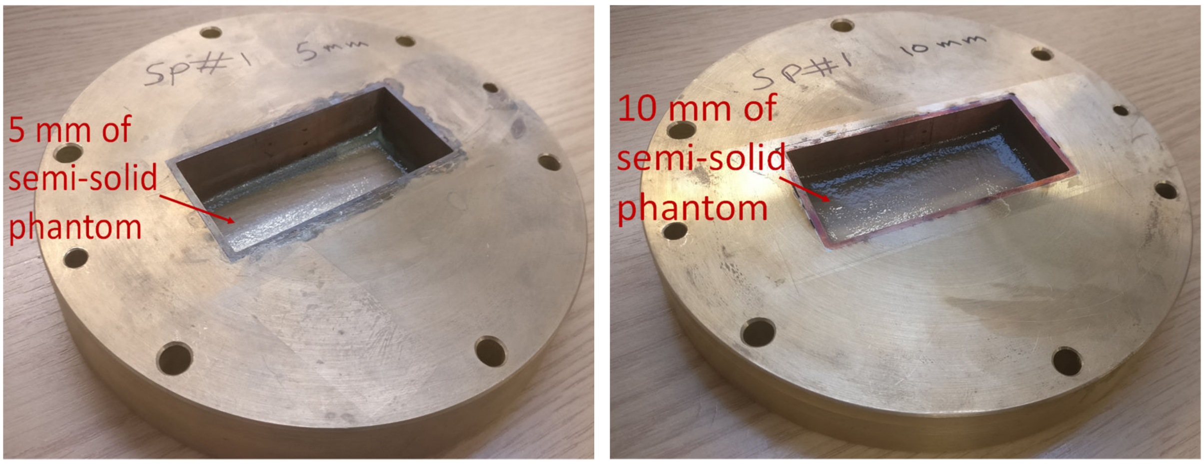

(a) (b)

Fig. 6.41 Semi-solid phantom in a waveguide section (a) 5 mm thick (b) 10 mm thick.

this project that dielectric media causes a frequency shift in the response of self-resonant tags. Thus, unloaded tag resonating within the waveguide window may not have a resonance within this window when a dielectric media exists in the proximity of the tag. In order to achieve a resonance within the waveguide window, the following steps have been followed in tag design:

- The dielectric properties of the phantom was measured using the dielectric probe kit.
- The measured properties of phantom was imported to CST.
- The created phantom material in CST was simulated inside a waveguide and tag designs were adjusted to make sure it resonates inside the waveguide operational window, with 5 mm and 10 mm thick layers of phantom.
- Two types of tags were designed and manufactured, a two–element and a 6x3 elements with IDC tags. Both tag types resonates at a similar frequency in free space.

The two-element tag is shown in Fig. 6.42. The 6x3 elements with IDC tag in complete and degraded states is shown in Fig. 6.43 and 6.44, respectively. A comparison between the response of two-element tag and 6x3 elements with IDC tag on 5 mm of dielectric phantom inside waveguide is shown in Fig. 6. 45. It can be seen that the 18 elements tag has a resonance at 3.5 GHz while the 2 elements tag does not exhibit a resonance, the reason behind that is dielectric phantom dominates the frequency response due to the high dielectric attenuation. This clearly demonstrates that the number of resonating elements in a tag plays a fundamental role in combating dielectric attenuation of human body. It is worth noting that both tag types have a similar resonance in free space as shown simulation results in Fig. 6.46.

A comparison between complete and fully degraded tag for the 6x3 with IDC tag is shown in Fig. 6.47. The impact of tag's degradation on dielectric phantom is shown to shift the resonance down in frequency, similar to the tag's behaviour in free space. The impact of doubling the thickness of the dielectric phantom has been studied as well. Fig. 6.48 shows the difference between the frequency response of 5 mm and 10 mm dielectric phantom. It is clear that the 10 mm phantom attenuates the signal more than the 5 mm phantom. Finally, Fig. 6.49 compares between the response of the complete and degraded 18 elements tag on 5 mm and 10

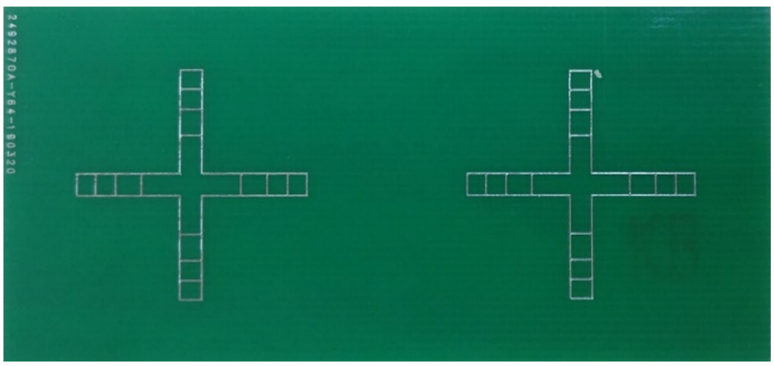

Fig. 6.42 Two-elements uniform cross tag with dimensions of 34.036x72.136 mm^2 and on 0.6 mm FR4.

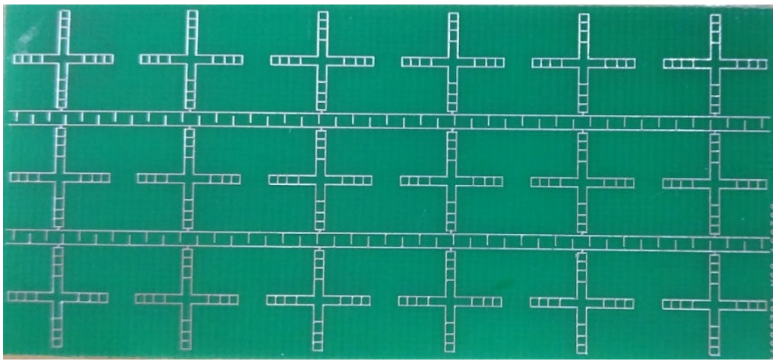

Fig. 6.43 6x3 elements uniform cross complete tag with dimensions of 34.036x72.136 mm^2 and on 0.6 mm FR4.

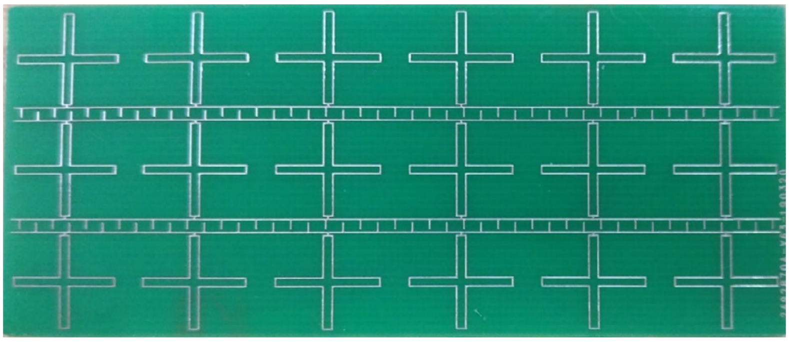

Fig. 6.44 6x3 elements uniform cross degraded tag with dimensions of 34.036x72.136 mm^2 and on 0.6 mm FR4.

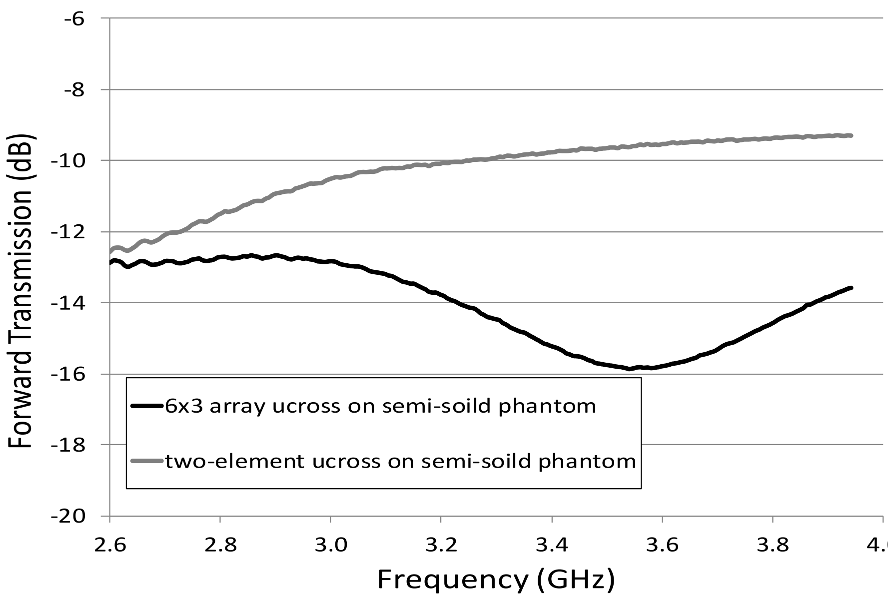

Fig. 6.45 Comparison between forward transmission of a two-element uniform cross tag and a 6x3 uniform cross array on a 5 mm dielectric phantom inside waveguide.

mm phantom. It can be observed that the extra thickness of phantom has caused a frequency shift and an unexpected increase in amplitude, similar to the findings in Fig. 6.33.

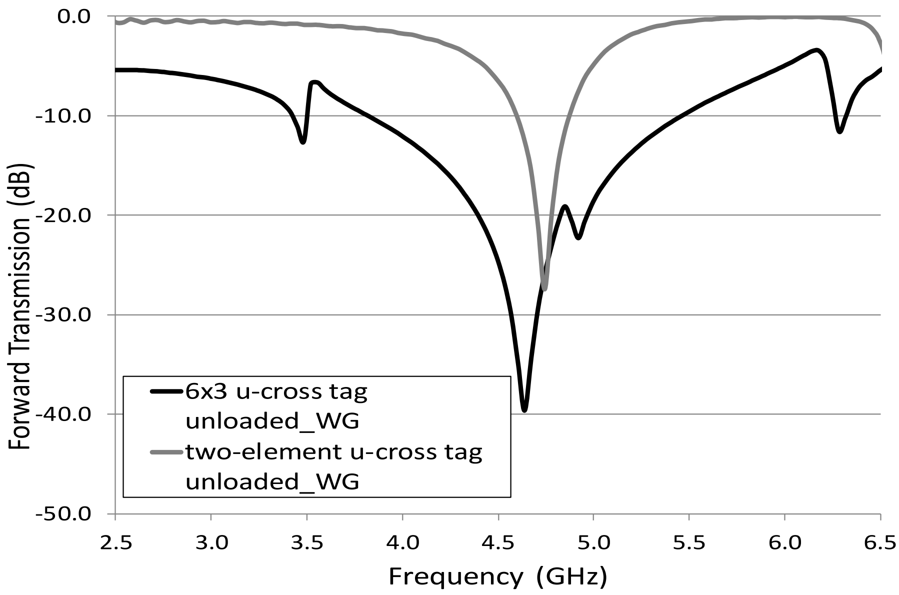

Fig. 6.46 Comparison between simulated results of two-element versus 6x3 uniform cross tags unloaded inside a waveguide.

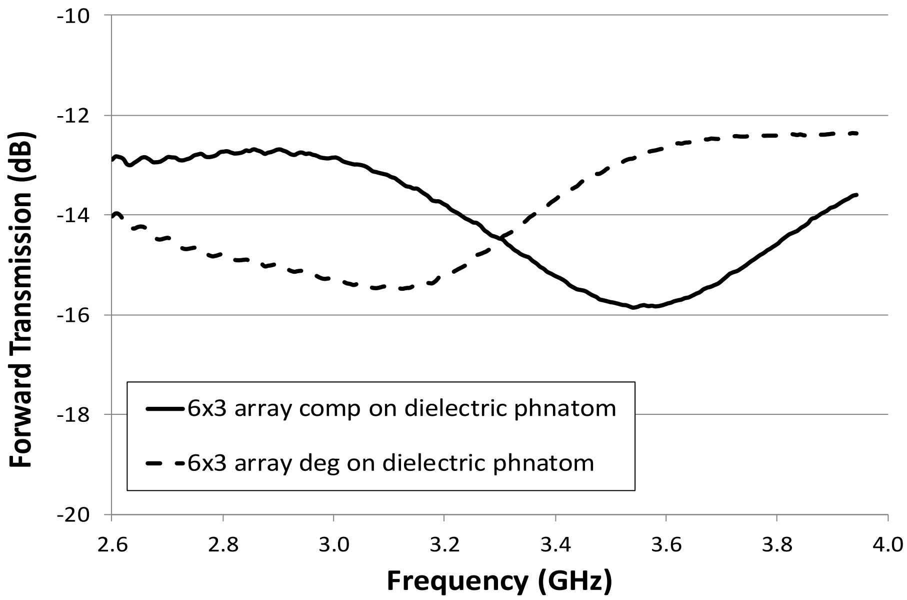

Fig. 6.47 Comparison between forward transmission 6x3 uniform cross array, complete versus degraded array on 5 mm thick dielectric phantom.

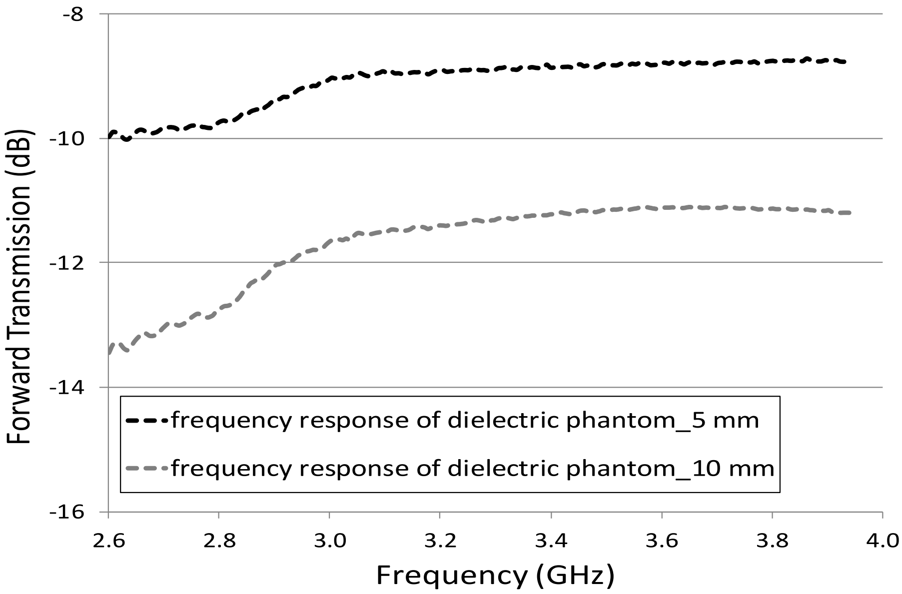

Fig. 6.48 Comparison between the frequency response of a 5 mm dielectric phantom versus 10 mm dielectric phantom inside waveguide.

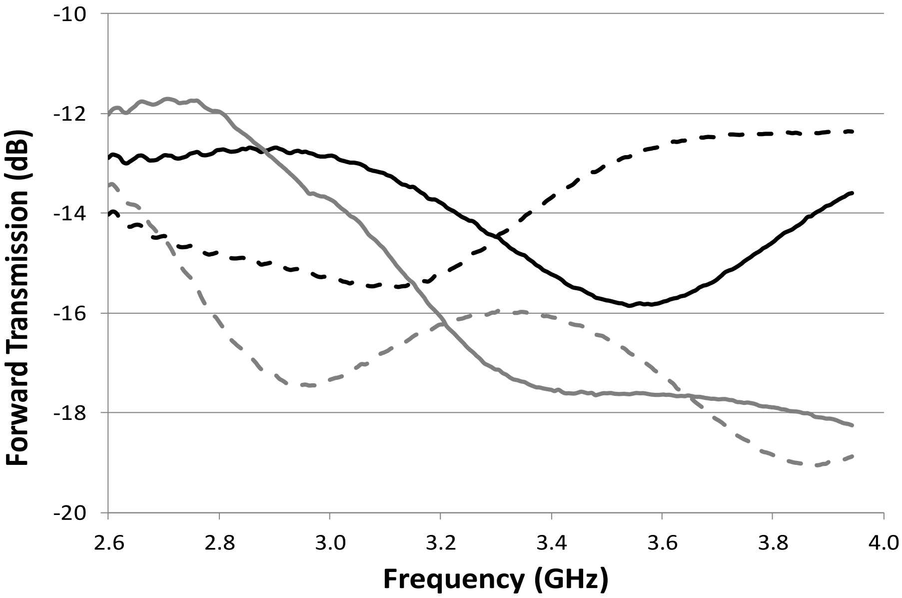

Fig. 6.49 Comparison between forward transmission of 6x3 uniform cross array complete (solid) and degraded (dashed) on 5 mm (black) and 10 mm (grey) thick dielectric phantom inside waveguide.

6.5 Tag response using flexible printing

The ultimate objective of this project is to design a biodegradable self-resonant tag. The substrate of the tag consists of a thin biocompatible and biodegradable polymer, while the resonating element is made from a degradable metal. Since such materials are not commercially available for PCB manufacturing, a non-degradable tag was manufactured using flexible printing technology. The manufactured tag is a step closer towards the implantable tag in terms of the thickness and flexibility of the substrate and the amount of conducting copper used. The four resonant states of the Maltese cross design (shown in Fig. 6.22) was fabricated on 0.1 mm Polyimide substrate ($\varepsilon_r \approx 3.45$) with a 35 μm thick copper layer. The manufactured flexible tags are shown in Fig. 6.49.

Firstly, the performance of the flexible tag has been compared to the rigid tag in free space and on dielectric phantom as shown in Fig 6.50. It can be seen that in free space the flexible tag has a higher resonance frequency than the rigid tag. This can be attributed to the difference in substrate thickness (0.1 mm for flexible tag and 0.6 mm for rigid tag) and also to the difference in the dielectric permittivity (3.45 for Polyimide and 4.3 for FR4). On the other hand, the flexible tag has a slightly lower resonance than rigid tag, on dielectric phantom. The response of the flexible tag in free space throughout degradation is shown in Fig. 6.51. The shift in resonance at each stage is clear, similar to the rigid tag response in Fig 6.23. The response of the degrading flexible tag has also been tested on dielectric phantom as shown in Fig. 6.52. The response does not exhibit a clear frequency shift. However, the gradual decrease in amplitude is indicative of degradation.

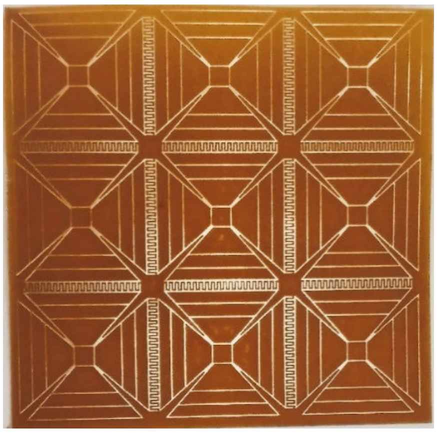

(a)

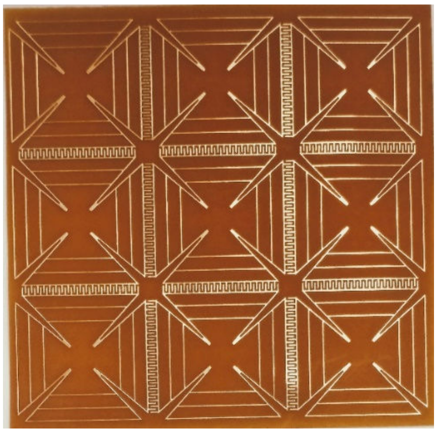

(b)

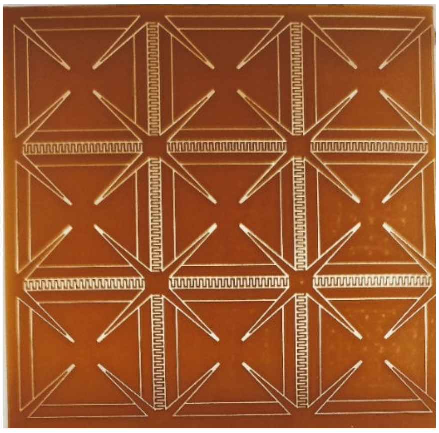

(c)

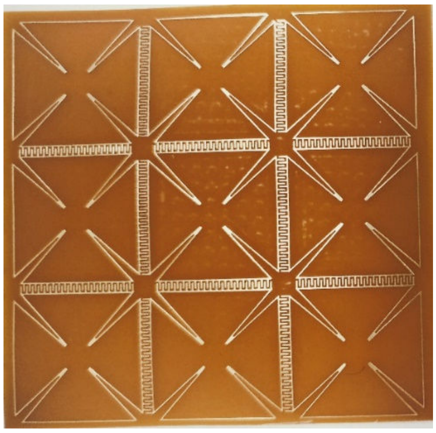

(d)

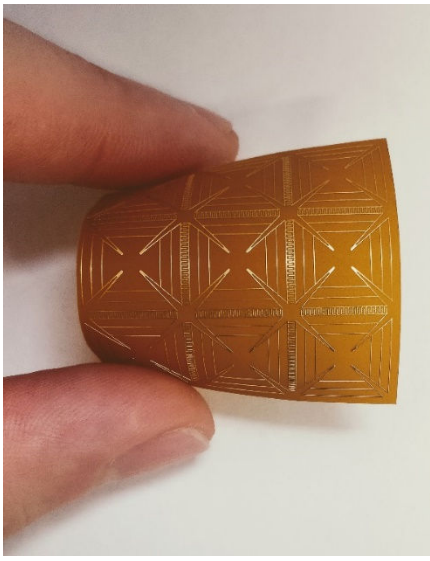

(e)

Fig. 6.50 Miniaturised Maltese cross on 0.1 mm Polyimide substrate with dimensions of 36x36 mm^2 (a) complete tag (b) first degradation stage (c) second degradation stage (d) third degradation (c) a picture showing the flexibility of the tag.

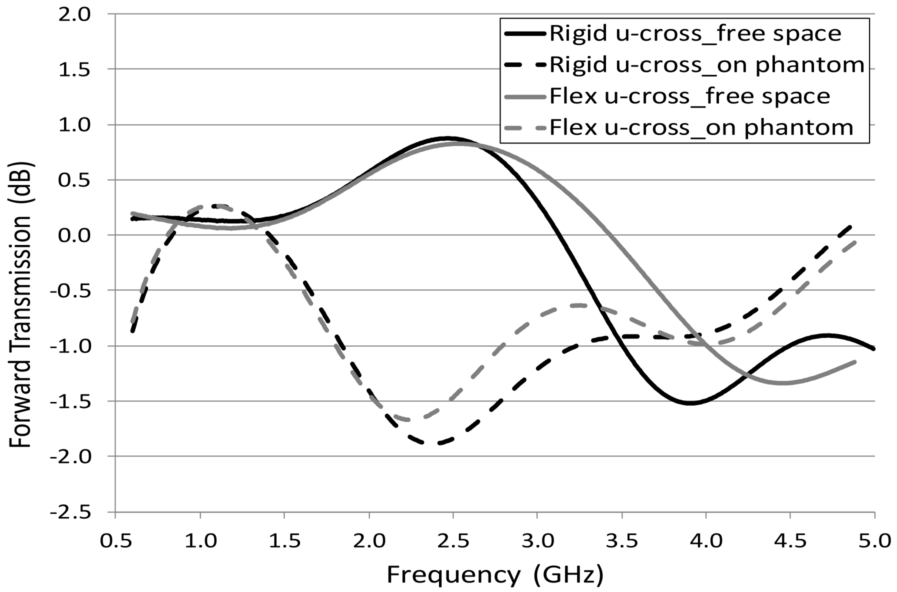

Fig. 6.51 Comparison between flexible Maltese cross tag and rigid Maltese cross tag in free space and on dielectric phantom.

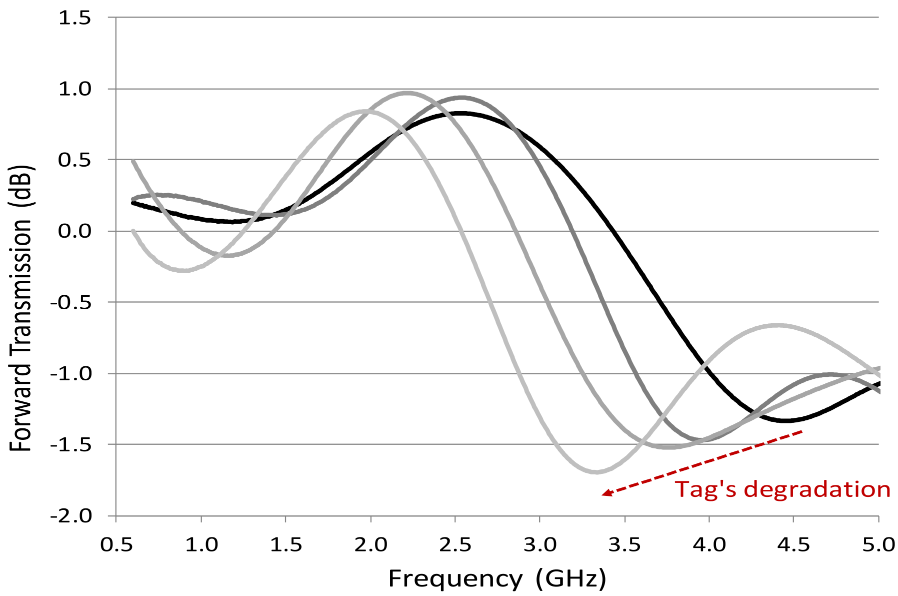

Fig. 6.52 Response of flexible Maltese cross tag in free space throughout degradation stages.

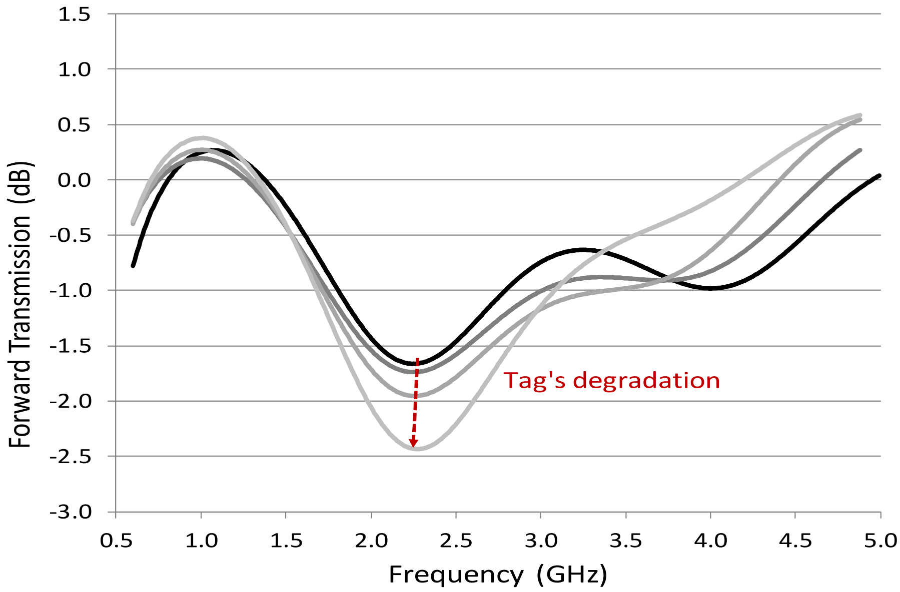

Fig. 6.53 Response of flexible Maltese cross tag on dielectric phantom throughout degradation stages.

6.6 Summary

This chapter has discussed self-resonant tag's miniaturisation using capacitive loading. SRS arrays with lumped capacitors, parallel plates, and interdigital capacitors have been measured experimentally. It has been shown that it is possible to miniaturise self-resonant tags by 3-4 times without affecting the resonance position. Self-resonant tags with IDC have shown a considerable frequency shift, making the concept of capacitive loading using IDC the best option for an implantable device in terms of biodegradability and biocompatibility. Miniaturised 3x3 uniform cross and Maltese cross tags with IDC have been tested in free space and on dielectric phantom. It has been shown that dielectric media reduces the distances between degradation stages, thus, it becomes more difficult to differentiate between the resonance states of the tag. Nonetheless, It has been found that miniaturised Maltese cross tag have better performance than uniform cross tag on the dielectric phantom as they have more identifiable degradation stages despite being physically smaller.

Waveguide measurements of two-element tag versus 6x3 elements with IDC tag on dielectric phantom have been conducted. It has been shown that as the number of resonating elements in a tag increase, the tolerance to dielectric attenuation improves. Finally, a miniaturised self-resonant tag has been manufactured using flexible printing technology. The flexible tag is a step closer towards the intended implantable biodegradable tag in terms of thickness and flexibility of the substrate, and also the amount of conducting metal that can be used. The performance of flexible tag has been compared to rigid tag and a similar frequency response have been obtained.

7. CHAPTER SEVEN

Conclusion and Future Work

7.1 Conclusion

This project presented design and analysis of implantable self-resonant tag for passive sensing inside the human body. In the first chapter, after discussing the main research question and the aims and objectives of this work, the research hypothesis was explained and supporting evidences were provided. It was stated that by using biodegradable materials, it is possible to use a self-resonant tag for passive sensing inside the body. The chemical changes inside the body characterised by the inflammatory response would alter the degradation rate of biodegradable material, and that can be sensed from outside the body through the RF signature of the tag. The latter would be safely absorbed by the human body eliminating the need for an extraction surgery. The concept of employing a self-resonant tag for early detection of surgical site infections can offer a partial solution to the increasing problem of antimicrobial resistance.

In the first part of chapter two, the area of implantable medical devices was reviewed. Firstly, the definition of IMDs was provided alongside the challenges associated with designing an implantable device. The selection of manufacturing material represents a challenge, as the material needs to be biocompatible so it does not cause the immune system to react against the implantable device. The size of the device is another critical factor, it needs to be as small as possible so it does not interfere with the normal biological activities of the human body nor cause a discomfort to the patient. Moreover, the impact of the biological media on the performance of implants and the wireless communication link was discussed. The limited available power for implantable devices inside the body is also a factor that limits the functions of these devices. Implantable devices can be categorised according to their powering mechanism into active and passive IMDs. The former have on-board battery, hence, they can perform sophisticated functions inside the body at the expense of limited lifetime and relatively large size. Passive IMDs, on the other hand, can operate using backscattering communication, or can rely on energy being harvested from within the body. Additionally, Some passive IMDs use wireless power transfer methods such as inductive coupling, capacitive coupling, ultrasonic transmission, and far field energy transfer. Irrespective of the powering mechanism, IMDs have been used in five main areas within the healthcare sector including diagnosis, telemetry, therapy, drug delivery, and to help the body restore a lost function. After that, the area of biodegradable IMDs was reviewed, as few attempts of designing bioresorbable devices have been reported in the literature for various applications and using different biodegradable materials. The last section of the first part discussed specific absorption rate and the limits that have been set to maintain safe electromagnetic exposure. The remaining parts of chapter two discussed self-resonant structures in the form of both passive chipless RFID and periodic FSS arrays. An in-depth review of the relevant work done in these fields for different applications was provided. Finally, the concept of modelling was explained and the main stages of any modelling process were discussed.

Chapter three introduced tag design and identified the degradation pattern of the tag. In order to have a controlled degradation, the tag needs to have specific points that break in sequence to change the RF signature of the tag in response to the changes in the surrounding tissues. Four different resonant states of the tag were manufactured from non-biodegradable materials, the response of the tag in these four states was measured inside a waveguide to prove the concept. The effect of degradation on tag's electrical properties was studied by resorting to an equivalent circuit model. It was shown that as tag degrades, the inductance increases while capacitance maintains the same value. After that, the equivalent circuit model was extended into a transmission line model to account for the dielectric media in the surroundings of the tag. Novel impedance expressions for self-resonant tag on and within multi-layer dielectric media for normal and oblique incidence were derived, these expressions were utilised to extract equivalent circuit parameters. The trends of equivalent circuit values were used to study the impact of angle of incidence and dielectric media's permittivity and thickness on the response of the tag. The accuracy of the equivalent model was assessed in comparison to full-wave simulation using MAE criteria, and it was shown that model's accuracy is directly proportional to permittivity and thickness of surrounding media. On the contrary, the accuracy is inversely proportional to angle of incidence. The response of the tag within dielectric layers was measured experimentally inside waveguide and compared to equivalent model results with excellent matching.

The transmission line model derived in chapter three was extended to represent lossy dielectric media. It was shown that it is possible to represent human body layers by lossy transmission line segments. In order to have a full electrical representation of biological layers, a distributed circuit representation can be adopted. The relationship between the number of blocks and the frequency response of the transmission line segment was discussed. After that, a step by step analysis of tag within bio tissues was carried out. The impact of dielectric attenuation on the response of self-resonant tags was investigated. It was shown that as the dielectric attenuation of the surrounding media increases, tag's response deteriorates and the frequency response of the dielectric media starts to dominate tag's response. Beyond a certain attenuation threshold, it would not be possible to track the changes in the response of the tag. Equivalent circuit parameters were used to explain the underlying physics of the structure, it was shown that capacitance is proportional to the thickness and permittivity of the dielectric media while resistance corresponds to dielectric attenuation. Nonetheless, inductance is only affected by tag's degradation, and surrounding media has no impact on that. Equivalent model results was compared to full-wave simulation with excellent agreement. The derived transmission line model was exploited to perform a SAR calculation. Knowing the reflection coefficient at each intersection of transmission line model, in addition to the amount of power dissipated at each segment, allows the calculation of power absorbed by any biological layer within the transmission line model. The analysis included different values of incident power and three different frequency points. Lastly, in order to verify equivalent TLM results, a semi-solid dielectric phantom was manufactured and tag response was measured on it inside a waveguide. Experimental results and equivalent model results showed a good matching.

It was shown in chapter four that as the dielectric attenuation increases, the response of tag weakens. Hence, techniques to make tag's response more resilient were investigated in chapter five. Some basic mathematical analysis of the difference between single-element SRS, finite array SRS, and infinite array SRS was introduced. A comparison between the response of a single-element tag versus 3x3 array tag measured experimentally was made. It was shown as the number of elements increases in an array, their resonance characteristics improves. However, this improvement comes at the expense of bigger size which is not favourable for an implantable device. Thus, tag's miniaturisation techniques using capacitive loading was examined in chapter six. It was demonstrated by full-wave simulation that it is possible to shift the resonance frequency of an SRS by using lumped capacitors, the amount of frequency shift is proportional to the value of capacitor. Nevertheless, lumped capacitors are not preferred in an implantable tag as they raise some biocompatibility concerns (also they are normally made from non-biodegradable materials). Hence, lumped capacitors were replaced by parallel plates and it was shown that they have same impact as conventional capacitors. In order to increase the capacitance generated by parallel plates, a number of interdigitated fingers were added on each side. A manufactured 3x3 arrays loaded with lumped capacitors, parallel plates, and interdigital capacitors were tested experimentally and a significant frequency shift was obtained. The capacitive loading using interdigital capacitor allowed the miniaturisation of the 3x3 array tag by 2.5 times while maintaining the same resonance position. Miniaturised tags on rigid and flexible substrates were manufactured and tested experimentally in free space and on dielectric phantom. It was noticed that dielectric phantom minimises the distances between the resonance stages of the tag significantly. However, it was shown that the changes in the response of the tag could still be tracked.

7.2 Future work

The following points outline some of the future research directions in the field of implantable self-resonant tags:

1- A special transmitting/receiving tag reader needs to be designed. The interrogating antenna needs to have a narrow beam width (ideally smaller than the tag's physical aperture) to maximise the reflected signal off the tag and to reduce edge effects. An advanced signal processing unit might be needed to filter out tag's response from a distorted and noisy received signal. Generally, in a communication system there are two approaches to deal with a weak received signal, this can either be achieved by trying to improve the level of the signal itself or through building a sophisticated receiver with an advanced signal processing technique. Throughout the project, the focus has been on improving tag's response. Hence, it might be a sensible research direction to work on the other end of the system in the future.

2- The tag has been tested on a single-layer dielectric phantom. The next step can be to test the tag on a multi-layer phantom. This can be easily done in a gel phantom. The layers of the phantom can be designed to resemble the properties of real bio tissues. Moreover, a real animal flesh such as pork meat can be used to test the tag inside it, as has been done in some implantable antenna projects [139].

3- Convoluted unit cell for self-resonant tag design can be studied. It can lead to a better miniaturisation ratio with an enhanced angular stability. However, finding the right degradation pattern will be challenging.

4- Moving away from the electromagnetic side of the problem, research can focus on developing a real biodegradable metal with the required characteristics such as high electrical conductivity, suitable degradation rate, and non-toxic debris. Additionally, the degradation behaviour of the metal needs to be in line with the inflammatory response of the human body (in other words the degradation rate is accelerated with higher temperature and acidity). From the literature survey that was made as part of this project, it looks like magnesium based alloys could be the best option. The position of the implant may also play an important role in the selection of alloy's chemical elements. For instance, a tag implanted in the torso could have a different material than a tag implanted in the neck due to different toxicity limits. On the other hand, although the selection of a biodegradable polymer is not as important as the biodegradable metal, polymers are basically needed as a substrate to support the resonating element. It looks like that the substrate material can be either PLA or silk protein.

5- Lastly, the next step after developing the right biodegradable material is to test the tag *in-vivo*. The tag needs to be implanted in a living animal for degradability measurements and to assess the electromagnetic response throughout material's degradation. An infection could be introduced in the form of bacteria to the tag's location to mimic an actual scenario of a surgical site infection.

REFERENCES

[1] D. Valderas, C. Schmidt, and X. Chen, "Broadband implanted UHF RFID antenna," in *2010 IEEE Antennas and Propagation Society International Symposium*, 11-17 July 2010 2010, pp. 1-4, doi: 10.1109/APS.2010.5561741.

[2] A. Sani, M. Rajab, R. Foster, and Y. Hao, "Antennas and Propagation of Implanted RFIDs for Pervasive Healthcare Applications," *Proceedings of the IEEE,* vol. 98, no. 9, pp. 1648-1655, 2010, doi: 10.1109/JPROC.2010.2051010.

[3] A. Kiourti and K. S. Nikita, "Recent Advances in Implantable Antennas for Medical Telemetry [Education Column]," *IEEE Antennas and Propagation Magazine,* vol. 54, no. 6, pp. 190-199, 2012, doi: 10.1109/MAP.2012.6387813.

[4] J. Gemio, J. Parron, and J. Soler, "Human body effects on implantable antennas for ISM bands applications: models comparison and propagation losses study," presented at the *Progress In Electromagnetics Research*, 2010.

[5] "3rd European Colorectal Cancer Days: Brno 2014 = Preventionand Screening." http://www.crcprevention.eu (accessed 2016).

[6] "World Health Organization. Colorectal Cancer " http://www.euro.who.int/en/health-topics/noncommunicable-diseases/cancer/news/news/2012/2/early-detection-of-common-cancers/colorectal-cancer (accessed 2016).

[7] H. R. Champion, R. F. Bellamy, C. P. Roberts, and A. Leppaniemi, "A profile of combat injury," vol. 54, no. no. 5, pp. S13–S19, 2003.

[8] J. Singleton, I. Gibb, H. Nicholas, A. Bull, and C. Jonathan, "Identifying future 'unexpected' survivors: a retrospective cohort study of fatal injury patterns in victims of improvised explosive devices " *BMJ Open,* vol. 3, no. 8, pp. 1–8, 2013.

[9] H. Hermawan, *Biodegradable Metals From Concept to Application*. Heidelberg, Germany Springer 2012.

[10] Y. F. Zheng, X. N. Gu, and F. Witte, "Biodegradable metals," *Materials Science and Engineering,* pp. 1-34, 2014, doi: http://dx.doi.org/10.1016/j.mser.2014.01.001.

[11] J. E. Hall and A. C. Guyton, *Guyton and Hall Textbook of Medical Physiology* (ClinicalKey 2012). Saunders/Elsevier, 2011.

[12] R. Rhoades and D. R. Bell, *Medical Physiology: Principles for Clinical Medicine*. Wolters Kluwer Health/Lippincott Williams & Wilkins, 2013.

[13] G. Villarreal, J. Zagorski, and S. Wahl, "Inflammation: Acute," *eLS,* 2003, doi: 10.1038/npg.els.0000943.

[14] V. Menkin, "The role of hydrogen ion concentration and the cytology of an exudate," *British Medical Journal,* pp. 66–103, 1956.

[15] S. Grinstein, C. J. Swallow, and O. D. Rotstein, "Regulation of cytoplasmic pH in phagocytic cell function and dysfunction," *Clinical Biochemistry,* vol. 24, no. 3, pp. 241-247, 1991, doi: http://dx.doi.org/10.1016/0009-9120(91)80014-T.

[16] M. H. Nekoofar *et al.*, "pH of pus collected from periapical abscesses," *International Endodontic Journal,* vol. 42, no. 6, pp. 534–538,, 2009.

[17] A. Health Protection and S. Nosocomial Infection National Surveillance, *Surveillance of Surgical Site Infection in English Hospitals: 1997-2002 : a National Surveillance and Quality Improvement Programme*. Health Protection Agency, 2002.

[18] N. Tomaselli, "Prevention and treatment of surgical-site infections," *Infection Control Resource,* vol. 2, no. 1.

[19] "Surgical Site Infections" http://www.hopkinsmedicine.org/healthlibrary/conditions/adult/dermatology/surgical_site_infections_134,144 (accessed 2016).

[20] J. O'Neill, "Antimicrobial resistance: tackling a crisis for the health and wealth of nations," *Review on Antimicrobial Resistance,*

[21] J. O'Neill, "Tackling Drug-Resistant Infections Globally: Final Report and Recommendations," *Review on Antimicrobial Resistance,*

[22] J. O'Neill "Rapid Diagnostics: Stopping Unnecessary Use of Antibiotics," *Review on Antimicrobial Resistance,*

[23] "Bacterial impact on wound healing: from contamination to infection," Australian Wound Management Association, 2011, vol. 1.5.

[24] "Biodegradable materials for medical applications," University of Pavia, Structural Mechanics Department.

[25] J. Ren, *Biodegradable Poly (lactic Acid): Synthesis, Modification, Processing and Applications*. Tsinghua University Press, 2010.

[26] G. D. a. K. D. a. L. J. a. K. D.-H. Cha, "Bioresorbable Electronic Implants: History, Materials, Fabrication, Devices, and Clinical Applications," *Advanced Healthcare Materials,* vol. 8, no. 11, p. 1801660, 2019, doi: 10.1002/adhm.201801660.

[27] H. Tao *et al.*, "Fully implantable and resorbable metamaterials," in *2012 Conference on Lasers and Electro-Optics (CLEO)*, 6-11 May 2012 2012, pp. 1-2, doi: 10.1364/CLEO_AT.2012.JTu1M.7.

[28] H. Tao *et al.*, "Implantable, multifunctional, bioresorbable optics," *Proceedings of the National Academy of Sciences,* vol. 109, no. 48, p. 19584, 2012, doi: 10.1073/pnas.1209056109.

[29] D.-H. Kim *et al.*, "Silicon electronics on silk as a path to bioresorbable, implantable devices," (in eng), *Applied physics letters,* vol. 95, no. 13, pp. 133701-133701, 2009, doi: 10.1063/1.3238552.

[30] M. J. Tan, C. Owh, P. L. Chee, A. K. K. Kyaw, D. Kai, and X. J. Loh, "Biodegradable electronics: cornerstone for sustainable electronics and transient applications," *Journal of Materials Chemistry C,* 10.1039/C6TC00678G vol. 4, no. 24, pp. 5531-5558, 2016, doi: 10.1039/C6TC00678G.

[31] Kenry and B. Liu, "Recent Advances in Biodegradable Conducting Polymers and Their Biomedical Applications," *Biomacromolecules,* vol. 19, no. 6, pp. 1783-1803, 2018/06/11 2018, doi: 10.1021/acs.biomac.8b00275.

[32] M. Boutry Clémentine, H. Chandrahalim, P. Streit, M. Schinhammer, C. Hänzi Anja, and C. Hierold, "Towards biodegradable wireless implants," *Philosophical Transactions of the Royal Society A: Mathematical, Physical and Engineering Sciences,* vol. 370, no. 1967, pp. 2418-2432, 2012/05/28 2012, doi: 10.1098/rsta.2011.0439.

[33] X.-N. Gu and Y.-F. Zheng, "A review on magnesium alloys as biodegradable materials," *Frontiers of Materials Science in China,* vol. 4, no. 2, pp. 111-115, 2010/06/01 2010, doi: 10.1007/s11706-010-0024-1.

[34] R. Oriňáková *et al.*, "Iron Based Degradable Foam Structures for Potential Orthopedic Applications," *International Journal of Electrochemical Science,* vol. 8, pp. 12451-12465, 12/01 2013.

[35] A. J. Domb, J. Kost, and D. M. Wiseman, *Handbook of biodegradable polymers*. Amsterdam: Harwood Academic Publishers (in English), 1997.

[36] E. Tamariz and A. Rios-Ramírez, "Biodegradation of Medical Purpose Polymeric Materials and Their Impact on Biocompatibility," in *Biodegradation- Life of Science*, R. Chamy and F. Rosenkranz Eds.: InTech, 2013, ch. One, pp. 4–29.

[37] S. Lyu and D. Untereker, "Degradability of Polymers for Implantable Biomedical Devices," *International Journal of Molecular Sciences,* vol. 10, no. 9, 2009, doi: 10.3390/ijms10094033.

[38] S. Lyu *et al.*, "In vitro biostability evaluation of polyurethane composites in acidic, basic, oxidative, and neutral solutions," *J Biomed Mater Res B Appl Biomater.,* vol. 85B, pp. pp. 509–518, 2008.

[39] R. Ward, J. Anderson, R. McVenes, and K. Stokes, "In vivo biostability of polysiloxane polyether polyurethanes: resistance to biologic oxidation and stress cracking," *J Biomed Mater Res A,* vol. 77A, pp. 580–589, 2006.

[40] A. C. Vieira , J. C. Vieira , R. M. Guedes , and A. T. Marques, "Degradation and Viscoelastic Properties of PLA-PCL, PGA-PCL, PDO and PGA Fibres," *Materials Science Forum,* vol. 636-637, pp. 825-832, 2010, doi: - 10.4028/www.scientific.net/MSF.636-637.825.

[41] L. Xu, K. Crawford, and C. B. Gorman, "Effects of Temperature and pH on the Degradation of Poly(lactic acid) Brushes," *Macromolecules,* vol. 44, no. 12, pp. 4777-4782, 2011/06/28 2011, doi: 10.1021/ma2000948.

[42] R. Li, L. Wang, D. Kong, and L. Yin, "Recent progress on biodegradable materials and transient electronics," *Bioactive Materials,* vol. 3, no. 3, pp. 322-333, 2018/09/01/ 2018, doi: https://doi.org/10.1016/j.bioactmat.2017.12.001.

[43] M. Esmaily *et al.*, "Fundamentals and advances in magnesium alloy corrosion," *Progress in Materials Science,* vol. 89, pp. 92-193, 2017/08/01/ 2017, doi: https://doi.org/10.1016/j.pmatsci.2017.04.011.

[44] A. Kiourti and K. S. Nikita, "A Review of In-Body Biotelemetry Devices: Implantables, Ingestibles, and Injectables," *IEEE Transactions on Biomedical Engineering,* vol. 64, no. 7, pp. 1422-1430, 2017, doi: 10.1109/TBME.2017.2668612.

[45] H. C. Koydemir and A. Ozcan, "Wearable and Implantable Sensors for Biomedical Applications," *Annual Review of Analytical Chemistry,* vol. 11, no. 1, pp. 127-146, 2018/06/12 2018, doi: 10.1146/annurev-anchem-061417-125956.

[46] M. M. Hugo Dinis and Paulo, "Recent Advances on Implantable Wireless Sensor Networks," 2017, doi: 10.5772/intechopen.70180.

[47] W. V. Shi and M. Zhou, "Body Sensors Applied in Pacemakers: A Survey," *IEEE Sensors Journal,* vol. 12, no. 6, pp. 1817-1827, 2012, doi: 10.1109/JSEN.2011.2177256.

[48] R. Das and H. Yoo, "Biotelemetry and Wireless Powering for Leadless Pacemaker Systems," *IEEE Microwave and Wireless Components Letters,* vol. 25, no. 4, pp. 262-264, 2015, doi: 10.1109/LMWC.2015.2400920.

[49] F. Zeng, S. Rebscher, W. Harrison, X. Sun, and H. Feng, "Cochlear Implants: System Design, Integration, and Evaluation," *IEEE Reviews in Biomedical Engineering,* vol. 1, pp. 115-142, 2008, doi: 10.1109/RBME.2008.2008250.

[50] H. Tao *et al.*, "Silk-based resorbable electronic devices for remotely controlled therapy and in vivo infection abatement," *Proceedings of the National Academy of Sciences,* vol. 111, no. 49, pp. 17385-17389, 2014.

[51] K. Fotopoulou and B. W. Flynn, "Wireless Power Transfer in Loosely Coupled Links: Coil Misalignment Model," *IEEE Transactions on Magnetics,* vol. 47, no. 2, pp. 416-430, 2011, doi: 10.1109/TMAG.2010.2093534.

[52] R. Jegadeesan, K. Agarwal, Y. Guo, S. Yen, and N. V. Thakor, "Wireless Power Delivery to Flexible Subcutaneous Implants Using Capacitive Coupling," *IEEE Transactions on Microwave Theory and Techniques,* vol. 65, no. 1, pp. 280-292, 2017, doi: 10.1109/TMTT.2016.2615623.

[53] R. Erfani, F. Marefat, A. M. Sodagar, and P. Mohseni, "Modeling and Experimental Validation of a Capacitive Link for Wireless Power Transfer to Biomedical Implants," *IEEE Transactions on Circuits and Systems II: Express Briefs,* vol. 65, no. 7, pp. 923-927, 2018, doi: 10.1109/TCSII.2017.2737140.

[54] R. V. Taalla, M. S. Arefin, A. Kaynak, and A. Z. Kouzani, "A Review on Miniaturized Ultrasonic Wireless Power Transfer to Implantable Medical Devices," *IEEE Access,* vol. 7, pp. 2092-2106, 2019, doi: 10.1109/ACCESS.2018.2886780.

[55] S. Ozeri and D. Shmilovitz, "Ultrasonic transcutaneous energy transfer for powering implanted devices," *Ultrasonics,* vol. 50, no. 6, pp. 556-566, 2010/05/01/ 2010, doi: https://doi.org/10.1016/j.ultras.2009.11.004.

[56] C. Liu, Y. Guo, H. Sun, and S. Xiao, "Design and Safety Considerations of an Implantable Rectenna for Far-Field Wireless Power Transfer," *IEEE Transactions on Antennas and Propagation,* vol. 62, no. 11, pp. 5798-5806, 2014, doi: 10.1109/TAP.2014.2352363.

[57] A. Cadei, A. Dionisi, E. Sardini, and M. Serpelloni, "Kinetic and thermal energy harvesters for implantable medical devices and biomedical autonomous sensors," *Measurement Science and Technology,* vol. 25, no. 1, p. 012003, 2013/11/13 2013, doi: 10.1088/0957-0233/25/1/012003.

[58] N. S. Shenck and J. A. Paradiso, "Energy scavenging with shoe-mounted piezoelectrics," *IEEE Micro,* vol. 21, no. 3, pp. 30-42, 2001, doi: 10.1109/40.928763.

[59] J. D. Griffin and G. D. Durgin, "Complete Link Budgets for Backscatter-Radio and RFID Systems," *IEEE Antennas and Propagation Magazine,* vol. 51, no. 2, pp. 11-25, 2009, doi: 10.1109/MAP.2009.5162013.

[60] H. N. Schwerdt, F. A. Miranda, and J. Chae, "Wireless Fully Passive Multichannel Recording of Neuropotentials Using Photo-Activated RF Backscattering Methods," *IEEE Transactions on Microwave Theory and Techniques,* vol. 63, no. 9, pp. 2965-2970, 2015, doi: 10.1109/TMTT.2015.2460746.

[61] D. Panescu, "An imaging pill for gastrointestinal endoscopy," *IEEE Engineering in Medicine and Biology Magazine,* vol. 24, no. 4, pp. 12-14, 2005, doi: 10.1109/MEMB.2005.1463383.

[62] S. Vaddiraju, M. Kastellorizios, A. Legassey, D. Burgess, F. Jain, and F. Papadimitrakopoulos, "Needle-implantable, wireless biosensor for continuous glucose monitoring," in *2015 IEEE 12th International Conference on Wearable and Implantable Body Sensor Networks (BSN)*, 9-12 June 2015 2015, pp. 1-5, doi: 10.1109/BSN.2015.7299421.

[63] E. Y. Chow, A. L. Chlebowski, S. Chakraborty, W. J. Chappell, and P. P. Irazoqui, "Fully Wireless Implantable Cardiovascular Pressure Monitor Integrated with a Medical Stent," *IEEE Transactions on Biomedical Engineering,* vol. 57, no. 6, pp. 1487-1496, 2010, doi: 10.1109/TBME.2010.2041058.

[64] W. Yu, R. Rahimi, M. Ochoa, R. Pinal, and B. Ziaie, "A Smart Capsule With GI-Tract-Location-Specific Payload Release," *IEEE Transactions on Biomedical Engineering,* vol. 62, no. 9, pp. 2289-2295, 2015, doi: 10.1109/TBME.2015.2418340.

[65] S.-K. Kang *et al.*, "Bioresorbable silicon electronic sensors for the brain," *Nature,* vol. 530, p. 71, 01/18/online 2016, doi: 10.1038/nature16492

[66] M. Luo, A. W. Martinez, C. Song, F. Herrault, and M. G. Allen, "A Microfabricated Wireless RF Pressure Sensor Made Completely of Biodegradable Materials," *Journal of Microelectromechanical Systems,* vol. 23, no. 1, pp. 4-13, 2014, doi: 10.1109/JMEMS.2013.2290111.

[67] C. M. Boutry, H. Chandrahalim, and C. Hierold, "RF conductivity of biodegradable conductive polymers used for a new generation of partially/fully resorbable wireless implantable sensors," in *2012 IEEE 25th International Conference on Micro Electro Mechanical Systems (MEMS)*, 29 Jan.-2 Feb. 2012 2012, pp. 468-471, doi: 10.1109/MEMSYS.2012.6170226.

[68] X. Xu and K. Eckerman, *Handbook of anatomical models for radiation dosimetry*. 2009.

[69] P. S. Hall and Y. Hao, *Antennas And Propagation for Body-Centric Wireless Communications*. Artech House, Inc., 2006.

[70] M. Nikolovski, "Detailed Modeling of the Human Body in Motion to Investigate the Electromagnetic Influence of Fields in a Realistic Environment," PhD, Technical University of Darmstadt, Darmstadt, Germany, 2018.

[71] A. Sani, "Modelling and characterisation of antennas and propagation for bodycentricwireless communication," PhD, Electronic Engineering, Queen Mary University of London, London, United Kingdom, 2010.

[72] A. Kiourti and K. S. Nikita, "Implantable Antennas: A Tutorial on Design, Fabrication, and In Vitro\/In Vivo Testing," *IEEE Microwave Magazine,* vol. 15, no. 4, pp. 77-91, 2014, doi: 10.1109/MMM.2014.2308765.

[73] K. a. F. K. a. O. Y. a. H. L. Ito, "Development and characteristics of a biological tissue-equivalent phantom for microwaves," *Electronics and Communications in Japan (Part I: Communications),* vol. 84, no. 4, pp. 67-77, 2001, doi: 10.1002/1520-6424(200104)84:4<67::AID-ECJA8>3.0.CO;2-D.

[74] T. Karacolak, A. Z. Hood, and E. Topsakal, "Design of a Dual-Band Implantable Antenna and Development of Skin Mimicking Gels for Continuous Glucose Monitoring," *IEEE Transactions on Microwave Theory and Techniques,* vol. 56, no. 4, pp. 1001-1008, 2008, doi: 10.1109/TMTT.2008.919373.

[75] Q. a. D. J. H. a. G. N. a. d. Z. J. A. a. v. G. P. a. S. D. K. a. B. R. Duan, "Characterization of a dielectric phantom for high-field magnetic resonance imaging applications," *Medical Physics,* vol. 41, no. 10, p. 102303, 2014, doi: 10.1118/1.4895823.

[76] J. Garrett and E. Fear, "Stable and Flexible Materials to Mimic the Dielectric Properties of Human Soft Tissues," *IEEE Antennas and Wireless Propagation Letters,* vol. 13, pp. 599-602, 2014, doi: 10.1109/LAWP.2014.2312925.

[77] D. Senic, A. Sarolic, C. L. Holloway, and J. M. Ladbury, "Whole-Body Specific Absorption Rate Assessment of Lossy Objects Exposed to a Diffuse Field Inside a Reverberant Environment," *IEEE Transactions on Electromagnetic Compatibility,* vol. 59, no. 3, pp. 813-822, 2017, doi: 10.1109/TEMC.2016.2626968.

[78] T. Qinghui, N. Tummala, S. K. S. Gupta, and L. Schwiebert, "Communication scheduling to minimize thermal effects of implanted biosensor networks in homogeneous tissue," *IEEE Transactions on Biomedical Engineering,* vol. 52, no. 7, pp. 1285-1294, 2005, doi: 10.1109/TBME.2005.847527.

[79] J. C. Lin, "Safety standards for human exposure to radio frequency radiation and their biological rationale," *IEEE Microwave Magazine,* vol. 4, no. 4, pp. 22-26, 2003, doi: 10.1109/MMW.2003.1266063.

[80] L. Subrt and P. Pechac, "Intelligent walls as autonomous parts of smart indoor environments," *IET Communications,* vol. 6, no. 8, pp. 1004-1010, 2012, doi: 10.1049/iet-com.2010.0544.

[81] L. Subrt and P. Pechac, "Controlling propagation environments using Intelligent Walls," in *2012 6th European Conference on Antennas and Propagation (EUCAP)*, 26-30 March 2012 2012, pp. 1-5, doi: 10.1109/EuCAP.2012.6206517.

[82] Y. E. Erdemli, R. A. Gilbert, and J. L. Volakis, "A reconfigurable slot aperture design over a broad-band substrate/feed structure," *IEEE Transactions on Antennas and Propagation,* vol. 52, no. 11, pp. 2860-2870, 2004, doi: 10.1109/TAP.2004.835565.

[83] A. Tennant and B. Chambers, "A single-layer tuneable microwave absorber using an active FSS," *IEEE Microwave and Wireless Components Letters,* vol. 14, no. 1, pp. 46-47, 2004, doi: 10.1109/LMWC.2003.820639.

[84] A. Abbaspour-Tamijani, K. Sarabandi, and G. M. Rebeiz, "Antenna-filter-antenna arrays as a class of bandpass frequency-selective surfaces," *IEEE Transactions on Microwave Theory and Techniques,* vol. 52, no. 8, pp. 1781-1789, 2004, doi: 10.1109/TMTT.2004.831572.

[85] R. S. Kshetrimayum and Z. Lei, "Guided-wave characteristics of waveguide based periodic structures loaded with various FSS strip layers," *IEEE Transactions on Antennas and Propagation,* vol. 53, no. 1, pp. 120-124, 2005, doi: 10.1109/TAP.2004.840527.

[86] F. Costa, A. Monorchio, S. Talarico, and F. M. Valeri, "An Active High-Impedance Surface for Low-Profile Tunable and Steerable Antennas," *IEEE Antennas and Wireless Propagation Letters,* vol. 7, pp. 676-680, 2008, doi: 10.1109/LAWP.2008.2006070.

[87] M. Niroo-Jazi and T. A. Denidni, "Electronically Sweeping-Beam Antenna Using a New Cylindrical Frequency-Selective Surface," *IEEE Transactions on Antennas and Propagation,* vol. 61, no. 2, pp. 666-676, 2013, doi: 10.1109/TAP.2012.2223440.

[88] A. Edalati and T. A. Denidni, "High-Gain Reconfigurable Sectoral Antenna Using an Active Cylindrical FSS Structure," *IEEE Transactions on Antennas and Propagation,* vol. 59, no. 7, pp. 2464-2472, 2011, doi: 10.1109/TAP.2011.2152327.

[89] N. J. G. Fonseca, "Dual-band (Tx/Rx) multiple-beam reflector antenna using a frequency selective sub-reflector for Ka-band applications," in *2015 9th European Conference on Antennas and Propagation (EuCAP)*, 13-17 April 2015 2015, pp. 1-5.

[90] F. Costa, S. Genovesi, and A. Monorchio, "A chipless RFID readable on metallic objects," in *2013 IEEE Antennas and Propagation Society International Symposium (APSURSI)*, 7-13 July 2013 2013, pp. 1498-1499, doi: 10.1109/APS.2013.6711408.

[91] F. Costa, S. Genovesi, and A. Monorchio, "A Chipless RFID Based on Multiresonant High-Impedance Surfaces," *IEEE Transactions on Microwave Theory and Techniques,* vol. 61, no. 1, pp. 146-153, 2013, doi: 10.1109/TMTT.2012.2227777.

[92] V. D. Hunt, A. Puglia, and M. Puglia, *RFID: A Guide to Radio Frequency Identification*. 2007.

[93] J. Banks, M. A. Pachano, L. G. Thompson, and D. Hanny, *Applied RFID*. Wiley, 2007.

[94] N. C. Karmakar, *Handbook of Smart Antennas for RFID Systems*. Wiley, 2011.

[95] M. Kony, M. Walter, T. Schlebusch, and S. Leonhardt, "An RFID Communication System for Medical Applications," in *2010 International Conference on Body Sensor Networks*, 7-9 June 2010 2010, pp. 71-75, doi: 10.1109/BSN.2010.20.

[96] C. Occhiuzzi, G. Contri, and G. Marrocco, "Design of Implanted RFID Tags for Passive Sensing of Human Body: The STENTag," *IEEE Transactions on Antennas and Propagation,* vol. 60, no. 7, pp. 3146-3154, 2012, doi: 10.1109/TAP.2012.2198189.

[97] X. Liu, J. L. Berger, A. Ogirala, and M. H. Mickle, "A Touch Probe Method of Operating an Implantable RFID Tag for Orthopedic Implant Identification," *IEEE Transactions on*

Biomedical Circuits and Systems, vol. 7, no. 3, pp. 236-242, 2013, doi: 10.1109/TBCAS.2012.2201258.

[98] M. S. Bhuiyan and N. Karmakar, "Chipless RFID tag based on split-wheel resonators," in *Antennas and Propagation (EuCAP), 2013 7th European Conference on*, 8-12 April 2013 2013, pp. 3054-3057.

[99] K. Sang-Dong Jang and Byung-Woo Kang and Jaehwan, "Frequency selective surface based passive wireless sensor for structural health monitoring," *Smart Materials and Structures,* vol. 22, no. 2, 2013.

[100] M. S. Bhuiyan and N. Karmakar, "A spectrally efficient chipless RFID tag based on split-wheel resonator," in *Antenna Technology: "Small Antennas, Novel EM Structures and Materials, and Applications" (iWAT), 2014 International Workshop on*, 4-6 March 2014 2014, pp. 1-4, doi: 10.1109/IWAT.2014.6958582.

[101] B. A. Munk, *Frequency Selective Surfaces: Theory and Design*. Wiley, 2005.

[102] B. Hooberman, "Everything You Ever Wanted to Know About Frequency-Selective Surface Filters but Were Afraid to Ask," 01/01 2005.

[103] E. Parker, "The Gentleman's Guide to Frequency Selective Surfaces," University of Kent Kent, UK, 1991.

[104] M. Garcia-Vigueras, F. Mesa, F. Medina, R. Rodriguez-Berral, and J. L. Gomez-Tornero, "Simplified Circuit Model for Arrays of Metallic Dipoles Sandwiched Between Dielectric Slabs Under Arbitrary Incidence," *IEEE Transactions on Antennas and Propagation,* vol. 60, no. 10, pp. 4637-4649, 2012, doi: 10.1109/TAP.2012.2207364.

[105] F. Costa, A. Monorchio, and G. Manara, "Efficient Analysis of Frequency-Selective Surfaces by a Simple Equivalent-Circuit Model," *IEEE Antennas and Propagation Magazine,* vol. 54, no. 4, pp. 35-48, 2012, doi: 10.1109/MAP.2012.6309153.

[106] C. Christos, *The Transmission-Line Modeling (TLM) Method in Electromagnetics* (The Transmission-Line Modeling (TLM) Method in Electromagnetics). Morgan & Claypool, 2006, p. 1.

[107] E. K. Miller, "A selective survey of computational electromagnetics," *IEEE Transactions on Antennas and Propagation,* vol. 36, no. 9, pp. 1281-1305, 1988, doi: 10.1109/8.8607.

[108] N. Marcuvitz, *Waveguide Handbook* (Electromagnetics and Radar Series). Peter Peregrinus Ltd., 1951.

[109] R. J. Langley and E. A. Parker, "Equivalent circuit model for arrays of square loops," *Electronics Letters,* vol. 18, no. 7, pp. 294-296, 1982, doi: 10.1049/el:19820201.

[110] R. J. Langley and E. A. Parker, "Double-square frequency-selective surfaces and their equivalent circuit," *Electronics Letters,* vol. 19, no. 17, pp. 675-677, 1983, doi: 10.1049/el:19830460.

[111] R. J. Langley and A. J. Drinkwater, "Improved empirical model for the Jerusalem cross," *Microwaves, Optics and Antennas, IEE Proceedings H,* vol. 129, no. 1, pp. 1-6, 1982, doi: 10.1049/ip-h-1.1982.0001.

[112] C. K. Lee and R. J. Langley, "Equivalent-circuit models for frequency-selective surfaces at oblique angles of incidence," *IEE Proceedings H - Microwaves, Antennas and Propagation,* vol. 132, no. 6, pp. 395-399, 1985, doi: 10.1049/ip-h-2.1985.0070.

[113] P. Callaghan, E. A. Parker, and R. J. Langley, "Influence of supporting dielectric layers on the transmission properties of frequency selective surfaces," *IEE Proceedings H - Microwaves, Antennas and Propagation,* vol. 138, no. 5, pp. 448-454, 1991, doi: 10.1049/ip-h-2.1991.0075.

[114] F. Mesa, M. García-Vigueras, F. Medina, R. Rodríguez-Berral, and J. R. Mosig, "Circuit-Model Analysis of Frequency Selective Surfaces With Scatterers of Arbitrary Geometry," *IEEE Antennas and Wireless Propagation Letters,* vol. 14, pp. 135-138, 2015, doi: 10.1109/LAWP.2014.2356012.

[115] S. Maci, M. Caiazzo, A. Cucini, and M. Casaletti, "A pole-zero matching method for EBG surfaces composed of a dipole FSS printed on a grounded dielectric slab," *IEEE Transactions on Antennas and Propagation,* vol. 53, no. 1, pp. 70-81, 2005, doi: 10.1109/TAP.2004.840520.

[116] J. E. Raynolds, B. A. Munk, J. B. Pryor, and R. J. Marhefka, "Ohmic loss in frequency-selective surfaces," *Journal of Applied Physics,* vol. 93, no. 9, pp. 5346-5358, 2003/05/01 2003, doi: 10.1063/1.1565189.

[117] M. N. O. Sadiku, *Elements of Electromagnetics* (Oxford series in electrical and computer engineering). Oxford University Press, 2001.

[118] F. Costa, A. Monorchio, and G. Manara, "An Overview of Equivalent Circuit Modeling Techniques of Frequency Selective Surfaces and Metasurfaces," *Applied Computational Electromagnetics Society,* vol. 29, no. 12 pp. 960-976, 2014.

[119] P. Callaghan, E. A. Parker, and R. J. Langley, "Influence of supporting dielectric layers on the transmission properties of frequency selective surfaces," *IEE Proc. Microw. Antennas Propag.,* vol. 138, no. 5, pp. 448-454, 1991, doi: 10.1049/ip-h-2.1991.0075.

[120] S. Orfanidis, *Electromagnetic Waves and Antennas*.

[121] D. M. Pozar, *Microwave engineering*. Fourth edition. Hoboken, NJ : Wiley, [2012] ©2012, 2012.

[122] "Mean Absolute Error," in *Encyclopedia of Machine Learning*, C. Sammut and G. I. Webb Eds. Boston, MA: Springer US, 2010, pp. 652-652.

[123] G. I. Kiani, L. G. Olsson, A. Karlsson, K. P. Esselle, and M. Nilsson, "Cross-Dipole Bandpass Frequency Selective Surface for Energy-Saving Glass Used in Buildings," *IEEE Transactions on Antennas and Propagation,* vol. 59, no. 2, pp. 520-525, 2011, doi: 10.1109/TAP.2010.2096382.

[124] P. Ragulis, P. Ängskog, R. Simniškis, B. Vallhagen, M. Bäckström, and K. Ž, "Shielding Effectiveness of Modern Energy-Saving Glasses and Windows," *IEEE Transactions on Antennas and Propagation,* vol. 65, no. 8, pp. 4250-4258, 2017, doi: 10.1109/TAP.2017.2718223.

[125] J. D. Kraus, *Electromagnetics* (McGraw-Hill Series in Electrical Engineering). McGraw-Hill, 1984.

[126] F. Costa, S. Genovesi, A. Monorchio, and G. Manara, "A Circuit-Based Model for the Interpretation of Perfect Metamaterial Absorbers," *IEEE Transactions on Antennas and Propagation,* vol. 61, no. 3, pp. 1201-1209, 2013, doi: 10.1109/TAP.2012.2227923.

[127] *Indwelling Neural Implants: Strategies for Contending with the In Vivo Environment* (Frontiers in Neuroengineering). CRC Press/Taylor & Francis, Boca Raton (FL) (in eng), 2008.

[128] A. Ferikoğlu, O. Çerezci, M. Kahriman, and Y. Ş. Ç, "Electromagnetic Absorption Rate in a Multilayer Human Tissue Model Exposed to Base-Station Radiation Using Transmission Line Analysis," *IEEE Antennas and Wireless Propagation Letters,* vol. 13, pp. 903-906, 2014, doi: 10.1109/LAWP.2014.2321283.

[129] K. Jaehoon and Y. Rahmat-Samii, "Implanted antennas inside a human body: simulations, designs, and characterizations," *IEEE Transactions on Microwave Theory and Techniques,* vol. 52, no. 8, pp. 1934-1943, 2004, doi: 10.1109/TMTT.2004.832018.

[130] T. Koleck, H. Diez, J. C. Bolomey, and R. Mittra, "A technique for analyzing finite frequency selective surfaces," in *IEEE Antennas and Propagation Society International Symposium 1997. Digest*, 13-18 July 1997 1997, vol. 4, pp. 2372-2375 vol.4, doi: 10.1109/APS.1997.625446.

[131] K. Merewether, "Spectral domain analysis of finite frequency selective surfaces," PhD, Electromagnetic Communication Laboratory, University of Illinois, Urbana, Illinois, 1989.

[132] S. Islam *et al.*, "Simulation and experimental verification of w-band finite frequency selective surfaces on infinite background with 3D full wave solver nspwmlfma," vol. 101, ed: *Progress In Electromagnetics Research*, 2010, pp. 189-202.

[133] C. A. Balanis, *Antenna Theory: Analysis and Design*. John Wiley & Sons, 2005.

[134] A. L. P. S. Campos, A. G. d'Assuncao, and L. M. d. Mendonca, "Scattering by FSS on anisotropic substrate for TE and TM excitation," *IEEE Transactions on Microwave Theory and Techniques,* vol. 50, no. 1, pp. 72-76, 2002, doi: 10.1109/22.981249.

[135] A. M. M. A. Allam and E. A. Parker, "Application of Pocklington's equation to analysis of dipole frequency-selective surfaces of finite size," *IEE Proceedings H - Microwaves, Antennas and Propagation,* vol. 134, no. 6, pp. 521-526, 1987, doi: 10.1049/ip-h-2.1987.0105.

[136] J. M. Rigelsford and C. J. Davenport, "A passive RFID implant for soft tissue trauma monitoring," in *Antennas and Propagation Conference (LAPC), 2013 Loughborough*, 11-12 Nov. 2013 2013, pp. 127-130, doi: 10.1109/LAPC.2013.6711866.

[137] H. Liu, K. L. Ford, and R. J. Langley, "Miniaturised artificial magnetic conductor design using lumped reactive components," *Electronics Letters,* vol. 45, no. 6, pp. 294-295, 2009, doi: 10.1049/el.2009.3369.

[138] I. J. Bahl, *Lumped Elements for RF and Microwave Circuits* (Artech House microwave library). Artech House, 2003.

[139] S. M. Alamri, "Implantable antennas for biomedical applications," PhD, Electronic and Electrical Engineering, University of Sheffield, Sheffield, UK, 2016.

APPENDIX A

A.1 Tag with two lossy dielectric layers on both sides

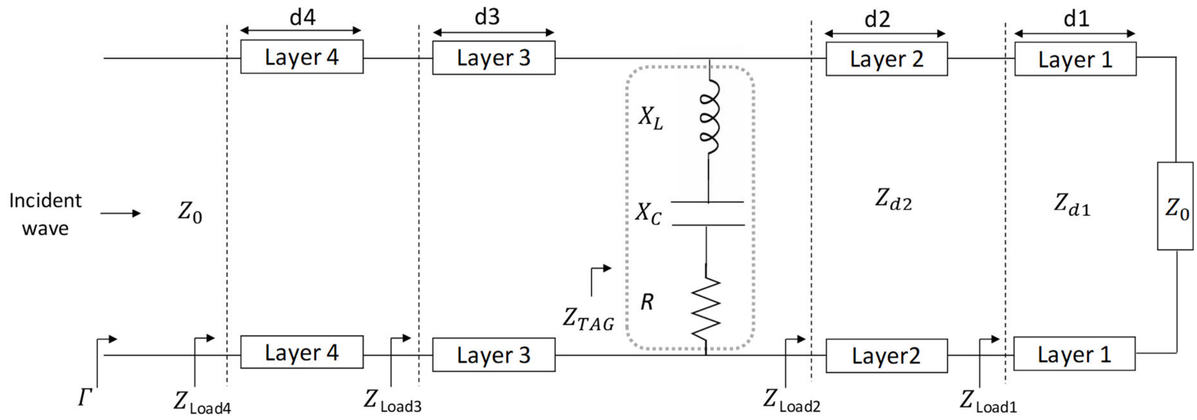

Fig. A.1 Equivalent transmission line model for self-resonant tag inside 4 layered dielectric medium.

Starting from the load end (or right side of Fig. A.1), the load impedance at each discontinuity needs to be calculated sequentially, starting from the load impedance at layer 1, $\mathrm{Z_{Load1}}$, which can be calculated as follows:

$$\mathrm{Z_{Load1}} = \mathrm{Z_{d1}} * \frac{\mathrm{Z_0} + \mathrm{Z_{d1}}\tanh(\gamma_{\mathrm{d1}}\mathrm{d1})}{\mathrm{Z_{d1}} + \mathrm{Z_0}\tanh(\gamma_{\mathrm{d1}}\mathrm{d1})} \tag{A.1}$$

And then $\mathrm{Z_{Load2}}$ using:

$$\mathrm{Z_{Load2}} = \mathrm{Z_{d2}} * \frac{\mathrm{Z_{Load1}} + \mathrm{Z_{d2}}\tanh(\gamma_{\mathrm{d2}}\mathrm{d2})}{\mathrm{Z_{d2}} + \mathrm{Z_{Load1}}\tanh(\gamma_{\mathrm{d2}}\mathrm{d2})} \tag{A.2}$$

And the equivalent impedance between $\mathrm{Z_{Load2}}$ and $\mathrm{Z_{Tag}}$ will be:

$$\mathrm{Z_{eq}} = \frac{\mathrm{Z_{Tag}} * \mathrm{Z_{Load2}}}{\mathrm{Z_{Tag}} + \mathrm{Z_{Load2}}} \tag{A.3}$$

Hence $\mathrm{Z_{Load3}}$ will be:

$$\mathrm{Z_{Load3}} = \mathrm{Z_{d3}} * \frac{\mathrm{Z_{eq}} + \mathrm{Z_{d3}}\tanh(\gamma_{\mathrm{d3}}\mathrm{d3})}{\mathrm{Z_{d3}} + \mathrm{Z_{eq}}\tanh(\gamma_{\mathrm{d3}}\mathrm{d3})} \tag{A.4}$$

And in the same way $\mathrm{Z_{Load4}}$ is given by:

$$\mathrm{Z_{Load4}} = \mathrm{Z_{d4}} * \frac{\mathrm{Z_{Load3}} + \mathrm{Z_{d4}}\tanh(\gamma_{\mathrm{d4}}\mathrm{d4})}{\mathrm{Z_{d4}} + \mathrm{Z_{Load3}}\tanh(\gamma_{\mathrm{d4}}\mathrm{d4})} \tag{A.5}$$

Thus, the reflection coefficient can be found using:

$$\Gamma = \frac{Z_{Load4} - Z_0}{Z_{Load4} + Z_0} \tag{A.6}$$

And by substituting (A.3) in (A.4), and substituting (A.4) in (A.5), and then (A.5) in (A.6) and solve for Z_{Tag}, the self-resonant tag's impedance will be:

$$Z_{Tag} = -\frac{\begin{gathered} Z_0 * Z_{d4} * Z_{d3} * Z_{Load2} - x3 * Z_{d4} * {Z_{d3}}^2 * Z_{Load2} - x4 * {Z_{d4}}^2 * Z_{d3} * Z_{Load2} + \\ \Gamma * Z_0 * Z_{d4} * Z_{d3} * Z_{Load2} + \Gamma * x4 * {Z_{d4}}^2 * Z_{d3} * Z_{Load2} + \\ \Gamma * x3 * Z_{d4} * {Z_{d3}}^2 * Z_{Load2} + x4 * x3 * Z_0 * {Z_{d3}}^2 * Z_{Load2} + \\ \Gamma * x4 * x3 * Z_0 * {Z_{d3}}^2 * Z_{Load2} \end{gathered}}{\begin{gathered} Z_0 * Z_{d4} * Z_{d3} - Z_{d4} * Z_{d3} * Z_{Load2} - x4 * {Z_{d4}}^2 * Z_{d3} - x3 * Z_{d4} * {Z_{d3}}^2 + \\ \Gamma * x4 * {Z_{d4}}^2 * Z_{d3} + \Gamma * x3 * Z_{d4} * {Z_{d3}}^2 + x4 * x3 * Z_0 * {Z_{d3}}^2 - \\ x4 * x3 * {Z_{d4}}^2 * Z_{Load2} + \Gamma * Z_0 * Z_{d4} * Z_{d3} + \Gamma * Z_{d4} * Z_{d3} * Z_{Load2} + \\ x4 * Z_0 * Z_{d3} * Z_{Load2} + x3 * Z_0 * Z_{d4} * Z_{Load2} + \Gamma * x4 * Z_0 * Z_{d3} * Z_{Load2} + \\ \Gamma * x3 * Z_0 * Z_{d4} * Z_{Load2} + \Gamma * x4 * x3 * Z_0 * {Z_{d3}}^2 + \Gamma * x4 * x3 * {Z_{d4}}^2 * Z_{Load2} \end{gathered}} \tag{A.7}$$

where $x3 = \tanh(\gamma_{d3} d3)$ and $x4 = \tanh(\gamma_{d4} d4)$.

A.2 Tag with three lossy dielectric layers on both sides

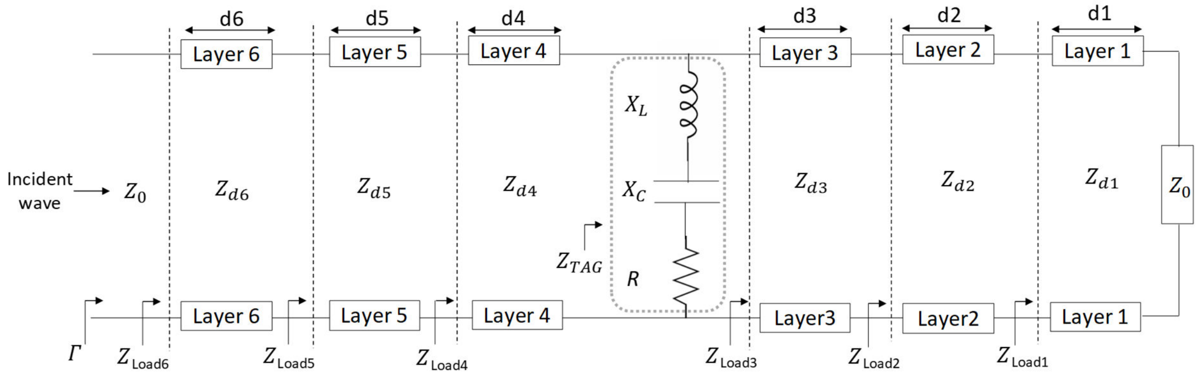

Fig. A.2 Equivalent transmission line model for self-resonant tag inside 6 layered dielectric medium.

Starting from the load end (or right side of Fig. A.2), the load impedance at each discontinuity needs to be calculated sequentially, starting from the load impedance at layer 1, $\mathrm{Z_{Load1}}$, which can be calculated as follows:

$$\mathrm{Z_{Load1}} = \mathrm{Z_{d1}} * \frac{\mathrm{Z_0} + \mathrm{Z_{d1}} \tanh(\gamma_{\mathrm{d1}} \mathrm{d1})}{\mathrm{Z_{d1}} + \mathrm{Z_0} \tanh(\gamma_{\mathrm{d1}} \mathrm{d1})} \quad (A.8)$$

And then $\mathrm{Z_{Load2}}$ using:

$$\mathrm{Z_{Load2}} = \mathrm{Z_{d2}} * \frac{\mathrm{Z_{Load1}} + \mathrm{Z_{d2}} \tanh(\gamma_{\mathrm{d2}} \mathrm{d2})}{\mathrm{Z_{d2}} + \mathrm{Z_{Load1}} \tanh(\gamma_{\mathrm{d2}} \mathrm{d2})} \quad (A.9)$$

$$\mathrm{Z_{Load3}} = \mathrm{Z_{d3}} * \frac{\mathrm{Z_{Load2}} + \mathrm{Z_{d2}} \tanh(\gamma_{\mathrm{d3}} \mathrm{d3})}{\mathrm{Z_{d2}} + \mathrm{Z_{Load2}} \tanh(\gamma_{\mathrm{d3}} \mathrm{d3})} \quad (A.10)$$

And the equivalent impedance between $\mathrm{Z_{Load2}}$ and $\mathrm{Z_{Tag}}$ will be:

$$\mathrm{Z_{eq}} = \frac{\mathrm{Z_{Tag}} * \mathrm{Z_{Load3}}}{\mathrm{Z_{Tag}} + \mathrm{Z_{Load3}}} \quad (A.11)$$

Hence $\mathrm{Z_{Load4}}$ will be:

$$\mathrm{Z_{Load4}} = \mathrm{Z_{d4}} * \frac{\mathrm{Z_{eq}} + \mathrm{Z_{d4}} \tanh(\gamma_{\mathrm{d4}} \mathrm{d4})}{\mathrm{Z_{d4}} + \mathrm{Z_{eq}} \tanh(\gamma_{\mathrm{d4}} \mathrm{d4})} \quad (A.12)$$

And in the same way $\mathrm{Z_{Load5}}$ is given by:

$$\mathrm{Z_{Load5}} = \mathrm{Z_{d5}} * \frac{\mathrm{Z_{Load4}} + \mathrm{Z_{d5}} \tanh(\gamma_{\mathrm{d5}} \mathrm{d5})}{\mathrm{Z_{d5}} + \mathrm{Z_{Load4}} \tanh(\gamma_{\mathrm{d5}} \mathrm{d5})} \quad (A.13)$$

And finally Z_{Load6} is given by:

$$Z_{Load6} = Z_{d6} * \frac{Z_{Load5} + Z_{d6}\tanh(\gamma_{d6}d6)}{Z_{d6} + Z_{Load5}\tanh(\gamma_{d6}d6)} \tag{A.14}$$

Thus, the reflection coefficient can be found using:

$$\Gamma = \frac{Z_{Load6} - Z_0}{Z_{Load6} + Z_0} \tag{A.15}$$

By substituting (A.12) in (A.13), and then (A.13) in (A.14) and solve for Z_{eq}, it can be given using:

$$Zeq = -\frac{\begin{gathered} Z_0 * Z_{d6} * Z_{d5} * Z_{d4} - x2 * Z_{d6} * {Z_{d5}}^2 * Z_{d4} - x3 * Z_{d6} * Z_{d5} * {Z_{d4}}^2 - \\ x6 * {Z_{d6}}^2 * Z_{d5} * Z_{d4} - x6 * x5 * x4 * {Z_{d6}}^2 * {Z_{d4}}^2 + \\ \Gamma * Z_0 * Z_{d6} * Z_{d5} * Z_{d4} + \Gamma * x6 * {Z_{d6}}^2 * Z_{d5} * Z_{d4} + \\ \Gamma * x5 * Z_{d6} * {Z_{d5}}^2 * Z_{d4} + \Gamma * x4 * Z_{d6} * Z_{d5} * {Z_{d4}}^2 + \\ x6 * x5 * Z_0 * {Z_{d5}}^2 * Z_{d4} + x6 * x4 * Z_0 * Z_{d5} * {Z_{d4}}^2 + \\ x5 * x4 * Z_0 * Z_{d6} * {Z_{d4}}^2 + \Gamma * x6 * x5 * Z_0 * {Z_{d5}}^2 * Z_{d4} + \\ \Gamma * x6 * x4 * Z_0 * Z_{d5} * {Z_{d4}}^2 + \Gamma * x5 * x4 * Z_0 * Z_{d6} * {Z_{d4}}^2 + \\ \Gamma * x6 * x5 * x4 * {Z_{d6}}^2 * {Z_{d4}}^2 \end{gathered}}{\begin{gathered} \Gamma * Z_{d6} * Z_{d5} * Z_{d4} - x6 * x5 * {Z_{d6}}^2 * Z_{d4} - x6 * x4 * {Z_{d6}}^2 * Z_{d5} - \\ x5 * x4 * Z_{d6} * {Z_{d5}}^2 - Z_{d6} * Z_{d5} * Z_{d4} + x6 * Z_0 * Z_{d5} * Z_{d4} + \\ x5 * Z_0 * Z_{d6} * Z_{d4} + x4 * Z_0 * Z_{d6} * Z_{d5} + s * x6 * Z_0 * Z_{d5} * Z_{d4} + \\ \Gamma * x5 * Z_0 * Z_{d6} * Z_{d4} + \Gamma * x4 * Z_0 * Z_{d6} * Z_{d5} + \Gamma * x6 * x5 * {Z_{d6}}^2 * Z_{d4} + \\ \Gamma * x6 * x4 * {Z_{d6}}^2 * Z_{d5} + \Gamma * x5 * x4 * Z_{d6} * {Z_{d5}}^2 + \\ x6 * x5 * x4 * Z_0 * {Z_{d5}}^2 + \Gamma * x6 * x5 * x4 * Z_0 * {Z_{d5}}^2 \end{gathered}} \tag{A.16}$$

And by rearranging (A.11), Z_{Tag} can be found using:

$$Z_{Tag} = -\frac{Z_{eq} * Z_{Load3}}{Z_{eq} - Z_{Load3}} \tag{A.17}$$

where $x4 = \tanh(\gamma_{d4}d4), x5 = \tanh(\gamma_{d5}d5)$, and $x6 = \tanh(\gamma_{d6}d6)$.